THÈSE

Pour obtenir le grade de

DOCTEUR DE L'UNIVERSITÉ GRENOBLE ALPES

École doctorale : EEATS - Electronique, Electrotechnique, Automatique, Traitement du Signal
Spécialité : Automatique - Productique
Unité de recherche : CEA LETI - Laboratoire d'électronique et de technologie de l'information

Modélisation de la rétrodiffusion électromagnétique en champ proche pour des applications radar et de détection multistatiques

Near-Field Electromagnetic Backscattering Modeling for Multi-Static Radar and Sensing applications

Présentée par :

Tom MALHERBE

Direction de thèse :

Christophe DELAVEAUD Directeur de recherche, CEA-LETI	Directeur de thèse
Raffaele D'ERRICO INGENIEUR DE RECHERCHE, CEA LETI	Co-encadrant de thèse

Rapporteurs :

Christophe BOURLIER
DIRECTEUR DE RECHERCHE, CNRS
Christophe ROBLIN
ASSOCIATE PROFESSOR, Télécom Paris

Thèse soutenue publiquement le **19 décembre 2025**, devant le jury composé de :

Christophe BOURLIER, DIRECTEUR DE RECHERCHE, CNRS	Rapporteur
Christophe ROBLIN, ASSOCIATE PROFESSOR, Télécom Paris	Rapporteur
Marina BARBIROLI, ASSOCIATE PROFESSOR, University of Bologna	Examinatrice
Cyril DECROZE, PROFESSEUR DES UNIVERSITES, Université de Limoges	Examinateur
Fabien NDAGIJIMANA, PROFESSEUR DES UNIVERSITES, Université Grenoble Alpes	Président
Christophe DELAVEAUD, DIRECTEUR DE RECHERCHE, CEA CENTRE DE GRENOBLE	Directeur de thèse

Invités :

Gildas KUBICKE
EXPERT TECHNIQUE, DGA
Raffaele D'ERRICO
INGENIEUR DE RECHERCHE, CEA LETI

Remerciements

Lorsque j'ai commencé ma thèse, je ne savais pas vraiment où j'allais ni pourquoi je la faisais. Tout ce que je savais, c'est que j'aimais le sujet et que je me sentais capable de tout réaliser. Imaginez : vous avez les bases de l'électronique, vous savez comment générer un signal, comment extraire des données de ce signal, mais il vous reste une boîte blanche : comment mon signal va-t-il se rendre de ma source à mon récepteur ? C'est là que l'étude de la propagation apparaît. Ce besoin de comprendre la chaîne dans sa globalité était pour moi une évidence. C'est pourquoi, grâce à Gloria, j'ai entrepris l'aventure au CEA-Leti en stage, qui s'est ensuite concrétisée par cette thèse.

Je voudrais tout d'abord remercier les membres de mon jury d'avoir accepté d'évaluer ce travail. Je vous suis reconnaissant pour le temps et l'attention que vous avez consacrés à la lecture de cette thèse. C'est un honneur pour moi de pouvoir vous présenter aujourd'hui le résultat de ces travaux.

Bien sûr, cette thèse n'aurait pas pu voir le jour sans Raffaele et Christophe, qui ont fait de leur mieux pour m'épauler et me faire avancer. Il m'aura fallu du temps pour appréhender votre fonctionnement, mais une fois fait, l'entente a été bonne. Je tiens également à vous remercier pour le temps que vous m'avez laissé, que ce soit pour développer mes idées pendant la thèse, mais aussi pour le temps après, lorsque j'oscillais entre perte de motivation et envie de passer à autre chose. Je remercie également Étienne Perret et Laurent Ferro-Famil, les deux membres de mon comité de suivi, pour leurs précieux conseils.

Merci aussi à tous les membres du LAPCI, qui m'ont apporté leur aide ou avec qui j'ai

simplement partagé de bons moments. Je remercie ainsi Gloria pour l'opportunité du stage ; Serge et Olivier pour l'utilisation de CST ; Francesco, Antonio et Camille pour l'aide sur les antennes ; Mathieu pour les problèmes de mesures ; et Laurent pour les commandes de pièces. Je remercie aussi Jeff, Mélanie, Yohann, Lotfi, Hussein et François pour les moments passés autour d'une pause café, d'un repas ou d'une course entre midi et deux.

Merci également aux anciens doctorants du laboratoire, ceux qui m'ont fait dire : « Finalement, une thèse, ce n'est peut-être pas si horrible ». Merci donc à Céline, Luis, Alessio, Orestis, Marwan et Pamela. Et pour finir, je tiens à remercier ceux qui n'ont jamais été contre une sortie au bar ou une activité le week-end : Fred, Marie, Joseph, Jules, Maha, Alessio et Paul.

Sans votre présence à tous, ces années de travail auraient été moins agréables. et les conférences moins mémorables, que ce soit en traversant une horde de zombies à Portland ou dans un bar collant de Juan-les-Pins.

Merci à mes amis. Je n'ai clairement pas assez profité de vous pendant cette thèse pour me redonner du baume au cœur dans les moments de doute. En écrivant ces remerciements, je réalise à quel point vous me manquez, et que j'aurais dû faire plus d'efforts pour passer du temps avec vous.

Merci également à ma famille, que j'aime de tout mon être. Je ne sais pas vraiment pourquoi je dois vous remercier... pour votre amour, pour votre présence, pour faire partie de ces lumières qui scintillent dans mon cœur ? Je vous remercie tout simplement pour tout. En soi, vous ne m'avez pas directement aidé pour la thèse, je ne pense pas vraiment que vous sachiez exactement ce que j'ai fait, ni à quoi ça sert, mais je vous remercie quand même.

Et pour finir merci à toi Mélina, je t'aime.

Abstract

This thesis presents a framework for modeling and predicting near-field electromagnetic backscattering, with the goal of enabling practical designs for next-generation radar and Joint Communication and Sensing (JCAS) in future wireless networks, exploiting multiple antennas systems. The focus is on modeling the backscattering of extended targets, for which the far-field condition is not satisfied at typical application ranges.

The proposed model combines Iterative Physical Optics (IPO) and Equivalent Edge Current (EEC) methods, capturing near-field phenomena such as diffraction, interference and multipath. It is further enhanced by advanced meshing strategies, ray-tracing-based shadowing, and acceleration techniques to balance accuracy with computational efficiency. The model can predict the near-field Radar Cross Section (RCS) or the full round-trip channel, including angular-dependent complex antenna factors, and multi-static conditions.

The framework is first developed for Perfect Electric Conductor (PEC) objects, then extended to lossy and dielectric materials. Validation is carried out through full-wave simulations and a dedicated measurement setup in the millimeter-wave bands, where the large electrical size of targets naturally leads to near-field conditions.

Contents

Remerciements **3**

List of acronyms **13**

Notations **15**

Résumé en français **23**

1 Introduction **31**

1.1 Context of the thesis 31

1.1.1 Historical background on radar 31

1.1.2 The future of Radar 32

1.2 Personal contribution and manuscript outline 33

2 Near field backscattering model **37**

2.1 Introduction 37

2.2 Theoretical electromagnetic backscattering 37

2.2.1 Propagation equation 37

2.2.2 Boundaries limits 40

2.2.3 Reflection Coefficients 40

2.2.4 Reflection and Scattering from Material Interfaces via Equivalent Surface Currents 41

2.2.5 Stratton-Chu integral equations 42

2.2.6 Near field Radar Cross Section 44

2.3 Model of the backscattering 47

2.3.1 Analytic method 47

2.3.2 Numerical discrete methods 47

2.3.2.1 Finite-Difference Time-Domain 48

2.3.2.2 Finite Element Method 48
2.3.2.3 Method of Moments 48
2.3.2.4 Geometrical Optics 49
2.3.2.5 Physical Optics 49
2.3.3 Equivalent Edge Current 52
2.3.3.1 Fringe currents 53
2.3.3.2 Physical optics currents 58
2.4 Choice of Physical Optics 59
2.5 Conclusion 62

3 Near Field Target Scattering Model by IPO 63
3.1 Introduction 63
3.2 Integral resolution 63
3.2.1 Plane surface meshing 63
3.2.2 Curved surface meshing adaptation 67
3.2.3 Edge meshing 71
3.2.4 Complexity and adaptation for multiple bounces 73
3.2.5 IPO and EEC model 75
3.3 Target shadowing 79
3.3.1 Antenna to target shadowing 80
3.3.2 Target to target shadowing 82
3.3.3 Edge illumination 83
3.4 Acceleration of the model 84
3.4.1 Segmented IPO 84
3.4.2 Matrix Resolution 85
3.4.3 Matrix compression 86
3.4.4 Fast Far Field Approximation 87
3.5 Conclusion 88

4 Antenna effects and measurement validation 89
4.1 Introduction 89
4.2 Antennas's integration 89
4.2.1 Limitation of the NF-RCS 89

4.2.1.1 Limitation due to incident wave . . . 90
4.2.1.2 Limitation due to the scattered wave . . . 90
4.2.2 Round-trip transfer function definition . . . 91
4.2.3 Antenna model integration . . . 93
4.2.3.1 Integration of dipole antennas . . . 93
4.2.3.2 Integration of horn antennas . . . 95
4.2.3.3 Implementation in a complex scenario . . . 99
4.3 Measurement validation . . . 101
4.3.1 Measurement setup . . . 101
4.3.1.1 Measurement setup presentation . . . 102
4.3.1.2 Alignment of the setup for high precision measurement . 102
4.3.1.3 Processing chain . . . 104
4.3.2 Measurement results . . . 105
4.3.2.1 Validation on a metallic plate . . . 105
4.3.2.2 Validation on a sphere . . . 106
4.3.2.3 Validation on a metallic trihedron . . . 107
4.4 Conclusion . . . 108

5 Modeling Wave Propagation in Dielectric and Lossy Targets: Validation and Application to Human Body Backscattering 111
5.1 Introduction . . . 111
5.2 Model application for dielectric and lossy media . . . 111
5.2.1 Adaptation of the IPO model . . . 111
5.2.2 Equivalent Edge Current adaptation . . . 115
5.2.3 Implementation in the model . . . 116
5.2.4 Results obtained without penetration . . . 119
5.2.4.1 Lossy metal . . . 119
5.2.4.2 Dielectric media . . . 120
5.2.4.3 Lossy dielectric media . . . 121
5.2.5 Experimental validation . . . 123
5.3 Application to human body sensing . . . 126
5.3.1 Validation using a cube made on human body mimic material . . 126
5.3.2 Human body scenario . . . 127

5.3.2.1 Human body scattering in close range 127
5.3.3 Round Trip Transfer Function 127
5.3.4 NF-RCS 129
5.4 Conclusion 130

6 Conclusions and perspectives **133**
6.1 Conclusions 133
6.2 Perspectives 135
6.2.1 Perspectives - Model amelioration 135
6.2.2 Perspectives - Model utilization 139

7 Appendix **141**

8 List of Publications **147**

List of acronyms

RCS	Radar Cross Section
RCSR	Radar Cross Section Reduction
NF	Near Field
NF-RCS	Near Field Radar Cross Section
PEC	Perfect Electric Conductor
PMC	Perfect Magnetic Conductor
EFIE	Electric Field Integral Equation
MFIE	Magnetic Field Integral Equation
AOD	Angle of Departure
AoA	Angle of Arrival
SC	Scattering coefficient
SC	Scattering coefficient
NURBS	Non-uniform Rational B-Splines
FDTD	Finite-Difference Time-Domain
FEM	Finite Element Method
PML	Perfectly Matched Layer
MOM	Method of Moments
IE	Integral Equation
GO	Geometrical Optics
GTD	Geometry Theory of Diffraction
UTD	Uniform Theory of Diffraction
PTD	Physical Theory of Diffraction
MEC	Method of Equivalent Current
EEC	Equivalent Edge Current
SAR	Synthetic Aperture Radar
JCAS	Joint Communication And Sensing
PO	Physical Optics
IPO	Iterative Physical Optics
PPO	Progressive Physical Optics
PPO	Segmented Iterative Physical Optics

ACA Adaptive Cross Approximation

FaFFA Fast Far Field Approximation

FIT Finite Integration Technique

RTF Round-Trip Transfer Function

VNA Vector Network Analyzer

IBC Impedance Boundary Conditions

MTPO Modified Theory of Physical Optics

MECA Modified Equivalent Current Approximation

MPOA Modified Physical Optics Approximation

RMSE Root Mean Square Error

Notations

We establish as a convention for the remainder of this document a time dependence in $e^{+j\omega t}$ *where* ω *represents the angular frequency. Furthermore, vectors will be denoted in bold* $\mathbf{X}$*, unit vectors in bold with a circumflex* $\hat{\mathbf{X}}$*, and the norm of the vector* $\mathbf{X}$ *will be noted as* $X = \|\mathbf{X}\|$

Quantity	**Notation**	**Unit**
Vector between two elements	$\mathbf{R}$	m
Position of elements	$\mathbf{r}$	m
Dimension of the target	D_{Targ}	m
Electric field	$\mathbf{E}$	$V \cdot m^{-1}$
Magnetic field	$\mathbf{H}$	$A \cdot m^{-1}$
Magnetic current density	$\mathbf{M}$	$V.m^{-2}$ or $V.m^{-1}$ (on interface)
Electric current density	$\mathbf{J}$	$A.m^{-2}$ or $A.m^{-1}$ (on interface)
Equivalent electric current of edge	$\boldsymbol{\mathcal{J}}$	$A.m^{-1}$
Equivalent magnetic current of edge	$\boldsymbol{\mathcal{M}}$	$V.m^{-1}$
Electric Charge density	ρ_e	$C \cdot m^{-3}$
Magnetic Charge density	ρ_m	-
Wavelength	λ	m
Frequency	f	Hz
Radian frequency	ω	$rad \cdot s^{-1}$
Wave vector	$\mathbf{k}$	m^{-1}
Speed of light in free space	c	$m \cdot s^{-1}$
Velocity of propagation	ν	$m \cdot s^{-1}$
Impedance	η	Ω
Admittance	Y	Ω^{-1}
Permeability	μ	$H \cdot m^{-1}$
Permittivity	ε	$F \cdot m^{-1}$
Conductivity	σ	$S \cdot m^{-1}$
Skin depth	δ	m

Reflection coefficient	Γ	-
Transmission coefficient	τ	-
Refers to parallel polarization	$-_{\parallel}$	-
Refers to perpendicular polarization	$-_{\perp}$	-
Refers to diffraction	$-_{dif}$	-
Refers to incidence	$-_{inc}$	-
Refers to reflection	$-_{ref}$	-
Refers to transmitted	$-_{tra}$	-
Refers to a source	$-_{sou}$	-
Refers to the total field	$-_{total}$	-
Refers to the receiver	$-_{R}$	-
Refers to a receiver position	$-_{rec}$	-
Refers to the transmitter	$-_{T}$	-
Refers to physical optics (EEC)	$-^{PO}$	-
Refers to fringe (EEC)	$-^{f}$	-
Volume of the target	V	m^3
Surface of the target	$\mathcal{S}$	m^2
Edge of the target	$\mathcal{C}$	m
Refers to material 1	$-_1$	-
Refers to material 2	$-_2$	-
Green function	ψ	-
Generator voltage	V	-
Step function for illumination	U	-

List of Figures

1 (a) Plaque : configuration de mesure ; (b) résultats de la rétrodiffusion en champ proche pour différents angles d'azimut 0° → 35° : modèle (trait continu) vs. mesure (trait pointillé). 27

2 (a) Configuration de mesure de la rétrodiffusion. (b) Résultats de la rétrodiffusion en champ proche pour différents angles d'azimut : modèle (trait continu) vs. mesure (trait pointillé). 29

1.1 Target radiation in near and far field 33

2.1 Presentation of the electromagnetic wave propagation 39
2.2 Boundary conditions - limits between medium 1 and medium 2 40
2.3 Reflection and Transmission at an interface, Parallel and perpendicular polarization . . . 42
2.4 Surface current on boundary between two media 1 and 2 43
2.5 Target scattering, bistatic far field RCS and NF-RCS 44
2.6 Physical optics equivalent for scattering by a PEC. **left**. Actual problem **right**. Physical equivalent 50
2.7 Physical optics, multiple bounces scenario. 51
2.8 Equivalent Edge Current Scenario 52
2.9 Edge radiation geometry for two surfaces 1 and 2 54
2.10 (a) SBR ray-tube evolution in far field (b) SBR ray-tube evolution in near field 61

3.1 Target geometry for sub-surface m, integration over the triangle m 64
3.2 Change of basis for the triangle ABC 66
3.3 NF-RCS evolution between 10 GHz and 30 GHz for different distances from a flat plate of 20 cm side 67
3.4 Illustration of meshing phenomenon: transformation of spherical wave and surface into planar approximation 68
3.5 Meshing for a curved surface 68
3.6 STL implementation: target geometry for sub-surface m 70
3.7 Definition of the sub-element meshing for curvature target 70
3.8 NF-RCS for the frequency range [20GHz;30GHz] for a 10 cm curved plate with a transceiver placed at 30 cm of the plate 71
3.9 Target geometry for sub-edge p, integration over the edge p 72

3.10 Pyramid diffraction in forward scattering **(a)** scenario with a 10 cm pyramid **(b)** Comparison of the forward scattering for four different receiver positions 73
3.11 Evolution of the near field RCS at 30 cm for a 20 cm dihedral plate for the frequency range [20GHz;30GHz]. One of the two plates is a curved plate. **a**. Geometry **b**. Comparison model with reference simulation 75
3.12 Evolution of the near field RCS at 30 cm for a 20 cm dihedral plate for the frequency range [20 GHz; 30 GHz] for several mesh sizes. Comparison with reference simulation. . 76
3.13 Evolution of the near field RCS at 30 cm for a 20 cm trihedral plate for the frequency range [20 GHz; 30 GHz] for several mesh sizes. Comparison with reference simulation. . 77
3.14 Edge diffraction: method under test. **a** scattering of the edge with both methods. **b** Equivalent current on the edge for both methods 78
3.15 Shadowing approach **(a)** scenario with one obstacle **(b)** Methods to resolve shadowing, **left** shape shadowing **right** Center of the surface shadowing 80
3.16 Antenna to target shadowing 81
3.17 Presentation of the meshing result for a rabbit STL source **(a)** initial shape **(b)** meshing result : white surfaces 82
3.18 Surface-to-surface shadowing: variation of the angle with respect to the distance from source n 83
3.19 Edge diffraction between two surfaces with different sizes 83
3.20 Application of the PPO and S-IPO models for cavity 84
3.21 Fast Far Field Approximation: comparison of a near field radiation and far field radiation 88

4.1 Calculation of the backscattering directly or by using the near field RCS 92
4.2 Electric field scattered by the dipole antenna at 1 m with a unit input power: **(a)** Vertical polarization: **(b)** Horizontal polarization 94
4.3 Transfer function of the plate answer according to the distance plate-antenna: Dipole antenna 94
4.4 (a) Geometry of the scenario (b) Transfer function of the plate response as a function of the number of bounces: Dipole antenna 95
4.5 Modeling of a horn antenna in the PO model 97
4.6 Electric field scattered by the horn antenna: **(a)** Vertical polarization: **(b)** Horizontal polarization 97
4.7 Transfer function of the plate response as a function of the plate–antenna distance: Horn antenna 98
4.8 (a) Geometry of the scenario (b) Transfer function of the plate answer according to the number of bounces: Horn antenna 99
4.9 (a) Geometry of the scenario (b) Transfer function of the box response as a function of the number of bounces 101
4.10 Measurement setup: antenna and target placement using positioners 102

4.11 (a) Alignment with the center of the target, (b) alignment with the center of the antennas 104
4.12 Round trip transfer function according to the rotation (**a**) close to the specular direction scattering (**b**) rotation of 20° from the specular direction 104
4.13 (a) Plate: measurement setup (b): results of the backscattering in the near field for different azimuthal angles $0° \rightarrow 35°$ 106
4.14 (a) Sphere: measurement setup (b): Results of the backscattering in the near field for different distances $1.2m \rightarrow 0.5m$ 107
4.15 (a) Trihedron: measurement setup (b): Results of the backscattering in the near field for different angles $0° \rightarrow 30°$ 108

5.1 Modified Equivalent Current Approximation geometry, parallel and perpendicular components 114
5.2 Targets geometry, respectively cube and dihedral 120
5.3 Round trip transfer function for $\sigma = 1e^5 S.m^{-1}$ (a) Geometry 1, (b) Geometry 2 120
5.4 Round trip transfer function for $\varepsilon = 5\ \varepsilon_1$ (a) Geometry 1, (b) Geometry 2 121
5.5 Round trip transfer function for $\varepsilon = 1.5\ \varepsilon$ (a) Geometry 1, (b) Geometry 2 121
5.6 Target geometry: 10 cm cube rotate along x and y 123
5.7 Round trip transfer function for the cube (a) rotation of 15°, (b) rotation of 30° 123
5.8 Presentation of the Teflon measurement setup 124
5.9 Presentation of the Teflon measurement **(a)** Time domain response of the measurement **(b)** comparison with the model 125
5.10 Decomposition of the Teflon scenario 125
5.11 Backscattering measurement setup (a). Results of the backscattering in the near field for different azimutal angles (b): model (continous line) vs. measurement (dashed line). 126
5.12 Human body mannequin geometry and initial meshing with antenna positioning 127
5.13 Normalized backscattered field, both antenna in front (a). Round trip transfer function of the scenario 1 (b). Normalized backscattered field TX on the side, RX on the front (c). Round trip transfer function of the scenario 2 (d). 128
5.14 Human body bistatic RCS at 50 cm and 10 m for three different incident angles corresponding to TX1 (a), TX2 (b), TX3 (c). Human body and antenna positioning(d). . . . 129
5.15 Evolution of human body monostatic RCS along distance 130

6.1 Presentation of the code implementation 136

List of Tables

3.1 Parameters: Impacts of the distance in the NF-RCS monostatic in normal incidence . . 67

3.2 Parameters used for Fig. 3.8 71

5.1 Size of the different matrix for M elements radiating towards N elements 118

5.2 Memory usage for two square plates with 20 cm side which radiate in a material with $\varepsilon = 5\varepsilon_0$ at 30 GHz with a meshing of $\lambda^2/10$ 119

5.3 Model performance for rotated cube using RMSE in dB for θ ranging from 0° to 30° . . 122

Résumé en français

Contexte et enjeux

Les systèmes radar modernes évoluent vers des architectures distribuées et des fréquences millimétriques afin d'améliorer la résolution angulaire, la sensibilité et la capacité de détection dans des scénarios complexes (automobile, robotique, santé, réseaux 6G). Dans certains cas d'usage à faible distance avec des cibles électriquement grandes, le champ incident n'est plus convenablement approché par une onde plane et les mécanismes de rétrodiffusion dépendent fortement de la géométrie locale, de la distance d'observation et des effets d'interactions multiples ainsi que l'ombrage et la diffraction des arêtes. Le régime champ proche se caractérise classiquement par le critère de Fraunhofer

$$R < \frac{2D_{\text{targ}}^2}{\lambda},$$

où D_{targ} représente la dimension caractéristique de la cible et λ la longueur d'onde. Dans ce régime, la définition usuelle de la Section Efficace Radar (SER ou Radar Cross Section RCS en anglais) intrinsèquement définie en champ lointain devient inadaptée : il faut recourir à une NF-RCS (Near-Field RCS) cohérente avec la physique locale et compatible avec l'équation radar. Pour modéliser la rétrodiffusion, il existe des méthodes analytiques exactes, limitées aux géométries canoniques (ex. sphère de Mie) et des méthodes numériques (FDTD, FEM, MoM) précises mais coûteuses pour des cibles grandes et des bandes larges en fréquence. Entre ces deux extrêmes, les approches asymptotiques (Optique Géométrique, Optique Physique, PTD/UTD) constituent un compromis attractif lorsque l'on sait combiner les contributions de surfaces et d'arêtes de la cible.

Objectifs de la thèse

Cette thèse vise à développer un modèle hybride IPO-EEC (Iterative Physical Optics- Equivalent Edge Current) capable de prédire de manière efficace et fiable la rétrodiffusion en champ proche d'objets électriquement grands, dans des configurations mono- et multi-statiques. Le modèle combine une formulation IPO adaptée au champ proche, permettant de prendre en compte les interactions multiples et les

fronts d'onde non plans, avec une modélisation EEC des arêtes, destinée à représenter rigoureusement les contributions diffractées et les discontinuités de densités de courants. L'approche s'appuie également sur des stratégies de maillage avancées, intégrant des surfaces planes et courbes, et sur une gestion précise des ombrages à l'aide d'un lancer de rayons entre les antennes et les différentes cibles.

Cadre théorique et choix méthodologiques

La formulation s'appuie sur les équations intégrales de Stratton-Chu et la représentation des densités de courant équivalentes de surface ($\mathbf{J} = \hat{\mathbf{n}} \times \mathbf{H}$, $\mathbf{M} = \hat{\mathbf{n}} \times \mathbf{E}$). L'optique physique (PO) fournit une approximation efficace des densités de courant de surface sur les zones éclairées, tandis que l'EEC (issue de la PTD) ajoute des densités de courant d'arêtes pour capturer correctement les champs diffractés en présence de discontinuités géométriques. L'IPO consiste à réinjecter itérativement le champ diffusé comme champ incident, ce qui rend possible la modélisation des multi-réflexions pertinentes en champ proche et dans les cavités ou géométries concaves.
Le maillage est crucial : des facettes triangulaires adaptées à la courbure limitent les erreurs de planéité effective du front d'onde local. Les ombrages sont traités via un lancer de rayons depuis les éléments rayonnants (antennes et facettes) pour déterminer visibilités, chemins multiples et illumination des arêtes. En prenant un élément suffisamment fin pour qu'il respecte le critère de Fraunhofer, le champ magnétique rétrodiffusé par l'élément m, $\mathbf{H}_{\text{scat}}^{(m)}$, au point de réception $\mathbf{r}_{\text{rec}}^{(m)}$, peut s'écrire sous la forme :

$$\begin{aligned}\mathbf{H}_{\text{scat}}^{(m)}\left(\mathbf{r}_{\text{rec}}^{(m)}\right) = \Bigg[& -\frac{jk\,R_{\text{rec}}^{(m)\prime}+1}{R_{\text{rec}}^{(m)\prime}}\left(\mathbf{J}^{(m)\prime}\times\hat{\mathbf{R}}_{\text{rec}}^{(m)\prime}\right)+\frac{1}{\eta}\,\frac{-1-jk\,R_{\text{rec}}^{(m)\prime}+\left(k\,R_{\text{rec}}^{(m)\prime}\right)^2}{jk\left(R_{\text{rec}}^{(m)\prime}\right)^2}\,\mathbf{M}^{(m)\prime} \\ & +\frac{1}{\eta}\,\frac{-3-3jk\,R_{\text{rec}}^{(m)\prime}+\left(k\,R_{\text{rec}}^{(m)\prime}\right)^2}{jk\left(R_{\text{rec}}^{(m)\prime}\right)^2}\left(\mathbf{M}^{(m)\prime}\cdot\hat{\mathbf{R}}_{\text{rec}}^{(m)\prime}\right)\hat{\mathbf{R}}_{\text{rec}}^{(m)\prime}\Bigg]\,\frac{e^{-jkR_{\text{rec}}^{(m)\prime}}}{4\pi R_{\text{rec}}^{(m)\prime}} \\ & \times\iint_{s^{(m)}}\exp\!\left\{-jk\left(R_{\text{rec}}^{(m)}-R_{\text{rec}}^{(m)\prime}\right)\right\}\exp\!\left\{-jk\left(R_{\text{sou}}^{(m)}-R_{\text{sou}}^{(m)\prime}\right)\right\}\mathrm{d}S^{(m)}.\end{aligned} \tag{1}$$

où $k = 2\pi/\lambda$ est le nombre d'onde, η l'impédance du milieu, $\hat{\mathbf{R}}_{\text{rec}}^{(m)\prime}$ le vecteur unitaire pointant du centre de l'élément m vers le récepteur, $\mathbf{J}^{(m)\prime}$ et $\mathbf{M}^{(m)\prime}$ les densités de courants équivalents (électrique et magnétique) évaluées au centre de l'élément,$R_{\text{rec}}^{(m)}$ et $R_{\text{sou}}^{(m)}$ représentent respectivement les distances entre l'élément m et le récepteur/la source,et la notation « $\cdot'$ » indique l'évaluation à partir du centre de l'élément. L'intégrale de surface somme de manière cohérente les contributions de phase. Pour l'optique physique, les densités de courant sont définies pour les éléments parfaitement conducteurs comme:

$$\mathbf{J}^{(\mathbf{m})'} = 2\hat{\mathbf{n}}\times\mathbf{H}_{inc}^{(m)'}\ \text{et}\ \mathbf{M}^{(\mathbf{m})'} = 0 \tag{2}$$

Pour les densités de courant équivalentes localisées sur les arêtes, leur expression résulte de deux contributions principales. La première consiste à introduire des courants de frange le long des arêtes, destinés à représenter les champs diffractés manquants dans la formulation d'optique physique. La seconde vise à corriger la PO afin d'assurer la continuité des champs tangents au voisinage des discontinuités

géométriques. En combinant ces deux effets, on obtient une expression des densités de courant d'arêtes en fonction des directions du champ incident et de celles du champ diffracté, ce qui permet de modéliser de manière cohérente la contribution diffractée au champ total.

Développement du modèle IPO-EEC en champ proche

Le modèle proposé calcule le champ rétrodiffusé ou, de manière équivalente, une NF-RCS compatible avec l'équation radar en champ proche. La NF-RCS s'exprime comme

$$\sigma_{NF-RCS} = \left\| \sqrt{4\pi} \frac{\sum_S R_T R_R \mathbf{E}_{scat} \cdot \hat{\mathbf{p}}}{\|V\|} \right\|^2 \tag{3}$$

où :

- $\sigma_{NF\text{-}RCS}$ désigne la section efficace radar en champ proche (en m^2) ;
- $\mathbf{E}_{\text{scat}}$ est le champ électrique rétrodiffusé complexe, incluant amplitude et phase, produit par chaque élément de surface considéré ;
- $\hat{\mathbf{p}}$ est le vecteur unitaire de polarisation de réception, permettant de projeter le champ sur la polarisation de l'antenne réceptrice ;
- $\sum_S$ représente la sommation cohérente (en phase) sur l'ensemble des éléments de surface ou d'arêtes S ;
- R_T et R_R sont respectivement les distances entre l'élément de surface et les antennes émettrice (TX) et réceptrice (RX) ;
- $\|V\|$ est le module de la tension générateur appliquée à l'antenne émettrice, servant à normaliser la grandeur par rapport au niveau d'excitation ;

Pour calculer la NF-RCS, la première étape est l'initialisation du champ incident à partir de la source, ou du facteur d'antenne, en tenant compte de la propagation sphérique, de la phase, de la polarisation et de l'amplitude locale. Le calcul des densités de courant de surface est ensuite effectué selon l'approximation de OP sur les facettes éclairées, tandis que la méthode EEC est utilisée pour modéliser les contributions des arêtes visibles. Le processus itératif IPO consiste alors à réinjecter les champs diffusés dans les itérations suivantes afin de prendre en compte les interactions multiples. Ce processus ne s'applique que pour l'IPO et non pour l'EEC car le coût en temps de calcul serait trop élevé. En effet, il est impossible d'écrire itérativement le courant comme le courant dépendra à la fois de la direction d'incidence et la direction de diffraction.

La gestion des ombrages et des trajets multiples repose sur une approche purement géométrique, prenant en compte les chemins antenne-surface, surface-surface et arête-surface. Pour déterminer la visibilité entre deux éléments, des rayons sont émis depuis la source en direction des facettes du maillage. Lorsqu'un rayon intersecte une autre surface avant d'atteindre l'élément cible, celui-ci est considéré comme masqué : la source et l'élément ne sont alors pas visibles l'un de l'autre, et la contribution correspondante est

annulée. Ce traitement d'illumination permet de gérer de manière cohérente les zones d'ombre et les interactions multiples entre les surfaces du modèle.

L'intégration des contributions au niveau du récepteur est réalisée par une sommation cohérente des champs issus des surfaces et des arêtes, en prenant en compte les ordres multiples d'itération. Le maillage étant un critère majeur, à la fois pour le temps de calcul et pour la précision, des études de sensibilité ont été menées pour du simple, double ou triple rebonds.

Pour valider la modélisation de la diffraction par les arêtes, il est souvent difficile d'isoler expérimentalement ou numériquement la contribution diffractée par l'EEC, car la réponse de PO domine généralement le champ total. Afin de mieux mettre en évidence le rôle spécifique de la diffraction, une étude en *forward scattering* a été réalisée dans un cas où la PO n'était plus applicable. Le scénario considéré correspond à une pyramide métallique, géométrie pour laquelle les contributions diffractées sont prépondérantes. Les résultats montrent un bon fonctionnement de l'EEC en champ proche.

Intégration des antennes et validation par mesure

Un point clé de la thèse est l'intégration explicite des antennes dans la modélisation (dipôle, cornet), afin de lever les limitations d'une NF-RCS dépendante d'un gain d'antenne fictif. La fonction de transfert aller-retour est définie en introduisant des facteurs d'antenne complexes dépendants de l'angle (AoD/AoA) et de la polarisation. La fonction de transfert $\mathcal{H}_{Rt}(f)$ se traduit comme la somme des fonctions de transfert pour chaque élément m

$$\mathcal{H}_{Rt}(f) = \sum_{m=1}^{M} \mathcal{H}_T^{(m)} \mathcal{H}_{T\to S}^{(m)} \rho_{SC}^{(m)} \mathcal{H}_{S\to R}^{(m)} \mathcal{H}_R^{(m)} \tag{4}$$

où $\mathcal{H}_T^{(m)}$ représente la fonction de transfert de la source dans la direction de l'élément m, $\mathcal{H}_{T\to S}^{(m)}$ la fonction de transfert entre l'antenne émettrice et la sous-surface m, $\rho_{SC}^{(m)}$ le coefficient de rétrodiffusion de la surface m, $\mathcal{H}_{S\to R}^{(m)}$ la fonction de transfert entre la sous-surface m et l'antenne réceptrice, et $\mathcal{H}_R^{(m)}$ la fonction de transfert du récepteur dans la direction de m. Le module au carré de la fonction de transfert aller-retour s'exprime alors comme :

$$|\mathcal{H}_{Rt}(f)|^2 = \frac{1}{P_T} \frac{c^2}{f^2 \eta} \frac{|\mathbf{E}_R(f) \times \mathbf{H}_R^*(f)|}{2} \tag{5}$$

Ici, le champ reçu est égal à la somme des contributions rétrodiffusées par chacun des éléments, mais le gain d'antenne doit être appliqué au préalable. Cela permet de lier la mesure du $S21$ au modèle d'IPO-EEC

$$\mathbf{E}_R(f) = \sum_{m=1}^{M} \mathcal{H}_R^{(m)} \mathbf{E}_{scat}^{(m)}(f) \qquad \mathbf{H}_R(f) = \sum_{m=1}^{M} \mathcal{H}_R^{(m)} \mathbf{H}_{scat}^{(m)}(f) \tag{6}$$

La validation expérimentale constitue une étape essentielle de cette thèse. Des mesures ont été réalisées en chambre anéchoïque sur plusieurs cibles canoniques, telles qu'une plaque plane, une sphère et un

trièdre, afin de confronter le modèle au comportement réel. Pour les mesures en champ proche, une chaîne d'alignement haute précision a été mise en œuvre, l'alignement jouant un rôle déterminant en raison des interférences entre les différentes contributions d'une même cible. Le paramètre S_{21}, mesuré entre l'antenne émettrice et l'antenne réceptrice, a ensuite été traité par transformation temporelle afin d'isoler la contribution directe et d'éliminer les trajets indésirables par filtrage temporel.

Les comparaisons entre le modèle et les mesures montrent un bon accord, y compris en présence de contributions diffractées lorsque l'on s'éloigne de la direction spéculaire. L'intégration explicite des antennes dans le modèle permet ainsi de reproduire fidèlement les configurations expérimentales réelles et renforce la robustesse des prédictions par rapport aux approches simplifiées reposant sur des gains maximaux théoriques.

Un exemple de mesure est présenté dans la Fig.1. Cette mesure a été réalisée pour des angles d'azimut compris entre 0° et 35°. Comme le montre la Fig. 1**(b)**, le modèle et les mesures présentent une bonne concordance, avec un écart inférieur à 1 dB pour les petits angles et inférieur à 2 dB au-delà de 20°.

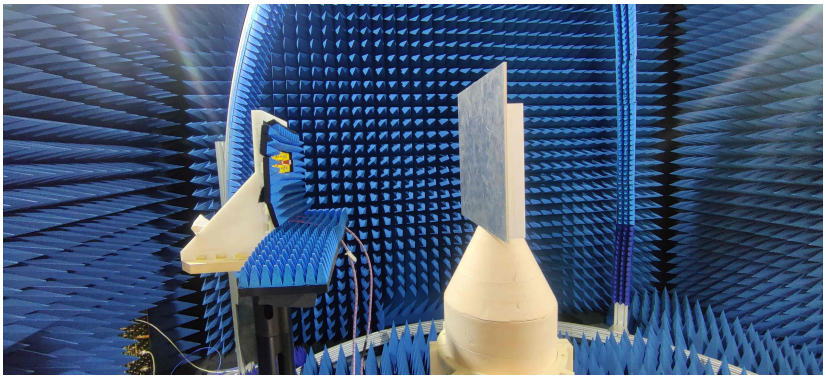

(a)

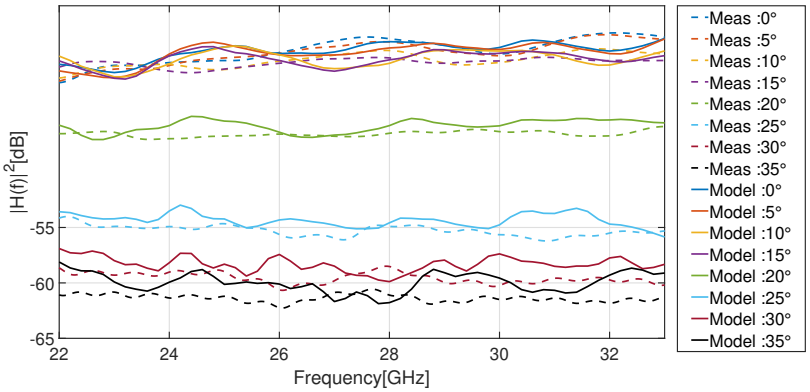

(b)

Figure 1: (a) Plaque : configuration de mesure ; (b) résultats de la rétrodiffusion en champ proche pour différents angles d'azimut 0° → 35° : modèle (trait continu) vs. mesure (trait pointillé).

Extension aux milieux diélectriques et conducteurs pertes

Le cadre du modèle a été étendu au-delà du cas de surface parfaitement conductrice (PEC) afin de traiter les milieux diélectriques et les matériaux présentant des pertes. L'adaptation de la méthode IPO prend en compte la pénétration du champ dans le matériau, les coefficients de Fresnel complexes associés à la réflexion et à la transmission, ainsi que les pertes volumiques qui en résultent. Quatre différentes méthodes ont été testées pour prendre en compte ces matériaux. Plusieurs scénarios de test, incluant un métal à pertes, un diélectrique et un diélectrique à pertes, ont permis de mettre en évidence la sensibilité de la NF-RCS aux paramètres électromagnétiques du matériau. La méthode EEC a été étendue aux matériaux diéléctriques via une équivalence également effectuée sur les surfaces. Enfin, des mesures réalisées sur des échantillons diélectriques, tels que le Teflon, ont permis de valider l'ordre de grandeur et la forme de la réponse fréquentielle, et d'affiner les paramètres physiques liés au matériau.
Un résultat marquant de la thèse est la modélisation et la mesure d'un cube constitué d'un matériau permettant de reproduire les propriétés électromagnétiques du corps humain. La mesure a été réalisée à une distance de 50 cm entre la cible et les antennes. La Fig. 2 illustre la configuration expérimentale. Les antennes utilisées sont des cornets fonctionnant de 22 GHz à 33 GHz. Dans cette plage de fréquences, la permittivité relative du cube varie de 20 à 21, tandis que sa conductivité s'étend de 4.11 $\mathrm{S.m^{-1}}$ à 5.7 $\mathrm{S.m^{-1}}$.
Les mesures ont été effectuées avec un pas de rotation de 5°. Lors du post-traitement, une erreur d'alignement de 1° a été identifiée, indiquant que le modèle doit être paramétré avec un pas de rotation de 5° centré sur 1° au lieu de 0°.
Les résultats présentés Fig. 2 montrent une excellente concordance entre le modèle et les mesures. L'écart inférieur à 1 dB peut être attribué à la précision des mesures ou à la modélisation des antennes.

Application à la rétrodiffusion du corps humain

Enfin, le modèle a été appliqué à la rétrodiffusion du corps humain en configuration de champ proche, un domaine d'intérêt croissant pour des applications telles que la santé connectée, la surveillance d'activité, la reconnaissance de gestes et l'imagerie à courte portée. Le mannequin humain a été discrétisé à l'aide d'un maillage de surface détaillé, intégrant les zones arrondies telles que les épaules, les coudes ou les genoux, afin de représenter fidèlement la géométrie globale du corps. Les antennes ont été disposées en configuration bistatique, permettant l'évaluation des cartes de champ rétrodiffusé normalisé pour différentes poses et angles d'incidence, ainsi que des fonctions de transfert aller-retour correspondant à diverses géométries d'émission et de réception. Dans cette première approche, le corps humain a été modélisé à partir d'un matériau homogène reproduisant la réponse électromagnétique moyenne des tissus biologiques. L'étude met en évidence la dépendance de la NF-RCS à la distance et à l'angle d'observation, en comparaison avec un cas de champ lointain de référence. Le modèle hybride IPO-EEC conserve ainsi sa pertinence dans ce contexte, à condition d'un maillage suffisamment fin et d'une calibration réaliste des propriétés électromagnétiques du matériau considéré.

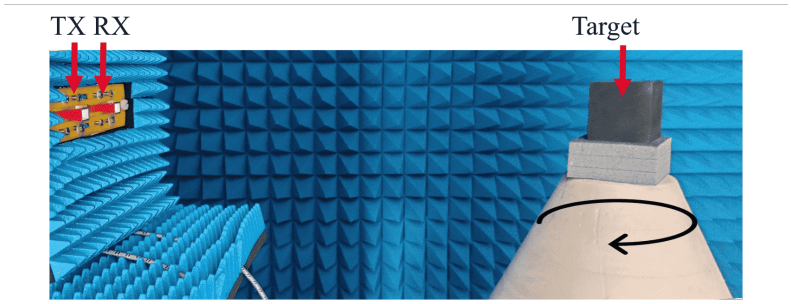

(a)

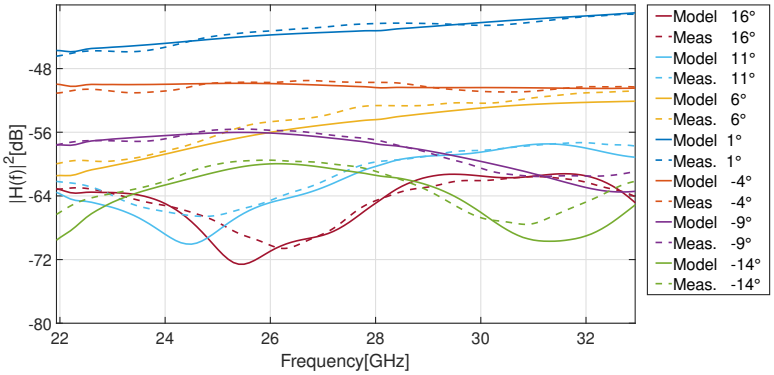

(b)

Figure 2: (a) Configuration de mesure de la rétrodiffusion. (b) Résultats de la rétrodiffusion en champ proche pour différents angles d'azimut : modèle (trait continu) vs. mesure (trait pointillé).

Résultats et apports principaux

Les contributions principales de cette thèse peuvent être résumées de la manière suivante. Tout d'abord, une formulation en champ proche d'un modèle hybride IPO-EEC a été développée pour des cibles électriquement grandes, intégrant explicitement l'effet des antennes au travers d'une fonction de transfert aller-retour cohérente. Ce modèle s'inscrit dans une chaîne complète de simulation combinant un maillage avancé capable de représenter aussi bien les surfaces planes que courbes et les arêtes, une gestion précise des ombrages multi-sources, le calcul itératif IPO, l'évaluation des densités de courant d'arêtes par la méthode EEC et l'intégration cohérente des contributions au niveau du récepteur. Le modèle a été validé expérimentalement en chambre anéchoïque sur plusieurs cibles canoniques tels qu'une plaque, une sphère et un trièdre. Les résultats montrent un bon accord entre les résultats simulés et mesurés sur des bandes de 20 à 30 GHz et pour des distances typiques du champ proche. Enfin, le modèle a été étendu à différents types de matériaux, incluant les conducteurs à pertes et les diélectriques, et appliqué à la rétrodiffusion du corps humain, ouvrant la voie à des applications d'imagerie à courte portée.

Perspectives

Concernant les perspectives, plusieurs axes d'amélioration sont envisagés. Le premier concerne l'évolution du modèle lui-même, avec l'introduction de lois d'illumination d'arêtes dépendant de la courbure locale, de schémas IPO adaptatifs selon les régions de la surface, et de critères d'arrêt a posteriori fondés sur l'énergie diffusée résiduelle, ainsi que la prise en compte de contributions parasites proches des interfaces. Le deuxième axe vise l'exploitation du modèle dans des chaînes intégrées de communication et détection conjointes (JCAS), pour la prédiction simultanée du canal et de la signature des cibles, la planification de scénarios multistatiques distribués ou encore l'inversion de la rétrodiffusion pour l'estimation de paramètres géométriques ou électromagnétiques. Enfin, un troisième axe porte sur l'extension de la validation expérimentale, incluant des campagnes sur matériaux souples ou biologiques, des scénarios dynamiques comme la reconnaissance de gestes.

Chapter 1

Introduction

1.1 Context of the thesis

1.1.1 Historical background on radar

Radar, short for Radio Detection and Ranging, is a major technological development of the 20th century. Building on Hertz's work on radio waves, radar was developed to detect objects because of its strong potential in military applications. Researchers began to explore ways to detect aircraft and ships using radio signals during World War II, which marked the start of radar applications [1]. After the war, radar technology advanced in both military and civilian applications. The United States and the Soviet Union focused heavily on radar for surveillance and defense, especially during the Cold War. During this period, radar systems were used to detect incoming missiles, and the concept of radar-guided missile systems emerged. Radar became widely used in civilian aviation for air traffic control, improving safety by enabling controllers to track aircraft which contributed to the rapid growth of air traffic. Weather radar also became widely used in meteorology, helping to detect storms and track precipitation [2]. Radar systems have become more precise, compact, and powerful. Digital signal processing has allowed radar to better distinguish between targets and noise. The diversity of radar applications and use cases has increased with systems like Synthetic Aperture Radar (SAR) and phased array radar systems. These technologies are now widely applied in fields such as meteorology, automotive safety, and even space exploration. Radar also plays a major role in the development of precision agriculture [3] or vehicle safety [4]. In recent years, one of the exciting radar developments has been the application of radar in self-driving cars. Radar helps these vehicles detect obstacles, pedestrians, and other vehicles, even in low visibility conditions such as fog or rain. A key capability is not only detection but also the recognition of all the possible elements in all situations [5].

Radar sensing refers to the use of radar technology to detect and analyze objects or changes in the environment by emitting electromagnetic waves and interpreting the reflected signals. By analyzing the target response, radar sensors can determine the different properties of the target which are commonly its target position, speed and shape.

1.1.2 The future of Radar

For the 6G and beyond, the future of radar will come from the integration of artificial intelligence. The target detection, tracking, and analysis should be enriched [6], [7]. Additionally, the miniaturization of radar components continues, allowing for the development of more affordable and versatile systems in applications ranging from drones to wearable technology. The gap between sensing and communication will be filled by the Joint Communication And Sensing (JCAS) technology [8]. Integrating sensing capabilities into a communication network is a highly promising area that offers numerous opportunities as well as challenges. There are use cases that can enhance the network's own performance, along with exciting possibilities where spatial sensing can be delivered as a service to external users or applications. The key advantage of the communication network in the context of future sensing is that much of the infrastructure is already established, ensuring complete area coverage. This setup enables the creation of a multistatic sensing mesh, allowing sensing to be provided at almost no additional cost.
With the increasing use of higher frequencies to enhance detection accuracy or transmission capabilities, new challenges arise. Moreover, radar is being used in increasingly complex scenarios where the targets are relatively close to both the transmitter and the receiver [9]. In close-range applications like gesture recognition, object tracking, and proximity sensing, radar can be used to detect objects and measure their relative movement [10]. It is also the case in automotive radar for parking assist and collision avoidance, radar systems need to work accurately in the near field, requiring sophisticated algorithms to interpret the distorted signals caused by the proximity of objects. It is important to note that the near field region corresponds to the target region, which means that the antenna is supposed to be operating in the far field. By comparing the far field propagation, where electromagnetic waves propagate in well-defined patterns, the near field backscattering exhibits complex interactions. The interaction of radar waves with the target can lead to multipath effects, where signals bounce off different parts of the target before returning to the receiver. The sum of these different responses can lead to errors in the analysis, as the radar might detect multiple signals from the same object at different times, leading to inaccuracies in determining distance or speed. To determine whether an element is radiating in the far field or the near field, the Fraunhofer criterion will be used. A target will be considered as emitting in the near field if the distance R with the receiver is less than:

$$R < 2\frac{D_{Targ}^2}{\lambda} \tag{1.1}$$

with D_{Targ} being the dimension of the target and λ the wavelength. Fig. 1.1 illustrates the separation between near field and far field regions, showing that when the target lies within the near field boundary, the incident wavefront can no longer be considered spherical, and the scattering response strongly depends on both distance and geometry. If the target is radiating in the far field, the wave can be modeled as a spherical wave propagation where the fields are considered to evolve perpendicularly to the direction of propagation. In the near field, the definition of the radiating element is more complex and needs to be properly modeled.

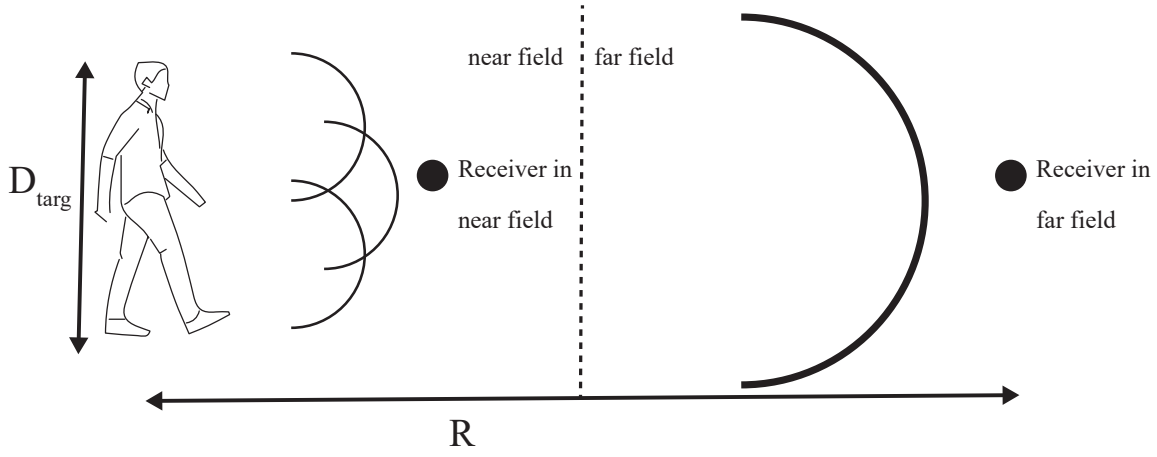

Figure 1.1: Target radiation in near and far field

1.2 Personal contribution and manuscript outline

Radar modeling is the calculation of how electromagnetic waves propagate, scatter on targets and return to the radar system. This modeling is crucial for the prediction of the behavior of radar in various environments in order to optimize the radar capabilities. The focus is often on target properties because in most applications propagation is not considered and is separate from the target. The near field region exhibits unique characteristics that differ from the far field where electromagnetic waves propagate outward in a more predictable manner. Not taking into account the near field effect will cause inaccuracies in the radar's detection capabilities, particularly for precise target detection. The need to simulate complex near field interactions such as diffraction and interference can make near field radar modeling computationally intensive. Solving Maxwell's equations by using numerical methods like Finite-Difference Time-Domain (FDTD) [11] or Method of Moments (MOM) [12] requires significant computational resources, particularly when the size of the elements is large compared to the wavelength. Defining an efficient model is challenging, it represents a balance between accuracy and computational efficiency. Approximations and simplifications are often used to perform modeling. These may reduce the model's accuracy in certain scenarios where a good precision is expected.
Many models have been developed to calculate the backscattering of a target in the near field. They can be classified into analytical and numerical methods. Analytical methods are fast methods developed using canonical targets. For numerical methods, the precision and computation time depend on the mesh of the target or the environment. The meshing is strongly linked to the frequency used: higher frequencies require a finer mesh. Faster numerical methods exist based on asymptotic approaches and give precise results depending on the meshing and the physical phenomena taken into account.

The goal of this thesis is to develop a model capable of accurately calculating the backscattering of a target when the receiver is located in the target's near field. To this end, the target is assumed to be

electrically large compared to the wavelength. The study focuses on millimeter-wave frequencies, which represent one possible future of communication and radar technologies. To handle large-scale targets, an asymptotic model based on Iterative Physical Optics (IPO) [13] and Equivalent Edge Current (EEC) [14] methods will be employed. This model allows precise computation of the fields scattered by both surface reflections and edge diffraction.

Recent research has emphasized improving IPO accuracy in near field configurations, where the curvature of the incident wavefront, evanescent components, and strong inter-facet interactions cannot be neglected [15]. NF-IPO have been proposed to enhance convergence and accuracy for both perfectly conducting and dielectric objects [16]. Hybrid approaches, such as IPO combined with the Multilevel Fast Multipole Method, further improve computational efficiency for electrically large conductors [17]. These developments are particularly relevant at millimeter-wave frequencies, where large-scale targets exhibit significant near field backscattering and multipath effects, critical for modern radar and imaging systems [18]. For edges, the induced surface current vanishes abruptly at shadow boundaries, leading to discontinuities and inaccuracies in predicting scattered fields near edges. The EEC concept, originally derived from the Physical Theory of Diffraction (PTD), introduces additional equivalent currents along the edges to model the diffracted fields radiated by these discontinuities [19]. This approach provides a more accurate representation of the total scattered field, especially in configurations involving complex geometries, sharp boundaries, or near field observation points. Recent research has focused on combining EEC with IPO to improve near field scattering predictions for electrically large conductors (EEC) and composite targets [20]. These hybrid PO–EEC or IPO–PTD formulations are particularly valuable at millimeter-wave frequencies, where diffraction and multiple reflections contribute significantly to the backscattering signature of large and detailed objects [21].

Our work bridges this gap by developing a near field IPO–EEC hybrid model, capable of predicting the backscattered field when the receiver lies within the target's near field region. Furthermore, the proposed formulation extends beyond conventional perfectly conducting assumptions by incorporating dielectric materials and their electromagnetic interactions. This enables a more realistic and comprehensive representation of complex targets at millimeter-wave frequencies, where multiple scattering plays a crucial role. In addition to the modeling effort, near field measurement campaigns are conducted to validate the proposed approach, allowing direct comparison between modeled and experimental backscattering data.

Chapter 2 presents a contextual study. Beginning with the propagation equation, the boundary conditions and integral field equations are derived, laying the preliminary work for the analysis of the Near Field Radar Cross Section (NF-RCS) [22]. It is a measure of a target's detectability by radar when the receiver is close enough. The chapter aims to differentiate the specific characteristics of the near field region. The classical Radar Cross Section (RCS) is defined in the far field. It is independent of parameters like distance and antenna radiation patterns. It cannot be directly used and measured in the near field region. Several models are examined to address the challenges of near field backscattering which must balance efficiency and accuracy. The chapter concludes with the selection of a near field IPO model, enhanced with the EEC method to accurately take into account the edge diffraction effects.

Chapter 3 focuses on the study of the model. It begins with the presentation of the implementation of the Physical Optics (PO) and IPO methods. A particular emphasis is placed on the meshing technique and its impact on shadowing effects. Meshing is a critical aspect of the model, as reducing the size of each element improves the model's accuracy but increases computational time. The shadowing implementation is discussed. It is achieved using ray-tracing methods from all radiating elements. The chapter then describes how the model is enhanced by incorporating the near field implementation of the EEC. The chapter concludes by introducing several acceleration techniques designed to reduce the computational time required by the model.

Chapter 4 focuses on the challenges associated with the near field region. It begins with the limitations of the NF-RCS which reduce the impact of the model. The implementation of the antenna is presented. Antenna integration improves model accuracy by providing a more accurate representation of backscattering behavior. To validate the model and to test its capabilities, validations against canonical targets are performed. The validations were performed with near field measurements conducted in an anechoic chamber. The measurement precision is analyzed to properly validate the model.
Chapter 5 presents the implementation of dielectric and lossy materials. The model is enhanced to account for complex materials, incorporating their electromagnetic properties. By considering both dielectric and lossy materials, the model's ability to predict radar performance in real-world scenarios is significantly improved. Several approaches were tested to accurately represent the currents. Model validation is performed through simulation and measurement. A possible application of the model to human body scenarios is presented.

Chapter 2

Near field backscattering model

2.1 Introduction

In order to model the electromagnetic scattering of a target, numerous techniques have been developed to solve these complex problems. As with any electromagnetic problem, the methods are based on the fundamental Maxwell's equations. These equations describe the behavior of electric and magnetic fields in different media. In this thesis, the scattering of the target will be limited to the boundaries between the different media. For this purpose, the focus will be placed on the integral equations and the boundary conditions which are derived from the Maxwell's equations [23].
In this chapter, the electromagnetic equations are recalled to establish the theoretical foundations of the thesis. The goal is to define the near field integral equations to model the NF-RCS and to characterize the target scattering.
Then, the methods for solving the diffraction problem will be discussed, with a particular emphasis on the case of large near field targets. This will make it possible to justify the choice of the method used to solve the problem of calculating the backscattering for large, complex targets.

2.2 Theoretical electromagnetic backscattering

We establish as a convention for the remainder of this document a time-harmonic dependence in $e^{+j\omega t}$*, where* ω *represents the angular frequency. Furthermore, vectors are denoted in boldface* $\mathbf{X}$*, unit vectors in boldface with a hat* $\hat{\mathbf{X}}$*, and the norm of the vector* $\mathbf{X}$ *is denoted by* $X = \|\mathbf{X}\|$

2.2.1 Propagation equation

Electromagnetic backscattering refers to the phenomenon where an electromagnetic wave is scattered back in the direction opposite to its initial path after interacting with an object or a surface. It is usually a diffuse reflection due to scattering, as opposed to specular reflection as from a mirror, although specular backscattering can occur at normal incidence with a surface. To understand backscattering, the

propagation of the electromagnetic fields needs to be considered. The electric field $\mathbf{E}$ in volts per meter $V.m^{-1}$, represents the force applied by charged particles, while the magnetic field $\mathbf{H}$ in amperes per meter $A.m^{-1}$, represents the moving charges. The equations which govern the propagation describe how electromagnetic waves travel through a medium over time and space. They describe the variations in the electric and magnetic fields due to sources and the properties of the environment. For the purposes of this thesis, these equations are crucial for understanding how the electromagnetic field interacts with its environment. Among these interactions, those occurring at material boundaries are particularly significant.

From Maxwell's equations, it is possible to derive the propagation equation. By using the curl of Faraday's law [24]:

$$\nabla \times (\nabla \times \mathbf{E}) = \nabla (\nabla \cdot \mathbf{E}) - \nabla^2 \mathbf{E} \tag{2.1}$$

where ∇^2 is the Laplace operator and $\nabla\times$ is the curl operator. It is possible by using Faraday's law and Gauss's law to obtain:

$$\nabla \times \left(-\mathbf{M} - \mu \frac{\partial \mathbf{H}}{\partial t} \right) = \nabla \frac{\rho_e}{\varepsilon} - \nabla^2 \mathbf{E} \tag{2.2}$$

where $\mathbf{M}$ is the equivalent magnetic current density ($V.m^{-2}$) and ρ_e the charge density ($C \cdot m^{-3}$). μ and ε correspond to the medium permeability and permittivity. In a linear, homogeneous, and isotropic medium, by using the previous equation 2.2 and Ampere's law, and by isolating the field $\mathbf{E}$, the Equation (2.2) is rewritten as:

$$\nabla^2 \mathbf{E} - \varepsilon\mu \frac{\partial^2 \mathbf{E}}{\partial t^2} = \frac{1}{\varepsilon} \nabla(\rho_e) + \mu \frac{\partial \mathbf{J}}{\partial t} + \nabla \times \mathbf{M} \tag{2.3}$$

where $\mathbf{J}$ represents the equivalent electric current density ($A.m^{-2}$). From the duality between the magnetic and the electric field, the equation for both electric and magnetic fields can be summarized as:

$$\begin{aligned} \nabla^2 \mathbf{E} - \varepsilon\mu \frac{\partial^2 \mathbf{E}}{\partial t^2} &= \frac{1}{\varepsilon} \nabla(\rho_e) + \mu \frac{\partial \mathbf{J}}{\partial t} + \nabla \times \mathbf{M} \\ \nabla^2 \mathbf{H} - \varepsilon\mu \frac{\partial^2 \mathbf{H}}{\partial t^2} &= \frac{1}{\mu} \nabla(\rho_m) + \varepsilon \frac{\partial \mathbf{M}}{\partial t} + \nabla \times \mathbf{J} \end{aligned} \tag{2.4}$$

In the case of a sourceless medium, D'Alembert's equations are obtained immediately:

$$\begin{aligned} \nabla^2 \mathbf{E} - \varepsilon\mu \frac{\partial^2 \mathbf{E}}{\partial t^2} &= 0 \\ \nabla^2 \mathbf{H} - \varepsilon\mu \frac{\partial^2 \mathbf{H}}{\partial t^2} &= 0 \end{aligned} \tag{2.5}$$

The two equations (2.5) govern the phenomenon of electromagnetic wave propagation. One solution of this wave equation is a plane wave extension which represents the far field expression where the spherical spreading is negligible:

$$\mathbf{E}(\mathbf{R}_{sou}, t) = \mathbf{E}_{0pw} e^{-j(\hat{\mathbf{k}} \cdot \mathbf{R}_{sou} - \omega t)} \tag{2.6}$$

It corresponds to a wave propagating in the direction $\hat{\mathbf{k}}$ with a wavelength λ and a radian frequency ω. $\mathbf{E}_{0pw}$ is the complex amplitude of the electric field of the plane wave. The vector $\mathbf{R}_{sou}$ corresponds to the displacement from the source position $\mathbf{R}_{sou} = \mathbf{r} - \mathbf{r}_{sou}$. It refers to the vector from the source S_{sou}

with vector position $\mathbf{r}_{sou}(x_{sou}, y_{sou}, z_{sou})$ to the target position $\mathbf{r}(x, y, z)$. Fig. 2.1 presents the different positions.

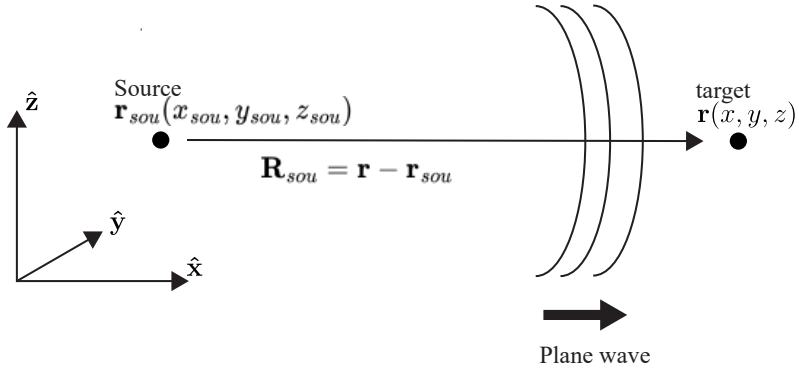

Figure 2.1: Presentation of the electromagnetic wave propagation

As mentioned earlier, the temporal aspect will not be addressed. The temporal derivation can be expressed as a multiplication by $j\omega$. The equation (2.3) is rewritten as:

$$\nabla^2\mathbf{E} + k^2\mathbf{E} = \frac{1}{\varepsilon}\nabla(\rho_e) + j\omega\mu\mathbf{J} \tag{2.7}$$

And with the far field approximation, the magnetic field can be expressed as:

$$\mathbf{H} = \frac{\hat{\mathbf{k}} \times \mathbf{E}}{\eta} \tag{2.8}$$

where η is the intrinsic impedance of the medium. The velocity of propagation ν can be linked to the speed of light in free space c (absence of material media) by the relation:

$$\nu = \frac{c}{\sqrt{\varepsilon\mu}} \tag{2.9}$$

The triplet $(\hat{\mathbf{k}}, \mathbf{E}, \mathbf{H})$ is mutually orthogonal and represents a direct coordinate system. The constant $\mathbf{E}_{0pw}$ in the wave equation 2.6 is established only in far field propagation. By considering more realistic spherical-wave propagation, the magnitudes fall off inversely with distance from their localized source point:

$$\mathbf{E}(\mathbf{R}) = \mathbf{E}_0 \frac{e^{-j\hat{\mathbf{k}}\cdot\mathbf{R}}}{R} \tag{2.10}$$

By comparison with the equation 2.6, the propagation is not a plane wave but rather a spherical wave. Unlike a plane wave, the complex amplitude is not constant across planes perpendicular to the propagation direction. Here the complex amplitude is equal to $\frac{\mathbf{E}_0}{R}$.

2.2.2 Boundaries limits

The backscattering phenomenon is inherently a study of what happens when an incident wave strikes a boundary. This study involves boundary conditions and reflection coefficients. The conditions can be derived from the integral form of Maxwell's equations applied to an interface. To express the boundary conditions, we will consider the case presented in Fig. 2.2. The two materials 1 and 2 are defined by their constitutive parameters where σ_1 and σ_1 are the conductivities of the media. If there are electric or magnetic sources along the interface between the two media, the boundary conditions on the tangential and normal components of the fields can be written, in general form, as:

$$\begin{aligned} -\hat{\mathbf{n}} \times (\mathbf{E}_1 - \mathbf{E}_2) &= \mathbf{M} \\ \hat{\mathbf{n}} \times (\mathbf{H}_1 - \mathbf{H}_2) &= \mathbf{J} \\ \hat{\mathbf{n}} \cdot (\varepsilon_1 \mathbf{E}_1 - \varepsilon_2 \mathbf{E}_2) &= \rho_e \\ \hat{\mathbf{n}} \cdot (\mu_1 \mathbf{H}_1 - \mu_2 \mathbf{H}_2) &= \rho_m \end{aligned} \tag{2.11}$$

In these equations, the current densities $(\mathbf{J}, \mathbf{M})$ and charge densities (ρ_e, ρ_m) are surface densities, defined per unit area on the interface. In the case of Perfect Electric Conductor (PEC), the wave does not penetrate into medium 2. The magnetic current $\mathbf{M}$ and the magnetic charge density ρ_m vanish. Similarly for Perfect Magnetic Conductor (PMC), the electric current $\mathbf{J}$ and the electric charge density ρ_e vanish.

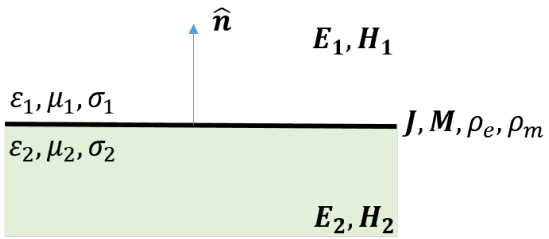

Figure 2.2: Boundary conditions - limits between medium 1 and medium 2

2.2.3 Reflection Coefficients

To properly describe the scattering of the target, the reflection coefficients are used to describe specular scattering from surfaces, which is the major scattering mechanism for most of the targets. Fig. 2.3 summarizes the scenario. A plane wave $(\mathbf{E}_{inc}, \mathbf{H}_{inc})$ arrives along the direction $\mathbf{k}_{inc}$ and hits the boundary between materials 1 and 2. A part of the incident wave is reflected along $\mathbf{k}_{ref}$ and a part is transmitted along $\mathbf{k}_{tra}$. This simple approach may not be applicable to all targets due to end-region, edge diffraction or surface wave scattering. From the Snell's laws:

$$k_{inc} \ \sin(\theta_{inc}) = k_{tra} \ \sin(\theta_{tra}) \tag{2.12}$$

and from the conservation of energy, it is possible to establish reflection coefficients $\Gamma_\perp$ and $\Gamma_\parallel$ for both polarizations and transmission coefficients $\tau_\perp$ and $\tau_\parallel$. Here the coefficients are defined as field ratios and not power ratios. These are functions of polarization, electromagnetic medium parameters and the angle of incidence. The four coefficients are :

$$\begin{aligned}
\Gamma_\parallel &= \frac{\eta_2 \cos(\theta_{tra}) - \eta_1 \cos(\theta_{inc})}{\eta_2 \cos(\theta_{tra}) + \eta_1 \cos(\theta_{inc})} \\
\Gamma_\perp &= \frac{\eta_2 \cos(\theta_{inc}) - \eta_1 \cos(\theta_{tra})}{\eta_2 \cos(\theta_{inc}) + \eta_1 \cos(\theta_{tra})} \\
\tau_\parallel &= \frac{2\eta_2 \cos(\theta_{inc})}{\eta_2 \cos(\theta_{tra}) + \eta_1 \cos(\theta_{inc})} \\
\tau_\perp &= \frac{2\eta_1 \cos(\theta_{inc})}{\eta_2 \cos(\theta_{inc}) + \eta_1 \cos(\theta_{tra})}
\end{aligned} \tag{2.13}$$

The reflection and transmission coefficients have been defined for fields quantities, hence conservation of energy requires that

$$|\Gamma|^2 + |\tau|^2 = 1 \tag{2.14}$$

For lossless media, the intrinsic impedance of the medium η is:

$$\eta = \sqrt{\frac{\mu}{\varepsilon}} \tag{2.15}$$

and the wave vector $\mathbf{k}$ is defined as

$$\mathbf{k} = \omega\sqrt{\mu\varepsilon}\hat{\mathbf{k}} \tag{2.16}$$

for lossy media, they are expressed as [25]:

$$\begin{aligned}
\eta &= \sqrt{\frac{\mu}{\varepsilon - j\frac{\sigma}{\omega}}} \\
\mathbf{k} &= \sqrt{-\omega^2\mu\varepsilon + j\omega\mu\sigma}\hat{\mathbf{k}}
\end{aligned} \tag{2.17}$$

The imaginary part of k directly leads to absorption of the wave, for a good conductor, the norm of the wave vector is:

$$k \approx \frac{1-j}{\delta_{sd}} \tag{2.18}$$

where δ_{sd} represents the skin depth which is defined by $\delta_{sd} = \frac{1}{\sqrt{\pi f \mu\sigma}}$. This distance represents an attenuation of 37% of a wave. For Radar Cross Section Reduction (RCSR), in order to design a target that absorbs most of the incident wave, large changes in impedance are not recommended. It is preferable to use a gradually varying impedance instead.

2.2.4 Reflection and Scattering from Material Interfaces via Equivalent Surface Currents

The development of reflection coefficients in terms of intrinsic material impedance and boundary conditions offers a clear understanding of wave behavior at interfaces. Alternatively, a second viewpoint

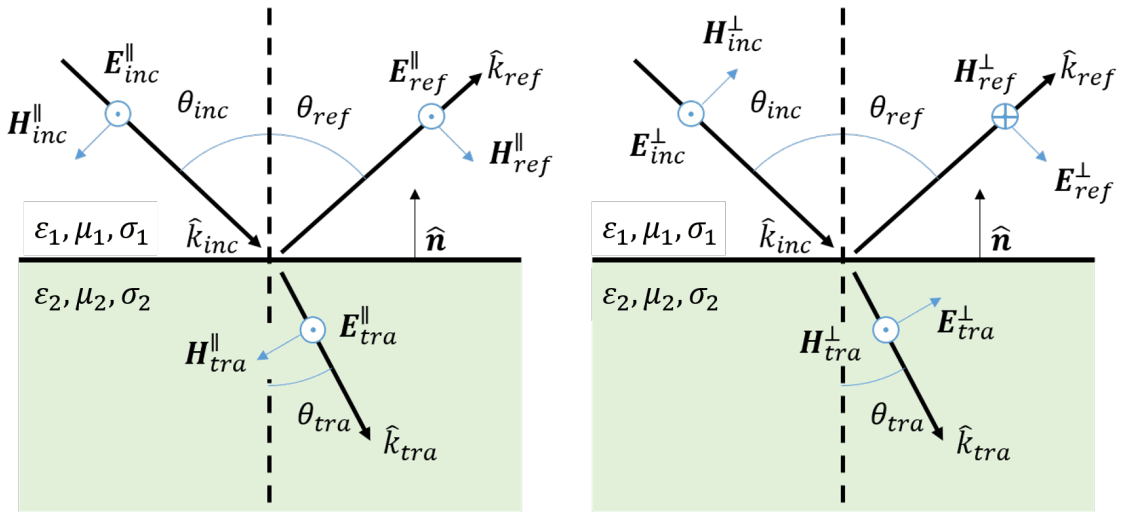

Figure 2.3: Reflection and Transmission at an interface, Parallel and perpendicular polarization

recognizes that the scattering phenomena of reflection and transmission arise from the interaction of the incident wave with the material interface, where it induces surface currents and charges. The induced currents and charges produce a scattered wave that radiates energy in various directions. Consider a source $(\mathbf{J}_{Sou}, \mathbf{M}_{Sou})$ outside the target in an unbounded medium with constitutive parameters μ_1 and ε_1 and radiating fields $(\mathbf{E}_{inc}, \mathbf{H}_{inc})$ everywhere, including the region V_1 enclosed by an imaginary surface S_1. By replacing the V_1 medium with μ_2, ε_2 and σ_2 different from the medium 1 as shown in Fig. 2.4 **(b)**. The total field outside V_1 is equal to the sum of the original field from the source and the perturbation fields $(\mathbf{E}_{scat}, \mathbf{H}_{scat})$ from the target. The total fields outside are expressed as:

$$\begin{aligned} \mathbf{H_{total}} &= \mathbf{H_{inc}} + \mathbf{H_{scat}} \\ \mathbf{E_{total}} &= \mathbf{E_{inc}} + \mathbf{E_{scat}} \end{aligned} \tag{2.19}$$

To apply the boundary conditions, it is necessary to use the total field at the interface. These boundary conditions may be represented as equivalent source currents and charges, which become the source of the scattered field. The surface electric and magnetic currents are interpreted in terms of the total tangential fields at the surface:

$$\begin{aligned} \mathbf{J} &= \hat{\mathbf{n}} \times (\mathbf{H}_{Total} - \mathbf{H}_{Tra}) \\ \mathbf{M} &= \hat{\mathbf{n}} \times (\mathbf{E}_{Total} - \mathbf{E}_{Tra}) \end{aligned} \tag{2.20}$$

In the general case of scattering from electric or magnetic bodies, the fields are finite and both $\mathbf{J}$ and $\mathbf{M}$ must be considered. For PEC or PMC boundaries, only one of the two equivalent currents is nonzero.

2.2.5 Stratton-Chu integral equations

When several regions are involved, as illustrated in Fig.2.4 **(b)**, Maxwell's equations coupled with the vector Green's theorem provides a set of field equations for the scattered field by a surface modeled by

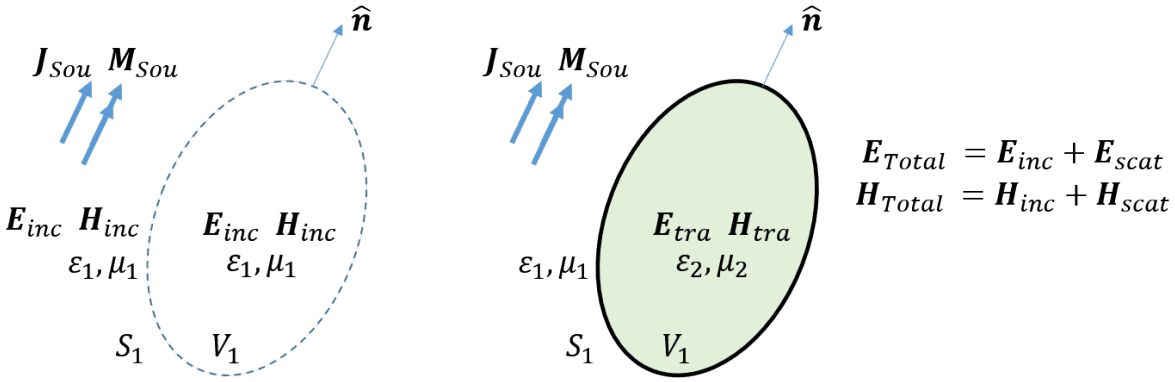

Figure 2.4: Surface current on boundary between two media 1 and 2

its current **J** and **M**. This was first formulated by Stratton and Chu [23]. We assume that the only sources are the equivalent currents **J** and **M** on the surface, with no sources present in regions 1 or 2. The field at any point in region 1 is given by the Stratton-Chu equations as a surface integral over the equivalent currents on surface S.

The Stratton-Chu equation for the scattered **E** field, also called the Electric Field Integral Equation (EFIE) is:

$$\mathbf{E}_{scat}(\mathbf{r}_{rec}) = \iint_s \left[-j\omega\mu \Big(\hat{\mathbf{n}} \times \mathbf{H}(\mathbf{r}) \Big) \psi(\mathbf{R}_{rec}) + \Big(\hat{\mathbf{n}} \times \mathbf{E}(\mathbf{r}) \Big) \times \nabla\psi(\mathbf{R}_{rec}) + \Big(\hat{\mathbf{n}} \cdot \mathbf{E}(\mathbf{r}) \Big) \nabla\psi(\mathbf{R}_{rec}) \right] dS \tag{2.21}$$

And the corresponding expression for the scattered **H** field, called the Magnetic Field Integral Equation (MFIE) is:

$$\mathbf{H}_{scat}(\mathbf{r}_{rec}) = \iint_s \left[j\omega\varepsilon \Big(\hat{\mathbf{n}} \times \mathbf{E}(\mathbf{r}) \Big) \psi(\mathbf{R}_{rec}) + \Big(\hat{\mathbf{n}} \times \mathbf{H}(\mathbf{r}) \Big) \times \nabla\psi(\mathbf{R}_{rec}) + \Big(\hat{\mathbf{n}} \cdot \mathbf{H}(\mathbf{r}) \Big) \nabla\psi(\mathbf{R}_{rec}) \right] dS \tag{2.22}$$

where ψ defines the Green function which represents the propagation from a point source and is the solution of the Helmholtz equation:

$$(\nabla^2 + k^2)\psi(\mathbf{R}_{rec}) = -\delta(\mathbf{R}_{rec}) \tag{2.23}$$

The vector $\mathbf{R}_{rec}$ corresponds to the distance vector from the surface integral to the receiver point $\mathbf{r}_{rec}(x_{rec}, y_{rec}, z_{rec})$. In the 3D scenario, the Green function is equal to:

$$\psi(\mathbf{R}_{rec}) = \frac{e^{-jkR_{rec}}}{4\pi R_{rec}} \tag{2.24}$$

where R_{rec} the norm of the vector $\mathbf{R}_{rec}$. This equation is crucial for the scattering problem, as it shows that if the current on the interface of medium 2 is known, there is no need to know the field in medium 1. To model the scattering, the only missing part is the knowledge of the current which directly depends on the tangential total fields. From the total field at the boundary, the electric and the magnetic currents

can be expressed as:

$$\begin{aligned} \mathbf{J} &= \hat{\mathbf{n}} \times \mathbf{H} \\ \mathbf{M} &= \hat{\mathbf{n}} \times \mathbf{E} \end{aligned} \tag{2.25}$$

In this formula, the total field corresponds to the sum of the incident field, the scattered field and the transmitted field by the surface. As mentioned in equation 2.20.

2.2.6 Near field Radar Cross Section

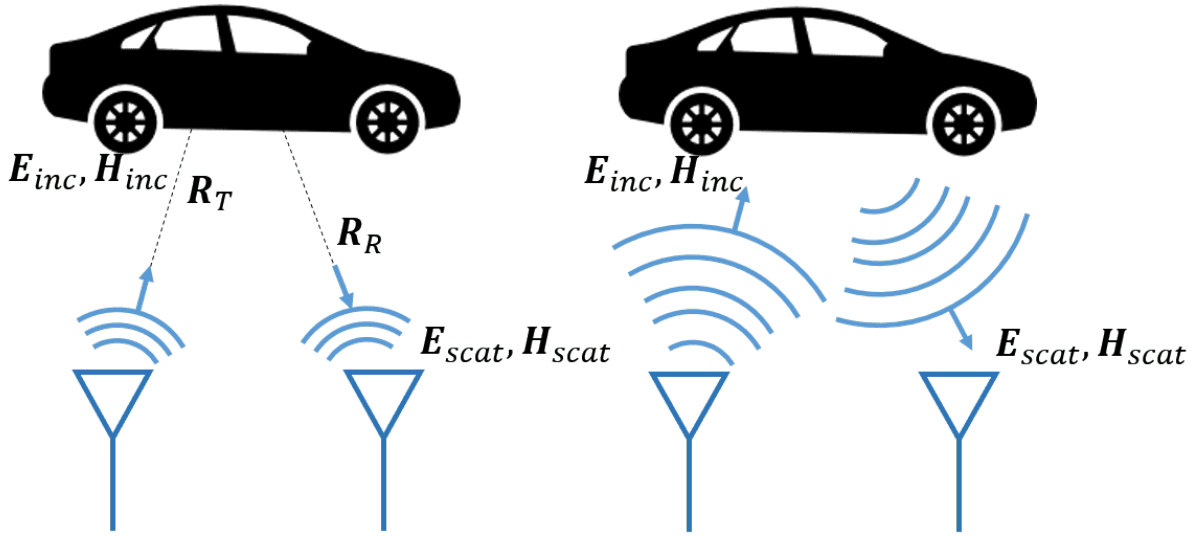

Figure 2.5: Target scattering, bistatic far field RCS and NF-RCS

The RCS of an object quantifies its detectability by radar systems. Fig. 2.5 represents the scenario considered in this work. The RCS represents the effective area that reflects radar signals back toward the radar source and is typically expressed in square meters. The value of the RCS indicates if an object is easily detectable. A smaller RCS implies that the object is more difficult to detect, and vice versa. Factors that affect RCS include the object's size, shape, material composition, and relative position to the radar elements. To derive the NF-RCS, we start from the basic RCS formulation by assuming that a radar transmitter has a power output of P_T through an antenna with gain $G_T(\theta_T, \phi_T)$ where θ_T and ϕ_T denote the Angle of Departure (AOD). The power density at the target, located at a distance R_T is:

$$P_D = \frac{P_T G_T}{4\pi R_T^2} \tag{2.26}$$

The RCS is defined as the hypothetical area that would intercept and reradiate isotropically the same power as that scattered by the target toward the radar receiver. The received power, for an antenna with gain $G_R(\theta_R, \phi_R)$ located at distance R_R , is equal to the product of the incident power density and

the antenna's effective aperture :

$$P_R = P_T \frac{G_T G_R \lambda^2 \sigma_{RCS}}{(4\pi)^3 R_T^2 R_R^2} \tag{2.27}$$

The IEEE Standard Dictionary of Electrical and Electronics Terms [26] defines the RCS as "4π times the ratio of the power per unit solid angle scattered in a specified direction to the power per unit area in a plane wave incident on the scatterer from a specified direction. More precisely, it is the limit of that ratio as the distance from the scatterer to the point where the scattered power is measured approaches infinity". The RCS is defined as:

$$\sigma_{RCS} = \lim_{R_R \to \infty} 4\pi R_R^2 \frac{\|\mathbf{E}_{scat} \times \mathbf{H}^*_{scat}\|}{\|\mathbf{E}_{inc} \times \mathbf{H}^*_{inc}\|} = \lim_{R_R \to \infty} 4\pi R_R^2 \frac{\|\mathbf{E}_{scat}\|^2}{\|\mathbf{E}_{inc}\|^2} = \lim_{R_R \to \infty} 4\pi R_R^2 \frac{\|\mathbf{H}_{scat}\|^2}{\|\mathbf{H}_{inc}\|^2} \tag{2.28}$$

where the scattered field is taken at the receiver location $\mathbf{r}_{rec}$ and the incident field is taken at the surface of the target. As it is a far field variable, it is only necessary to have the electric or magnetic field to describe the electromagnetic wave. The classical RCS depends on:

- Relative position of the source and receiver to the target
- The target's geometry and material properties
- Angular orientation of target relative to the source and receiver
- Frequency
- Polarization

The conventional RCS definition is valid only in the far-field region. When the radar antennas operate within the object's near field region, the target behaves as an extended scatterer with distributed sources over a wide angular range. The gain and the distance cannot be singularly defined. To address the need for a measure of near field scattering characteristics analogous to RCS, Lee, Wang, and Labarre [22] modified the radar range equation to resolve ambiguities related to range and antenna gain. Instead of calculating the range from the antennas to an arbitrary point on the object, the range is defined as the distance from the antennas to the volume centroid of the object, termed the near field range. For antenna gain, the maximum gains replace the actual gain values of each antenna. To simplify calculations, the actual directional gains of the transmitting and receiving antennas are replaced by their maximum values. Under these assumptions, the NF-RCS can be expressed as:

$$\sigma_{NF-RCS} = \frac{G_T G_R}{G_T(max) G_R(max)} \sigma_{RCS} \tag{2.29}$$

However, this definition of NF-RCS does not resolve all the issues associated with applying RCS concepts in the near field. One of the main discrepancies appears during the transition from the near field to the far-field boundary. As the antenna range increases to infinity, the value of the NF-RCS does not converge to the RCS. From this perspective, it is evident that this definition does not always recover the classical RCS value as the observation range increases. Another issue is that it can give misleading results for antennas with high directivity, especially when the main beam of the antenna is not aligned with the

target. With this formulation, the maximum theoretical detection is obtained rather than the actual measured NF-RCS. To achieve better consistency in NF-RCS estimation, another approach is to use the antenna gain in the direction of the object's centroid [22]. This implies that the NF-RCS depends on the location of the chosen centroid. The NF-RCS can be expressed as [27]:

$$\sigma_{NF-RCS} = 4\pi R_R^2 \frac{\|\mathbf{E}_{scat} \times \mathbf{H}_{scat}^*\|}{\|\mathbf{E}_{inc} \times \mathbf{H}_{inc}^*\|} \tag{2.30}$$

This relation is theoretically suitable. The major difference between RCS and NF-RCS is the dependence on the target distance. This relation can be simplified by using far-field properties to express the result in terms of either the electric or the magnetic field. To apply this equation in near field, it is not feasible directly because it needs to consider the electric and the magnetic field incident on each point of the target surface. Pouliguen [28] proposed to define the NF-RCS by using a fictitious incidents fields originating from the transmitting point. As classic RCS does not depend on antennas, it is possible to express the field from an isotropic antenna and define a more tractable relation to calculate NF-RCS:

$$\sigma_{NF-RCS} = 4\pi R_R^2 R_T^2 \eta \frac{\|\mathbf{E}_{scat} \times \mathbf{H}_{scat}^*\|}{\|V\|} \tag{2.31}$$

with V the generator voltage. By applying this solution, the NF-RCS is comparable to the RCS. In the previous equation the target is supposed to be at a fixed distance. To overcome this limitation, the NF-RCS can be obtained from the Scattering coefficient (SC) which refers to a field ratio and not a power ratio [29]. The SC is equal to:

$$\rho_{SC} = \sqrt{4\pi} R_R R_T \eta \frac{\mathbf{H}_{scat} \cdot \hat{\mathbf{p}}}{\|V\|} \tag{2.32}$$

and the NF-RCS is equal to:

$$\sigma_{NF-RCS} = \|\rho_{SC}\|^2 \tag{2.33}$$

One of the advantages of using the SC is the possibility of doing field summation. This means that for very large targets, the distance to the receiver cannot be assumed constant across the entire surface.

$$\sigma_{NF-RCS} = \left\| \int_S \rho_{SC} dS \right\|^2 \tag{2.34}$$

The integral can be calculated as a sum for different parts of the target :

$$\sigma_{NF-RCS} = \left\| \sum_S \rho_{SC} \right\|^2 \tag{2.35}$$

This notation is the most tractable definition of NF-RCS. It leads to the closest representation of RCS which could be integrated into the radar equation. The radar equation is defined through a single value equation. This means one gain and one distance for the target. In the case of NF-RCS this limitation is not necessarily accurate. The NF-RCS calculated with (2.35) can be considered as a field sum only if

the the product $R_R R_T$ doesn't vary much. In this case the previous equation lead to

$$\sigma_{NF-RCS} = \left\| \sqrt{4\pi}\eta \frac{\sum_S R_T R_R \mathbf{H}_{scat} \cdot \hat{\mathbf{p}}}{\|V\|} \right\|^2 \tag{2.36}$$

Otherwise, the equation (2.35) only gives an approximation of the NF-RCS, specifically of the field scattered by the target. In the near field backscattering regime, the electric and magnetic fields are not orthogonal. Another version of the SC could be made by using the **E** field:

$$\sigma_{NF-RCS} = \left\| \sqrt{4\pi} \frac{\sum_S R_T R_R \mathbf{E}_{scat} \cdot \hat{\mathbf{p}}}{\|V\|} \right\|^2 \tag{2.37}$$

In most cases, using either the electric or magnetic field leads to similar results but since these are near field scenarios, the results can vary significantly. The NF-RCS can be considered as an approximate indicator of how an object re-radiates energy. As the measurement is performed in the near field region, deviations may occur depending on the modeling approach. The objective here is primarily to determine a value to provide a rough estimation of the radar equation in near field conditions.

2.3 Model of the backscattering

2.3.1 Analytic method

For canonical geometries, exact solutions exist for the scattering of a target because a separation of variables in the Helmholtz equation allows the field to be rigorously modeled. These methods have been widely theorized, notably by Mie [30], who developed an exact analytical solution for electromagnetic scattering by a sphere. Using spherical coordinates, Mie expanded the incident and scattered fields in terms of spherical harmonics and Bessel functions, allowing for precise predictions of scattering, absorption, and extinction. However, this approach is not generalizable to complex targets, which usually lack the symmetry or simplicity that makes analytical solutions feasible. For these non-canonical shapes, the lack of separable coordinates means that an exact solution to the scattering problem cannot be obtained through this method, necessitating alternative approaches to understand the scattering behavior.

2.3.2 Numerical discrete methods

Numerical methods are computing techniques used to approximate solutions for complex problems or equations where an exact solution is difficult or impossible to derive. In these approaches, the target and the environment are decomposed through line, surface, or volume meshing. The goal here is to transform a complex geometry into several easier shapes to apply partial differential equations to model the electromagnetic field. In meshing theory, the goal is to discretize the target/environment finely enough to achieve sufficiently high precision, so that the results can be considered accurate. For surface meshing, the shape of the sub-element can first be modeled with triangular facets which have the

advantage of being simple shapes and give a better approximation for curved targets. To get a better meshing, Non-uniform Rational B-Splines (NURBS) [31] which are mathematical representations used to accurately describe curves are used. NURBS are an extension of B-splines and Bezier curves, providing greater flexibility and precision in modeling complex shapes. The Stationary Phase Approximation is an asymptotic method used to evaluate rapidly oscillating integrals, where the main contribution to the integral arises from points at which the phase is stationary [32]

2.3.2.1 Finite-Difference Time-Domain

The FDTD [33] is a numerical method which solves Maxwell's equations for electromagnetic wave propagation in both time and space. It is a method based on volume meshing and a time resolution, which means that it solves equations along time and is suitable for broadband analyses where multiple frequencies are studied simultaneously. The computational domain is discretized into a uniform or non-uniform grid, with the field components computed at staggered points in space and time, following the Yee grid scheme [11]. For each time step, the fields in each meshing element are computed with the field values in neighboring cells from the previous time step. One of the main challenges of this method lies in defining appropriate boundary conditions for the computational domain. This can be addressed using Perfectly Matched Layer (PML), which are absorbing boundaries that minimize reflections . This approach is suitable for antenna or target scattering at an infinite distance but in the case of complex scenarios where spherical expansion is used for the source antenna and complex scattering from the target, the method is too computationally expensive.

2.3.2.2 Finite Element Method

The Finite Element Method (FEM) is a method used to solve frequency-domain boundary value electromagnetic problems by using a variational form. The FEM is often used in the frequency domain for computing the frequency field distribution in complex, closed regions such as cavities and waveguides. As in the FDTD method, the solution domain must be truncated, making the FEM unsuitable for radiation or scattering problems unless combined with a boundary integral equation approach [34].

2.3.2.3 Method of Moments

The MOM [12] is a surface meshing method based on Integral Equation (IE) in the frequency domain. The method relies on the development of expansion of unknown surface currents in terms of basis functions. Once the currents are expressed, the integral equations (2.21,2.22) are then expressed as sums and projected onto test functions in order to minimize the error. The resulting system of integral equations is transformed into a system of linear equations, which can be written in matrix form. The solution is obtained by inverting the impedance matrix of the system. MOM is widely used with a mesh resolution of approximately $\lambda/10$. Its main drawback is its complexity. Specifically, matrix inversion can be computationally expensive, especially for large targets with dimensions comparable to the wavelength,

where the number of mesh points becomes a significant factor.

2.3.2.4 Geometrical Optics

The Geometrical Optics (GO) is based on a rays-based model of light propagation. It assumes that the dimension of the objects or structures encountered is large compared to the size of a wavelength. In this model, rays are represented as straight lines that change direction due to reflection and refraction. It is based on two main theories. Fermat's principle for the straight line propagation and Snell's law (equation 2.12) for the reflection and refraction. The Fresnel coefficients are then used to calculate the reflected and refracted fields. This method works well for simple propagation phenomena but it does not account for surface features such as edges or curvature. Consequently, if the receiver is not located in the specular direction, the field is assumed to be zero.
To have a better analysis of the scattered field, the Geometry Theory of Diffraction (GTD) was introduced to represent the diffraction by the edge for the Keller cone [35]. The spreading, amplitude intensity and decay in a ray bundle are computed from Fermat's principle and the radius of curvature at reflection points. The GTD attempts to account for the fields diffracted by edges, allowing for a calculation of the fields in shadow regions. The GTD is fast but often yields poor accuracy for more complex geometries. In order to get the edge diffraction outside the Keller cone, the Uniform Theory of Diffraction (UTD) [36] was developed as a refinement of GTD to address its limitations, particularly near shadow boundaries and caustics. UTD smooths out the singularities in GTD by introducing a uniform diffraction coefficient, which ensures continuous and physically meaningful results across all regions. UTD's robustness and continuity make it more widely applicable in modern electromagnetic simulations compared to GTD.

2.3.2.5 Physical Optics

Based on a similar approach to that illustrated in Fig. 2.6, the scattering problem can be formulated using a physical equivalent model. Similarly to the induction theorem [25], for PEC, the fields outside the target are equal to the sum of the incident and scattered fields and the inside fields are zero. In this case due to the uniqueness theorem [25] only $\mathbf{J}$ or $\mathbf{M}$ is necessary. By using only the electric current ($\mathbf{M} = 0$) the equation 2.25 is now rewritten as:

$$\begin{aligned} \mathbf{M} = 0 \rightarrow -\hat{\mathbf{n}} \times \mathbf{E}_{inc} &= \hat{\mathbf{n}} \times \mathbf{E}_{scat} \\ \mathbf{J} &= \hat{\mathbf{n}} \times (\mathbf{H}_{inc} + \mathbf{H}_{scat}) \end{aligned} \tag{2.38}$$

Therefore the equivalent problem can be summarized in Fig. 2.6 where the inverse of the incident field is set inside the target and the scattered fields are outside the target. In this equivalent formulation, the volume V_1 is filled with the same medium as the exterior, so that the fields $(\mathbf{E}_{inc}, \mathbf{H}_{inc})$ are solutions of Maxwell's equations. In this equivalent problem the current $\mathbf{J}$ radiates into a single medium, the knowledge of the $\mathbf{H}$ field at the border is necessary. In this case, the scattered field $\mathbf{H}_{scat}$ can be written

in terms of the incident field. The electric current is equal to:

$$\mathbf{J} = \hat{\mathbf{n}} \times \mathbf{H} = 2\hat{\mathbf{n}} \times \mathbf{H}_{inc} \tag{2.39}$$

As the tangential components of the scattered and incident fields are in phase and have the same value, the scattered field is equal to the incident field $\mathbf{H}_{inc} = \mathbf{H}_{scat}$.

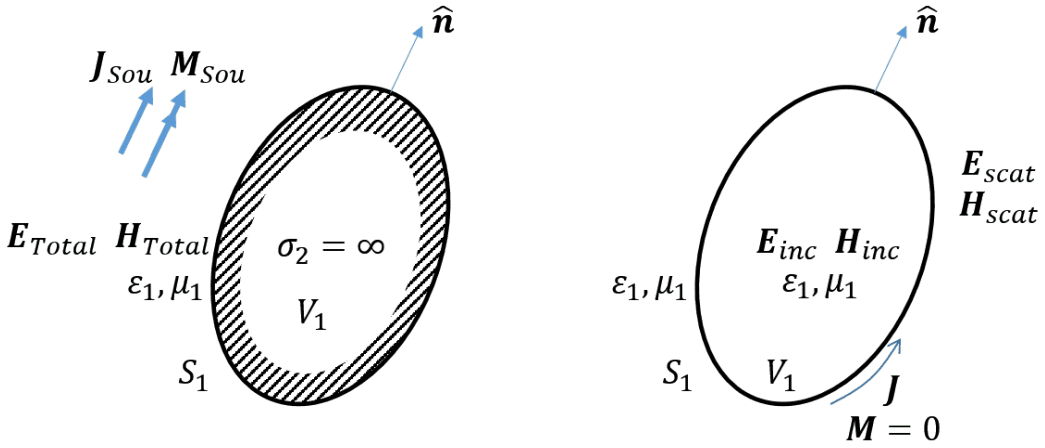

Figure 2.6: Physical optics equivalent for scattering by a PEC. **left**. Actual problem **right**. Physical equivalent

In this case, the equation 2.22 is simplified. Only the term along **J** remains and the scattered field is equal to:

$$\mathbf{H}_{scat}(\mathbf{r}_{rec}) = \iint_s \Big(\hat{\mathbf{n}} \times \mathbf{H}(\mathbf{r})\Big) \times \nabla\psi(\mathbf{R}_{rec}) dS \tag{2.40}$$

The gradient of the Green function can be directly calculated from the Green function, as it depends only on $\mathbf{R}_{\text{rec}}$. The result is:

$$\nabla\psi(\mathbf{R}_{rec}) = \left[-\frac{(jkR_{rec}+1)}{R_{rec}}\hat{\mathbf{R}}_{rec}\psi(\mathbf{R}_{rec})\right] \tag{2.41}$$

By combining 2.39, 2.40, and 2.41, the scattered magnetic field can be expressed as an integral that depends on the incident field and the receiver position:

$$\mathbf{H}_{scat}(\mathbf{r}_{rec}) = \iint_S \left[-\frac{(jkR_{rec}+1)}{R_{rec}}\Big(2\hat{\mathbf{n}} \times \mathbf{H}_{inc} \times \hat{\mathbf{R}}_{rec}\Big)\psi(\mathbf{R}_{rec})\right] dS \tag{2.42}$$

Similarly, here we have described the scattered magnetic field. In the same way, the electric field can be written as:

$$\mathbf{E}_{scat}(\mathbf{r}_{rec}) = \iint_s \left[-j\omega\mu\mathbf{J}\psi(\mathbf{R}_{rec}) + \frac{j}{\omega\varepsilon}\Big(\mathbf{J}\cdot\nabla\Big)\nabla\psi(\mathbf{R}_{rec})\right] ds \tag{2.43}$$

and according to [37] and using the relation $(\nabla \cdot \mathbf{J})\nabla\psi(\mathbf{R}) = \nabla(\mathbf{J} \cdot \nabla\psi(\mathbf{R}))$, the fields is expressed as:

$$\mathbf{E}_{scat}(\mathbf{r}_{rec}) = \iint_s \left[\frac{(-1 + jkR_{rec} + k^2R_{rec}^2)}{R_{rec}} \mathbf{J} + \frac{3 - j3kR_{rec} - k^2R_{rec}^2}{R_{rec}} \Big(\mathbf{R_{rec}} \cdot \mathbf{J} \Big) \mathbf{R_{rec}} \right] \psi(\mathbf{R}_{rec}) dS \tag{2.44}$$

the two equations 2.42 and 2.44 give the fields radiated by the current as a function of the incident field according to the PO formulation.

In the previous equation, only the electric current is used in order to simplify the calculation. The current is obtained by equivalence. Another equivalence can be made, which is linked to the induction theorem. In this case, both currents are necessary and are defined as:

$$\begin{aligned} \mathbf{J} &= -\hat{\mathbf{n}} \times \mathbf{H}_{inc} \\ \mathbf{M} &= \hat{\mathbf{n}} \times \mathbf{E}_{inc} \end{aligned} \tag{2.45}$$

Theoretically, it gives the same results as physical optics when the obstacle is an infinite plate. PO and induction theorem are suitable when problems are solved where exact solution is not easily obtainable. In fact, for complex problems with simplifications applied, they may not lead to identical results. The two solutions lead to close results but the choice of one or the other model is mainly due to the complexity of both methods [38]. When the currents are defined on the border of the target, the fields scattered are calculated by the Stratton Chu's equation.

PO is adapted to surface radiation, but in many cases, PO must be applied to multiple bounces, which may occur in cavities as illustrated in Fig. 2.7. The PO method is applied for each bounce.

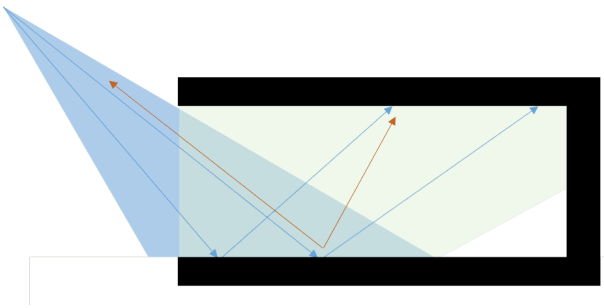

Figure 2.7: Physical optics, multiple bounces scenario.

As with GTD and UTD for GO, their exist solutions to overcome the edge problem, Firstly, Ufimtsev [20] defined the PTD. Like Keller, he relied on the canonical solution for wedge scattering to derive his diffraction coefficients, but he also considered the approximate physical optics result and sought a correction to improve this approximation . In his solution, the edges are separated from the surface contribution in order to have the contribution of the edge itself. As for the GTD, PTD relies on the exact solution of the two-dimensional wedge problem, they are only applicable in the Keller cone. To extend PTD, several methods exist based on the Method of Equivalent Current (MEC) such as EEC [14] which is presented just after.

2.3.3 Equivalent Edge Current

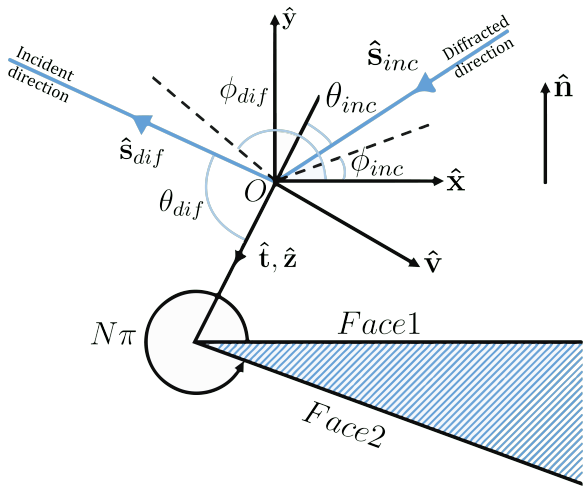

Figure 2.8: Equivalent Edge Current Scenario

To describe the diffraction of an edge, we will consider the case presented in Fig. 2.8. The incident wave in the direction $\hat{\mathbf{s}}_{inc}$ is disturbed by the edge with center O and direction vector $\hat{\mathbf{t}}$, and is then diffracted in the direction $\hat{\mathbf{s}}_{dif}$. As in the previous analysis on surfaces, the curvature of the target will be neglected, and the edge will be considered locally straight. To do this, the chord criterion and the Fraunhofer criterion will be used.

It is possible to analyze edge diffraction using the MEC. The fields diffracted by a discontinuity associated with an edge can be expressed in terms of equivalent currents on the edge $\boldsymbol{\mathcal{J}}$ and $\boldsymbol{\mathcal{M}}$. The magnetic field diffracted by the discontinuity associated with edge l can be expressed as:

$$\begin{aligned}\mathbf{H}_{dif}(\mathbf{r}_{rec}) = \int_l \Bigg[&-\frac{(jkR_{rec}+1)}{R_{rec}}\Big(\boldsymbol{\mathcal{J}} \times \hat{\mathbf{s}}_{dif}\Big) + \frac{1}{\eta}\frac{-jkR_{rec}+(kR_{rec})^2}{jkR_{rec}^2}\boldsymbol{\mathcal{M}} \\ &+\frac{1}{\eta}\frac{-j3kR_{rec}+(kR_{rec})^2}{jkR_{rec}^2}\Big(\boldsymbol{\mathcal{M}} \cdot \hat{\mathbf{s}}_{dif}\Big)\hat{\mathbf{s}}_{dif}\Bigg]\psi(\mathbf{R}_{rec})dl\end{aligned} \tag{2.46}$$

where $\mathbf{R}_{rec} = R_{rec}\hat{\mathbf{s}}_{dif}$ being the vector between the target and the receiver. This equation is similar to the MFIE. The goal is to extrapolate $\boldsymbol{\mathcal{J}}$ and $\boldsymbol{\mathcal{M}}$ from the equation 2.46. The first point is to rewrite the total diffracted fields from the two faces which are linked to the edge l, $Face$ 1 and $Face$ 2 under the assumption of PEC target ($\mathbf{M} = 0$):

$$\mathbf{H}_{scat} = \sum_{i=1}^{2}\iint_{S_i}\left[-\frac{(jkR_{rec}+1)}{R_{rec}}\Big(\mathbf{J} \times \hat{\mathbf{R}}_{rec}\Big)\psi(\mathbf{r}_{rec})\right]dS_i \tag{2.47}$$

Only the electric current $\mathbf{J}$ on the surface will be considered in equation 2.47. The integration is performed on the two surfaces associated with the edge, surface 1 S_1 and surface 2 S_2. The total field diffracted by the two faces is considered as the sum of the fields diffracted by the two surfaces. In this study, since

the two faces will play a symmetric role, only the case of $Face$ 1 will be considered.
To apply the transition from $Face$ 1 to $Face$ 2, the analogy is made by performing the following substitutions:

$$\begin{aligned} &\mathbf{t} \rightarrow -\mathbf{t}, \quad \theta_{inc} \rightarrow \pi - \theta_{inc} \quad \theta_{dif} \rightarrow \pi - \theta_{dif} \\ &\phi_{inc} \rightarrow N\pi - \phi_{inc} \quad \phi_{dif} \rightarrow N\pi - \phi_{dif} \end{aligned} \tag{2.48}$$

where θ_{inc} and θ_{dif} are defined as:

$$\theta_{inc} = \cos^{-1}(\hat{\mathbf{s}}_{inc} \cdot \hat{\mathbf{t}}) \qquad \theta_{dif} = \cos^{-1}(\hat{\mathbf{s}}_{dif} \cdot \hat{\mathbf{t}}) \tag{2.49}$$

and the angles ϕ_{inc} and ϕ_{dif} are defined as the angles between the intersection of $Face$ 1 and the plane containing the direction vector of the edge $\hat{\mathbf{t}}$, and respectively the vectors $\hat{\mathbf{s}}_{inc}$ and $\hat{\mathbf{s}}_{dif}$. To perform the calculation, a new basis is defined, the vector $\hat{\mathbf{x}}$ is normal to the edge contained in $Face$ 1, $\hat{\mathbf{y}}$ is normal to $Face$ 1, and $\hat{\mathbf{z}}$ is the direction of the edge. The incident and scattered direction vectors can be written as:

$$\begin{aligned} \hat{\mathbf{s}}_{\mathbf{inc}} &= \sin(\theta_{inc})\cos(\phi_{inc})\hat{\mathbf{x}} + \sin(\theta_{inc})\sin(\phi_{inc})\hat{\mathbf{y}} + \cos(\theta_{inc})\hat{\mathbf{z}} \\ \hat{\mathbf{s}}_{\mathbf{dif}} &= \sin(\theta_{dif})\cos(\phi_{dif})\hat{\mathbf{x}} + \sin(\theta_{dif})\sin(\phi_{dif})\hat{\mathbf{y}} + \cos(\theta_{dif})\hat{\mathbf{z}} \end{aligned} \tag{2.50}$$

The field scattered by a face can also be split into two parts, first is the radiation of the surface and second is the radiation of the edge or near the edge. The diffraction from the edges is primarily due to the surface currents near the edge l.
According to [39], the currents $\boldsymbol{\mathcal{J}}_1$ and $\boldsymbol{\mathcal{M}}_1$ on the edges can be decomposed into two components: fringe currents and currents associated with physical optics.

$$\boldsymbol{\mathcal{J}}_1 = (\boldsymbol{\mathcal{J}}_1^{PO} + \boldsymbol{\mathcal{J}}_1^{f}) \qquad \boldsymbol{\mathcal{M}}_1 = (\boldsymbol{\mathcal{M}}_1^{PO} + \boldsymbol{\mathcal{M}}_1^{f}) \tag{2.51}$$

The component used for the fringe refers to the equivalent current on the edges, which is directly linked to the fringe current on the surface. The PO component is used to remove the radiation from the surface, which is originally intended for an infinite surface.

2.3.3.1 Fringe currents

A fringe current refers to the current distribution along the edges of a conducting surface. It contributes to the overall field radiated by the surface and is due to the discontinuity created by the edge. To best define the equivalent currents associated with the fringe current, we will consider the electric current $\mathbf{J}_1^f$ as a current propagating along the vector $\hat{\mathbf{v}}_1$ (Fig. 2.9), where $\hat{\mathbf{v}}_1$ is defined as $\hat{\mathbf{v}}_1 = \sin\theta_{inc}\hat{\mathbf{x}}_1 + \cos\theta_{inc}\hat{\mathbf{z}}$ [40]. This refers to the projection of the incident direction on the surface.
The technique used to transform this surface current into an edge current consists in taking the limit of equation (2.47) as the surface S_1 toward the edge. This means that the surface S_1 will tend toward

the edge l. The remaining radiation will correspond solely to the radiation of the edge due to the *Face* 1. Combined with the *Face* 2. The equivalent fringe current for the edge $\boldsymbol{\mathcal{J}}^f$ can be defined as $\boldsymbol{\mathcal{J}}^f = \boldsymbol{\mathcal{J}}_1^f + \boldsymbol{\mathcal{J}}_2^f$

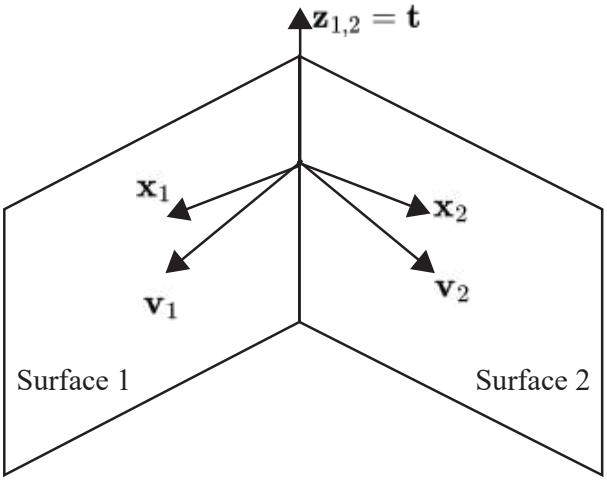

Figure 2.9: Edge radiation geometry for two surfaces 1 and 2

To perform the integral, instead of integrating over the surface, we will separate the surface integral into two integrals, one along the edge l with direction vector $\mathbf{t}$ and one along the axis $\mathbf{v}$. The scattered magnetic field $\mathbf{H}_{scat}^f$ derived from equation 2.47 when studying the case where $\mathbf{v}$ is approaches zero, is:

$$\mathbf{H}_{scat}^f(\mathbf{r_{rec}}) = \sin(\theta_{inc}) \int_l \left[\sum_{i=1}^{2} \int_0 -\frac{(jkR_{rec}+1)}{R_{rec}} \left(\mathbf{J}_i^f \times \hat{\mathbf{R}}_{rec} \right) \psi(\mathbf{R}_{rec}) dv_i \right] dl \tag{2.52}$$

The limit $\mathbf{v} \to 0$ is taken for both surfaces. Since the two surfaces share the same edge l with direction vector $\mathbf{t}$, we can perform the integral along this axis after summing and taking the limit at $\mathbf{v} \to 0$. In this case, the Green function can be written as a function of the distance to its projection on the edge. For *Face* 1, it is rewritten as $\psi(\mathbf{R_{rec}}) = \psi(\mathbf{R}_{rec,l}) e^{jk\mathbf{v}_1 \cdot \hat{\mathbf{s}}_{dif}}$. The vector $\mathbf{R}_{rec,l}$ refers to the distance from the projection on the edge to the receiver. It can be defined from this equation $\mathbf{R}_{rec} = \mathbf{R}_{rec,l} + \mathbf{v_1}$. For the non-exponential terms, we can write the substitution $\mathbf{R}_{rec} \to \mathbf{R}_{rec,l}$. In this case, the equation 2.52 can be rewritten as:

$$\mathbf{H}_{scat}^f(\mathbf{r_{rec}}) = \int_l \left[\sum_{i=1}^{2} -\frac{(jkR_{rec,l}+1)}{R_{rec,l}} \psi(\mathbf{R_{rec,l}}) \mathbf{K}_i^f \times \hat{\mathbf{s}}_{dif} \right] dl \tag{2.53}$$

where

$$\mathbf{K}_1^f = \sin(\theta_{inc}) \int_0 \mathbf{J}_1^f \left(v_1 \sin(\theta_{inc}), v_1 \cos(\theta_{inc}) \right) e^{jk\mathbf{v}_1 \cdot \hat{\mathbf{s}}_{dif}} dv_1 \tag{2.54}$$

and similarly for $\mathbf{K}_2^f$. Here, the remaining integral over the axis $\mathbf{v}_1$ contains only exponentially varying terms. From equations 2.53 and 2.54 the objective is to establish a link between the fringe current on the surfaces and the equivalent fringe current on the edge l. This means to link $\mathbf{J}_i^f$ with $\boldsymbol{\mathcal{J}}_i^f$ and $\boldsymbol{\mathcal{M}}_i^f$. The two terms 2.53 and 2.46 are equal and the equation is:

$$-\frac{(jkR_{rec,l}+1)}{R_{rec,l}}\psi(\mathbf{R_{rec,l}})\mathbf{K}_1^f\times\hat{\mathbf{s}}_{dif}=-\frac{(jkR_{rec}+1)}{R_{rec}}\left(\boldsymbol{\mathcal{J}}_1^f\times\hat{\mathbf{s}}_{dif}\right)+\frac{1}{\eta}\frac{-jkR_{rec}+(kR_{rec})^2}{jkR_{rec}^2}\boldsymbol{\mathcal{M}}_1^f \\ +\frac{1}{\eta}\frac{-j3kR_{rec}+(kR_{rec})^2}{jkR_{rec}^2}\left(\boldsymbol{\mathcal{M}}_1^f\cdot\hat{\mathbf{s}}_{dif}\right)\hat{\mathbf{s}}_{dif} \tag{2.55}$$

In the left part, only one current is used: the electric fringe current $\mathbf{J}_1^f$, but in the right part there are both $\boldsymbol{\mathcal{J}}_1^f$ and $\boldsymbol{\mathcal{M}}_1^f$. Since the goal is to obtain the expressions of $\boldsymbol{\mathcal{J}}_1^f$ and $\boldsymbol{\mathcal{M}}_1^f$, which are expressed in terms of the vector $\mathbf{t}$, we have a system of 3 equations and 2 unknowns. Indeed, since we are working in 3D, we proceed by equating coordinates component by component. In order to obtain a proper linear combination that isolates only the term $\boldsymbol{\mathcal{J}}_1^f$, we examine the direction vectors of the three terms on the right-hand side:

$$\begin{aligned}-\frac{(jkR_{rec}+1)}{R_{rec}}\left(\boldsymbol{\mathcal{J}}\times\hat{\mathbf{s}}_{dif}\right)&\rightarrow\mathbf{t}\times\hat{s}_{dif}\\ \frac{1}{\eta}\frac{-jkR_{rec}+(kR_{rec})^2}{jkR_{rec}^2}\boldsymbol{\mathcal{M}}&\rightarrow\mathbf{t}\\ \frac{1}{\eta}\frac{-j3kR_{rec}+(kR_{rec})^2}{jkR_{rec}^2}\left(\boldsymbol{\mathcal{M}}\cdot\hat{\mathbf{s}}_{dif}\right)\hat{\mathbf{s}}_{dif}&\rightarrow\hat{\mathbf{s}}_{dif}\end{aligned} \tag{2.56}$$

The first term, which depends on $\boldsymbol{\mathcal{J}}$, is oriented perpendicularly to both the edge and the scattering direction. There are two terms involving $\boldsymbol{\mathcal{M}}$: the first is directed along the edge, and the second along the scattering direction. To eliminate the first $\boldsymbol{\mathcal{M}}$-related term in equation 2.56, it is possible to apply a cross product with the direction $\mathbf{t}$. The three components then become:

$$\begin{aligned}-\frac{(jkR_{rec}+1)}{R_{rec}}\left(\boldsymbol{\mathcal{J}}\times\hat{\mathbf{s}}_{dif}\right)\times\mathbf{t}&\rightarrow(\mathbf{t}\times\hat{s}_{dif})\times\mathbf{t}\\ \frac{1}{\eta}\frac{-jkR_{rec}+(kR_{rec})^2}{jkR_{rec}^2}\boldsymbol{\mathcal{M}}\times\mathbf{t}&\rightarrow0\\ \frac{1}{\eta}\frac{-j3kR_{rec}+(kR_{rec})^2}{jkR_{rec}^2}\left(\boldsymbol{\mathcal{M}}\cdot\hat{\mathbf{s}}_{dif}\right)\hat{\mathbf{s}}_{dif}\times\mathbf{t}&\rightarrow\hat{\mathbf{s}}_{dif}\times\mathbf{t}\end{aligned} \tag{2.57}$$

Since there is still a remaining term along $\boldsymbol{\mathcal{M}}$, a second cross product is applied in order to retain only the terms associated with $\boldsymbol{\mathcal{J}}$.

$$\begin{aligned}-\frac{(jkR_{rec}+1)}{R_{rec}}\left(\boldsymbol{\mathcal{J}}\times\hat{\mathbf{s}}_{dif}\right)\times\mathbf{t}\times(\mathbf{t}\times\hat{\mathbf{s}}_{dif})&\rightarrow((\mathbf{t}\times\hat{s}_{dif})\times\mathbf{t})\times(\mathbf{t}\times\hat{\mathbf{s}}_{dif})\\ \frac{1}{\eta}\frac{-jkR_{rec}+(kR_{rec})^2}{jkR_{rec}^2}\boldsymbol{\mathcal{M}}\times\mathbf{t}&\rightarrow0\\ \frac{1}{\eta}\frac{-j3kR_{rec}+(kR_{rec})^2}{jkR_{rec}^2}\left(\boldsymbol{\mathcal{M}}\cdot\hat{\mathbf{s}}_{dif}\right)(\hat{\mathbf{s}}_{dif}\times\mathbf{t})\times(\mathbf{t}\times\hat{\mathbf{s}}_{dif})&\rightarrow0\end{aligned} \tag{2.58}$$

From equation 2.58, when doing two cross products, only the term along $\mathcal{J}_1^f$ remains. This means that

after doing the cross product along $\hat{\mathbf{t}}$ and $\hat{\mathbf{t}} \times \hat{\mathbf{s}}_{dif}$ and with simplifications, the equation 2.55 becomes:

$$(\hat{\mathbf{t}} \times \hat{\mathbf{s}}_{dif}) \times \left(\hat{\mathbf{t}} \times \left(\hat{\mathbf{t}} \times \hat{\mathbf{s}}_{dif}\right)\right) \mathcal{J}_1^f = (\hat{\mathbf{t}} \times \hat{\mathbf{s}}_{dif}) \times \left(\hat{\mathbf{t}} \times \left[\mathbf{K}_1^f \times \hat{\mathbf{s}}_{dif}\right]\right) \tag{2.59}$$

In order to simplify the previous equation, we can make use of the properties of the cross product to ease the calculations: $||\hat{\mathbf{t}} \times \hat{\mathbf{s}}_{dif}|| = \sin(\theta_{inc})$ and $(\hat{\mathbf{t}} \times \hat{\mathbf{s}}_{dif}) \times \left(\hat{\mathbf{t}} \times \left(\hat{\mathbf{t}} \times \hat{\mathbf{s}}_{dif}\right)\right) = \sin^2(\theta_{dif})\,\hat{\mathbf{t}}$.

For the left-hand side, by using the identity $\mathbf{a} \times (\mathbf{b} \times \mathbf{c}) = (\mathbf{a} \cdot \mathbf{c})\,\mathbf{b}$ when $\mathbf{a} \perp \mathbf{b}$ which means:

$$(\hat{\mathbf{t}} \times \hat{\mathbf{s}}_{dif}) \times \left(\hat{\mathbf{t}} \times \left[\mathbf{K}_1^f \times \hat{\mathbf{s}}_{dif}\right]\right) = \left(\left[\hat{\mathbf{t}} \times \hat{\mathbf{s}}_{dif}\right] \cdot \left[\mathbf{K}_1^f \times \hat{\mathbf{s}}_{dif}\right]\right) \hat{\mathbf{t}} \tag{2.60}$$

By combining equation 2.60 and equation 2.59, the equation is simplified, and the equivalent electric current on the edge is equal to:

$$\boldsymbol{\mathcal{J}}_1^f = \frac{1}{\sin(\theta_{dif})^2} \left(\left[\hat{\mathbf{t}} \times \hat{\mathbf{s}}_{dif}\right] \cdot \left[\mathbf{K}_1^f \times \hat{\mathbf{s}}_{dif}\right]\right) \hat{\mathbf{t}} \tag{2.61}$$

As the current on surface 1 is defined only along its component along $\mathbf{x}$ and $\mathbf{y}$, the vector $\mathbf{K}_1^f$ can be rewritten as a sum over $\mathbf{x}$ and $\mathbf{z}$ and by using the Cartesian decomposition of $\hat{\mathbf{s}}_{dif}$,

$$\mathcal{J}_1^f = K_{1,z}^f - K_{1,x}^f \cot(\theta_{dif}) \cos(\phi_{dif}) \tag{2.62}$$

where

$$\mathbf{K}_{x,z,1}^f = \sin(\theta_{inc}) \int_0 \mathbf{J}_{x,z,1}^f \left(v_1 \sin(\theta_{inc}), v_1 \cos(\theta_{inc})\right) e^{jk\mathbf{v}_1 \cdot \hat{\mathbf{s}}_{dif}} dv_1 \tag{2.63}$$

and

$$\mathbf{J}_{x,z,1}^f = \mathbf{J}_{x,1}^f + \mathbf{J}_{z,1}^f = \hat{\mathbf{y}}_1 \times (H_z(y_1 = 0) - H_x(y_1 = 0)) \tag{2.64}$$

One major issue here is that the fringe current depends on the total field, whereas in our case only the incident field is known. The goal is to use the canonical solution of the edge problem, specifically to remove the component along $\mathbf{x}$ and express it along $\mathbf{z}$. For the case under consideration, the total field depends on $\mathbf{z}$ only through the factor $e^{-jk\cos(\theta_{inc})}$. Maxwell's equations then become:

$$\nabla \times \mathbf{E} = -jk\eta\mathbf{H} \tag{2.65}$$

$$\nabla \times \mathbf{H} = jkY\mathbf{E} \tag{2.66}$$

The current on the surface can be developed by the three-dimensional solution of the canonical wedge problem [19]. The component along $\mathbf{x}$ of the magnetic field $\mathbf{H}_x$ is equal to:

$$\mathbf{H}_x = \frac{1}{jk\sin^2(\theta_{inc})} \left(-Y\frac{\partial E_z}{\partial y} + \cos(\theta_{inc})\frac{\partial H_z}{\partial x}\right) \tag{2.67}$$

where Y is the admittance of the medium. We now use the canonical solutions of the edge problem to relate the fields in z to the components in z at the point O of the incident field [41]

$$\begin{aligned}\mathbf{E}_z^f &= \mathbf{E}_{inc,z,O}[u^f(X,\Psi-\phi_{inc}) - u^f(X,\Psi+\phi_{inc})] \\ \mathbf{H}_z^f &= \mathbf{H}_{inc,z,O}[u^f(X,\Psi-\phi_{inc}) - u^f(X,\Psi+\phi_{inc})]\end{aligned} \tag{2.68}$$

where Ψ is the polar angle in the plane $(\mathbf{v},\mathbf{y})$(equal to 0 when viewed directly onto the surface), and

$$u^f = \frac{1}{2\pi jN}\int_{\Gamma'}\frac{\sin(\xi/N)e^{jX\cos\xi}}{\cos(\xi/N)-\cos(\phi_{inc}/N)} \tag{2.69}$$

where Γ' is the distorted contour of integration for the canonical wedge problem [40]. X is defined as:

$$X = kv\sin^2\theta_{inc} \tag{2.70}$$

From equations 2.67, 2.68 and 2.62 the equivalent electric current can be derived as:

$$\begin{aligned}\mathcal{J}_1^f = {} & E_{inc,z,O}\frac{2jY}{k\sin^2\theta_{inc}}\int_0\frac{1}{X}\frac{\partial u^f(X,\phi_{inc})}{\partial\phi_{inc}}e^{jk\mathbf{v}_1\cdot\hat{\mathbf{s}}_{dif}}dX \\ & + \frac{2H_{inc,z,O}}{k\sin(\theta_{inc})}\int_0\left[j\cot\theta_{inc}\frac{\partial u(X,\phi_{inc}}{\partial X} - \cot(\theta_{dif})\cos(\phi)u(X,\phi_{inc})\right]e^{jk\mathbf{v}_1}dX\end{aligned} \tag{2.71}$$

and by a same analysis done by Michaeli in [40], the electric equivalent current for fringe currents is:

$$\begin{aligned}\mathcal{J}_1^f = {} & \frac{2j}{k\sin(\theta_{inc})}\frac{1/N}{\cos(\phi_{inc}/N)-\cos(\frac{\pi-\alpha_1}{N})}\left(\frac{\sin(\phi_{inc}/N)}{\eta\sin(\theta_{inc})}\hat{\mathbf{z}}\cdot\mathbf{E}_{inc}+\right. \\ & \left.\frac{\sin(\frac{\pi-\alpha_1}{N})}{\sin(\alpha_1)}(\cos(\alpha_1)\cot(\theta_{inc})-\cot(\theta_{dif})\cos(\phi_{dif})\hat{\mathbf{z}}\cdot\mathbf{H}_{inc}\right) - \frac{2j\cot(\theta_{inc})}{kN\sin(\theta_{inc})}\hat{\mathbf{z}}\cdot\mathbf{H}_{inc}\end{aligned} \tag{2.72}$$

where

$$\begin{aligned}\alpha_1 &= \cos^{-1}\left(\frac{(\cos(\gamma)-\cos^2(\theta_{inc})}{\sin^2\theta_{inc}}\right) \\ \cos(\gamma) &= \sin(\theta_{inc})\sin(\theta_{dif})\cos(\phi_{dif})+\cos(\theta_{inc})\cos(\theta_{dif})\end{aligned} \tag{2.73}$$

Similarly to the calculation made for the electric current, the magnetic current for the fringe current can be calculated by using a far field approximation and a similar approach as:

$$\mathcal{M}_1^f = \frac{2j\eta\sin(\phi_{dif})}{k\sin(\theta_{inc})\sin(\theta_{dif})}\frac{-1/N}{\cos(\phi_{dif}/N)-\cos(\frac{\pi-\alpha_1}{N})}\sin(\frac{\pi-\alpha_1}{N})csc(\alpha_1)\hat{\mathbf{z}}\cdot\mathbf{H}_{inc} \tag{2.74}$$

The expression derived for the fringe components $\mathcal{M}_1^f$ and $\mathcal{J}_1^f$ have only one singularity remaining which is the Ufimtsev singularities [20], which exists in the special situation where the observation direction is the continuation of a glancing incident ray. The situation occurs only in forward scattering, it exists solution for removing this singularity [42]. In order to remove the singularity, the integral is not simplified to a region close to the edge. All the strip is taken into account. The non-uniqueness of equivalent current

should not cause concern so long as the radiation integral is unique.

2.3.3.2 Physical optics currents

The PO component of the surface currents, contrary to the fringe component, has the advantage of being expressed in closed form in terms of the incident field (due to PO) and the surface equation, and, as a result, can be calculated numerically. To perform the calculation, we define the surface dS_1 as:

$$dS_1 = \left| \frac{\partial \mathbf{p}}{\partial z} \times \frac{\partial \mathbf{p}}{\partial x} \right| dx\ dz \tag{2.75}$$

where $\mathbf{p}$ is the position vector of a point on S_1 and $\mathbf{x}$ is a coordinate measured from the edges along a tangent to S_1 and skew with respect to $\mathbf{z}$. Similarly to the equation defining the equivalent edge currents for the fringe component, the currents are expressed as:

$$\begin{aligned} \boldsymbol{\mathcal{M}}_1^{PO} &= \eta \frac{-1}{\sin^2(\theta_{dif})} \hat{\mathbf{z}} \cdot \left[\mathbf{K}_1^{PO} \times \hat{\mathbf{s}}_{dif} \right] \\ \boldsymbol{\mathcal{J}}_1^{PO} &= \frac{-1}{\sin^2(\theta_{dif})} \hat{\mathbf{s}}_{dif} \cdot \left(\hat{\mathbf{z}} \times \left[\mathbf{K}_1^{PO} \times \hat{\mathbf{s}}_{dif} \right] \right) \end{aligned} \tag{2.76}$$

where

$$\mathbf{K_1^{PO}} = \int_0 \mathbf{J}_1^{PO} e^{jk\hat{\mathbf{v}}\cdot\hat{\mathbf{s}}_{dif}} dq \tag{2.77}$$

To find the amplitude of $\mathbf{J}_1^{PO}$, the surface is simply described by the tangent plane, and the incident wave by a plane wave propagating along $\hat{\mathbf{s}}_{inc}$. The electric current is expressed as

$$\begin{aligned} \mathbf{J}_1^{PO} =& 2\hat{\mathbf{n}} \times \mathbf{H_{inc}} = \\ & 2(\hat{\mathbf{z}} \cdot \mathbf{H_{inc}})\hat{\mathbf{x}} + 2Y \frac{\sin(\phi_{inc})}{\sin(\theta_{inc})} \hat{\mathbf{z}} \cdot \mathbf{E_{inc}} - 2\cot(\theta_{inc})\cos(\phi_{inc})\hat{\mathbf{z}} \cdot \mathbf{H_{inc}} \end{aligned} \tag{2.78}$$

By following the same procedure as Michaeli, the equivalent currents for PO are obtained as :

$$\begin{aligned} \mathcal{J}_1^{PO} =& \frac{2jU_1}{k\sin(\theta_{inc})(\cos(\phi_{inc}) + \cos(\alpha_1))} \left(\frac{\sin(\phi_{inc})}{\eta \sin(\theta_{inc})} \hat{\mathbf{z}} \cdot \mathbf{E}_{inc} - \right. \\ & \left. (\cot(\theta_{inc})\cos(\phi_{inc}) + \cot(\theta_{dif})\cos(\phi_{dif}))\hat{\mathbf{z}} \cdot \mathbf{H}_{inc} \right) \\ \mathcal{M}_1^{PO} =& \frac{-2j\eta \sin(\phi_{dif})U_1}{k\sin(\theta_{inc})\sin(\theta_{dif})} \frac{1}{(\cos(\phi_{inc}) + \cos(\alpha_1))} \hat{\mathbf{z}} \cdot \mathbf{H}_{inc} \end{aligned} \tag{2.79}$$

where U_1 is the step function that defines if the surface S_1 is illuminated or not by the incident wave. This function occurs only for PO currents.

Once both currents are combined, the possible singularities vanish except in the case of the Ufimtsev singularity. To apply the EEC, the current must not be used when θ and ϕ are close to 0.

Let us have a look at the possible singularities that may occur in the previous formulas. Firstly when $\cos(\theta_{inc}) = -\cos(\alpha_1)$, this means that $\alpha_1 \equiv \pi - \theta_{inc} \bmod 2\pi$. The four currents become singular in this

case $\boldsymbol{\mathcal{J}}_1^{PO}, \boldsymbol{\mathcal{M}}_1^{PO}$ and $\boldsymbol{\mathcal{J}}_1^{f}, \boldsymbol{\mathcal{M}}_1^{f}$. This means that they cannot be referred to as equivalent currents, but as components of the current $\boldsymbol{\mathcal{J}}_1, \boldsymbol{\mathcal{M}}_1$. In order to find the value of the current at this point, we are going to make a Taylor series expansion of α_1 around $\pi - \theta_{inc}$ and to simplify the readability of the derivation, the term $\alpha_1' = \pi - \alpha_1$ is defined. The Taylor expansion is done at $\alpha_1' = \theta_{inc}$ to first order :

$$\begin{aligned} \cos(\phi_{inc}/N) - \cos(\frac{\alpha_1'}{N}) &\approx \sin(\phi_{inc}/N)\frac{\phi_{inc} - \alpha_1'}{N} \\ \cos(\phi_{inc}) - \cos(\alpha_1') &\approx \sin(\phi_{inc})\phi_{inc} - \alpha_1' \end{aligned} \tag{2.80}$$

By combining the equations 2.72 and 2.79 the limit is expressed as:

$$\begin{aligned} &\lim_{\alpha_1' \to \theta_{inc}} \boldsymbol{\mathcal{J}}_1^{f} - \boldsymbol{\mathcal{J}}_1^{PO} = \frac{2j}{k\sin(\theta_{inc})}\Bigg[\left(\frac{\sin(\phi_{inc}/N)/N}{\cos(\phi_{inc}/N) - \cos(\frac{\alpha_1'}{N})} - \frac{\sin(\phi_{inc})}{\cos(\phi_{inc}) - \cos(\alpha_1')}\right) \\ &\frac{1}{\eta\sin(\theta_{inc})}\hat{\mathbf{z}} \cdot \mathbf{E}_{inc} + \big(\cos(\alpha_1)\cot(\theta_{inc}) - \cot(\theta_{dif})\cos(\phi_{dif})\big) \\ &\left(\frac{\sin(\frac{\alpha_1'}{N})}{\sin(\alpha_1')}\frac{1/N}{\cos(\phi_{inc}/N) - \cos(\frac{\alpha_1'}{N})} - \frac{1}{(\cos(\phi_{inc}) - \cos(\alpha_1'))}\right)(\hat{\mathbf{z}} \cdot \mathbf{H}_{inc})\Bigg] - \frac{2j\cot(\theta_{inc})}{kN\sin(\theta_{inc})}\hat{\mathbf{z}} \cdot \mathbf{H}_{inc} \\ &= -\frac{2j\cot(\theta_{inc})}{kN\sin(\theta_{inc})}\hat{\mathbf{z}} \cdot \mathbf{H}_{inc} \end{aligned} \tag{2.81}$$

In this case, we can therefore define:

$$\boldsymbol{\mathcal{J}}_1(\alpha_1' = \theta_{inc}) = -\frac{2j\cot(\theta_{inc})}{kN\sin(\theta_{inc})}\hat{\mathbf{z}} \cdot \mathbf{H}_{inc} \tag{2.82}$$

For the magnetic current:

$$\begin{aligned} \lim_{\alpha_1' \to \theta_{inc}} \boldsymbol{\mathcal{M}}_1^{f} - \boldsymbol{\mathcal{M}}_1^{PO} =& \frac{2j\eta\sin(\phi_{dif})}{k\sin(\theta_{inc})\sin(\theta_{dif})}\frac{-1/N}{\cos(\phi_{dif}/N) - \cos(\frac{\pi - \alpha_1}{N})}\sin(\frac{\pi - \alpha_1}{N}) \\ & csc(\alpha_1)\hat{\mathbf{z}} \cdot \mathbf{H}_{inc} + \frac{1}{(\cos(\phi_{inc}) + \cos(\alpha_1))}\hat{\mathbf{z}} \cdot \mathbf{H}_{inc} = 0 \end{aligned} \tag{2.83}$$

Similarly, we can define

$$\boldsymbol{\mathcal{M}}_1(\alpha_1' = \theta_{inc}) = 0 \tag{2.84}$$

2.4 Choice of Physical Optics

In this thesis, as mentioned in Chapter 1, the goal is to manage the scattering of very large targets compared to the wavelength. According to the Fraunhofer criterion, the equivalent radiating surface of the target will be considered to radiate in the near field. To select one of the model presented before, we are going to exclude models where the complexity is too high:

- **FDTD**: full-wave simulation like FDTD would be excessively costly in terms of computation time. Mainly due to the environment meshing. FDTD is not a good model when several items are radiating (Source and target)

- **FEM**: It meshes the volume of the target, the source and receiver. as for FDTD, the large size of the target leads to computational issues.
- **MOM** This methods only meshes the surfaces of the different targets which is more suitable for large scale scenarios. The MOM needs a fine meshing, which may also raise issues.

The two last approach are the GO and the PO and their enhancements via edge diffraction. If we want to compare them, the GO is faster with a low complexity whereas there is an integral calculation for PO method. In theory, when the target is an infinite plane surface with a far field receiver, both methods are going to lead to the same result. However, working with infinite targets is not suitable for near-field scenarios. In this case, the diffraction of the different element is important. The PO approach gives more realistic results due to the surface scattering whereas the GO method focuses on surface reflection. Furthermore, these methods can be combined to handle complex situation like [25] where the internal bounces on the target (i.e. a dihedral target with 2 bounces) are handled by GO and the last bounce is handle by PO. The result obtained by this method is limited to the precision of the GO result but, it has the advantage of modeling the scattering with more precision rather than only GO. To be applied to complex target, several approaches exist to take into account the multiple bounces:

- Iterative Physical Optics (**IPO**) as for PO, it is a surface-based method where currents are iteratively calculated as a function of the current on the other element of the target. It can be enhanced by using EEC for edges diffraction. The IPO method is limited by the integral calculation which needs to be handled numerically.
- Shooting and Bouncing Ray (**SBR**) method coupled to uniform theory of diffraction is a powerful method which can accurately be used to model the backscattering of large targets. It is a ray launch model where geometrical optics is used to predict the direction and a PO-scheme is used to calculate the currents at each bouncing point. An appropriate method in order to have good results is to use ray tube. This method can be seen as faster than IPO, because the scattered field is not calculated all around the scattered element but just in the main cone of radiation. This method leads to good results however, it is limited for scattering directions far from specular diffraction.

Both methods adequately address the problem: they are computationally inexpensive and sufficiently accurate for near-field applications. When looking for differences, it is shown that [43] SBR is faster when the number of bounces is sufficiently low. The SBR model is time-saving due to the ray-tube approach, but it has the drawback of requiring the scattering direction to be recalculated at each bounce. This leads to a major drawback, if a surface is illuminated from multiple Angle of Arrival (AoA), for each incident ray, the current cannot be summed. Each current needs to be handle individually. This means that on the same surface, one current can be used to radiate in a direction and an other for a second direction. Therefore for complex target, it will be common that a surface is illuminated by more than two surfaces. The complexity of SBR is then exponential.
The classic algorithm for IPO will be:

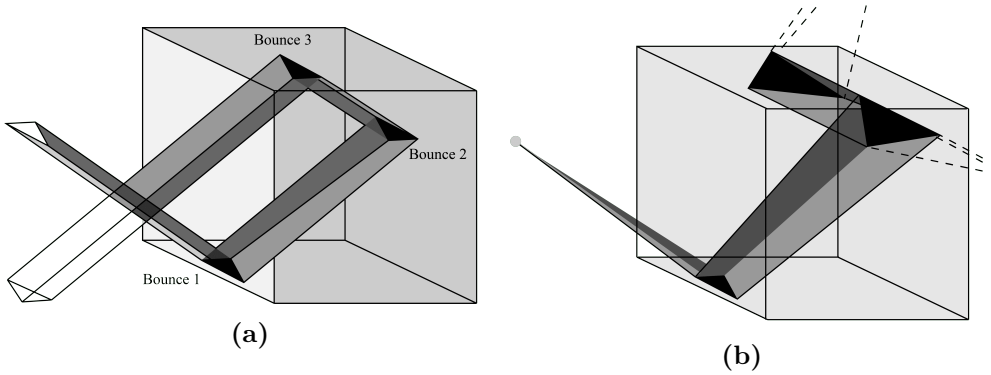

Figure 2.10: (a) SBR ray-tube evolution in far field (b) SBR ray-tube evolution in near field

- Find illuminated part by the antenna source
- Find the illuminated function: which parts of the target seen which others parts
- Find which part can scatter in direction of the antenna
- Calculate the currents iteratively on the parts of the target
- Calculate the field scattered in direction of the receiving antenna

For the SBR the algorithm will look to:

- Find illuminated part by the antenna source
- Calculate the current on this surface
- Scatter in direction of the ray-tube reflection
- Calculate the currents on this second surface
- Repeat iteratively the two last steps

For several bounces, SBR needs to recalculate the direction, which means for complex targets a necessity to recalculate intersections which can make the algorithms less efficient. Another main problem that can appear in the SBR algorithm is the spray of near field scattering. When looking to far field scattering the SBR ray-tube surface does not change. In near field, the ray-tube will be larger at each new bounce [44]. Fig. 2.10 shows the difference of the evolution of the ray-tube in far field and near field. In near field, the ray expands progressively. In this example the currents are limited to simple shapes where intersections are relatively simple. In some case the ray should be subdivided into sub-rays. For IPO, there are fewer issues referring to iteration. The IPO algorithm complexity can be seen as linear as the illuminated function does not change and more particularly does not need to be recalculated. IPO also performs better in modeling currents on surfaces. For all these reasons, it should be more interesting to work with IPO rather than SBR.

2.5 Conclusion

This chapter presents an overview of the theoretical foundations necessary for modeling the electromagnetic scattering of a target. Based on Maxwell's equations, the derivation of the near field integral equations and the boundary conditions that characterize electromagnetic scattering at medium interfaces are presented.

To model the target response, the NF-RCS concept was introduced, and a tractable definition was established.

Furthermore, various methods for solving diffraction problems were discussed, with a particular focus on large targets in the near field region. This analysis justified the choice of the most suitable approach for computing the backscattering of complex and large-scale targets.

For the implementation of a backscattering model, IPO coupled with EEC was chosen instead of the SBR model.

This chapter provides the theoretical groundwork for the subsequent sections, where the model will be implemented and analyzed in detail.

Chapter 3

Near Field Target Scattering Model by IPO

3.1 Introduction

In the previous chapter, the framework and theoretical background underlying this thesis were presented. Regarding the modeling approach, an overview of the PO and IPO methods, coupled with the EEC formulation, was discussed. These methods provide a framework for understanding the near field scattering of targets.

3.2 Integral resolution

As seen in the previous part, the PO theory in the near field is based on the equation previously derived:

$$\begin{aligned}\mathbf{H}_{scat}(\mathbf{r}_{rec}) = \iint_s \Bigg[& -\frac{(jkR_{rec}+1)}{R_{rec}}\left(\mathbf{J}\times\hat{\mathbf{R}}_{rec}\right) + \frac{1}{\eta}\frac{-1-jkR_{rec}+(kR_{rec})^2}{jkR_{rec}^2}\mathbf{M} \\ & + \frac{1}{\eta}\frac{-3-j3kR_{rec}+(kR_{rec})^2}{jkR_{rec}^2}\left(\mathbf{M}\cdot\hat{\mathbf{R}}_{\mathbf{rec}}\right)\hat{\mathbf{R}}_{rec}\Bigg]\frac{e^{-jkR_{rec}}}{4\pi R_{rec}}ds\end{aligned} \tag{3.1}$$

where only the electric current is necessary in the case of a PEC target.

3.2.1 Plane surface meshing

When trying to perform the integral directly on the total surface, for complex targets in the near field, it cannot be computed analytically. The first approach that can be taken is to mesh the target in order to transform the single target problem into a multiple smaller-target problems. The goal here is to reduce the complexity of the target for the integration. One initial approach is to perform the integration only on the rapidly varying term, which is linked to the exponential. There are two exponentials in the integral: one related to the current directly linked to the incident field on the target $e^{-jkR_{sou}}$ where

R_{sou} is the distance from the source, and the other corresponding to the Green's function, $e^{-jkR_{rec}}$. For this purpose, the variation along R_{rec} and analogously R_{sou} need to be small enough in the integration part. To reach this goal, one can express the vector $\mathbf{R}_{rec}$ and $\mathbf{R}_{sou}$ from the receiver and the source to an arbitrary point $\mathbf{M}$ on the surface as:

$$\begin{aligned} \mathbf{R}_{rec} &= \mathbf{R}_{rec}^{'} + \mathbf{O}'\mathbf{M} \\ \mathbf{R}_{sou} &= \mathbf{R}_{sou}^{'} + \mathbf{O}'\mathbf{M} \end{aligned} \tag{3.2}$$

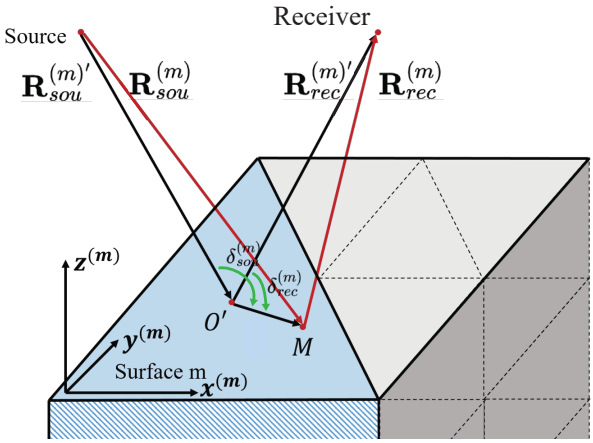

Figure 3.1: Target geometry for sub-surface m, integration over the triangle m

where $\mathbf{O}'$ is the center of an arbitrary sub-element m of the surface. Fig. 3.1 presents the geometry used and the new basis used. In this case the vector to an arbitrary point M is rewritten in the new basis associated with the sub-surface m as $\mathbf{R}_{rec}^{(m)}$ and $\mathbf{R}_{sou}^{(m)}$ and the vector to the center of the sub-surface as $\mathbf{R}_{rec}^{(m)'}$ and $\mathbf{R}_{sou}^{(m)'}$. In this case, to simplify the integral, the vectors $\mathbf{R}_{rec}^{(m)'}$ and $\mathbf{R}_{sou}^{(m)'}$ can be used instead of $\mathbf{R}_{rec}^{(m)}$ and $\mathbf{R}_{sou}^{(m)}$. For this simplification to be valid, the vector $\mathbf{O}'\mathbf{M}$ needs to be small enough. To determine the maximum acceptable value of $\mathbf{O}'\mathbf{M}$ that allows for this approximation, a second-order Taylor series expansion is applied:

$$R_{rec}^{(m)} \approx R_{rec}^{(m)'} + ||\mathbf{O}^{'}\mathbf{M}|| \cos(\delta_{rec}^{(m)}) + \frac{||\mathbf{O}^{'}\mathbf{M}||^2}{2R_{rec}^{(m)}} \sin(\delta_{rec}^{(m)})^2 \tag{3.3}$$

where $\delta_{rec}^{(m)}$ is the angle between the vector $R_{rec}^{(m)}$ and $\mathbf{O}^{'}\mathbf{M}$. When looking at this expression, the combination of the first two terms is equal to a plane wave propagation. In this case, the wave is locally plane. By using the third term, we also take into account the sphericity of the wave. To simplify the integral, the wave must be locally plane, which means that the term $\frac{||\mathbf{O}^{'}\mathbf{M}||^2}{2R_{rec}^{(m)}} \sin(\delta_{rec}^{(m)})^2$ needs to be small

enough to neglect it in the exponential phase kernel $e^{-jk(R_{rec}^{(m)}+R_{sou}^{(m)})}$:

$$\begin{aligned}\mathbf{H}_{scat}^{(m)}(\mathbf{r}_{rec}^{(m)}) = \Bigg[& -\frac{(jkR_{rec}^{(m)'}+1)}{R_{rec}^{(m)'}}\left(\mathbf{J}^{(\mathbf{m})'}\times\hat{\mathbf{R}}_{rec}^{(m)'}\right)+\frac{1}{\eta}\frac{-1-jkR_{rec}^{(m)'}+(kR_{rec}^{(m)'})^2}{jkR_{rec}^{(m)'2}}\mathbf{M}^{(\mathbf{m})'} \\ & +\frac{1}{\eta}\frac{-3-j3kR_{rec}^{(m)'}+(kR_{rec}^{(m)'})^2}{jkR_{rec}^{(m)'2}}\left(\mathbf{M}^{(\mathbf{m})'}\cdot\hat{\mathbf{R}}_{\mathbf{rec}}^{(\mathbf{m})'}\right)\hat{\mathbf{R}}_{rec}^{(m)'}\Bigg]\frac{e^{-jkR_{rec}^{(m)'}}}{4\pi R_{rec}^{(m)'}} \\ & \iint_{s^{(m)}} e^{-jk(R_{rec}^{(m)}-R_{rec}^{(m)'})}e^{-jk(R_{sou}^{(m)}-R_{sou}^{(m)'})}ds\end{aligned} \tag{3.4}$$

For all variable $X^{'}$, it refers to the variable X at the center of an arbitrary sub-element O'. In order to make this approximation, the second-order term must satisfy the following condition:

$$\frac{||\mathbf{O}^{'}\mathbf{M}||^2}{2R_{rec}^{(m)}}\sin(\delta_{rec}^{(m)})^2 < \frac{||\mathbf{O}^{'}\mathbf{M}||^2}{2R_{rec}^{(m)}} < \frac{\lambda}{4} \tag{3.5}$$

By rearranging the terms, the far field Fraunhofer condition is derived:

$$R_{rec}^{(m)} > 2\frac{||\mathbf{O}^{'}\mathbf{M}||^2}{\lambda} \tag{3.6}$$

In order to evaluate the integral in equation 3.4, the terms $R_{rec}^{(m)} - R_{rec}^{(m)'}$ and $R_{sou}^{(m)} - R_{sou}^{(m)'}$ can be simplified. The coordinate system used is $(O';\mathbf{x}^{(m)},\mathbf{y}^{(m)},\mathbf{z}^{(m)})$, associated with the surface m. The coordinates of point M in this system are $(\mathbf{x}'_{\mathbf{M}},\mathbf{y}'_{\mathbf{M}},\mathbf{z}'_{\mathbf{M}}=0)$. By applying Fraunhofer condition, we have

$$\begin{aligned}R_{rec}^{(m)} - R_{rec}^{(m)'} &\approx \|\mathbf{O'M}\|\cos(\delta_{rec}^{(m)}) \\ &\approx \hat{\mathbf{R}}_{rec}^{(m)'}\cdot\mathbf{O'M} \\ &\approx x'_M\hat{R}_{rec,x}^{(m)'}+y'_M\hat{R}_{rec,y}^{(m)'}+z'_M\hat{R}_{rec,z}^{(m)'} \\ &\approx x'_M\hat{R}_{rec,x}^{(m)'}+y'_M\hat{R}_{rec,y}^{(m)'},\end{aligned} \tag{3.7}$$

where $\hat{\mathbf{R}}_{rec}^{(m)'} = (\hat{R}_{rec,x}^{(m)'},\hat{R}_{rec,y}^{(m)'},\hat{R}_{rec,z}^{(m)'})$ is the unit vector in the direction of the receiver. The last approximation is due to the fact that the contribution along the local $\mathbf{z}^{(m)}$ axis is null.

This allows the integral to be separated, enabling it to be solved analytically. The calculation of the integration is presented in the Appendix 1. The main technique is to transform the arbitrary triangle in a unitary rectangular triangle where the integration will be easier. Fig. 3.2 presents the variable change. The integral of (3.4) will be denoted as I.

The scattered field from the target is equal to the sum of the responses from each sub-element. The total scattered field is given by:

$$\mathbf{H}_{scat}(\mathbf{r}_{rec}) = \sum_{m=1}^{M}\mathbf{H}_{scat}^{(m)}(\mathbf{r}_{rec}) \tag{3.8}$$

with M the number of sub-surface and m the index of the sub-surface. For the scattered electric field

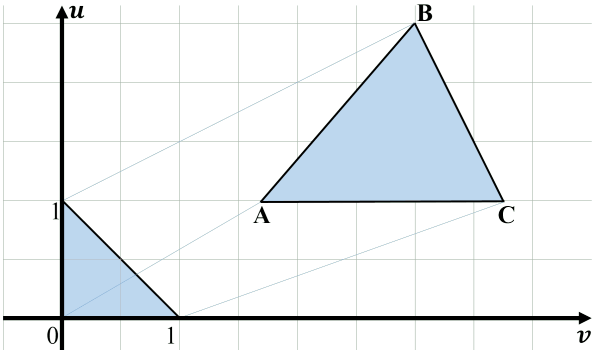

Figure 3.2: Change of basis for the triangle ABC

$\mathbf{E}_{scat}$, as each scattered field is assumed to be in the near field, it is obtained by:

$$\mathbf{E}_{scat}(\mathbf{r}_{rec}) = \sum_{m=1}^{M} \mathbf{E}_{scat}^{(m)}(\mathbf{r}_{rec}) = \eta \sum_{m=1}^{M} \left(\mathbf{H}_{scat}^{(m)}(\mathbf{r}_{rec}) \times \hat{\mathbf{R}}_{rec}^{'(m)} \right) \tag{3.9}$$

It should be noted that the total scattered field is the sum of far field scattered fields. This means that the two fields are not orthogonal to each other.

$$\mathbf{E}_{scat}(\mathbf{r}_{rec}) \not\perp \mathbf{H}_{scat}(\mathbf{r}_{rec}) \tag{3.10}$$

Using the equations 3.4 and 2.36, the NF-RCS can be studied. To account for the distance in the NF-RCS calculation, the simple case of a flat plate is studied. The Table. 3.1. shows the parameters used. In the study, the distance and the frequency vary but only one meshing is used and it is not updated for all the frequencies and distances. As it shows in equation (3.5), taking into account only the extreme case is sufficient. Since this is a simple case, the computation time is not significant here. The results shown in Fig. 3.3 clearly highlight the influence of distance on the RCS. It can be observed that, from a certain distance onwards, the NF-RCS converges towards the classical RCS. The Fraunhofer distance for the plate is calculated as:

$$R_{FF} = \frac{2d^2}{\lambda_{min}} = 16 \ m \tag{3.11}$$

The results show, that for a distance > 10 m the NF-RCS converges to the RCS. Here, results obtained are below the Fraunhofer distance due to the sin^2 term presents in equation 3.5. This term vanishes because of the normal observation of the target. When getting closer to the target ($<$ 2 m), the NF-RCS varies with distance. The closer we are to the target, the more oscillations appear in the target response. If we look to the results obtained at 20 cm of the target, there is an oscillation every 6 GHz which corresponds to a wavelength of 5 cm. When looking at the distance antenna-target, the distance ranges from 20 cm to the target center, and 22.36 cm for the closest edge, which means the round trip distance are 40 cm and 44.72 cm, corresponding to the oscillations observed. The same conclusion about oscillations applies to the target at 50 cm. The NF-RCS takes into account the distance for the absolute value. It also changes the backscattering of all the different parts of the target. When summing all the

Parameters	Value
Frequency	[10 GHz- 30 GHz]
Target	20 cm square plate
Mesh	$\sqrt{\frac{R_{min}\lambda_{min}}{2}}$
Distance	20 cm - 50 m
Sample points	101
Material	PEC

Table 3.1: Parameters: Impacts of the distance in the NF-RCS monostatic in normal incidence

responses of the target, interference due to near field appears.

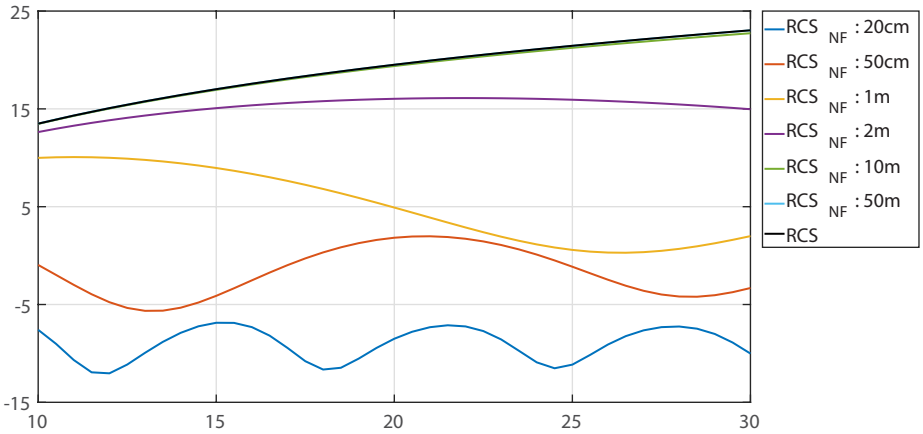

Figure 3.3: NF-RCS evolution between 10 GHz and 30 GHz for different distances from a flat plate of 20 cm side

3.2.2 Curved surface meshing adaptation

Another criterion is necessary to validate the simplification of the integral in Equation 3.4. This time, it is not about the sphericity of the wave, but the sphericity of the target. If the target curvature is too large, the simplified integral cannot be applied because it would not account for this curvature. Similarly to the first criterion, the curvature needs to be small enough to consider the surface as plane. In this case, the integration will be performed on a surface that receives a plane wave and is itself planar. Fig. 3.4 presents the problem from 3 surfaces. Instead of using the actual curvature, it will be replaced by a planar sub-surface. To model the sub-surface, it is defined using the tangent plane at the center of the sub-surface. To do this, we are going to use the chord criterion [29]. To properly express the curvature of the target, we are going to rewrite $R_{rec}^{(m)}$ as:

$$R_{rec}^{(m)} \approx R_{rec}^{(m)'} + ||\mathbf{O}'\mathbf{M}|| \cos(\delta_{rec}^{(m)}) = R_{rec}^{(m)'} + \mathbf{O}'\mathbf{M} \cdot \hat{\mathbf{R}}_{rec}^{(m)'} \tag{3.12}$$

Fig. 3.5 presents the sub-surface used. In order to perform the integral, we aim to express the surface

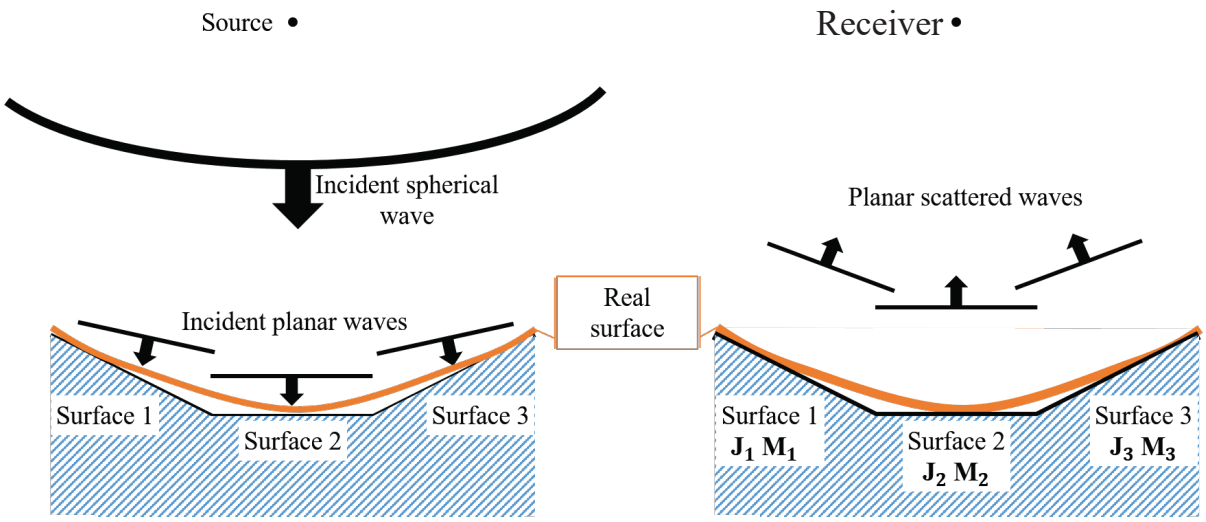

Figure 3.4: Illustration of meshing phenomenon: transformation of spherical wave and surface into planar approximation

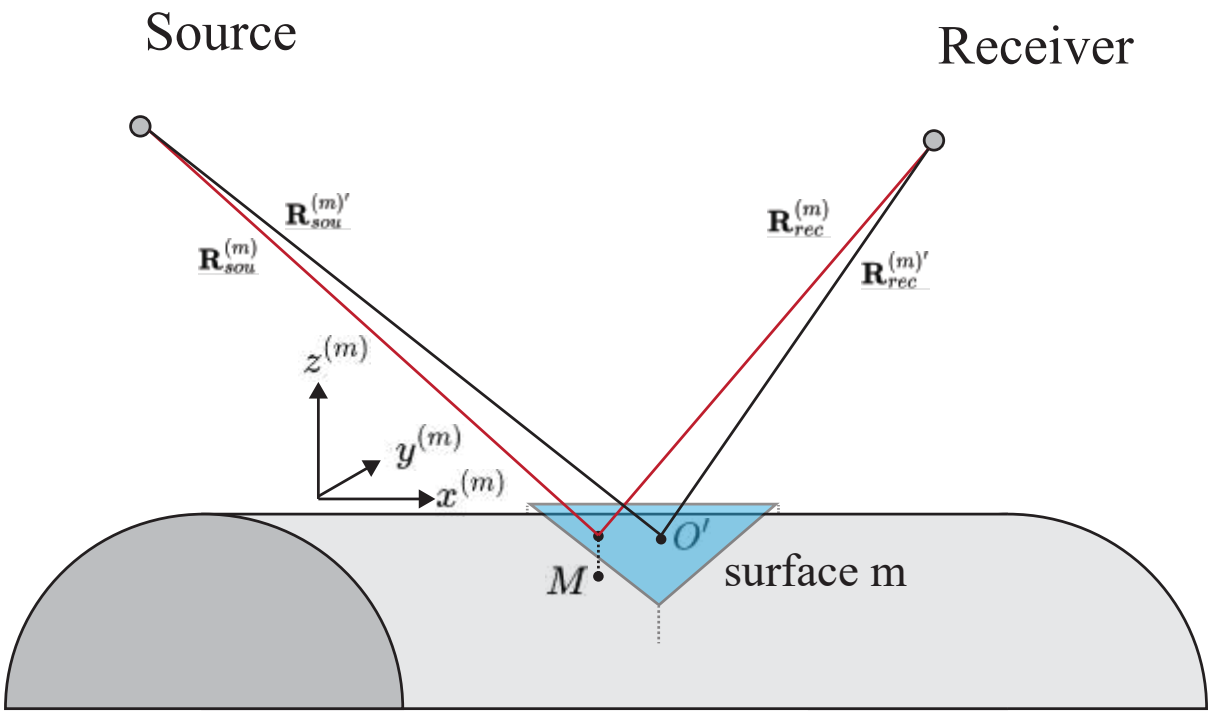

Figure 3.5: Meshing for a curved surface

using only two coordinates instead of three. This means on a subsurface, for a random $\mathbf{M}$ we use a coordinate system $(O';\mathbf{x}^{(m)},\mathbf{y}^{(m)},\mathbf{z}^{(m)})$, where $\mathbf{M}$ has coordinate $(x_M^{'},y_M^{'},z_M^{'})$, in other word, the subsurface is plane as for the previous part. For this purpose, the coordinate of $z_M^{'}$ needs to be small enough. The coordinate in $\mathbf{z^{(m)}}$ can be expressed using a closed-form expression over $\mathbf{x}^{(m)}$ and $\mathbf{y}^{(m)}$:

$$z_M^{'} \approx x_M^{'}\frac{\partial z}{\partial x} + y_M^{'}\frac{\partial z}{\partial y} \tag{3.13}$$

with the partial integral taken at O', we approximate the target curvature by considering only the curvature at O'. To consider the previous approximation, it is valid if:

$$|\hat{R}_{rec,z}^{(m)'} + \hat{R}_{sou,z}^{(m)'}|F' < \frac{\lambda}{4} \tag{3.14}$$

Where F' is equal to a term linked to the curvature of the target:

$$F^{'} = \left|\frac{x_M^{'2}}{2}\frac{\partial^2 z}{\partial x^2} + \frac{y_M^{'2}}{2}\frac{\partial^2 z}{\partial y^2} + \frac{y_M^{'}x_M^{'}}{2}\frac{\partial^2 z}{\partial x \partial y}\right| \tag{3.15}$$

In conclusion of the chord error criterion, the vector R_{rec} can be written as:

$$\mathbf{R}_{rec}^{(m)} = \begin{bmatrix} R_{rec,x}^{(m)} \\ R_{rec,y}^{(m)} \\ R_{rec,z}^{(m)} \end{bmatrix} \approx \begin{bmatrix} R_{rec,x}^{(m)'} + x_M' \left(\hat{R}_{rec,x}^{(m)'} + \frac{\partial z}{\partial x}\hat{R}_{rec,z}^{(m)'}\right) \\ R_{rec,y}^{(m)'} + y_M' \left(\hat{R}_{rec,y}^{(m)'} + \frac{\partial z}{\partial y}\hat{R}_{rec,z}^{(m)'}\right) \\ R_{rec,z}^{(m)'} \end{bmatrix} \tag{3.16}$$

By applying both criteria, the simplification for the integral is:

$$R_{rec}^{(m)} - R_{rec}^{(m)'} = x_M^{'}(\hat{R}_{rec,x}^{(m)'} + \frac{\partial z}{\partial x}\hat{R}_{rec,z}^{(m)'}) + y_M^{'}(\hat{R}_{rec,y}^{(m)'} + \frac{\partial z}{\partial y}\hat{R}_{rec,z}^{(m)'}) \tag{3.17}$$

As the model is based on flat triangular surfaces due to the STL shape definition, which describes the object by its external surface, the curvature of the target needs to be taken into account. Fig.3.4 shows the problem: based on the chord criterion, the surfaces are meshed finely enough to approximate flat surfaces instead of spherical ones. The real surface in orange is approximated by the black surface. In order to calculate the equation 3.15, the derivation along vectors $(\mathbf{x},\mathbf{y},\mathbf{z})$ cannot be implemented. Instead of this, the curvature is estimated only by using the center of the sub-surfaces. In the case of flat triangular surfaces, $z_M' = 0$. Instead of M the points that will be used are the centers of the neighboring sub-surfaces of the sub-surface m as illustrated in Fig. 3.6. It should be noticed that as the sphericity of the target needs to be small enough, the criterion is rewritten as:

$$|\hat{R}_{rec,z}^{'} + \hat{R}_{sou,z}^{'}|\sum_{i=1}^{3}\frac{(O'^{(m)}O_i^{'(m)})_z}{2} < \frac{\lambda}{4} \tag{3.18}$$

The replacement of equation 3.15 by the equation 3.18 is more suitable for implementation. If a surface is not small enough, it is divided into three parts. Splitting a triangle into three parts allows us to

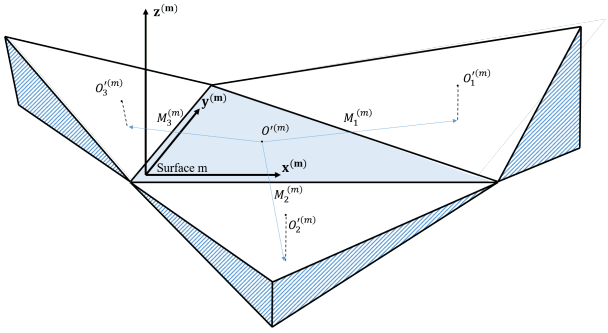

Figure 3.6: STL implementation: target geometry for sub-surface m

modify only that specific triangle. The point $O^{'(m)}$ cannot be used as the common vertex of the three new triangles because it would not reduce the previously established criterion. To reduce the criterion while preserving the curvature of the target, the new shared vertex retains the same $x^{'(m)}$ and $y^{'(m)}$ coordinates, but the third coordinate is replaced by:

$$z^{'(m)} = \frac{3z^{'(m)} + z_1^{'(m)} + z_2^{'(m)} + z_3^{'(m)}}{6} \tag{3.19}$$

Where $z_i^{'(m)}$ is the intersection between the plane containing surface m_i and the line along $\hat{\mathbf{z}}^{(m)}$ passing through $O^{'(m)}$ and $z^{'(m)}$ the coordinate of $O^{'(m)}$ along $\hat{\mathbf{z}}^{(m)}$. This becomes the wedge of the three new triangles. Fig. 3.7 explains how the triangle surface is split. The validation is done with the parameters

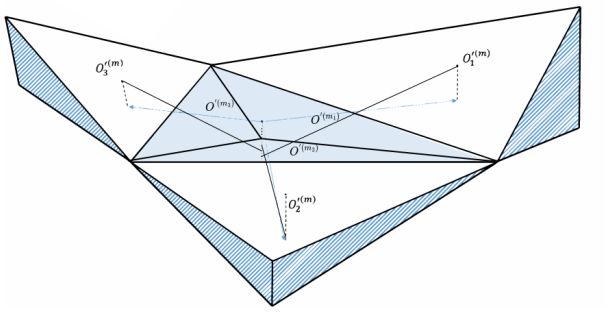

Figure 3.7: Definition of the sub-element meshing for curvature target

shown in Tab. 3.2 and is compared with reference simulations. The validation simulations are explained in Appendix 2. The target is illuminated with a plane wave, and the receiver is placed 30 cm away from the target. The chord criterion is applied to all sub-surfaces of the target, except those near the edges. The sub-surfaces linked to an edge cannot satisfy this criterion. The model provides results consistent with the reference simulations. Since there is only one bounce, the computational time is not significant yet.

Parameters	Value
Frequency	[20 GHz- 30GHz]
Target Distance to receiver	10 cm curved plate 30 cm
Sample points	101
Material	PEC
Incident Plane wave	Plane wave

Table 3.2: Parameters used for Fig. 3.8

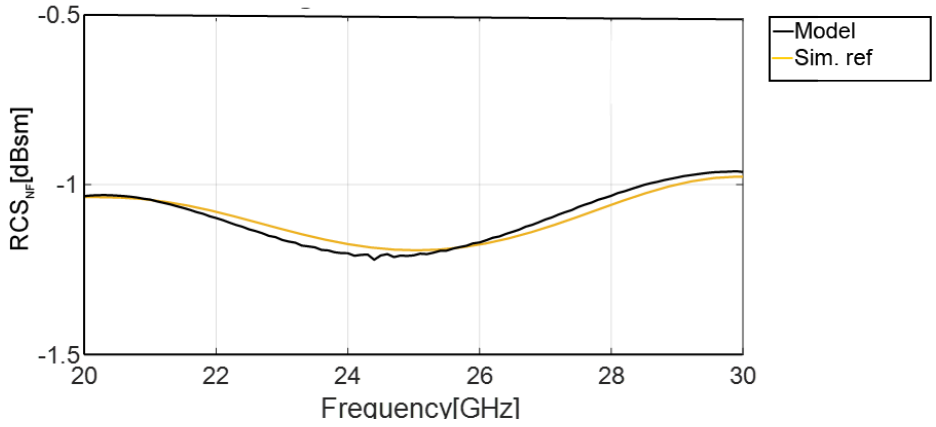

Figure 3.8: NF-RCS for the frequency range [20GHz;30GHz] for a 10 cm curved plate with a transceiver placed at 30 cm of the plate

3.2.3 Edge meshing

In order to model the edge of the target, the limit between an edge and a curvature needs to be defined. To define if a wedge is an edge or a curve, a simple threshold is defined as a limit. If the criterion exceeds this threshold, the feature is classified as an edge; otherwise, it is considered a curved region. The target is defined using STL file which is basically the coordinates of the three wedges of the target. The edges are defined for each sub-surface. The equation 2.46 can be used for backscattering and as for PO, the goal is to perform integration only on the phase term. Similarly to PO, terms with notation X' will refer to the center of the edges The goal is to write $\mathbf{H}_{dif}$ from equation 2.46 for a sub-edge p as:

$$\mathbf{H}_{dif}^{(p)}(\mathbf{r}_{rec}^{(p)}) = \left[-\frac{(jkR_{rec}^{(p)'}+1)}{R_{rec}^{(p)'}} \left(\boldsymbol{\mathcal{J}}^{(p)'} \times \hat{\mathbf{s}}_{dif} \right) + \frac{1}{\eta} \frac{-jkR_{rec}^{(p)'} + (kR_{rec}^{(p)'})^2}{jkR_{rec}^{(p)'2}} \boldsymbol{\mathcal{M}}^{(p)'} \right.$$
$$\left. + \frac{1}{\eta} \frac{-j3kR_{rec}^{(p)'} + (kR_{rec}^{(p)'})^2}{jkR_{rec}^{(p)'2}} \left(\boldsymbol{\mathcal{M}}^{(\boldsymbol{p})'} \cdot \hat{\mathbf{s}}_{\boldsymbol{dif}} \right) \hat{\mathbf{s}}_{dif} \right] \frac{e^{-jkR_{rec}^{(p)'}}}{4\pi R_{rec}^{(p)'}} \int_{l^{(p)}} e^{-jk(R_{rec}^{(p)} - R_{rec}^{(p)'})} e^{-jk(R_{sou}^{(p)} - R_{sou}^{(p)'})} dl^{(p)} \tag{3.20}$$

In order to perform such transformations, the ame criteria as for PO are going to be used. First of all, the sub-edges need to be small enough to meet the Fraunhofer criterion. As we don't want to disconnect

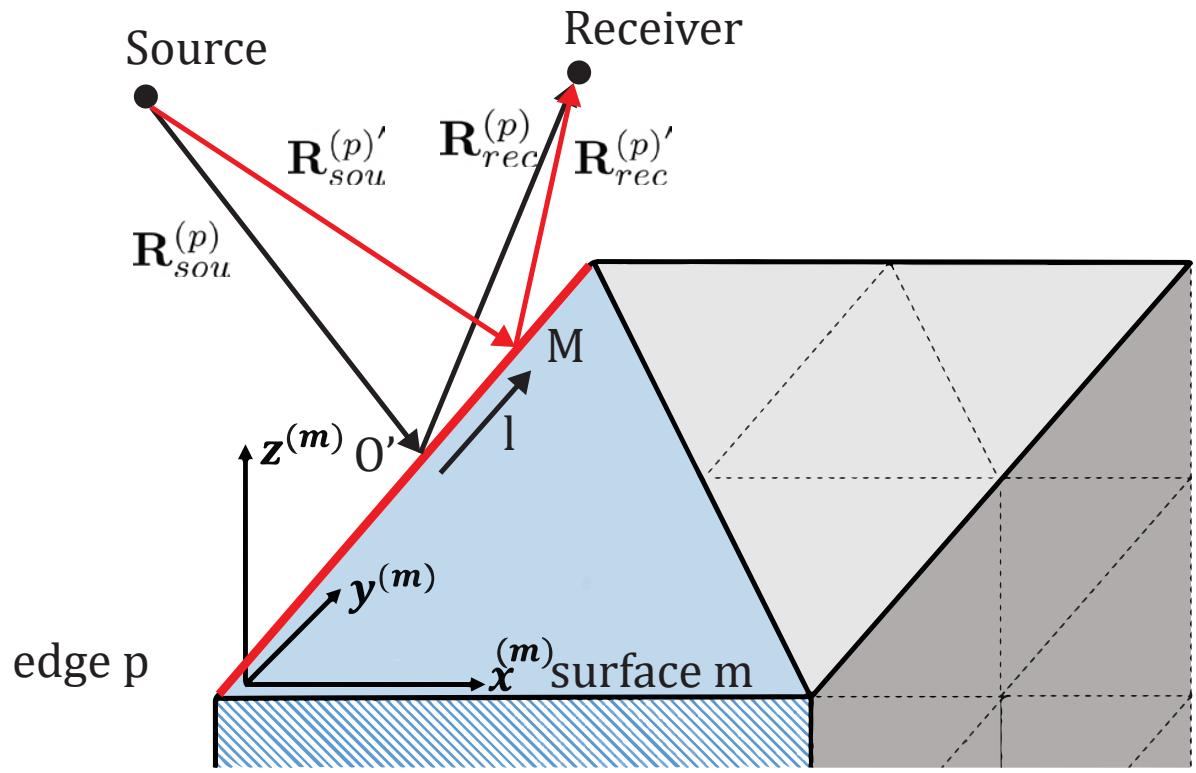

Figure 3.9: Target geometry for sub-edge p, integration over the edge p

the edges from the surfaces, the edge criterion descends from the criterion for sub-surfaces.
The integral can be applied independently on the three edges of the triangle sub-surface. The vector $R_{rec}^{(p)}$ is written using the Fraunhofer criterion as $R_{rec}^{(p)}=R_{rec}^{(p)'}+\mathbf{l}\cdot\hat{\mathbf{R}}_{\mathbf{rec}}^{(\mathbf{p})'}$ where $\mathbf{l}$ the vector from the center to the edge. Fig. 3.9 presents the geometry used. The integration over the edge

$$\begin{aligned} I_{edge}^{(p)} &= \int_{l^{(p)}} e^{-jk(R_{rec}^{(p)}-R_{rec}^{(p)'})} e^{-jk(R_{sou}^{(p)}-R_{sou}^{(p)'})} dl^{(p)} \\ &= \int_{-0.5}^{0.5} e^{-jk(\mathbf{l}\cdot(\hat{\mathbf{R}}_{\mathbf{rec}}^{(\mathbf{p})'}+\hat{\mathbf{R}}_{\mathbf{sou}}^{(\mathbf{p})'}))} L dl \\ &= L\frac{\sin(\frac{k\hat{\mathbf{l}}\cdot(\hat{\mathbf{R}}_{\mathbf{rec}}^{(\mathbf{p})'}+\hat{R}_{sou}^{(p)'})}{2})}{\frac{k\hat{\mathbf{l}}\cdot(\hat{\mathbf{R}}_{\mathbf{rec}}^{(\mathbf{p})'}+\hat{\mathbf{R}}_{\mathbf{sou}}^{(\mathbf{p})'})}{2}} \end{aligned} \tag{3.21}$$

with L the length of the edge. The total field scattered by all the edges P is written as:

$$\begin{aligned} \mathbf{H}_{dif}(\mathbf{r}_{rec}) = \sum_{p=1}^{P} \mathbf{H}_{dif}^{(p)}(\mathbf{r}_{rec}) = \Bigg[&-\frac{(jkR_{rec}^{(p)'}+1)}{R_{rec}^{(p)'}}\left(\boldsymbol{\mathcal{J}}^{(p)'}\times\hat{\mathbf{s}}_{dif}\right)+\frac{1}{\eta}\frac{-jkR_{rec}^{(p)'}+(kR_{rec}^{(p)'})^2}{jkR_{rec}^{(p)'2}}\boldsymbol{\mathcal{M}}^{(p)'} \\ &+\frac{1}{\eta}\frac{-j3kR_{rec}^{(p)'}+(kR_{rec}^{(p)'})^2}{jkR_{rec}^{(p)'2}}\left(\boldsymbol{\mathcal{M}}^{(\mathbf{p})'}\cdot\hat{\mathbf{s}}_{\boldsymbol{dif}}\right)\hat{\mathbf{s}}_{dif}\Bigg]\frac{e^{-jkR_{rec}^{(p)'}}}{4\pi R_{rec}^{(p)'}}I_{edge}^{(p)} \end{aligned} \tag{3.22}$$

In order to validate the EEC in the near field, the case of forward scattering by a pyramid is studied. The studied case considers a plane wave incident in the 20–30 GHz band, with the objective of analyzing the scattered field beneath the pyramid. The edges are meshed finely enough to allow treating each sub-edge as a source of near field radiation. In order to mesh the edges with an appropriate size, the surface under the target is radiating with a zero current and the surface above receives field from the source. The target and the receiver are placed as in Fig. 3.10 **(a)**. The goal here is to have only the response of the edges and not the surface. In the case presented here, only the upper faces are illuminated but only the bottom face see the receiver. This means that no surface radiation is present here. Moreover, in equation 2.79, the function U_1 and U_2 vanish, and therefore the equivalent current on the edges will depend only on the fringe currents. The results are shown in Fig. 3.10 **b**. and are compared to results obtain from reference simulations. The results obtained are in very good agreement with the model. Here only one interaction is modeled, which is the edge diffraction, this means that the model complexity is very low. When comparing the results, one can observe a maximum difference of 1 dB between the simulation and the reference simulation. Moreover, the frequency dependence of the scattered field is consistent in both cases.

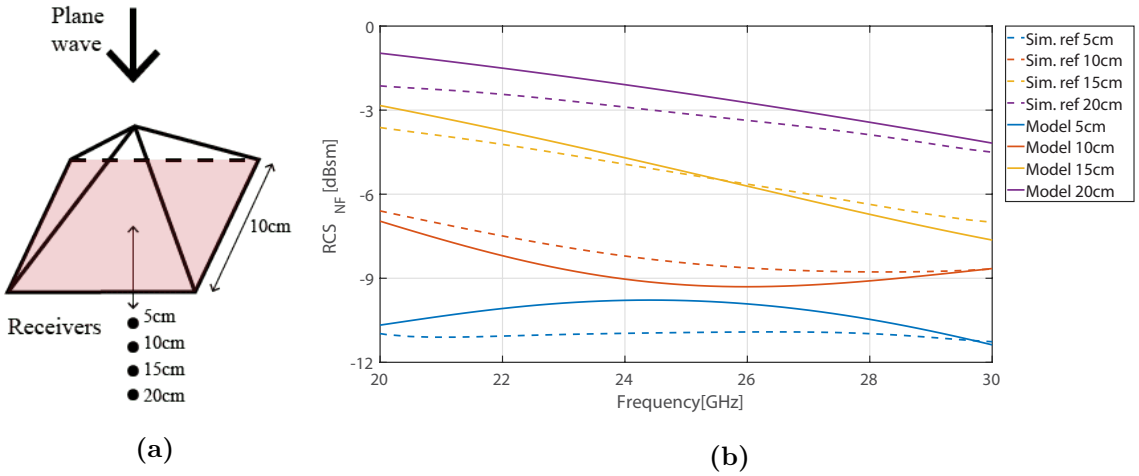

Figure 3.10: Pyramid diffraction in forward scattering **(a)** scenario with a 10 cm pyramid **(b)** Comparison of the forward scattering for four different receiver positions

3.2.4 Complexity and adaptation for multiple bounces

Now that the model is defined for a single bounce, both the surfaces and the edges are radiating toward the receiver as well as toward other sub-surfaces. In order to model the multiple scattering interactions between different parts of the target, Adaptations are required to simplify the calculation. When a surface is radiating in the direction of another subsurface, the complexity becomes $O(M^3)$ with M the number of sub-surfaces. This is due to the integration done in the scattering equation. Since the equation depends on both the incident and scattered fields, the computational complexity increases significantly. For a single bounce, it is $O(M)$ and for double bounce it is $O(M^2)$. The complexity for single and double bounce stays low, and this means that it is possible to use equation 3.4 directly. For a double bounce,

the integral must be solved twice; in the second PO equation, the incident fields are computed from the scattered fields of the first surface. The scattered field by surface n in the direction of surface m is given by

$$\begin{aligned}
&\mathbf{H}_{scat}^{(n\to m)}(\mathbf{O}^{'(m)}) = -\frac{(jkR_{rec}^{(n\to m)'}+1)}{R_{rec}^{(n\to m)'}}\left(\mathbf{J}^{'(\mathbf{n})}\times\hat{\mathbf{R}}_{rec}^{(n\to m)'}\right)\\
&\iint_{s(m)} e^{-jk(R_{rec}^{(n\to m)}-R_{rec}^{(n\to m)'})} - e^{-jk(R_{sou}^{(n\to m)}-R_{sou}^{(n\to m)'})}ds\\
&\mathbf{J}^{'(\mathbf{n})} = 2\hat{\mathbf{n}}\times\mathbf{H}_{inc}^{'(n)}(\mathbf{O}^{'(\mathbf{n})})
\end{aligned} \tag{3.23}$$

In this equation, surface m, and more precisely the center of surface m, plays the role of the receiver which means $\mathbf{R}_{rec}^{(n\to m)'} = \mathbf{O}^{'(\mathbf{n})}\mathbf{O}^{'(\mathbf{m})}$. The scattered field by the surface m by supposing that it is only illuminated by the surface n is

$$\begin{aligned}
&\mathbf{H}_{scat}^{(m)}(\mathbf{r}_{rec}) = -\frac{(jkR_{rec}^{'(m)}+1)}{R_{rec}^{'(m)}}\left(\mathbf{J}^{'(\mathbf{m})}\times\hat{\mathbf{R}}_{rec}^{'(m)}\right)\iint_{s(m)} e^{-jk(R_{rec}^{(m)}-R_{rec}^{'(m)})}e^{-jk(R_{sou}-R_{sou}^{'(m)})}ds\\
&\mathbf{J}^{'(\mathbf{m})} = 2\hat{\mathbf{n}}\times\mathbf{H}_{inc}^{'(m)}(\mathbf{O}^{'(\mathbf{m})}) = 2\hat{\mathbf{n}}\times\mathbf{H}_{scat}^{(n\to m)'}(\mathbf{O}^{'(\mathbf{m})})
\end{aligned} \tag{3.24}$$

For three or more bounces, the integration method cannot be used directly. This is due to the fact that the result of the integration depends on both the incident and the scattered fields. This implies that if three surfaces A, B, and C are mutually visible and finely meshed, a large number of integrals will have to be computed. In the case where the radiation propagates along the path $A \to B \to C$, the currents on C are equal to

$$\mathbf{J}^{(c)} = 2\hat{\mathbf{n}}\times\sum_{b=1}^{B}\mathbf{H}_{scat}^{(b\to c)'}(\mathbf{O}^{'(\mathbf{m})}) \tag{3.25}$$

But the scattered current $\mathbf{H}_{scat}^{(b\to c)'}(\mathbf{O}^{'(\mathbf{m})})$ are calculated from all the sub-surface from A. The complexity is $O(M^3)$. The current is expressed as:

$$\mathbf{J}^{(c)} = 2\hat{\mathbf{n}}\times\sum_{a=1}^{A}\sum_{b=1}^{B}\mathbf{H}_{scat}^{(a\to b\to c)'}(\mathbf{O}^{'(\mathbf{m})}) \tag{3.26}$$

One possible approach to reduce the complexity would be to split the problem into two steps: first, compute the current on B due to A, and then compute the current on C due to B. The problem is that the integration over the phase difference with respect to the center of the surface depends on both the incident and scattered directions, and therefore cannot be separated. In Appendix I, it can be seen that the divisor depends on both the incident field and the scattered field. This means that an equivalent current cannot be defined. At iteration k, corresponding to bounce k, the current at the center of surface m can be written as:

$$\mathbf{J}'^{(k,m)} = \sum_{n=1\neq m}^{N}\mathbf{J}'^{(k,n\to m)} \tag{3.27}$$

However the integral needs to be solved for each individual incident direction. For EEC, the same results are obtained, the scattered field by an edge depends on the incident and scattered direction. So as for

PO, two iterations are still possible, but the third one raises the complexity to a cubic order.

A result for double bounce for dihedral is presented in Fig. 3.11. The evolution of the NF-RCS is measured at a distance of 30 cm from a 20 cm dihedral plate over the frequency range [20 GHz; 30 GHz]. In this configuration, one of the two plates is plane and the other is curved. Fig. 3.11**(a)** illustrates the geometry of the studied structure. Fig. 3.11**(b)** shows the comparison between the results obtained from the developed model and the reference simulation. A good agreement is observed over the considered frequency band, validating the proposed modeling approach for this specific near field configuration.

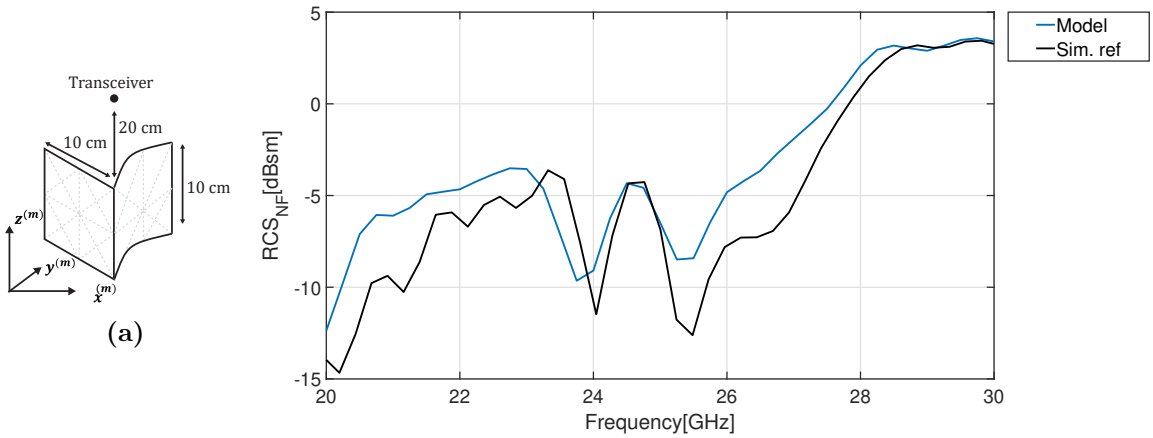

Figure 3.11: Evolution of the near field RCS at 30 cm for a 20 cm dihedral plate for the frequency range [20GHz;30GHz]. One of the two plates is a curved plate. **a**. Geometry **b**. Comparison model with reference simulation

3.2.5 IPO and EEC model

One possible approach to reduce the complexity is to split the problem into two steps: first, compute an equivalent current on the edge, and then compute the radiation of this current. However, the integration over the phase difference with respect to the center of the surface depends on both the incident and scattered directions and therefore cannot be separated. To overcome this issue, the integral must be eliminated from the calculation. In classical IPO [45], the mesh size is defined to be smaller than that used for PO and double-bounce PO. The objective here is to mesh the target finely enough to completely eliminate the need for integration:

$$\mathbf{H}_{scat}(\mathbf{r}_{rec}) = A\left[-\frac{(jkR'_{rec}+1)}{R'_{rec}}\left(\mathbf{J}'\times\hat{\mathbf{R}}'_{rec}\right)\right]\frac{e^{-jkR'_{rec}}}{4\pi R'_{rec}} \tag{3.28}$$

with A the area of the sub-surface.

In order to reduce the integral, the term $e^{-jk(R_{rec}-R'_{rec})}e^{-jk(R_{sou}-R'_{sou})}$ needs to be close to 1 which means that $k(R_{rec}-R'_{rec}) \ll 1$ and similarly for the source. As $R_{rec} \approx R'_{rec} + |\mathbf{O}'\mathbf{M}|\cos(\delta^{(m)}_{rec})$, the equation becomes:

$$k(R_{rec}-R'_{rec}) \approx k|\mathbf{O}'\mathbf{M}|\cos(\delta^{(m)}_{rec}) < k|\mathbf{O}'\mathbf{M}| \ll 1 \tag{3.29}$$

The IPO equation for iteration k for surface m can be written as:

$$\begin{aligned}\mathbf{J}'^{(k,m)} &= \sum_{n=1\neq m}^{N} \mathbf{J}'^{(k,n\to m)} = \sum_{n=1\neq m}^{N} 2\hat{\mathbf{n}}^{(m)} \times \mathbf{H}_{inc}^{(k,n\to m)} = \sum_{n=1\neq m}^{N} 2\hat{\mathbf{n}}^{(m)} \times \mathbf{H}_{scat}^{(k-1,n\to m)}(\mathbf{O}'^{(m)}) \\ \mathbf{H}_{scat}^{(k,m)}(\mathbf{r}_{rec}) &= A^{(m)} \left[-\frac{(jkR_{rec}^{(m)'} + 1)}{R_{rec}^{(m)'}} \left(\mathbf{J}'^{(k,m)} \times \mathbf{R}^{(\hat{\mathbf{m}})'}{}_{rec} \right) \right] \frac{e^{-jkR_{rec}^{(m)'}}}{4\pi R_{rec}^{(m)'}}\end{aligned} \tag{3.30}$$

In order to analyze the evolution of the IPO with respect to meshing, the variation of the NF-RCS is compared for several sub-surface areas ranging from $\lambda^2/10$ to $2\lambda^2$. The results are benchmarked against a reference simulation. In Fig. 3.12 the results are compared for a dihedral plate at 30 *cm*. The dihedral is 20 *cm* width and the frequency used range from 20 to 30 GHz. It can be observed that the mesh must be sufficiently fine to obtain results close to the reference simulation. The results converge towards the reference when the mesh size is finer than $\lambda^2/5$, which corresponds to more than 2000 sub-surfaces. To study the evolution of the IPO in terms of bounce complexity, the same comparison is performed using a trihedral. The simulation setup remains the same, but in this case, three bounces are involved. The results in Fig. 3.13 show that the accuracy is lower than in the dihedral case. The trihedral requires at least $\lambda^2/10$ mesh resolution to produce reliable results. This indicates that, for accurate simulations, the mesh must be sufficiently fine to mitigate this issue. For scenarios involving even more bounces, the IPO would require an even finer mesh. In order to link the IPO to the EEC, let's first take a look at

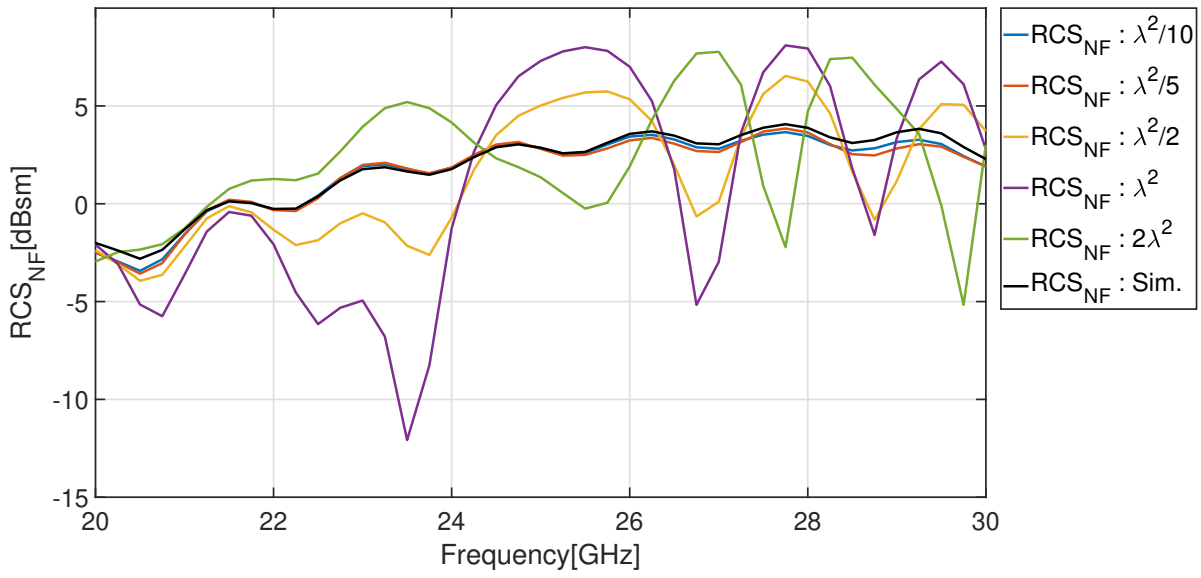

Figure 3.12: Evolution of the near field RCS at 30 cm for a 20 cm dihedral plate for the frequency range [20 GHz; 30 GHz] for several mesh sizes. Comparison with reference simulation.

the EEC. In EEC, the scattered field depends on both the incident and scattered directions due to the term $I_{edge}^{(p)}$ in the equation 3.21. This integral couples the incident and scattered directions. However, similarly to the IPO, by applying a fine mesh, these two terms can be approximately decoupled. Unlike the IPO, though, the equivalent currents $\boldsymbol{\mathcal{J}}'$ and $\boldsymbol{\mathcal{M}}'$ depend on the angle $\theta_{inc}, \phi_{inc}, \theta_{dif}, \phi_{dif}$, and these

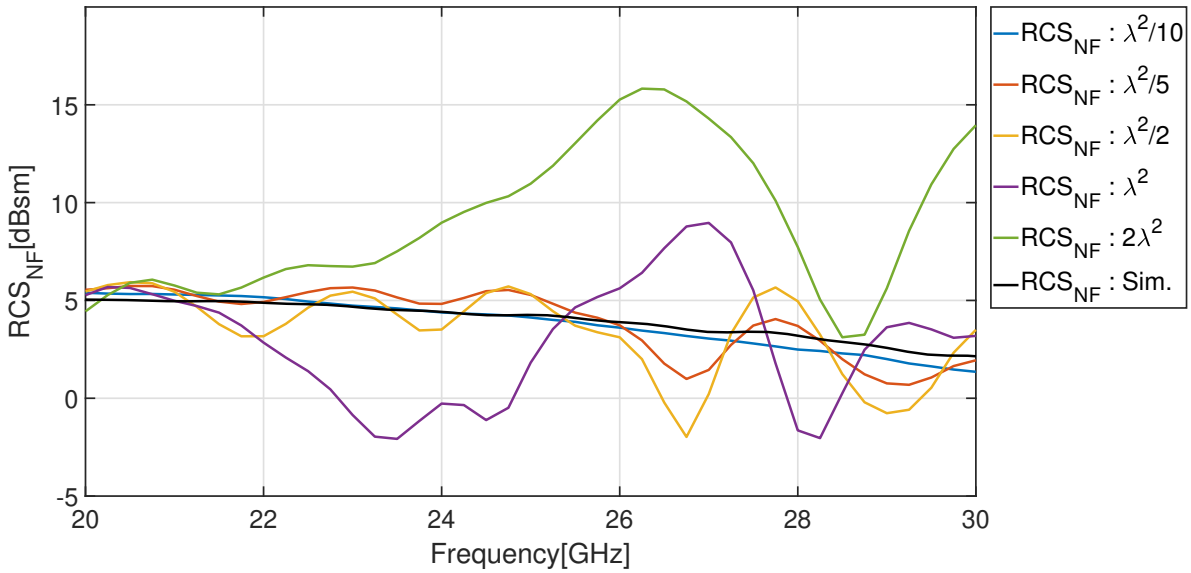

Figure 3.13: Evolution of the near field RCS at 30 cm for a 20 cm trihedral plate for the frequency range [20 GHz; 30 GHz] for several mesh sizes. Comparison with reference simulation.

angular dependencies cannot be easily separated. As a result, the scattered field depends on all incident directions. One proposed solution for combining IPO and EEC is to apply the EEC only to the first and last bounce [46]. The edge diffraction maximal complexity is reduced to approximately $O(P(M+P))$ where P is the number of edges and M the number of surface elements. The P edges radiate toward $M+P$ different elements. Furthermore the IPO complexity scales as $O(M(M+P))$ for the iteration. The M surfaces radiate toward of $M+P$ different elements. Another possible approach to reduce the complexity of the EEC and make it more amenable to iterative methods similar to IPO would be to sum the fields instead of the currents.

$$\begin{aligned}\mathbf{E}_{inc}^{(p)} &= \sum_{n=1}^{N} \mathbf{E}_{scat}^{(n\to p)} + \sum_{l=1}^{P} \mathbf{E}_{dif}^{(l\to p)} \\ \mathbf{H}_{inc}^{(p)} &= \sum_{n=1}^{N} \mathbf{H}_{scat}^{(n\to p)} + \sum_{l=1}^{P} \mathbf{H}_{dif}^{(l\to p)}\end{aligned} \tag{3.31}$$

The incident fields on the edges are equal to the sum of the field scattered by the other elements. These equations result in two fields that are not necessarily orthogonal to each other. The classical definition of the wave vector cannot always be applied due to the non-planar nature of the wavefront. In the case of a plane wave, the direction of wave propagation and the direction of local electromagnetic power density are identical. This is one reason why applying the EEC iteratively could be a viable solution.
By calculating the complex Poynting vector:

$$\boldsymbol{\mathcal{S}}_{inc}^{(p)} = \mathbf{E}_{inc}^{(p)} \times \mathbf{H}_{inc}^{(p)*} \tag{3.32}$$

The real part of the complex Poynting vector defines the local electromagnetic power density, while the

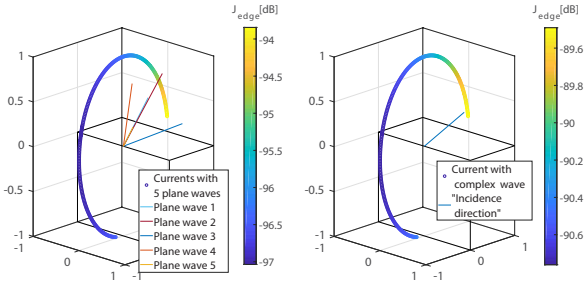

(a)

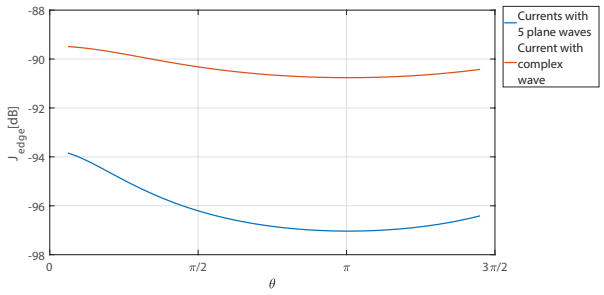

(b)

Figure 3.14: Edge diffraction: method under test. **a** scattering of the edge with both methods. **b** Equivalent current on the edge for both methods

imaginary part represents the reactive component. The reactive part of an electromagnetic wave refers to energy that is temporarily stored in the fields and then returned, rather than being continuously transported in the direction of wave propagation. By using this approach, only a single incident direction is considered. As a result, the incident angles become straightforward to compute.

In the following example, the equivalent currents are computed under illumination by five random plane waves. These currents radiate with $\theta_{\text{dif}} = 0°$, and the edge forms a 90° angle. The power of each plane wave is randomly assigned to highlight the differences.

The results are plotted in Fig. 3.14. The overall radiation pattern remains essentially unchanged, but the new method shows an approximately 6 dB offset (for this simple example) relative to the reference solution. In this configuration, the five incident directions are close together, so the local electromagnetic power density is also directed along the same axis. When the sources are more widely separated, the incident directions and the power-density vector no longer coincide because of interference effects at the observation point.

This means that for more than two bounces, the iterative EEC model cannot be used in the same way as for IPO. Consequently, there are three main scenarios to consider:

- **For a single bounce:** IPO is not necessary. EEC and PO can be used with acceleration techniques. The computational complexity depends on the number of elements in the target (surfaces and edges) and the number of antennas. It scales as $O(N_{TX}N_{RX}(P+M))$, where N_{TX} and N_{RX} are the numbers of transmitting and receiving antennas, respectively.
- **For two bounces:** IPO is still not required, as it is a non-accelerated algorithm with a complexity

of $O(M^2)$ for fine meshing. Instead, using an accelerated double-bounce PO method coupled with a double-bounce EEC model is sufficient. In this case, the incident field on the elements at the second bounce is the field radiated by the elements involved in the first bounce. The overall complexity is then $O(N_{TX}N_{RX}(P+M)^2)$.

- **For three or more bounces:** The IPO algorithm becomes necessary, particularly for complex targets or cavities. However, in such cases, IPO cannot be directly linked with EEC because EEC is not suitable for iterative use. The most practical approach is to apply the EEC only twice: once to model the scattering at the first bounce, and once when the target radiates toward the receiver.

3.3 Target shadowing

To determine which parts of the target are illuminated, several methods can be employed, either based on GO or on PO shadowing. The first one based on GO shadowing relies purely on geometric considerations to determine whether a surface is illuminated, while PO shadowing aims to model the scattered field more realistically by taking into account wave behavior. In this work, we focus on geometrical shadowing specifically with the goal of determining whether a surface element is illuminated or not. As we work with triangular surface elements, our analysis is limited to triangles. Fig. 3.15 illustrates a typical scenario: a target illuminated by an incident wave with an obstacle situated between the source and the target. In such cases, the shadowed region typically does not lie entirely within a single triangle. Instead, the shadow will span multiple triangles, and each triangle may have only a portion that is actually shadowed. From this, two main approaches can be considered:

- **Geometry-based subdivision:** (Fig. 3.15**(b-left)**) In this method, the original surface is taken as the reference, and the shadowed area is subdivided into smaller sub-triangles. This is done by projecting the shape of the obstacle onto the surface and computing the intersections. In order to compute this method, the projection of the three edges of the obstacle is calculated. New sub-triangles are generated where they intersect. This approach is applicable to single-bounce PO models since only one source is involved. However, for multi-bounce scenarios, this becomes computationally expensive due to the need to compute and store new triangle geometries.

- **Center-point approximation:** (Fig. 3.15**(b-right)**) A simpler approach is to consider only the center of each surface element. If the center is illuminated, the entire element is assumed to be illuminated. This greatly simplifies the shadowing computation and it is the approach adopted in our model. The accuracy of this method compared to the first one depends mainly on the mesh resolution. Finer meshes will yield better agreement between the two models but may become too time-consuming in some scenarios. Importantly, there is no need to use the same fine mesh required for PO or IPO calculations just to determine whether a target is illuminated. Doing so would be unnecessarily time-consuming and inefficient.

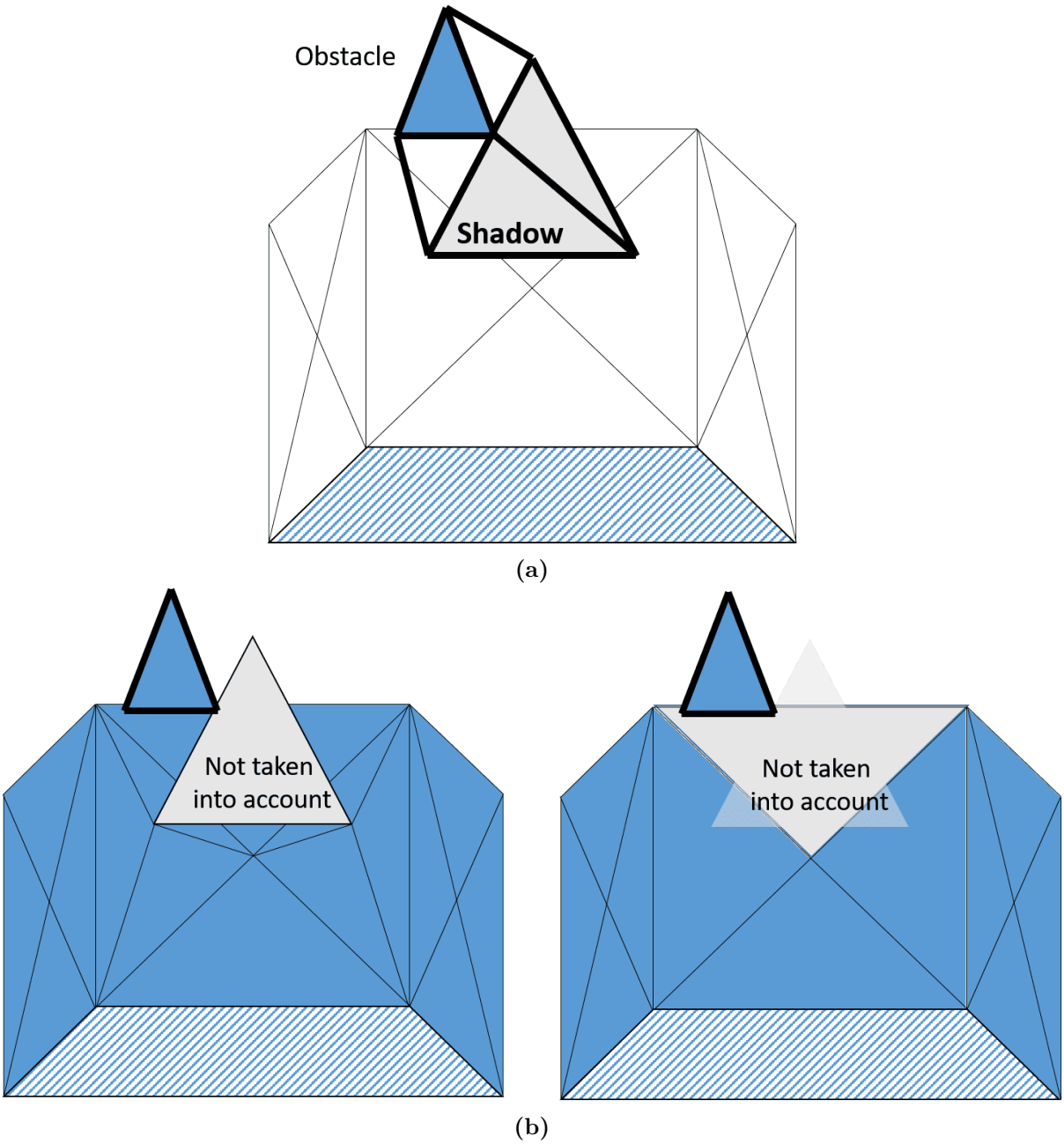

Figure 3.15: Shadowing approach **(a)** scenario with one obstacle **(b)** Methods to resolve shadowing, **left** shape shadowing **right** Center of the surface shadowing

3.3.1 Antenna to target shadowing

For antenna-to-target shadowing, in order to determine if an element is illuminated by the antenna or not, the possible obstacles are identified for each sub-surface. As the target is relatively far from the element, the technique used to identify potential obstacles is to take the antenna as the origin of the coordinate system and transform the position of each sub-surface into a spherical coordinate system. To be a possible obstacle for sub-element m, the distance to the obstacle R_{obs} needs to be smaller than the distance to the sub-element m and the AoD needs to be similar for both obstacle and sub-element m. The conditions $R_{obs} < R^{(m)}$ and $\theta_{obs} \approx \theta^{(m)}$ and $\phi_{obs} \approx \phi^{(m)}$ are sufficient. Once this is done, the

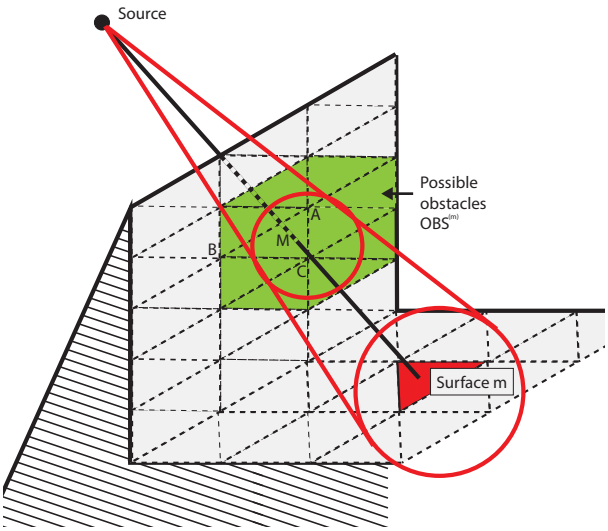

Figure 3.16: Antenna to target shadowing

list of sub-surfaces $OBS^{(m)}$ is defined. Fig. 3.16 presents the geometry. To verify whether a possible obstacle is real or not, simply taking θ and ϕ sufficiently small is not enough. The intersection between the potential ray and the sub-surface is calculated. After computing the intersection, it remains to determine whether the intersection point M lies inside the triangle ABC. To verify this, we compute scalar products between the vectors defined by the triangle's vertices and the intersection point. Using properties of the scalar product: if the sign of the scalar products is not the same for each pair of lines, then point M is considered to be outside the triangle:

$$\begin{cases} (\mathbf{AB} \cdot \mathbf{AC})(\mathbf{AB} \cdot \mathbf{AM}) < 0 \\ (\mathbf{BA} \cdot \mathbf{BC})(\mathbf{BA} \cdot \mathbf{BM}) < 0 \\ (\mathbf{CA} \cdot \mathbf{CB})(\mathbf{CA} \cdot \mathbf{CM}) < 0 \end{cases} \tag{3.33}$$

When applied to a complex target, the illuminated sub-surfaces for each element can be determined as shown in Fig. 3.17 where an STL file of a rabbit is used. The incident field comes from above the rabbit, and the receiver is positioned at 45° relative to the source.

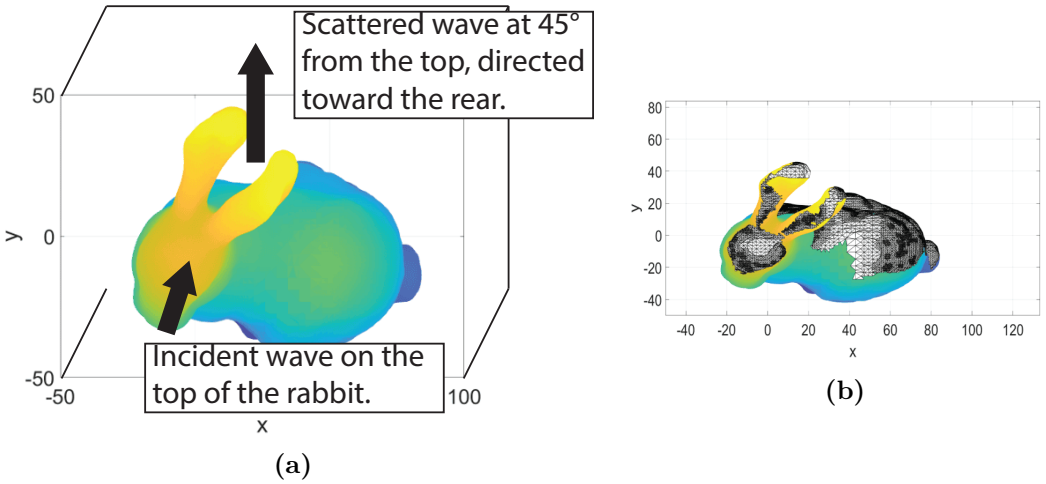

Figure 3.17: Presentation of the meshing result for a rabbit STL source **(a)** initial shape **(b)** meshing result : white surfaces

3.3.2 Target to target shadowing

In order to model target-to-target shadowing, the mesh size becomes more important for several reasons. Since surfaces are relatively close to one another, if a surface is shadowed by another surface that is very close to the emitter, angle spreading becomes significant. This means that the previous conditions are no longer sufficient: the closer a surface is to the source element, the wider the angular spread that must be considered. When looking if a surface n is radiating towards a surface m a possible obstacle q must verify:

$$\begin{cases} R_{obs}^{(n\to q)} < R^{(n\to m)} \\ angle(\mathbf{O}^{(n)'}\mathbf{O}^{(q)'}, \mathbf{O}^{(n)'}\mathbf{O}^{(m)'}) < D(R_{obs}) \end{cases} \tag{3.34}$$

where D is a function of the distance between the source and the obstacle, $R_{obs}^{(n\to q)}$ the distance to the obstacle q from the surface n and $R^{(m)}$ the distance to surface m from surface n. A good optimization of the function D would allow for a reduction in the size of the obstacle list and, consequently, a decrease in computational complexity. In this thesis, the optimization of D was not a priority. However, in order to avoid any false positives, the function D was modeled as a hyperbola. When checking for the presence of an obstacle between n and m, if a surface is close to m, the angle between the center of the surface and the rest of the surface is small. But when approaching the source n, this difference becomes larger. Fig. 3.18 illustrates this case, In this example, the angle formed with obstacle q_2 is larger than that with q_1, but surface q_2 is actually the obstacle between n and m.

Naturally, an accurate optimization of the function D should account for the size of each sub-surface.

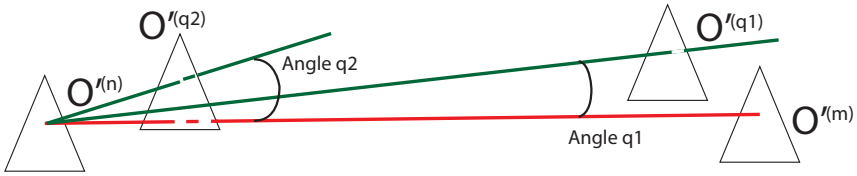

Figure 3.18: Surface-to-surface shadowing: variation of the angle with respect to the distance from source n

3.3.3 Edge illumination

For edge illumination, surface shadowing and radiating regions can be used. By definition, an edge is the boundary between two surfaces. If a surface n illuminates one of the two surfaces that form the edge, the edge is considered illuminated. When computing the $\boldsymbol{\mathcal{J}}_{PO}$ and $\boldsymbol{\mathcal{M}}_{PO}$ terms from equation 2.79, the functions U_1 and U_2 are obtained by evaluating the angle conditions $\phi_{dif,1} < \pi$ for the first surface and $\phi_{dif,2} < \pi$ for the second surface. After meshing the target for IPO or PO, situations like the one in Fig. 3.19 may occur, where an edge is not correctly defined between two triangles because one meets the criterion while the other does not. In such cases, measuring edge diffraction becomes problematic. To avoid this issue, edges are meshed separately from the surfaces.

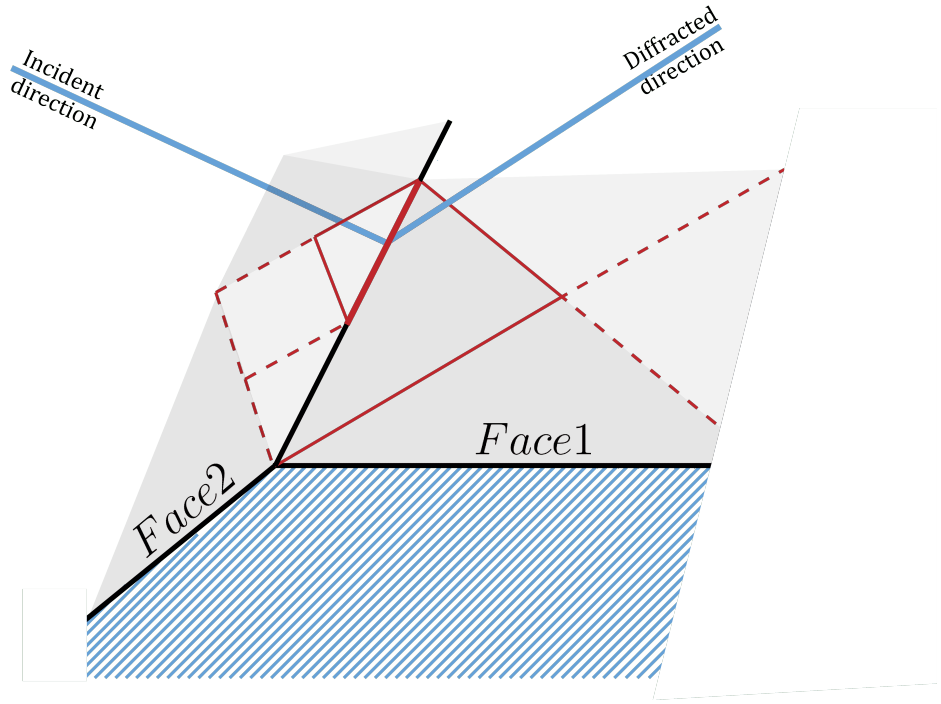

Figure 3.19: Edge diffraction between two surfaces with different sizes

3.4 Acceleration of the model

3.4.1 Segmented IPO

To accelerate the model, several approaches have been proposed and can be used to improve computational efficiency [17], [47]. These accelerations fall into different categories. Firstly, some optimizations focus on reducing the number of scattering directions. In the standard PO and EEC models, scattering is computed in all directions, but in certain cases, it may be beneficial to restrict the scattering directions. It should be noted that SBR can be viewed as an extreme case of such reduction, where scattering is computed only in specific directions. In our case, we implement two acceleration strategies: Segmented Iterative Physical Optics (PPO) [48] and Progressive Physical Optics (PPO) [49]. S-IPO is a model in which the scattered field is radiated only toward an equivalent surface, thereby reducing complexity. As illustrated in Fig. 3.20, the incident field from the antenna illuminates only the opening of the cavity, represented by the yellow equivalent surface. The currents on this surface then re-radiate toward other elements. This introduces an extra step by adding an additional surface. In the end, this reduces complexity, as the size of the receiving region is smaller. This approach can also be applied inside the cavity. For example, Surface 1 illuminates only the first section. Coupled with S-IPO, PPO can also be used. The PPO model splits the problem into two stages: first, radiation is directed toward the bottom of the cavity, and then toward the exit of the cavity. This means that the current radiates in only one direction at a time. In the case of a cavity, this approach effectively reduces the computational complexity by a factor of two as we only radiate only in one of the two directions.

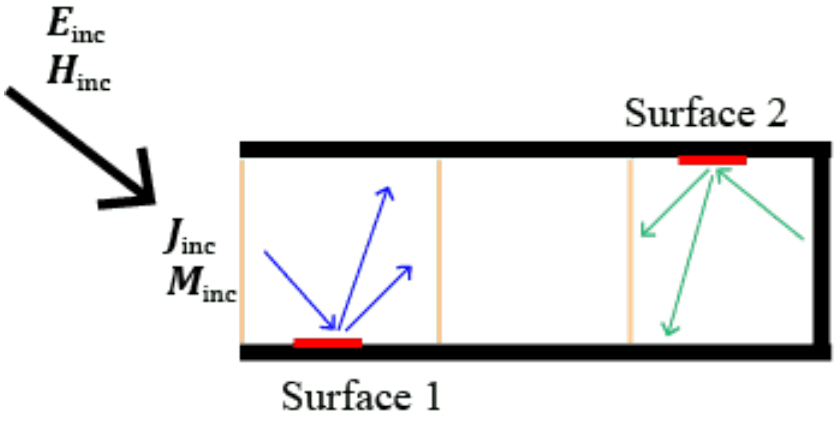

Figure 3.20: Application of the PPO and S-IPO models for cavity

3.4.2 Matrix Resolution

For the IPO model, the current at iteration $k+1$ can be derived from the current at iteration k as a matrix calculation. The current can be written as:

$$\mathbf{J}'_{k+1} = \begin{bmatrix} \mathbf{J}'^{(0)}_{k+1} \\ . \\ . \\ \mathbf{J}'^{(M)}_{k+1} \end{bmatrix} = 2 \begin{bmatrix} \hat{\mathbf{n}}^{(0)} \\ . \\ . \\ \hat{\mathbf{n}}^{(M)} \end{bmatrix} \times \begin{bmatrix} \mathbf{C}^{(0\to 0)}_{k+1} & . & . & \mathbf{C}^{(0\to M)}_{k+1} \\ & & & . \\ & & & . \\ \mathbf{C}^{(M\to 0)}_{k+1} & . & . & \mathbf{C}^{(0\to M)}_{k+1} \end{bmatrix} \times \begin{bmatrix} \mathbf{J}'^{(0)}_{k} \\ . \\ . \\ \mathbf{J}'^{(M)}_{k} \end{bmatrix} \tag{3.35}$$

where $\mathbf{C}^{(n\to m)}_{k+1}$ are defined from equation 3.30 as:

$$\mathbf{C}^{(n\to m)}_{k+1} = U^{(n\to m)} A^{(n)} \left[\frac{(jkR'^{(n\to m)} + 1)}{R'^{(n\to m)}} \left(\hat{\mathbf{R}}'^{(n\to m)} \right) \right] \frac{e^{-jkR'^{(n\to m)}}}{4\pi R'^{(n\to m)}} \tag{3.36}$$

In equation 3.35, all the elements are 3D vectors. Furthermore, the matrix C depends on both the frequency and the distance between elements. $A^{(n)}$ is the area of sub-surface n. The term $e^{-jkR'^{(n\to m)}}$ depends on both the source and observation elements and cannot be factored or simplified to reduce computational complexity, as the matrices involved do not commute. Writing the IPO in matrix form accelerates the algorithm due to efficient matrix computations; however, some issues may arise:

1. **Large matrices**: When the matrix becomes too large due to a high number of sub-surfaces or a wide frequency range the required memory may exceed the available RAM, leading to computational failure.

2. **Complex targets**: In most cases, the matrix U contains many zero entries because some surfaces are not directly illuminated by others. This results in numerous unnecessary computations.

These issues are especially critical in near field scattering problems, where the number of sub-surfaces is large. When memory limitations arise, one solution is to leverage the matrices already used for shadowing and illumination. The goal is to partition the original matrix into smaller sub-matrices that exclude zero entries. For example, in the case of a dihedral shape, half of the sub-surfaces radiate toward the other half of the sub-surfaces. In this case, the matrix can be rearranged into the form:

$$\begin{bmatrix} 0 & 0 & 0 & \mathbf{C}^{(0\to M/2+1)}_{k+1} & . & \mathbf{C}^{(0\to M)}_{k+1} \\ . & . & . & . & . & . \\ . & . & . & . & . & . \\ 0 & . & 0 & \mathbf{C}^{(M/2\to M/2+1)}_{k+1} & . & \mathbf{C}^{(M/2\to M)}_{k+1} \\ \mathbf{C}^{(M/2+1\to 0)}_{k+1} & . & \mathbf{C}^{(M/2+1\to M/2)}_{k+1} & 0 & . & 0 \\ . & . & . & . & . & . \\ . & . & . & . & . & . \\ \mathbf{C}^{(M\to 0)}_{k+1} & . & \mathbf{C}^{(M\to M/2)}_{k+1} & 0 & 0 & 0 \end{bmatrix} \tag{3.37}$$

Moreover, the matrix computation can be efficiently divided into two parts to further accelerate the algorithm. Similar matrix simplifications can be applied to many other geometries in which not all surfaces are mutually illuminated. To further speed up the algorithm and reduce the size of the matrix $\mathbf{C}$, it is important to note that this matrix is skew-symmetric, meaning that only half of it needs to be stored, thereby reducing computational complexity. In the algorithm used during this thesis, when the geometry does not contain curved surfaces, the various parts of the STL file (i.e., the discrete geometric elements) are directly used to define the matrix operations. This leads to faster calculations, as the resulting matrices avoid redundant zero entries.

Another strategy to reduce computational complexity in the matrix calculation is to represent the surface current using only two tangential vectors lying on the surface. This approach simplifies the operations involved in equation 3.35. Since the normal vector $\hat{\mathbf{n}}^{(m)}$ has only one non-zero component, the cross product involving the normal becomes unnecessary. Specifically, the component along $\hat{\mathbf{x}}^{(m)}$ contributes to $\hat{\mathbf{y}}^{(m)}$, while the component along $\hat{\mathbf{y}}^{(m)}$ contributes to $-\hat{\mathbf{x}}^{(m)}$.

This simplification reduces the surface current to a two-element vector, which decreases memory requirements and also reduces the size of the matrix $\mathbf{C}$. Similarly, the distance matrix $\mathbf{R}$ can be reduced to a matrix of two-component vectors, as the third component is not relevant in this context. The current vectors $\mathbf{J}_k^{'(m)}$, initially defined in their respective local bases, can also be transformed into the reduced basis.

However, this reduction comes with a trade-off. While it avoids two cross products involving full 3-component vectors, the change of basis introduces new operations. Specifically, the transformation requires a cross product between a 2-component and a 3-component vector (when converting $\mathbf{J}_k^{'(m)}$ into the new basis), followed by a cross product involving the transformed $\mathbf{C}$ matrix, and finally a scalar product between $\mathbf{J}_k^{'(m)}$ and $\mathbf{C}$, both treated as 3-component vectors.

The key advantage is that the basis transformation of the $\mathbf{C}$ matrix can be precomputed once at the beginning, as it does not directly depend on frequency. This allows for a significant reduction in computational cost and memory during iterative frequency-dependent calculations.

3.4.3 Matrix compression

To reduce memory usage for matrix storage, compression methods such as Adaptive Cross Approximation (ACA) [50] can be employed. ACA is an efficient algorithm for approximating low-rank matrices by adaptively selecting rows and columns without requiring access to the full matrix. It is commonly used in MOM algorithms and has also been adapted for use with IPO.

The objective is to exploit the low-rank nature of the matrix and replace the full matrix $\mathbf{C}$ with the product of two smaller matrices, $\mathbf{U}$ and $\mathbf{V}$, as follows:

$$\mathbf{C} \approx \mathbf{U}\mathbf{V}^T \tag{3.38}$$

where $\mathbf{U}$ and $\mathbf{V}$ consist of a limited number of sampled columns and rows, respectively. Together, they form a low-rank approximation of the original matrix.

The matrices that contribute most significantly to the computational complexity are the IPO interaction matrices, which are used during the iterative updates of the currents. The ACA algorithm can be applied either to the full IPO interaction matrix or to its sub-blocks.
In this thesis, the use of ACA is discussed but not fully implemented. In practice, the compression algorithm becomes advantageous in terms of computation time only when the number of iterations is sufficiently high. Otherwise, it may actually require more time than the standard (non-compressed) approach.

3.4.4 Fast Far Field Approximation

Another approach to accelerate the computation of the IPO matrix is to apply the Fast Far Field Approximation (FaFFA) [51] within this near field model. This approximation uses the Fraunhofer and chord error criteria to define both the scattering directions and the observation points. To reduce the matrix size, the method introduces the concept of super-surfaces, which group multiple smaller surfaces into a single radiating group.
The idea is to treat all currents within a super-surface as a unique source of radiation. By assuming that the observation point is sufficiently far from the radiating super-surface, FaFFA allows the use of asymptotic far field expressions. This approach is especially effective for interactions between distant surfaces or in scenarios involving directional scattering, as illustrated in Fig. 3.21.
In this framework, all surfaces within a super-surface m_s radiate toward the center of a super-surface n_s. The distances involved are:

$$\begin{aligned} \mathbf{R}^{(m\to n_s)} &= \mathbf{R}^{(m\to m_s)} + \mathbf{R}^{(m_s\to n_s)} \\ R^{(m\to n_s)} &\approx R^{(m_s\to n_s)} + \mathbf{R}^{(m\to m_s)} \cdot \hat{\mathbf{R}}^{(m_s\to n_s)} \end{aligned} \tag{3.39}$$

This means that:

$$\mathbf{H}_{scat}^{(k,m\to n_s)} = A^{(m)} \left[-jk \left(\mathbf{J}'^{(k,m)} \times \hat{\mathbf{R}}_{rec}^{(m_s\to n_s)} \right) \right] \frac{e^{-jkR^{(m_s\to n_s)}} e^{-jk\mathbf{R}^{(m\to m_s)}\cdot\hat{\mathbf{R}}^{(m_s\to n_s)}}}{4\pi R^{(m_s\to n_s)}} \tag{3.40}$$

For the sum of all the element presented in super-surface m_{sou}:

$$\mathbf{H}_{scat}^{(k,m_s\to n_s)} = \sum \mathbf{H}_{scat}^{(k,m\to n_s)} = A^{(m)} \left[-jk \left(\sum \left(\mathbf{J}'^{(k,m)} e^{-jk\mathbf{R}^{(m\to m_s)}\cdot\hat{\mathbf{R}}^{(m_s\to n_s)}} \right) \times \hat{\mathbf{R}}^{(m_s\to n_s)} \right) \right] \frac{e^{-jkR^{(m_s\to n_s)}}}{4\pi R^{(m_s\to n_s)}} \tag{3.41}$$

Similarly for the receiving part, the same approach can be applied to reduce complexity for a sub-surface n in n_s:

$$\begin{aligned} \mathbf{R}^{(m_s\to n)} &= \mathbf{R}^{(m_s\to n_s)} + \mathbf{R}^{(n_s\to n)} \\ R^{(m_s\to n)} &\approx R^{(m_s\to n_s)} + \mathbf{R}^{(n_s\to n)} \cdot \hat{\mathbf{R}}^{(m_s\to n_s)} \end{aligned} \tag{3.42}$$

By combining both simplifications:

$$\mathbf{H}_{scat}^{(k,m_{sou}\to n)} = \sum \mathbf{H}_{scat}^{(k,m\to n)} = A^{(m)} \left[-jk \left(\sum \left(\mathbf{J}'^{(k,m)} e^{-jk\mathbf{R}^{(m\to m_s)}\cdot\hat{\mathbf{R}}^{(m_s\to n_s)}} \right) \times \hat{\mathbf{R}}^{(m_s\to n_s)} \right) \right] \frac{e^{-jkR^{(m_s\to n_s)}} e^{-jkR^{(n_s\to n)}\cdot\hat{\mathbf{R}}^{(m_s\to n_s)}}}{4\pi R^{(m_s\to n_s)}} \tag{3.43}$$

From this last equation, the term can be numerically decomposed into three parts: the projection of the currents at the center of the super-surface, the scattering toward the center of the receiving sub-surface, and finally the radiation from the current distribution centered at each sub-surface.

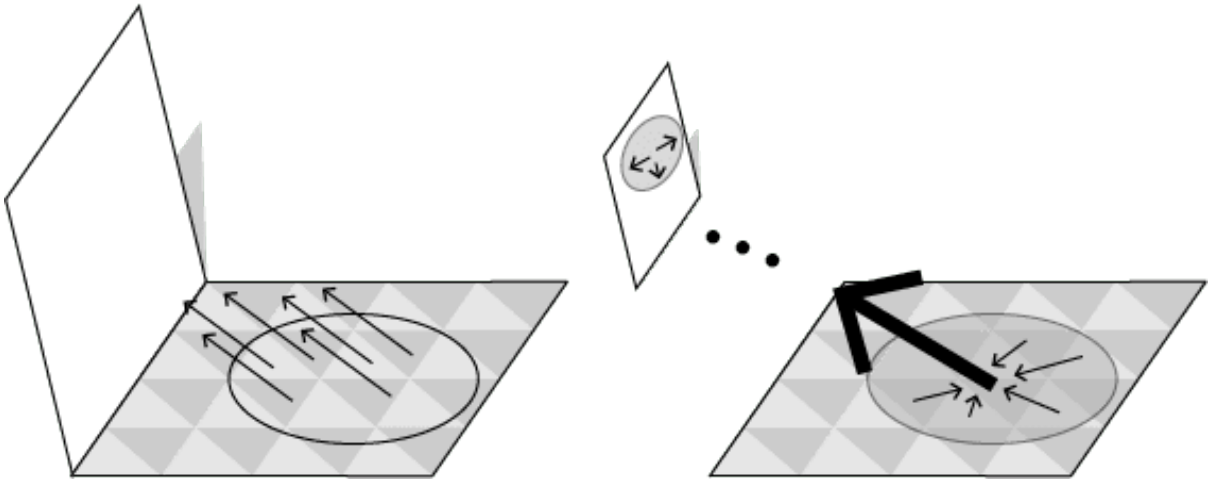

Figure 3.21: Fast Far Field Approximation: comparison of a near field radiation and far field radiation

3.5 Conclusion

This chapter presented and detailed the near field backscattering model. Based on PO and EEC, the equations used in the model were thoroughly explained, along with the implementation, to provide a clear understanding of how the equations are defined. First, the implementation of PO using a refined mesh for single and double reflections was introduced. Two criteria are used: the first is a distance-based criterion that defines far field sub-surfaces even when the target is in the near field, and the second is a chord-length criterion used for curved surfaces. By reducing both the curvature of both the target and the incident wave through smaller sub-surfaces, these two methods help to simplify the computations. When coupled with EEC, the model is further refined using the IPO approach. To determine which elements interact with one another, a geometric optics-based algorithm is employed to identify the visibility relationships between emitters and receivers, including mutual visibility between surfaces and edge contributions to illumination. To accelerate the IPO and EEC algorithms, several techniques are presented to simplify or reduce their computational complexity. In the thesis, all of these methods were analyzed and compared. Most of these techniques are applied on a case-by-case basis. This chapter places particular emphasis on detailing the implementation of the model.

Chapter 4

Antenna effects and measurement validation

4.1 Introduction

In this chapter, the objective is to study the specific aspects related to near field radiation. In our backscattering model, both the transmitter and the receiver are located in the near field of the target. First, the limitations associated with NF-RCS are presented. This leads to the necessity of taking antennas into account. The model is general and can be applied to any type of antenna. However, in this thesis, it is employed specifically for dipole and horn antennas. The implementation of these antennas is validated using simple case and the performance is tested on more complex test cases.
To further validate the relevance of our model, a near field measurement campaign is conducted. The experimental setup and alignment process are first presented, as high precision between the different components is essential to ensure good agreement between the model and the measurements. For validation purposes, several canonical targets are used.

4.2 Antennas's integration

4.2.1 Limitation of the NF-RCS

In the previous chapter, the metric used was the NF-RCS, which has certain limitations that will be discussed in the following paragraph. As a brief reminder, the NF-RCS is a metric designed to mimic the classical RCS, but in the near field regime. The objective is to define a function that models the scattering behavior of the target while accounting for the dependence on distance. In this context, both the transmitter and the receiver are located in the near field of the target (i.e., at a distance less than $2R_T^2/\lambda$). In the following, we examine the various issues that may arise when using this metric.

4.2.1.1 Limitation due to incident wave

Firstly, the NF-RCS is defined as:

$$\sigma_{NF-RCS} = 4\pi R_R^2 \frac{\|\mathbf{E}_{scat} \wedge \mathbf{H}_{scat}^*\|}{\|\mathbf{E}_{inc} \wedge \mathbf{H}_{inc}^*\|} \tag{4.1}$$

However, in the near field scenario, the incident field cannot be approximated as a plane wave due to the relatively short distance between the target and the source, and because this distance is not uniform across the target. Nevertheless, using equation 2.31:

$$\sigma_{NF-RCS} = \|\sqrt{4\pi}\frac{\sum_m R_T^{(m)} R_R^{(m)} \mathbf{E}_{scat}^{(m)} \cdot \hat{\mathbf{p}}}{\|V\|}\|^2 \tag{4.2}$$

Using this equation appears to be the closest possible definition of the NF-RCS. In this formulation, the field does not depend on the antenna characteristics, the incident field is replaced by the source voltage, which effectively simulates an isotropic antenna with a gain of 0 dBi (omnidirectional). However, one major issue arises from this approach: it becomes impossible to directly relate the result to the radar equation. Since the model decomposes the scattering process into several parts, the same should apply to the radar equation:

$$P_R = P_T \sum_{m=1}^{M} \frac{G_T^{(m)} G_R^{(m)} \lambda^2 \sigma_{RCS}^{(m)}}{(4\pi)^3 R_T^{(m)2} R_R^{(m)2}} \tag{4.3}$$

In order to use the radar equation with the NF-RCS, an alternative approach could be to consider a single incidence and scattering direction when performing the calculation. In this case, either the mean or maximum antenna gain can be used, and similarly, the mean or minimum distance between the antenna and the target can be considered. However, this approach introduces significant approximations, making the metric imprecise for accurate radar equation calculations. To properly account for the incident field in the IPO and EEC formulations, the antenna gain must be applied individually for each element of the target. To model this correctly, the incident field on the target can be expressed as:

$$\begin{aligned} \mathbf{E}_{inc}^{(m)} &= \mathbf{E}_T(\theta_{inc}^{(m)}, \phi_{inc}^{(m)}) \frac{e^{-jk_0 R_{inc}^{(m)}}}{R_{inc}^{(m)}} \\ \mathbf{H}_{inc}^{(m)} &= \mathbf{H}_T(\theta_{inc}^{(m)}, \phi_{inc}^{(m)}) \frac{e^{-jk_0 R_{inc}^{(m)}}}{R_{inc}^{(m)}} \end{aligned} \tag{4.4}$$

with $\mathbf{H}_T$ and $\mathbf{E}_T$ the scattered field by the source at a distance of 1 m using the direction $\theta_{inc}^{(m)}$ and $\phi_{inc}^{(m)}$.

4.2.1.2 Limitation due to the scattered wave

When analyzing the scattered wave from the target, it should be noted that Near Field (NF) radiation is already accounted for in the model. The scattered field is computed as the sum of the contributions from all the sub-surfaces of the target. In the SC approach for RCS calculation, either the electric or magnetic field can be used, both generally leading to similar results, although minor differences may

arise.

A major challenge when attempting to use the NF-RCS lies in the calculation of the antenna gain. Using a mean or maximum gain value can be problematic, as each incident ray does not necessarily share the same gain. In fact, it is important to emphasize that the summation involved in the NF-RCS computation should incorporate the complex gain of the antenna for each direction. Doing so leads to more accurate and physically meaningful results.

$$G_{R,mean} \sum_{m=1}^{M} \mathbf{E}_{scat}^{(m)} \neq \sum_{m=1}^{M} G_R^{(m)} \mathbf{E}_{scat}^{(m)} \tag{4.5}$$

Where $G_{R,mean}$ is the mean complex gain for the receiver. This takes into account the complexity of the gain and assigns an appropriate gain to each ray.

4.2.2 Round-trip transfer function definition

In order to overcome the limitations associated with the NF-RCS, a straightforward solution is to move away from using it altogether. In some cases, the precision of the NF-RCS may not be sufficient for accurate modeling. To address this, the Round-Trip Transfer Function (RTF) can be used instead. It can be defined as a sum from each sub-element m:

$$\mathcal{H}_{Rt}(f) = \sum_{m=1}^{M} \mathcal{H}_T^{(m)} \mathcal{H}_{T\to S}^{(m)} \rho_{SC}^{(m)} \mathcal{H}_{S\to R}^{(m)} \mathcal{H}_R^{(m)} \tag{4.6}$$

where $\mathcal{H}_T^{(m)}$ is the transfer function of the source in direction of m, $\mathcal{H}_{T\to S}^{(m)}$ is the transfer function from the antenna to the sub-surface m, $\rho_{SC}^{(m)}$ is the scattered coefficient of surface m, $\mathcal{H}_{S\to R}^{(m)}$ is the transfer function from the sub-surface m to the receiver antenna and $\mathcal{H}_R^{(m)}$ the transfer function of the receiver in direction of m. The square modulus of the round-trip transfer function is calculated as:

$$|\mathcal{H}_{Rt}(f)|^2 = \frac{1}{P_T} \frac{c^2}{f^2 4\pi} \frac{|\mathbf{E}_R(f) \times \mathbf{H}_R^*(f)|}{2} \tag{4.7}$$

Here, the received field is equal to the sum of the scattered contributions from each element, but the antenna gain must be applied beforehand:

$$\mathbf{E}_R(f) = \sum_{m=1}^{M} \mathcal{H}_R^{(m)} \mathbf{E}_{scat}^{(m)}(f) \qquad \mathbf{H}_R(f) = \sum_{m=1}^{M} \mathcal{H}_R^{(m)} \mathbf{H}_{scat}^{(m)}(f) \tag{4.8}$$

To compare the results obtained from equation 4.7 with those from the RTF derived using the NF-RCS, a test case is considered involving a horn antenna placed 20 cm away from a 2 m metallic plate, as illustrated in Fig. 4.1. The integration of the antenna into the model will be presented in the next section. The antenna operates over a frequency range of 20 to 30 GHz. When using the NF-RCS, the choice of gain and distance parameters is critical. Given that the antenna is directive and the plate is illuminated normally, a geometric perspective justifies using the antenna gain at boresight (i.e., at the center) for each frequency, and a fixed distance of 20 cm. This approximation is expected to produce

results close to those obtained by directly evaluating the transfer function on each sub-element. The results, shown in Fig. 4.1, indicate that both methods yield similar levels (around $-28\ dB$). However, the plots exhibit noticeably different shapes, suggesting that a fundamental difference exists between the two approaches. The round-trip transfer function offers the advantage of being directly comparable with measurement results extracted from S-parameters. The scattered fields from each individual sub-element

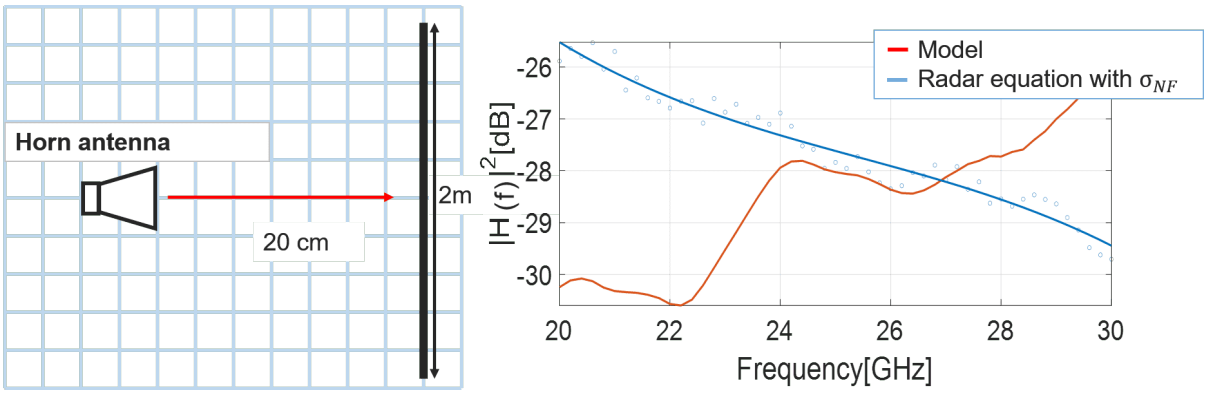

Figure 4.1: Calculation of the backscattering directly or by using the near field RCS

m toward the antenna are calculated. The fields are expressed on the $\hat{\mathbf{e}}_\theta$ and $\hat{\mathbf{e}}_\phi$ vectors as:

$$\mathbf{E}_{scat}^{(m)} = E_{scat,\theta}^{(m)}\hat{\mathbf{e}}_\theta + E_{scat,\phi}^{(m)}\hat{\mathbf{e}}_\phi \tag{4.9}$$

$$\mathbf{H}_{scat}^{(m)} = H_{scat,\theta}^{(m)}\hat{\mathbf{e}}_\theta + H_{scat,\phi}^{(m)}\hat{\mathbf{e}}_\phi \tag{4.10}$$

To consider the transfer function of the receiver, it is decomposed into $\mathcal{H}_{R,\theta}^{(m)}$ and $\mathcal{H}_{R,\phi}^{(m)}$, which characterize the radiation of the antenna. These dimensionless values represent the complex gain of the antenna as applied to the electric field. Using E_{R} for the receiver raises an issue of units, which is why the transfer function is used. In fact, they play the exact same role as for the incident wave. The electric field is rewritten on both $\hat{\mathbf{e}}_\theta$ and $\hat{\mathbf{e}}_\phi$ vectors as:

$$\mathbf{E}_R^{(k,m)} = \mathcal{H}_{R,\theta}^{(m)} E_{scat,\theta}^{(k,m)}\hat{\mathbf{e}}_\theta + \mathcal{H}_{R,\phi}^{(m)} E_{scat,\phi}^{(k,m)}\hat{\mathbf{e}}_\phi \tag{4.11}$$

For the magnetic field, the coefficients are reversed due to the orthogonality of the scattered electric field E_{scat} and magnetic field H_{scat} in a plane wave. The total field perceived by the receiver is obtained by summing the contributions of individual plane waves from all M elements over K iterations. To accurately compute the transfer function, it is essential to take into account both the electric and magnetic fields at the receiver.

$$\mathbf{E}_R = \sum_{k=1}^{K}\sum_{m=1}^{M}\mathbf{E}_R^{(k,m)} \qquad \mathbf{H}_R = \sum_{k=1}^{K}\sum_{m=1}^{M}\mathbf{H}_R^{(k,m)} \tag{4.12}$$

4.2.3 Antenna model integration

To model the antenna's complex gain, a different approach must be used. Since many models exist for the antenna's far field behavior, the CST Studio software will be employed with Finite Integration Technique (FIT) simulation. The goal is to accurately model the antenna's far field radiation pattern for use in our model. Given that the antennas considered are relatively simple and small, the far field criterion will be applied. This approach is justified by the relationship between frequency and distance: at higher frequencies, the target's near field region extends farther, but the antenna's physical size decreases, thereby reducing its own near field distance. For this thesis, two types of antennas are studied: a dipole antenna and a horn antenna.

4.2.3.1 Integration of dipole antennas

To model the dipole antenna, the scattered electric field can be approximated as being radiated from a single point source. Since the antenna's phase center coincides with its physical center, representing the antenna as a single point is a reasonable approximation. To model the radiated field from the antenna the initial incident field for the sub-element m is defined using the equation 4.4. The fields are defined for each frequency individually. In this equation, the terms $E_T(\theta^{(m)}, \phi^{(m)})$ and $H_T(\theta^{(m)}, \phi^{(m)})$ refer to the scattered field by the source antenna along the two direction $\hat{\mathbf{e}}_\theta$ and $\hat{\mathbf{e}}_\phi$. This means that the equation can be written as:

$$E_T(\theta^{(m)}, \phi^{(m)}) = \mathcal{H}_{T,\theta}^{(m)} E_0 \hat{\mathbf{e}}_\theta + \mathcal{H}_{T,\phi}^{(m)} E_0 \hat{\mathbf{e}}_\phi \tag{4.13}$$

Here E_0 represents the field associated with a unit input power. In the case of the dipole, Fig. 4.2 shows the radiation pattern of the dipole used at 27 GHz with a unit input power. For the case study in this thesis, the modeled dipole operates over the frequency range from 24 GHz to 30 GHz. Considering both $\hat{\mathbf{e}}_\theta$ and $\hat{\mathbf{e}}_\phi$ components may be more complex than necessary, as there is a difference of approximately 50 dBV/m between these two directions.

To validate the model and verify whether representing the antenna as a single radiating point is sufficient, Fig. 4.3 presents the RTF as a function of frequency for three different distances between a 10 cm metallic plate and the dipole antenna: 10 cm, 20 cm, and 30 cm. Here, the distance is defined between the center of the antenna and the center of the plate. For each distance, both simulation results and model predictions are shown. As expected, the overall level of the transfer function decreases with increasing distance, reflecting propagation loss. Moreover, the frequency response is not flat; noticeable curvature indicates frequency-dependent behavior, likely caused by multipath effects related to the near field radiation from the plate. These results suggest that the antenna integration in the model effectively captures the essential scattering characteristics.

To increase the model's validity and test it with multiple bounce interactions, Fig. 4.4 illustrates the impact of multipath on the transfer function between two dipoles in the presence of three nearby reflecting plates. In this scenario, the plates are 10 cm wide and positioned to create strong first- and second-order reflections. The frequency response shown in Fig. 4.4(**b**) reveals pronounced frequency-selective behav-

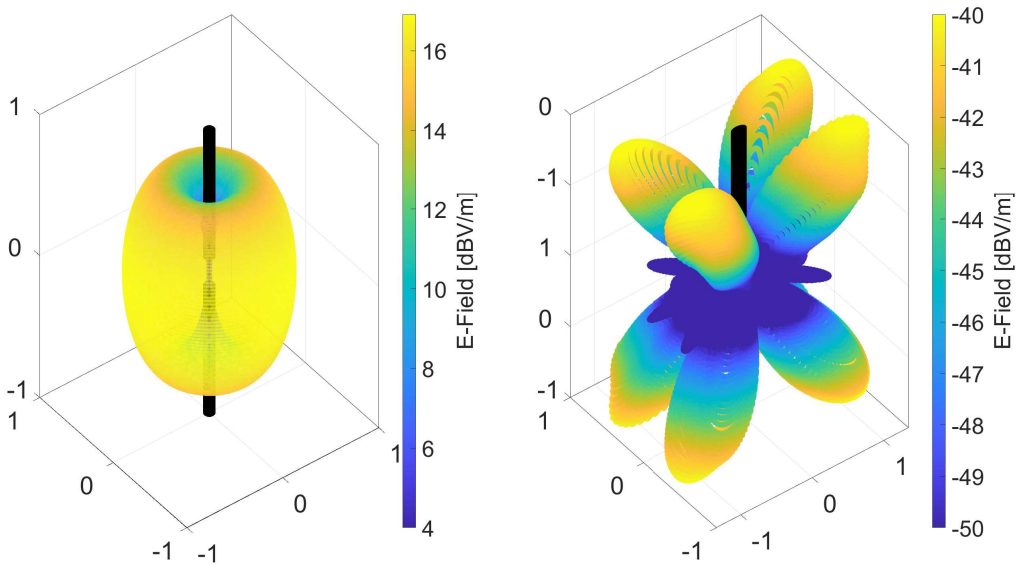

Figure 4.2: Electric field scattered by the dipole antenna at 1 m with a unit input power: **(a)** Vertical polarization: **(b)** Horizontal polarization

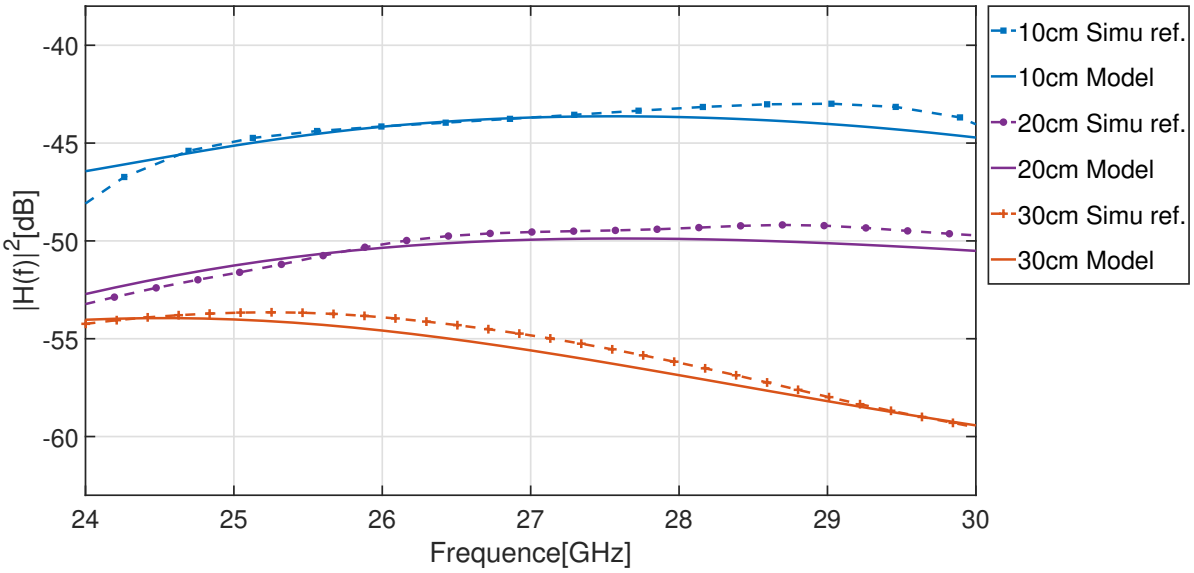

Figure 4.3: Transfer function of the plate answer according to the distance plate-antenna: Dipole antenna

ior, with periodic notches caused by interference between the main propagation paths. The model closely matches the reference simulation results, confirming its accuracy. Notably, the first-order reflection dominates the response and largely shapes the transfer function, while higher-order bounces particularly the third have significantly lower amplitudes and negligible impact. This analysis confirms that considering only the dominant paths is sufficient to capture the main propagation effects in this configuration.

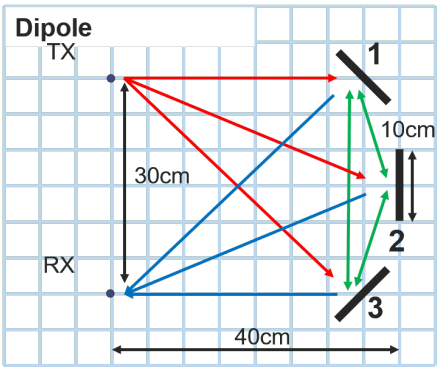

(a)

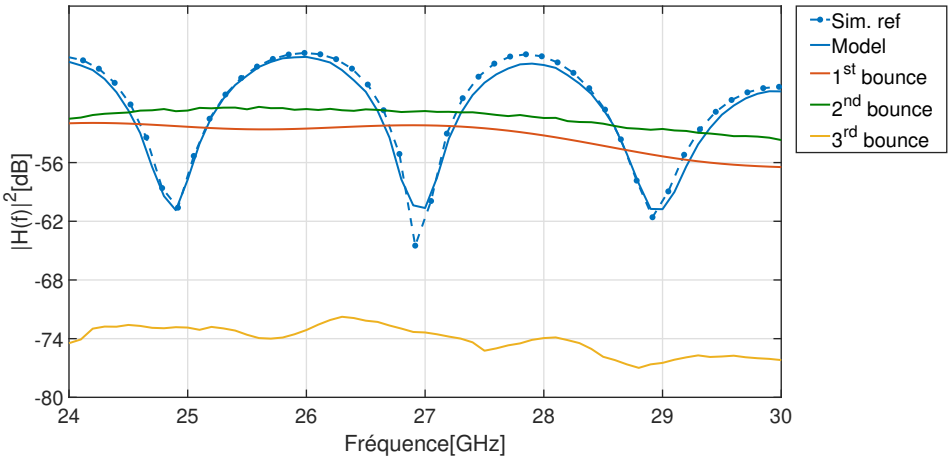

(b)

Figure 4.4: (a) Geometry of the scenario (b) Transfer function of the plate response as a function of the number of bounces: Dipole antenna

4.2.3.2 Integration of horn antennas

For the integration of a non-dipole antenna, the antenna cannot be simply modeled as a radiating point source. First, antenna sizes can vary significantly, and the object may lie within the antenna's near field. Moreover, representing the antenna radiation as a point source can have limitations even when the far field condition is theoretically met. In the case of a horn antenna, several factors must be taken into account depending on the horn's size. As a first approximation, we assume that the RTF is calculated from the center of the antenna port. However, unlike the dipole, when calculating the transfer function of the antenna, the phase reference is taken from the antenna's phase center rather than from the physical center of the antenna port. The phase center is defined as the point from which the electromagnetic radiation appears to spread spherically outward, resulting in a constant phase over any spherical wavefront centered on this point. With these considerations, several possible approaches can be explored to define the antenna in our model:

1. In this approach, the radiated field from the antenna is defined similarly to that of a dipole. However, there are two potential pitfalls. First, the amplitude: for a horn antenna, the propagation inside the horn cannot be accurately modeled as free-space propagation. Second, as mentioned

earlier, the field phase reference is taken from the phase center, not the physical center of the antenna port. Consequently, the angles of arrival and departure can differ depending on whether the vector is referenced from the phase center or the antenna port center.

2. If only the phase center is used, the incident and scattered fields will match the theoretical scattered field of the simulated antenna. However, a subtle issue remains when summing the fields: for reception, the summation cannot be performed at the phase center because the interference patterns observed at the phase center and at the antenna port differ. In S_{21} measurements, the key information is the transmission between the two antennas. This is determined by the fields present at the ports of the transmitting and receiving antennas.

3. A combination of both the phase center and the center of the port can be used. As mentioned earlier, phase summation should be performed at the port to properly model interference effects. According to horn antenna theory, the phase center lies along the central axis of the port and is located approximately two-thirds of the antenna's length from the feed point. This two-thirds estimate is approximate, as it depends on the operating frequency. For scattering primarily in the antenna's main beam, the phase center can be effectively represented as a simple offset from the port center. Thus, the scattered field at element m is given by:

$$\begin{aligned}\mathbf{E}_{\text{inc}}^{(m)}(f) &= \mathbf{E}_{\text{T}}(\theta^{(m)},\phi^{(m)},f)\frac{e^{-jk_0(f)R_{inc}^{(m)}}}{R_{inc}''^{(m)}} \approx \mathbf{E}_{\text{T}}(\theta^{(m)},\phi^{(m)},f)\frac{e^{-jk_0(f)R_{inc}^{(m)}}}{R_{inc}^{(m)}-D}\\ \mathbf{H}_{\text{inc}}^{(m)}(f) &= \mathbf{H}_{\text{T}}(\theta^{(m)},\phi^{(m)},f)\frac{e^{-jk_0(f)R_{inc}^{(m)}}}{R_{inc}''^{(m)}} \approx \mathbf{H}_{\text{T}}(\theta^{(m)},\phi^{(m)},f)\frac{e^{-jk_0(f)R_{inc}^{(m)}}}{R_{inc}^{(m)}-D}\end{aligned} \tag{4.14}$$

Here, $R_{inc}^{(m)}$ is the distance measured from the center of the antenna port, and $R_{inc}''^{(m)}$ is the distance measured from the phase center. D is the distance between the phase center and the port center. When operating in the main beam of the antenna or close to it, the approximation $(R_{inc}^{(m)}-D)\approx R_{inc}''^{(m)}$ is valid. In other cases, for example if the radiation is emitted behind the antenna, this approximation does not hold. Fig. 4.5 presents the definition of the scattered field by the antenna and by the target.
For reception, the total received field is:

$$\mathbf{E}_{\text{R}} = \sum_{m=1}^{M}\mathbf{E}_s^{(m)} = \sum_{m=1}^{M}\left(\mathcal{H}_{R,\theta}^{(m)}E_{scat,\theta}^{(m)}\hat{\mathbf{e}}_\theta + \mathcal{H}_{R,\phi}^{(m)}E_{scat,\phi}^{(m)}\hat{\mathbf{e}}_\phi\right)\frac{R_{scat}^{(m)}}{R_{scat}^{(m)}+D} \tag{4.15}$$

where the scattered field is taken at the center of the antenna port. An alternative approach would be to use the distance $R_{scat}''^{(m)}$ which is the distance measured from the phase center of receiving antenna instead of $R_{scat}^{(m)}+D$.
Similarly to the tests performed for the dipole antenna, simulations were conducted for a horn antenna model using CST Studio. The antenna operates over a frequency range of 20 to 30 GHz with a maximum gain of approximately 20 dBi. The antenna size is approximately 2.5 cm, which corresponds to a near field distance of about 10 cm. The antenna radiation pattern is shown in Fig. 4.6 for a unit power. In this case, both polarizations are important for accurately describing the radiation, especially outside the main beam.

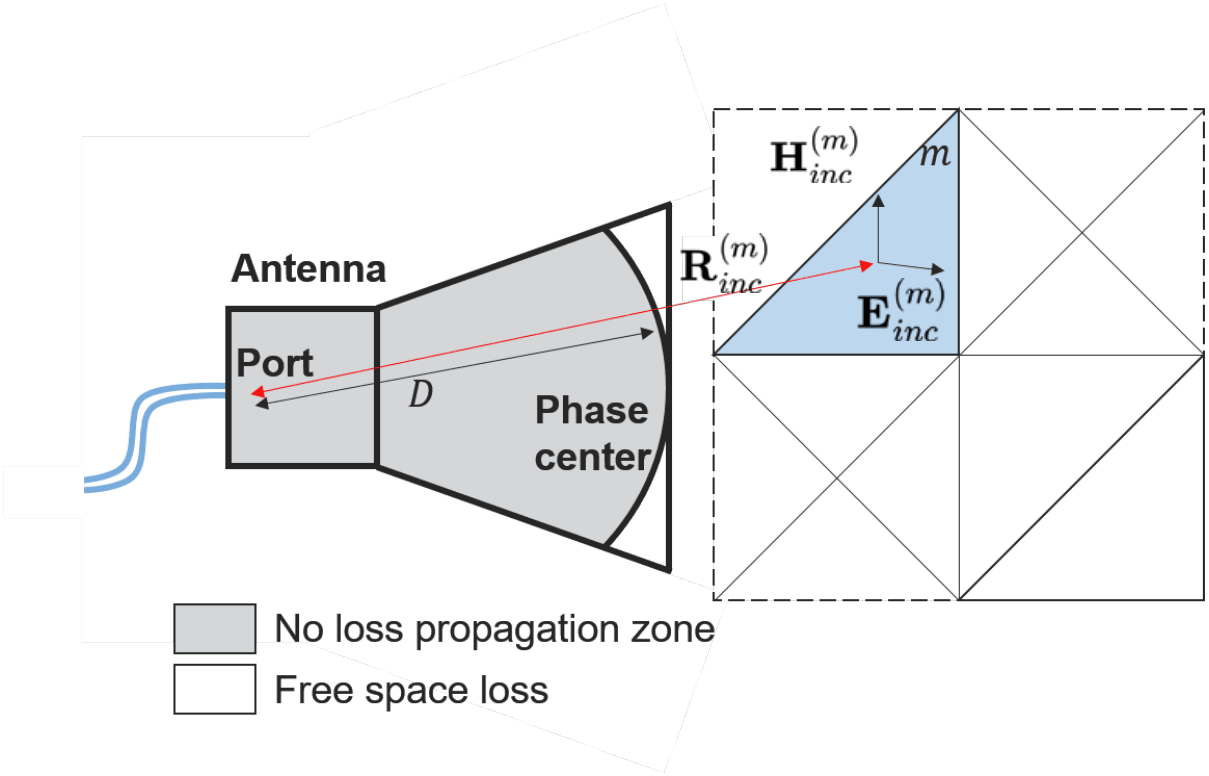

Figure 4.5: Modeling of a horn antenna in the PO model

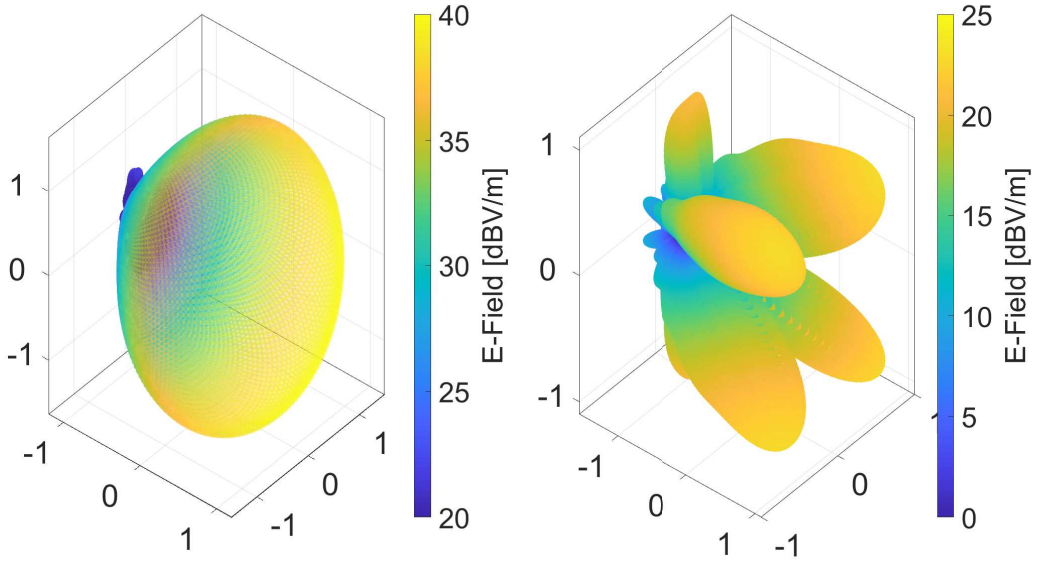

Figure 4.6: Electric field scattered by the horn antenna: **(a)** Vertical polarization: **(b)** Horizontal polarization

As with the dipole, the first case study involves a single 10 *cm* metallic plate positioned close to the antenna's near field. According to the Fraunhofer criterion, the far field distance ranges from 10 to 13 *cm*, meaning that when the plate is at 10 *cm*, it lies within the antenna near field. The results presented in Fig. 4.7 show that the RTF yields similar results when comparing the model (solid lines) to the reference simulation (dashed lines) at 20 and 30 *cm*. At 10 *cm*, the simulation results generally agree well with the

reference, although a closer examination reveals a missing modulation effect, which can be attributed to the target being located within the antenna near field region. As in the dipole scenario, the case with

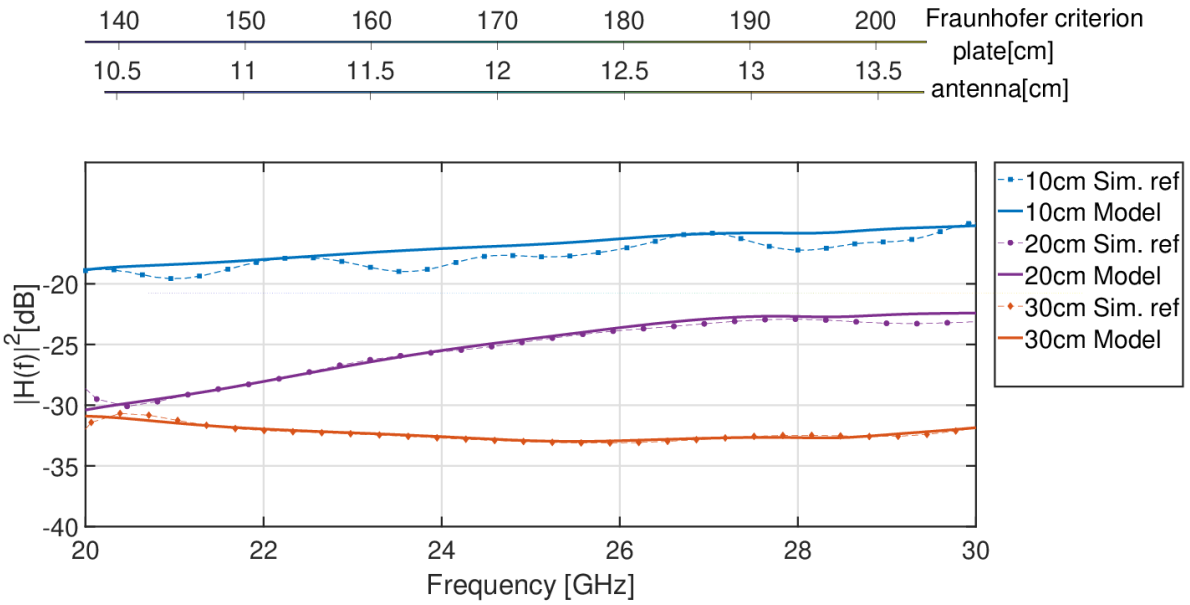

Figure 4.7: Transfer function of the plate response as a function of the plate–antenna distance: Horn antenna

three plates compares the simulated transfer function and the analytical model for a plate illuminated by a horn antenna. The total modeled response is broken down into contributions from the first, second, and third-order bounces, shown in red, green, and orange, respectively.

We observe good overall agreement between the simulation and the model, especially across the main frequency range. The oscillations are well captured by the model and are primarily due to the first and second bounces. In the case of the horn antenna, the double bounces carry most of the transmitted energy, which is mainly a consequence of the antenna's directivity and the scenario geometry.

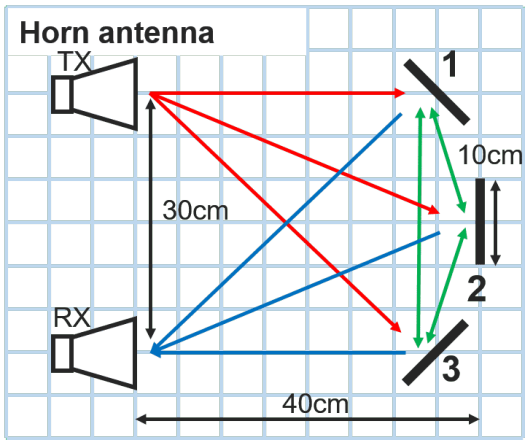

(a)

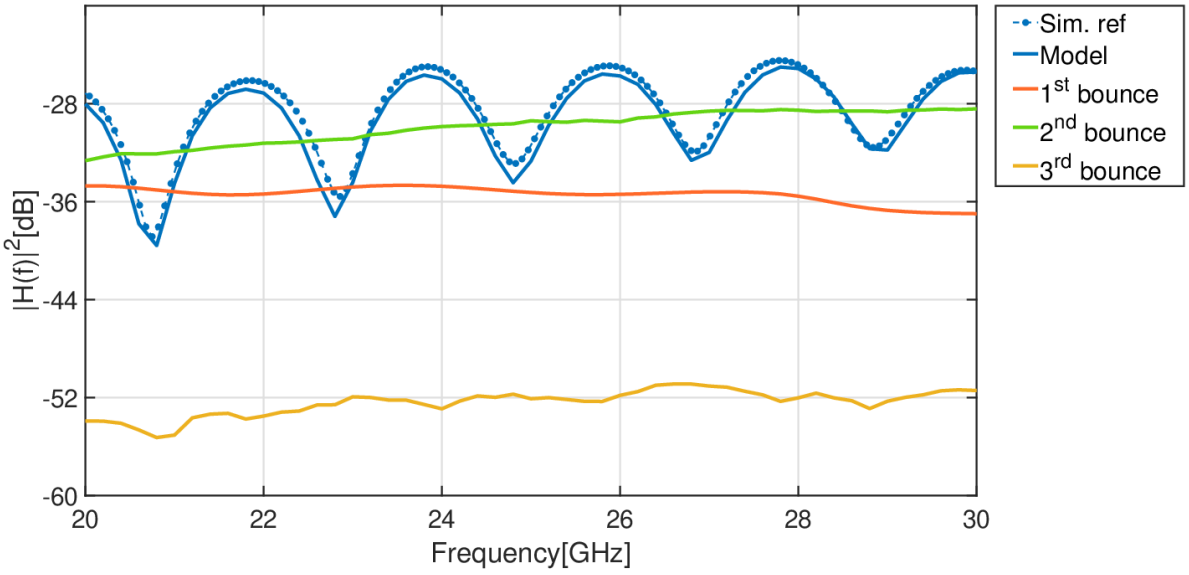

(b)

Figure 4.8: (a) Geometry of the scenario (b) Transfer function of the plate answer according to the number of bounces: Horn antenna

4.2.3.3 Implementation in a complex scenario

To verify the capability of the model, its implementation on an open cavity (open box) will be detailed. First, dipole antennas are placed 10 cm from the open box; these are the same antennas used in the previous section. First, the meshing shown in Fig. 4.9 **(a)** is examined. The thickness of the cube's walls is approximately 0.5 mm, and the meshes on the two faces are independent. The figure illustrates the different mesh sizes used. On the face at $y = 5cm$, the initial meshing is displayed. Since there is no complex angle or geometry involved, this meshing is used for shadowing and illumination calculations. On the face at $x = 5$ cm, the surface is illuminated by only one antenna. The surfaces are then meshed to satisfy far field conditions. However, these surfaces relate solely to the transmitting antenna and therefore do not require meshing. Inside the cube, the mesh size depends on the distance to the closest related surface. As the mesh approaches an edge, the element size becomes very small, which can cause

computational issues. To achieve a good approximation, the distance is measured from the center of the initial surface, not from the sub-surface itself.In this example, the meshing and illumination are not time-consuming because the surfaces used are relatively large. The computation time is around 2 to 3 seconds. Once the meshing and illumination are defined, the currents are calculated on the sub-surfaces. For this example, PPO could have been used to speed up the model. The currents are calculated for 7 bounces. In order to define the number of bounces, the ending of the iterative process is generated using the mean of the currents. When the mean current at the k iterative is small enough the process stops. To determine the number of bounces, the iterative process is stopped based on the mean current on the sub-surface. When the mean current at iteration k becomes sufficiently small, the process terminates. This criterion is calculated by comparing the current at iteration k to the sum of the currents from all previous iterations. In this example, the criterion led to six bounce iterations; however, to verify its adequacy, a seventh iteration was also performed. The results shown in Fig. 4.9**(b)** demonstrate good agreement between the model and the simulation. To verify the model's capabilities, the results were plotted for each bounce individually. To minimize the first-bounce response which is the simplest to model the antennas were positioned to reduce the single-bounce contribution by eliminating the direct reflection from the bottom of the box. When comparing the model to the reference simulation, the overall shape of the response is similar; however, the interference patterns, visible as notches in the response, are less pronounced in our model. In the model, the response is mainly composed of the second, fourth, and first bounces. The antennas are positioned to align the center of the antenna, the top edge, and the center of the bottom plate. The first bounce is primarily due to diffraction at the edges and from the left and right walls. The second bounce mainly arises from scattering off the walls and bottom, linked to the edges and the bottom plate. The edge diffraction model was tested with two setups: first, considering the edge angle as 90° while accounting for the wall thickness; and second, using an angle of 360° while neglecting the wall thickness. The results were similar and close, which neither validates nor invalidates either model. The third bounce response was smaller than expected, but a closer analysis of the geometry showed that the antenna positioning did not include the triple reflection path (opposite wall/bottom/close wall). The fourth bounce accounts for a significant portion of the response. After the fourth bounce, the response diminishes significantly, and the sixth and seventh bounces confirm the iterative process, indicating that the currents are sufficiently small to be neglected.

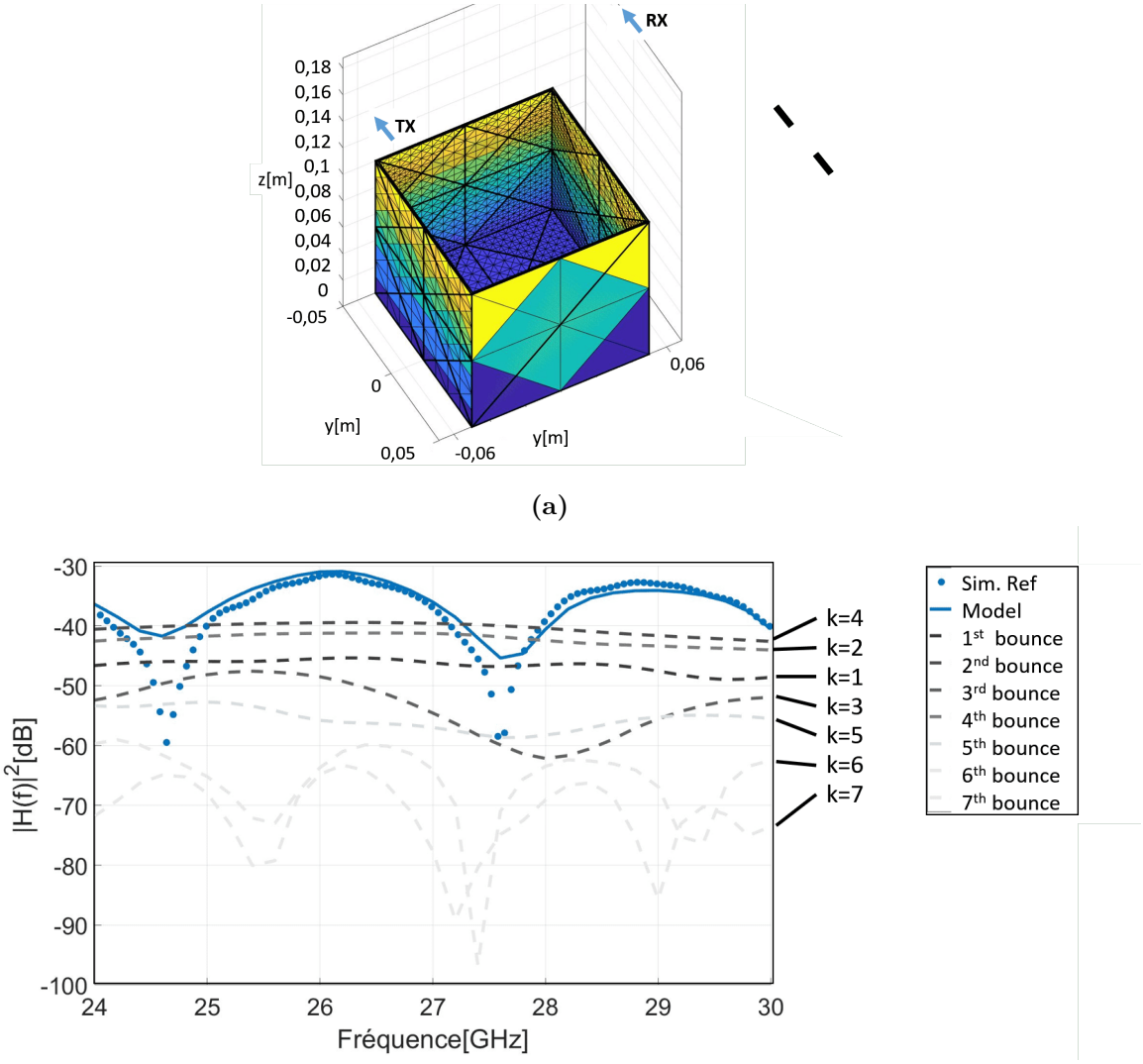

Figure 4.9: (a) Geometry of the scenario (b) Transfer function of the box response as a function of the number of bounces

4.3 Measurement validation

4.3.1 Measurement setup

Now that the model has been validated through simulations, an experimental validation should be conducted to verify its real-world accuracy. To do this, the validation will be performed on targets placed inside an anechoic chamber. Measuring in the near field is more challenging than in the far field, mainly due to the precision required for an accurate interference model. In [52], the measurement results show that, even with a well-performing model, good agreement is not achieved due to limited measurement precision.

4.3.1.1 Measurement setup presentation

The model validation setup is presented in Fig. 4.10. This image shows the experimental configuration used for near field radar measurements inside an anechoic chamber at CEA-LETI. A pair of horn antennas (Tx/Rx), each with a gain of 10 dBi and operating in the $22 - 33$ GHz frequency band, are mounted on a mechanical positioner allowing precise movements along the $\boldsymbol{y}$ and $\boldsymbol{z}$-axes. These antennas are directed toward a metallic target mounted on a polystyrene support, which itself is placed on a motorized positioner enabling translation along the $\boldsymbol{x}$ axis and rotation around the $\boldsymbol{z}$-axis. The use of polystyrene minimizes unwanted scattering from the support structure.

The target and antennas are carefully aligned to ensure accurate characterization of the radar scattering response. For proper alignment, the two positioners (antenna and target) are precisely coordinated. The antennas are mounted on a plastic support and spaced 8 cm apart to reduce mutual coupling. The target is positioned at the rotation center to allow rotation around its center while maintaining a fixed position relative to the antennas. Because the antennas operate in the near field, the setup requires careful handling to maintain precision.

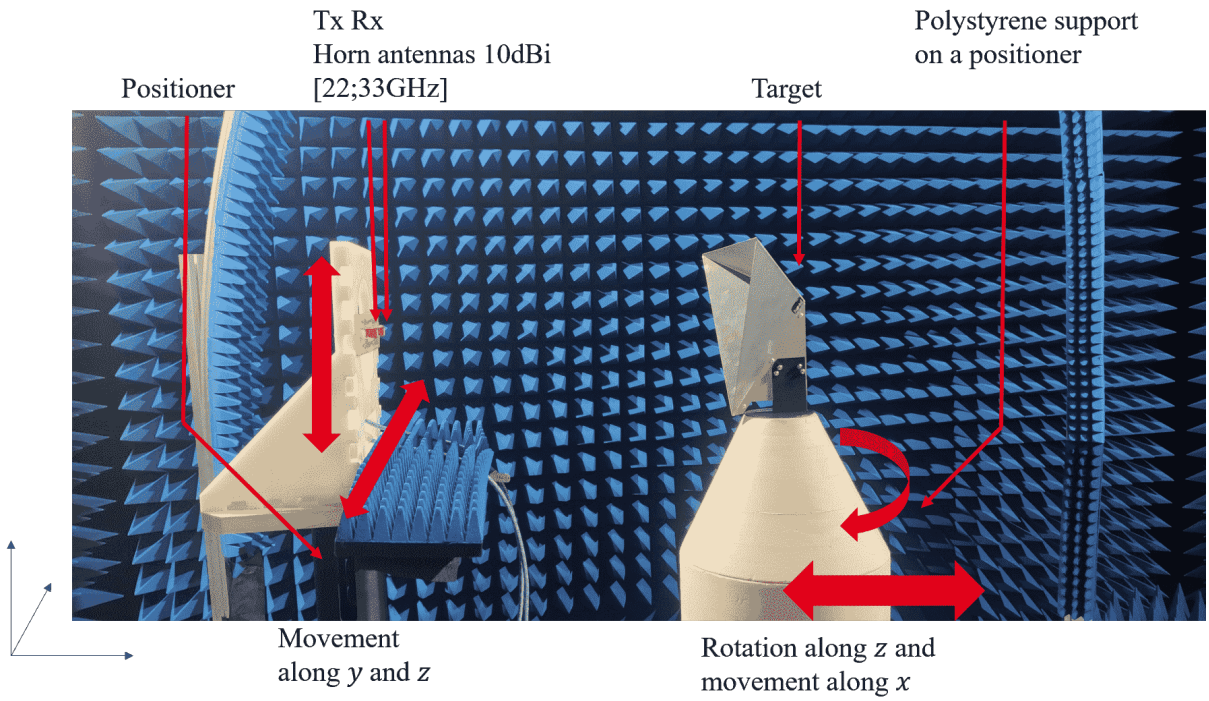

Figure 4.10: Measurement setup: antenna and target placement using positioners

4.3.1.2 Alignment of the setup for high precision measurement

Positioning done by eye provides a reasonably good alignment, but to reduce the model error sufficiently low (< 0.5 dB), laser measurement is necessary. The alignment procedure starts by placing a green cross laser at the position where the antennas will be. The laser is carefully positioned at the center of the target to ensure that the experimental setup accurately corresponds to the modeled geometry. This

step allows precise rotation alignment of the antenna support. Next, the laser is placed on the target position, which is then rotated to ensure it illuminates the center of the antenna support. It is important to note that vertical alignment is performed twice during this process: first by aligning to the center of the target, and second by aligning with the center of the antennas.

The laser alignment setup is shown in Fig. 4.11. After completing the alignment, the distance between the target and the antennas is precisely set using the positioners and a laser rangefinder. During the measurement, the weight of the components on the positioner caused a slight tilt of more than 0.5°from the horizontal axis. This was corrected by placing shims under the positioner to level it properly. To verify the accuracy of the setup, a final check is performed by rotating the target around the **z**-axis in both clockwise and counterclockwise directions. The expected result is that, for example, the measured response of a flat plate should remain exactly the same for both rotation directions, confirming proper alignment and setup stability.

Measurements shown in Fig. 4.12 present the RTF of the target for rotation angles of $-3°, -2°, -1°, 0°, 1°, 2°, 3°$ in part **(a)** It should be noted that the results are very close to each other. For the initial measurements performed during the thesis, the alignment was limited to the described procedure, but small rotations of a few degrees could still occur. To improve the alignment accuracy on the test bench, the alignment is performed not at 0° but rather around 20°. At distances of 50 cm or 1 m, the scattering response varies significantly with angle.

From 0° to 15°, the scattering is strong since the receiver is positioned close to the specular reflection direction. Between 15° and 25°, the scattering evolves rapidly due to diffraction and scattering from various parts of the plate. Beyond 25° to 40°, the response is dominated primarily by diffraction effects, and the overall variation in scattering becomes much weaker.

The optimal angular range for alignment is between 15° and 25°. In Fig.4.12**(b)** the alignment is done at $19°, 20°$ and 21°. In this case, there is approximately a 2 dB difference in the scattering response between each degree of rotation. This sensitivity makes the angular gap a useful metric for precise model alignment. Even a small misalignment of about 0.5°, which might not be detectable through laser positioning can cause significant discrepancies in the measurements and model results: The 20° and $-20°$ responses will be uncorrelated. In the example shown, the measurements for the three degrees of rotation produce consistent results for both positive and negative directions. The measurement alignment results in an error below 0.5 dB between the two rotation directions. For all targets considered symmetric (imperfections on the target are not taken into account), the positioning will be performed following this procedure. To accurately account for the exact distance, time-domain measurements of the S_{21} parameter can be used for distance validation. The cable calibration is a limitation of this method. During cable calibration, a connector is used between the cable for TX and the cable for RX. This connector is removed when the cables are connected to antennas. This connector limits the precision in the time-domain.

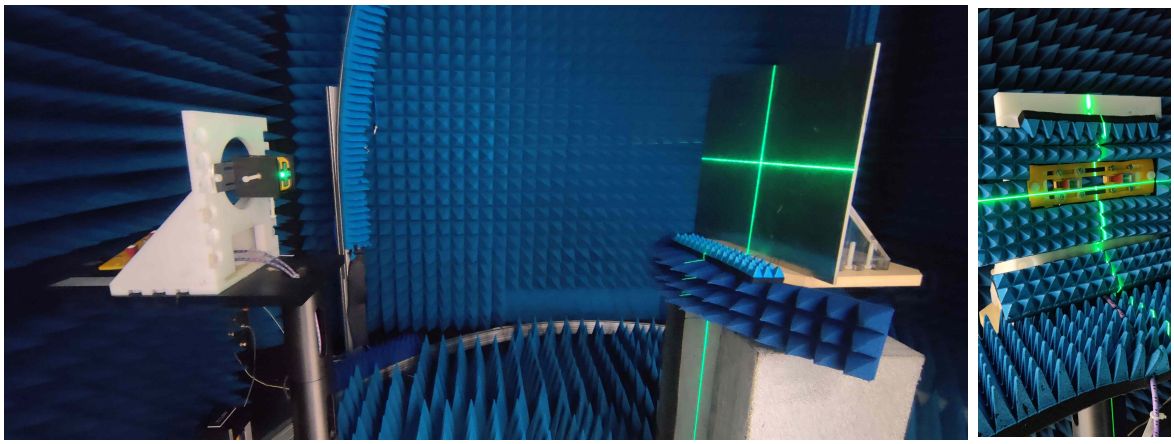

(a) **(b)**

Figure 4.11: (a) Alignment with the center of the target, (b) alignment with the center of the antennas

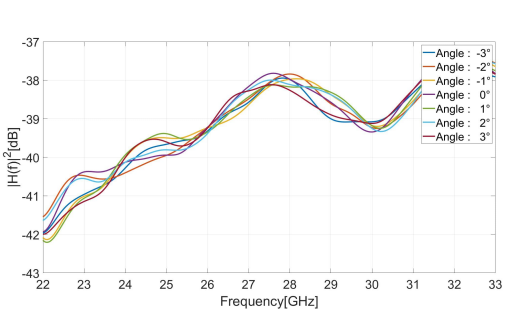

(a)

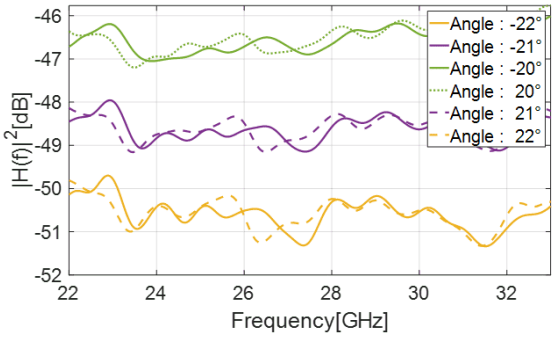

(b)

Figure 4.12: Round trip transfer function according to the rotation (**a**) close to the specular direction scattering (**b**) rotation of 20° from the specular direction

4.3.1.3 Processing chain

When measuring with a Vector Network Analyzer (VNA), the transfer function can be decomposed into several components. To accurately extract the round-trip transfer function from the measured transfer function, it is necessary to remove several additional contributions.

1. The response of the anechoic chamber
2. The response of the polystyrene which supports the target
3. The response of the interaction between the target and the other elements (support, anechoic chamber, antenna support, ...)

To eliminate the influence of the anechoic chamber and the polystyrene support, an empty measurement denoted as $\mathcal{H}_{Empty}$ is performed. Starting from the calibrated measurement $\mathcal{H}_{meas}$, the response associated with the target alone is obtained by removing the empty measurement contribution:

$$\mathcal{H}_{target}(f) = \mathcal{H}_{meas}(f) - \mathcal{H}_{Empty}(f) \tag{4.16}$$

The response $\mathcal{H}_{target}(f)$ accounts for the target's response as well as its interactions with other elements. To isolate all interactions related to the target, except those involving the support, an inverse Fourier transform is applied to convert the signal into the time domain. Before performing the inverse Fourier transform, a raised cosine window is applied to reduce spectral leakage.
In the time-domain response $h_{target}(\tau)$ the $h_{rt}(\tau)$ can be extracted by applying a time window. In $h_{target}(\tau)$, there is the round-trip response but also the interaction between the target and the element of the anechoic chamber. Since the walls of the anechoic chamber and other elements are sufficiently distant, the response $TX \rightarrow Target \rightarrow Other\ elements \rightarrow RX$ can be accurately separated from the response $TX \rightarrow Target \rightarrow RX$ by using a time gating. The only interaction that cannot be fully isolated is the $TX \rightarrow Target \rightarrow support \rightarrow RX$ interaction. To minimize this effect, the support is made of low-reflection polystyrene and shaped to reduce unwanted reflections from its surfaces. From $h_{rt}(\tau)$, the $\mathcal{H}_{rt}(f)$ is obtain by doing an inverse Fourier transform.

4.3.2 Measurement results

4.3.2.1 Validation on a metallic plate

Firstly, to verify and validate the measurement setup, a metallic plate was measured. The target is modeled as a PEC plate, which is not perfectly square. The measured plate dimensions were 38 $cm \times$ 37.5 cm. The edges of the target were sharpened, and a small size difference of only 0.5 cm significantly affected the response. Initially, the target was assumed to be a perfect 38 $cm \times 38$ cm square, but this led to discrepancies with the expected results. Such small details must be taken into account to ensure accurate measurements that align with the model.
Measurements were performed for azimuthal angles ranging from 0° to 35°. As shown in Fig. 4.13 **(b)**, the target model and the measurements exhibit similar results. The RTF shows a difference of less than 1 dB for small angles and less than 2 dB for rotation angles above 20°.
In the model, the rotation is not performed around the center of the plate. As visible in Fig. 4.13 **(a)**, the plate is placed near the edge of the support, while the rotation axis corresponds to the center of the support.

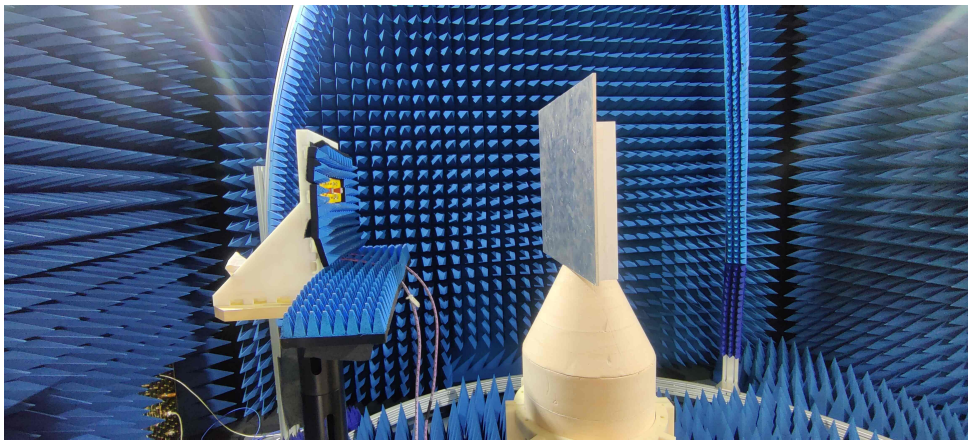

(a)

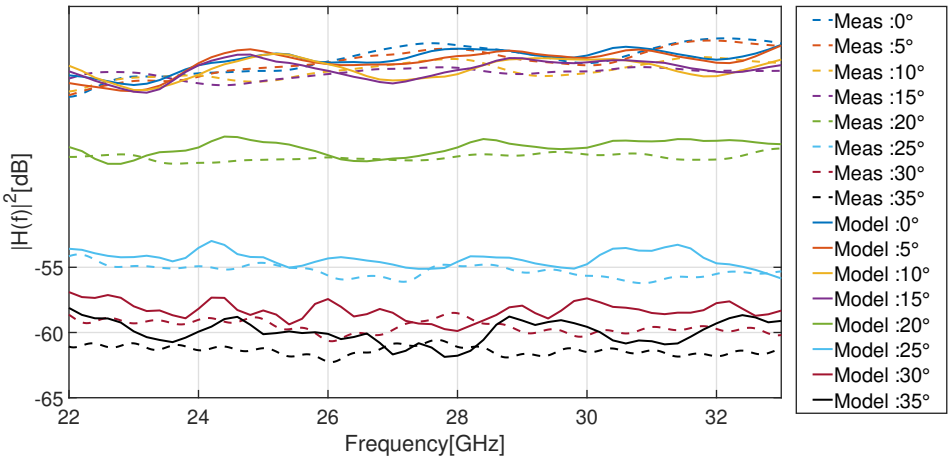

(b)

Figure 4.13: (a) Plate: measurement setup (b): results of the backscattering in the near field for different azimuthal angles $0° \rightarrow 35°$

4.3.2.2 Validation on a sphere

In order to validate the curved criterion and to test the model on a spherical target, a metallic sphere was tested. It is assumed to be a PEC (perfect electric conductor). To validate the placement of the target, three measurements are performed at 120° intervals, yielding consistent results. This setup corresponds to the support, which has three branches spaced by 120° from each other. Once the position is determined, measurements are conducted at distances ranging from 50 cm to 1.3 m. In this case, the sphere is relatively small, and the far field distance is approximately 2 m.

The measurements are presented in Fig. 4.14. The results demonstrate good agreement across multiple distances, validating the accuracy of the electromagnetic model. The difference between the model and the measurements could be linked to creeping waves. For spheres, creeping waves are particularly significant at high frequencies, where the curvature supports efficient surface-guided propagation. These waves are not captured by the model. According to Mie theory, for a sphere in the optical regime, the contribution of creeping waves is expected to be small.

Another aspect not included in the model is the plastic support in front of the target. Although the support is removed during pre-measurements, the interaction between the target and the support may be strong enough to contribute to the discrepancy between the model and the measurements. For all distances tested, the discrepancy appears consistent and does not seem to depend on the near field criterion.

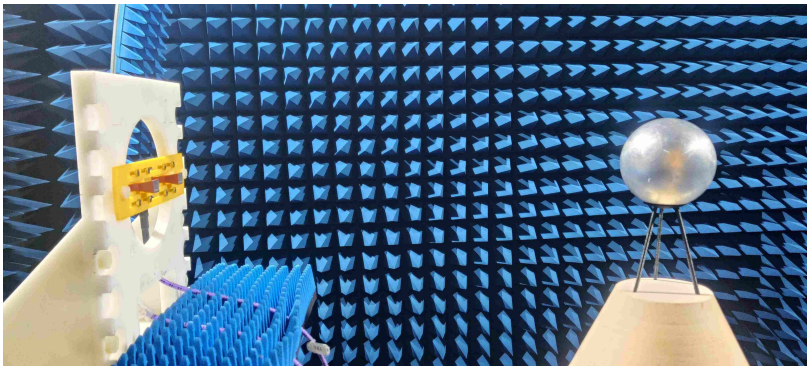

(a)

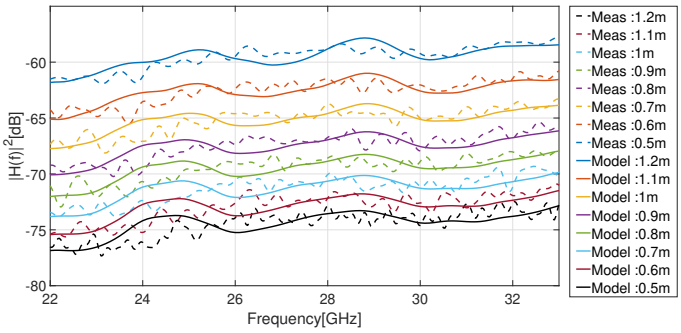

(b)

Figure 4.14: (a) Sphere: measurement setup (b): Results of the backscattering in the near field for different distances $1.2m \rightarrow 0.5m$

4.3.2.3 Validation on a metallic trihedron

For a more complex target, a metallic trihedral model was modeled as a PEC. Some adjustments needed to be made. Firstly, the trihedral support exhibited mechanical looseness in the screws, which made the alignment of the trihedral more difficult to define. The results for the trihedral are shown in Fig. 4.15 for three different azimuthal angles: 0°, 15°, and 30°. The three responses show agreement within approximately 1 dB and exhibit similar trends. The three different responses show an agreement around 1 dB with a similar evolution.

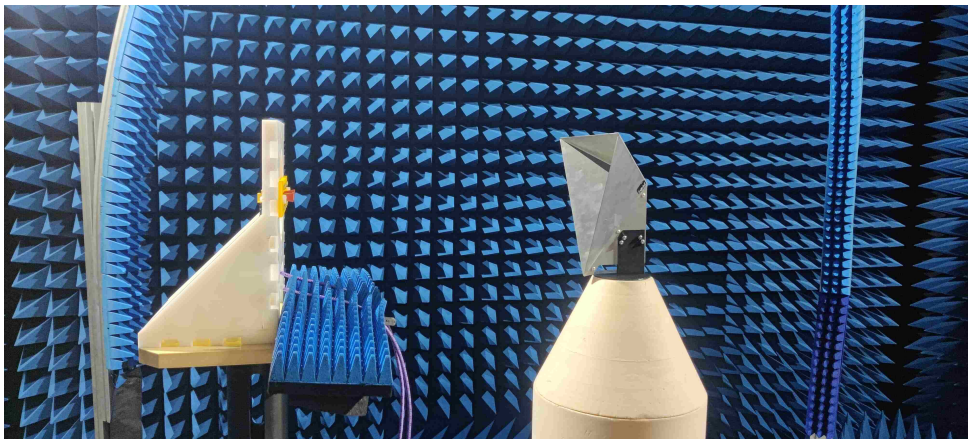

(a)

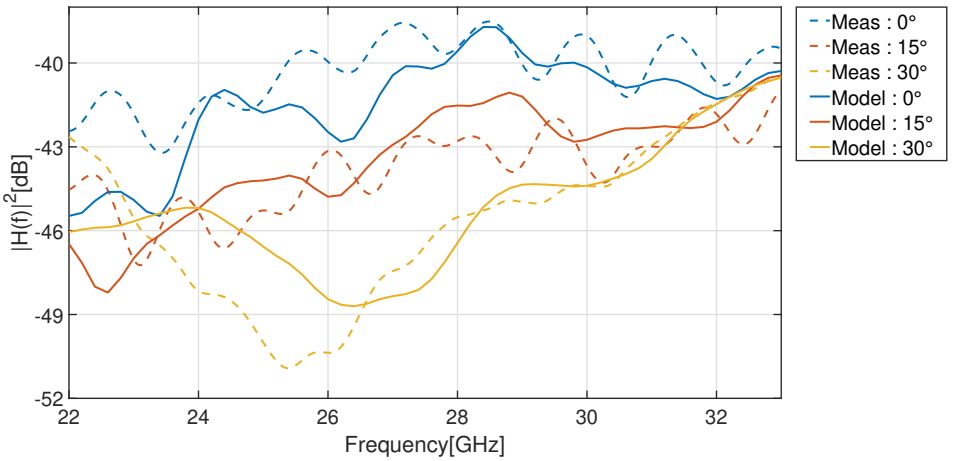

(b)

Figure 4.15: (a) Trihedron: measurement setup (b): Results of the backscattering in the near field for different angles $0° \rightarrow 30°$

4.4 Conclusion

This chapter has presented a comprehensive modeling approach for the RTF instead of the NF-RCS. Using RTF is easier because it can be extracted from measurements of realistic targets. Using the RTF requires particular attention to antenna integration. The model incorporates antennas through their complex far field characteristics.

The antenna integration is presented for two types of antennas: a dipole and a horn antenna. The dipole has the advantage of being easily simulated as a radiating point. For the horn antenna, the description of the antenna as a point radiator is not enough. The antenna's radiation properties must be explicitly included in the model.

In order to perform measurements to validate the model, precise positioning is done. The alignment is done using positioners, a 2-plane laser for precise angles, and a laser rangefinder. To properly perform the positioning of the elements, measurements were done with a rotation around $20°$ and $-20°$ for symmetric targets.

Experimental validation in an anechoic chamber further confirmed the model's robustness, with measured RTFs showing agreement within 1 dB across a range of angles and distances for targets such as the sphere, plate, and trihedral reflector. The careful antenna-target alignment and calibration procedures were key factors in reaching this level of precision.

Chapter 5

Modeling Wave Propagation in Dielectric and Lossy Targets: Validation and Application to Human Body Backscattering

5.1 Introduction

This chapter presents improvements to the model that take into account dielectric and lossy materials. Unlike in the previous chapter, the target here is not composed solely of PEC. In such cases, part of the wave propagates inside the target. The goal of this chapter is to account for this propagation, i.e., to accurately model both the reflections on the external surfaces and the wave penetration inside the target.

To achieve this, several models are tested with the objective of accurately predicting the response of the target. These models are validated on simple shapes, both in simulations and in measurements, particularly in scenarios far from the specular direction. A concrete application of the model is then presented through the study of the backscattering from a human body, including measurements performed on a mannequin torso.

5.2 Model application for dielectric and lossy media

5.2.1 Adaptation of the IPO model

Initially used to analyze the backscattering from PEC targets, the IPO method has been extended to lossy surfaces through the incorporation of Impedance Boundary Conditions (IBC) [53]. Several other methods

have been developed to accurately account for material properties in the IPO method, such as Modified Theory of Physical Optics (MTPO) [54] for impedance surfaces. For dielectric targets, two approaches have been proposed based on Fresnel coefficients: Modified Equivalent Current Approximation (MECA) [55] and Modified Physical Optics Approximation (MPOA) [56].

This section aims to present the IPO techniques for dielectric and lossy media and to analyze their results and capabilities. First, the models are introduced, followed by their implementation within the near field IPO framework.

Impedance Boundary Condition The impedance surface boundary condition states that the relationship between the tangential electric and magnetic fields is governed by the surface impedance. This impedance depends solely on the material's properties and configuration and remains independent of the characteristics of the incident wave. This theory stems from the mutual orthogonality of the electric and magnetic fields, which are related through the intrinsic impedance of the homogeneous medium in which they propagate:

$$\mathbf{E} = \eta \, \hat{\boldsymbol{k}} \times \mathbf{H} \tag{5.1}$$

where η is the intrinsic impedance. Leontovich boundary condition [25] also called the impedance surface boundary condition is written as:

$$\mathbf{E} - (\hat{\mathbf{n}} \cdot \mathbf{E})\hat{\mathbf{n}} = \eta_S \hat{\mathbf{n}} \times \mathbf{H} \tag{5.2}$$

where η_S is the surface impedance and $\hat{\mathbf{n}}$ the normal vector to the surface. In the non-PEC case, both electric and magnetic surface currents, respectively $\mathbf{J}$ and $\mathbf{M}$ are required. They are expressed as:

$$\begin{aligned} \mathbf{J} &= 2\hat{\mathbf{n}} \times \mathbf{H_{inc}} \\ \mathbf{M} &= -\eta_S \hat{\mathbf{n}} \times \mathbf{J} \end{aligned} \tag{5.3}$$

where $\mathbf{H}_{inc}$ is for the magnetic incident field. However, this method is limited to the cases described by Senior [57] and, more particularly, by Wang [58] in the context of penetrable surfaces. The theory is formulated for lossy media, characterized by a complex refractive index n_2 that must satisfy the following condition:

$$|n_2| = \sqrt{\frac{\mu_2}{\mu_1}\left(\frac{\varepsilon_2}{\varepsilon_1} + j\frac{\sigma_2}{\omega\epsilon_1}\right)} \gg 1 \tag{5.4}$$

where ε_2 is the permittivity of the target, σ_2 the conductivity, and μ_2 the permeability of the material and likewise for free space with the $_1$ index. This condition is satisfied by materials with high dielectric constants or high conductivity. It has been widely used to simulate the RCS of coated PEC targets, where the surface impedance depends on the thickness and properties of the coating material.

Modified theory of physical optics Similarly, the MTPO is a method based on axioms that has been extended to impedance surfaces. This method aims to represent the pseudo-impedance boundary by introducing a new vector, $\hat{\mathbf{n}}_\perp$, which replaces the surface normal vector $\hat{\mathbf{n}}$, and is defined in terms of the incidence and scattering directions. This new vector implies that the equivalent currents are not

confined to the original surface, but rather lie in the plane perpendicular to $\hat{\mathbf{n}}_\perp$. The equivalent currents can be defined as:

$$\mathbf{J} = \hat{\mathbf{n}}_\perp \times \mathbf{H}, \quad \mathbf{M} = -\hat{\mathbf{n}}_\perp \times \mathbf{E}$$

Where:

$$\hat{\mathbf{n}}_\perp = \cos(u + \phi_1)\hat{\mathbf{u}}_1 + \sin(u + \phi_1)\hat{\mathbf{u}}_2 \tag{5.5}$$

and $u = (\pi - \phi_1 - \beta)/2$ and $\hat{\mathbf{u}}_1$ is the projection of the incident ray on the surface and $\hat{\mathbf{u}}_2 = \hat{\mathbf{n}}$. ϕ_1 denotes the incident angle and β is the scattered angle. The pseudo impedance boundary condition on an impedance surface can be expressed with vector $\hat{\mathbf{n}}_\perp$ and the currents can be defined as:

$$\begin{aligned} \mathbf{J} &= \frac{2\eta_1 \cos(u)}{\eta_2 \cos(u) + \eta_1} \hat{\mathbf{n}}_\perp \times \mathbf{H}_{inc} \\ \mathbf{M} &= \frac{2\eta_1 \cos(u)}{\eta_2 \cos(u) + \eta_1} \hat{\mathbf{n}}_\perp \times \mathbf{E}_{inc} \end{aligned} \tag{5.6}$$

It can be shown that these estimated currents do not satisfy the Helmholtz equation in the bistatic case [59].

Modified Equivalent Current Approximation

In the MECA formulation, the incident fields are decomposed into their components parallel and perpendicular to the surface:

$$\begin{aligned} \mathbf{E}_{inc} &= E^{\parallel}_{inc}\hat{\mathbf{e}}^{\parallel} + E^{\perp}_{inc}\hat{\mathbf{e}}^{\perp} \\ \mathbf{H}_{inc} &= H^{\parallel}_{inc}\hat{\mathbf{e}}^{\perp} + H^{\perp}_{inc}\hat{\mathbf{e}}^{\parallel} \end{aligned} \tag{5.7}$$

With $\hat{\mathbf{e}}_{\parallel,\perp}$ denoting the unit vectors corresponding to the incident polarization components, Fig. 5.1 illustrates the geometry of the model. By considering this decomposition, the reflected fields $\mathbf{E}_{\text{ref}}$ and $\mathbf{H}_{\text{ref}}$ are computed using the Fresnel reflection coefficients $\Gamma_\parallel$ and $\Gamma_\perp$ as follows:

$$\begin{aligned} \mathbf{E_{ref}} &= \Gamma_\parallel E^{\parallel}_{inc}\hat{\mathbf{e}}^{\parallel} + \Gamma_\perp E^{\perp}_{inc}\hat{\mathbf{e}}^{\perp} \\ \mathbf{H_{ref}} &= \Gamma_\parallel H^{\parallel}_{inc}\hat{\mathbf{e}}^{\perp} + \Gamma_\perp H^{\perp}_{inc}\hat{\mathbf{e}}^{\parallel} \end{aligned} \tag{5.8}$$

Where the Fresnel coefficients expressed as:

$$\begin{aligned} \Gamma_\parallel &= \frac{\eta_2 \cos(\theta_{inc}) - \eta_1 \cos(\theta_{tra})}{\eta_2 \cos(\theta_{inc}) + \eta_1 \cos(\theta_{tra})} \\ \Gamma_\perp &= \frac{\eta_2 \cos(\theta_{tra}) - \eta_1 \cos(\theta_{inc})}{\eta_2 \cos(\theta_{tra}) + \eta_1 \cos(\theta_{inc})} \end{aligned} \tag{5.9}$$

with η_2 the impedance of the medium:

$$\eta_2 = \sqrt{\frac{\mu_2}{\varepsilon_2 - j\sigma_2/\omega}} \tag{5.10}$$

It is possible to approximate the total field on the upper face as the sum of the incident and reflected fields. Consequently, using the Fresnel coefficients in equation 5.9, the currents used in the MFIE are

expressed in terms of the incident field [55] as:

$$\begin{aligned}\mathbf{J} &= \frac{1}{\eta_1}\left(\left(1-\Gamma_\perp\right)E^\perp_{inc}\left(\hat{\mathbf{n}}\times\hat{\mathbf{e}}_\parallel\right)\right.\\ &\qquad\left.+\left(1-\Gamma_\parallel\right)E^\parallel_{inc}\cos(\theta_{inc})\hat{\mathbf{e}}_\parallel\right)\\ \mathbf{M} &= \left(\left(1+\Gamma_\perp\right)E^\parallel_{inc}\left(-\hat{\mathbf{n}}\times\hat{\mathbf{e}}_\parallel\right)\right.\\ &\qquad\left.+\left(1+\Gamma_\parallel\right)E^\perp_{inc}\cos(\theta_{inc})\hat{\mathbf{e}}_\parallel\right)\end{aligned} \tag{5.11}$$

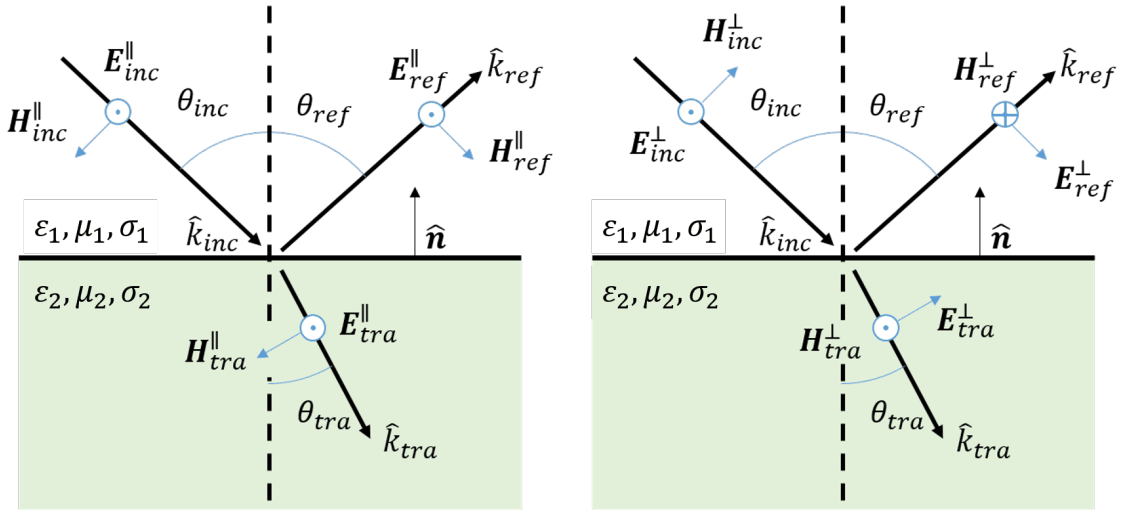

Figure 5.1: Modified Equivalent Current Approximation geometry, parallel and perpendicular components

Modified physical optics approximation

For the MPOA algorithm, the approximate distributed currents outside the target are defined from the reflected fields and are used to represent the scattered field. However, these currents may not accurately represent the actual currents that scatter outside the target. As discussed in [24], the current expressions cannot be straightforwardly defined for non-PEC surfaces. An alternative approach to establish equivalent currents is to utilize boundary conditions and image theory for large bodies. Starting from the reflected fields $\mathbf{H}_{\text{ref}}$ and $\mathbf{E}_{\text{ref}}$, as well as the transmitted fields $\mathbf{H}_{\text{tra}}$ and $\mathbf{E}_{\text{tra}}$, the induced currents $\mathbf{J}_{\text{ind}}$ and $\mathbf{M}_{\text{ind}}$ on the surface are given by:

$$\begin{aligned}\mathbf{J_{ind}} &= \hat{\mathbf{n}}\times(\mathbf{H_{ref}}-\mathbf{H_{tra}})\\ \mathbf{M_{ind}} &= -\hat{\mathbf{n}}\times(\mathbf{E_{ref}}-\mathbf{E_{tra}})\end{aligned} \tag{5.12}$$

As the transmitted fields are not taken into account, with Love's principle they can be set to zero [24]. Using equation 5.8, incident currents are rewritten as:

$$\begin{aligned}\mathbf{J_{ind}} &= \hat{\mathbf{n}}\times(\mathbf{H_{ref}}) = \hat{n}\times(\Gamma_\parallel H^\parallel_{inc}\hat{\mathbf{e}}^\perp+\Gamma_\perp H^\perp_{inc}\hat{\mathbf{e}}^\parallel)\\ \mathbf{M_{ind}} &= -\hat{\mathbf{n}}\times(\mathbf{E_{ref}}) = \hat{n}\times(\Gamma_\parallel E^\parallel_{inc}\hat{\mathbf{e}}^\perp+\Gamma_\perp E^\perp_{inc}\hat{\mathbf{e}}^\parallel)\end{aligned} \tag{5.13}$$

In this case, since no transmitted fields are considered, the equivalence principle can be applied as in the classical PO formulation, assuming a non-penetrable target [24]. The equivalent currents on the surface are equal to:

$$\begin{aligned}\mathbf{J} &= \frac{1}{\eta_1}\left(-2\Gamma_\perp E^\perp_{inc}\left(\hat{\mathbf{n}}\times\hat{\mathbf{e}}_\parallel\right) - 2\Gamma_\parallel E^\parallel_{inc}\cos(\theta_{inc})\hat{\mathbf{e}}_\parallel\right)\\ \mathbf{M} &= 0\end{aligned} \tag{5.14}$$

With this approximation, the magnetic current is always zero. This can potentially lead to an incomplete understanding and inaccurate predictions in scenarios where magnetic interactions play a key role.

5.2.2 Equivalent Edge Current adaptation

In order to adapt the EEC model to lossy or dielectric materials, a method similar to that used for IPO formulation can be applied based on the previous model. First, let us analyze the problem by separating the EEC components. When examining the equation used for the EEC, equation 2.53 depends only on the electric current. Defining both the electric and magnetic currents would make equation 2.59 significantly more complex, as the PO term would depend on both currents. A first approximation is to focus solely on one current by employing a method similar to MPOA. In fact, this approach relies only on a single current, which means that equation 2.59 remains applicable. For the calculation of the fringe current, nothing changes except that the current is replaced by the equivalent current. Instead of using the incident field directly, the incident field is replaced by the incident field multiplied by the Fresnel coefficients, as done in MPOA:

$$\mathbf{E}_{inc} \rightarrow \Gamma_\perp \mathbf{E}^\perp_{inc} + \Gamma_\parallel \mathbf{E}^\parallel_{inc} \tag{5.15}$$

The Fresnel coefficients depend on the angle of incidence, which means that for the fringe currents, the Fresnel coefficients should be defined differently. To calculate the Fresnel coefficients, the orientation of the two plates is used to define the currents. This means that the substitution is as follows:

$$\mathbf{E}_{inc} \rightarrow \begin{cases}\Gamma^1_\perp \mathbf{E}^\perp_{inc} + \Gamma^1_\parallel \mathbf{E}^\parallel_{inc}, & \text{for surface 1}\\ \Gamma^2_\perp \mathbf{E}^\perp_{inc} + \Gamma^2_\parallel \mathbf{E}^\parallel_{inc}, & \text{for surface 2}\end{cases} \tag{5.16}$$

For the PO currents linked to edge diffraction, the same modification is applied to the incident current. The combination of both currents will exhibit similar singularities and behaviors as the currents defined for the EEC model presented in Chapter 3. However, one point remains unresolved: when one of the two faces is not illuminated. In this case, for the currents linked to Physical Optics, no calculations are needed, but for the fringe currents, the term must still be evaluated. Under these conditions, the current definition can be modified and defined as follows:

1. Do not change the coefficient of the incident field for the fringe current. This method should work in most cases, but some singularities that are removed for PEC surfaces may appear.

2. Define the incident field using only the Fresnel coefficient of the second face. This means that for both surfaces, a common coefficient will be used. This method works and no singularities will appear.

3. Define the incident field using the Fresnel coefficient of the second face only in cases where the plate is not illuminated. This method is the easiest to implement and will not cause singularities.

The third method appears to yield the best results, although the approximations made are less precise than those for PEC surfaces. The new current definition is used only for edge diffraction within the same medium as the incident wave, whether outside or inside the target. To model the scattered wave inside the target, the same approach as in MPOA for penetration can be applied. The incident field is replaced by an incident field mirrored across the surface inside the target, which leads to the same current. So far, only the application for outside radiation has been implemented in the model. As mentioned in Chapter 3, the EEC is used only for the first and last bounces of the iterative process.

5.2.3 Implementation in the model

In order to implement these currents into the model, the model needs to be modified to facilitate their incorporation. For the IBC, the model does not account for penetration inside the target. This means that the implementation of this method is essentially the same as for the standard IPO, and the size of the sub-surfaces does not depend on the internal parameters.
However, for the MECA theory, the model requires changes. First, it becomes possible for radiation to occur inside the target, which necessitates several modifications. When measuring shadowing, surfaces now radiate on both sides, leading to longer computation times due to increased interactions. Additionally, the size of the sub-surfaces varies: according to the far-field criterion, their size depends not only on the distance to other sub-surfaces but also on the material through which the wave propagates, as defined by:

$$D = \min\left(\sqrt{\frac{R\lambda}{2}}\right)$$

Another important point concerns the magnetic current. The formulas used are:

$$\begin{aligned}\mathbf{H}_{scat}^{(k,m)} = \iint_s \Bigg[& -\frac{(jkR_r+1)}{R_r}\left(\mathbf{J}^{(\mathbf{k},\mathbf{m})} \times \hat{\mathbf{R}}_r\right) \\ & + \frac{1}{\eta_1}\frac{-1-jkR_r+(kR_r)^2}{jkR_r^2}\left(\mathbf{M}^{(\mathbf{k},\mathbf{m})}\right) \\ & + \frac{1}{\eta_1}\frac{-3-j3kR_r+(kR_r)^2}{jkR_r^2}\left(\mathbf{M}^{(\mathbf{k},\mathbf{m})} \cdot \hat{\mathbf{R}}_r\right)\hat{\mathbf{R}}_r\Bigg] \\ & \frac{e^{-jk(R_r)}}{4\pi R_r} dS\end{aligned} \tag{5.17}$$

And analogously for the electric field:

$$\begin{aligned}\mathbf{E}_{scat}^{(k,m)} = \iint_s \Bigg[& -\frac{(jkR_r+1)}{R_r}\left(\mathbf{M}^{(\mathbf{k},\mathbf{m})} \times \hat{\mathbf{R}}_r\right) \\ & +\eta_1 \frac{-1-jkR_r+(kR_r)^2}{jkR_r^2}\left(\mathbf{J}^{(\mathbf{k},\mathbf{m})}\right) \\ & +\eta_1 \frac{-3-j3kR_r+(kR_r)^2}{jkR_r^2}\left(\mathbf{J}^{(\mathbf{k},\mathbf{m})} \cdot \hat{\mathbf{R}}_r\right)\hat{\mathbf{R}}_r \Bigg] \\ & \frac{e^{-jk(R_r)}}{4\pi R_r} dS\end{aligned} \tag{5.18}$$

The integration is performed exactly as presented in the previous chapter. This means that the current calculation requires twice the computational effort compared to IPO, since both electric and magnetic currents are evaluated.

For the MPOA model, the implementation differs from the previous methods. On the same surface, two currents are defined: one on the upper face and one on the lower face. Each current radiates only into its respective material, and the sub-surface sizes on the two faces can differ. Defining different sub-surface sizes may introduce complications, as it effectively doubles the number of surfaces compared to using the same size. Both faces share the same incident fields $\mathbf{E}_{\text{inc}}$ and $\mathbf{H}_{\text{inc}}$ but the currents must be computed separately for each face. For the MTPO, the implementation within the IPO framework is considerably more complex. The currents now depend on both the incident and scattering directions, which implies that the computational complexity remains cubic. As a result, this model is best suited for single- and double-bounce scenarios.

Now that the models have been presented, we can examine the implementation of these theories within the numerical model. In the scenario where both electric and magnetic currents are used, the matrix calculation presented in equation 3.35 becomes more complex. Indeed, the iterative current processes are now rewritten. First of all, the incident field at iteration $k+1$ can be calculated as:

$$\mathbf{H}_{k+1}^{'} = \begin{bmatrix} \mathbf{H}_{k+1}^{'(0)} \\ \cdot \\ \cdot \\ \mathbf{H}_{k+1}^{'(M)} \end{bmatrix} = \mathbf{C}_{k+1} \times \begin{bmatrix} \mathbf{J}_{k}^{'(0)} \\ \cdot \\ \cdot \\ \mathbf{J}_{k}^{'(M)} \end{bmatrix} + C_{k+1}^{'} \begin{bmatrix} \mathbf{M}_{k}^{'(0)} \\ \cdot \\ \cdot \\ \mathbf{M}_{k}^{'(M)} \end{bmatrix} + \mathbf{C}_{k+1}^{"} \begin{bmatrix} \mathbf{M}_{k}^{'(0)} \\ \cdot \\ \cdot \\ \mathbf{M}_{k}^{'(M)} \end{bmatrix} \cdot \mathbf{C}_{k+1}^{'''} \tag{5.19}$$

Where:

$$\begin{aligned} C_{k+1}^{'} &= \frac{1}{\eta_1}\frac{-jk+(kR_r)}{jkR_r}\frac{e^{-jk(R_r)}}{4\pi R_r} \\ C_{k+1}^{''} &= \frac{1}{\eta_1}\frac{-j3k+(kR_r)}{jkR_r}\hat{\mathbf{R}}_r\frac{e^{-jk(R_r)}}{4\pi R_r} \\ C_{k+1}^{'''} &= \hat{\mathbf{R}}_r \end{aligned} \tag{5.20}$$

The matrix $C_{k+1}^{\prime}$ contains scalar elements, while the other matrices consist of 3D vectors. Clearly, storing all four matrices would require too much memory to fit in RAM. To reduce memory usage, only the matrix containing the vectors $\mathbf{R}_r$ needs to be stored. As a result, the memory requirements remain

	$MECA$	$MPOA$
$\mathbf{J}$	$[M+N, N_{ite}, 3]$	$[2(M+N), N_{ite}, 3]$
$\mathbf{M}$	$[M+N, N_{ite}, 3]$	0
R_r	$[M, N, 3]$	$[M, N, 3]$
$\hat{\mathbf{n}}$	$[M+N, 3]$	$[M+N, 3]$
$\hat{\mathbf{e}}_{\parallel}$	$[M, N, 3]$	$[M, N, 3]$
$\hat{\mathbf{e}}_{\perp}$	$[M, N, 3]$	$[M, N, 3]$
C_{k+1}	$[M, N, 3, N_f]$	$[M, N, 3, N_f]$
$C^{'}_{k+1}$	$[M, N, N_f]$	0
$C^{''}_{k+1}$	$[M, N, 3, N_f]$	0
$\Gamma_{\parallel}$	$[M, N]$	$[M, N]$
$\Gamma_{\perp}$	$[M, N]$	$[M, N, 3]$
$\tau\parallel$	0	$[M, N, 3]$
$\tau\perp$	0	$[M, N, 3]$

Table 5.1: Size of the different matrix for M elements radiating towards N elements

comparable to those of the standard matrix IPO approach. Moreover, compression algorithms can be directly applied to the vector $\mathbf{R}_r$. When only $\mathbf{R}_r$ is saved, the overall complexity is higher than in the classic IPO method due to the increased number of calculations required. In the case where $kR_r \gg 1$, the terms are simplified and the calculation of both currents are faster because of the symmetry in far field radiation. The last method is the MPOA. In order to apply the IPO in near field, two currents on the face are defined $\mathbf{J}^{'+}_{k+1}$ and $\mathbf{J}^{'-}_{k+1}$ for the two faces of the surfaces. The incident field for the two faces are equal to:

$$\mathbf{H}^{'\pm}_{k+1} = \begin{bmatrix} \mathbf{H}^{'(0)\pm}_{k+1} \\ \\ . \\ \\ . \\ \\ \mathbf{H}^{'(M)\pm}_{k+1} \end{bmatrix} = \mathbf{C}_{k+1} \times \begin{bmatrix} \mathbf{J}^{'(0)\pm}_{k} \\ \\ . \\ \\ . \\ \\ \mathbf{J}^{'(M)\pm}_{k} \end{bmatrix} \tag{5.21}$$

One remaining calculation required for dielectric or lossy materials is the determination of the currents from the incident fields. For both methods, the currents are computed using both polarizations. The vector $\hat{\mathbf{e}}_{\parallel}$ is obtained by normalizing $\hat{\mathbf{n}}\times\mathbf{R_r}$ and the orthogonal polarization is given by $\hat{\mathbf{e}}_{\perp} = \hat{\mathbf{n}}\times\hat{\mathbf{e}}_{\parallel}$. These vectors can either be computed once and stored or recalculated at each iteration to reduce memory usage. Once they are defined for both methods, the penetration or reflection must be computed. To determine the incident and scattered angles, a scalar product is calculated between $\hat{\mathbf{n}}$ and $\hat{\mathbf{R}}_r$. To summarize the memory requirements of each element, Table. 5.1 presents the memory size of each elements in the case of M sub-elements which radiates in direction of N sub-elements. To provide an order of magnitude, consider two square plates with a side length of 20 cm, radiating in a medium with permittivity $\varepsilon = 5\varepsilon_0$ at a frequency of 30 GHz. Using a meshing density of $\lambda^2/10$, this configuration results in $M = N = 20000$ sub-surfaces. Under these conditions, storing the vector $\mathbf{R}_r$ requires approximately 9.6 GB with double precision (64 bits) or 4.8 GB with single precision (32 bits).

The vector $\mathbf{R}_r$ does not necessarily need to be stored as a full square matrix; due to symmetry, it can be

	MECA	MPOA
Everything is saved	37.3 GB	28.3 GB
symmetry	18.6 GB	14.1 GB
2D vectors	24.8 GB	18.8 GB
Only R_r	4.47 GB	4.47 GB
R_r + symmetry	2.23 GB	2.23 GB
R_r + 2D vectors	2.98 GB	2.98 GB

Table 5.2: Memory usage for two square plates with 20 cm side which radiate in a material with $\varepsilon = 5\varepsilon_0$ at 30 GHz with a meshing of $\lambda^2/10$

stored as a triangular matrix, reducing the storage requirement by a factor of two. Another possibility is to retain the square matrix structure but define $\mathbf{R}_r$ only in the plane of the plate (i.e., in 2D rather than 3D). In that case, symmetry no longer applies, but the computational complexity is reduced by a factor of 3/2.

To compute the target response over a wide frequency band, suppose 100 frequency steps are considered. The memory requirement for storing C_{k+1} becomes approximately 960 GB, which is clearly impractical for in-memory storage. Naturally, looping over the frequency steps is necessary to reduce memory usage. Table 5.2 summarizes the total memory usage for one frequency and one iteration. The table only accounts for the parameters defined in the previous section. As shown, the computational burden becomes extremely large. For extended targets, the size of the different data structures may cause compilation issues. The code is implemented in Matlab with parallel processing over different parts of the target, but it is not optimized for extremely large variables as used in this example.

To accelerate the model under such conditions, only the parameters related to the sub-elements are stored explicitly.

5.2.4 Results obtained without penetration

To perform the analysis, the backscattering of a cube with a 10 cm side length and a dihedral target with dimensions shown in Fig. 5.2 is modeled. The analysis is conducted under normal incidence, with the antenna placed at a distance of 15 cm from the target. Using the Fraunhofer criterion for the cube scenario, the maximum size of each subsurface is set to 1.37 λ. Since only one bounce is performed, it should be noted that phase integration can be easily implemented. For the dihedral target, the maximum subsurface size based on the Fraunhofer criterion is smaller near the central edge. The maximum subsurface size close to the edge is 0.2 λ, while farther from the edge, it increases to approximately 1.1 λ.

5.2.4.1 Lossy metal

Firstly, a lossy metal with a conductivity of $\sigma = 1 \times 10^5$ S/m was analyzed. With these parameters, the refractive index is sufficiently high to validate the assumptions required by the IBC. The results shown in Fig. 5.3 indicate that all the methods converge to similar outcomes. It is important to note that

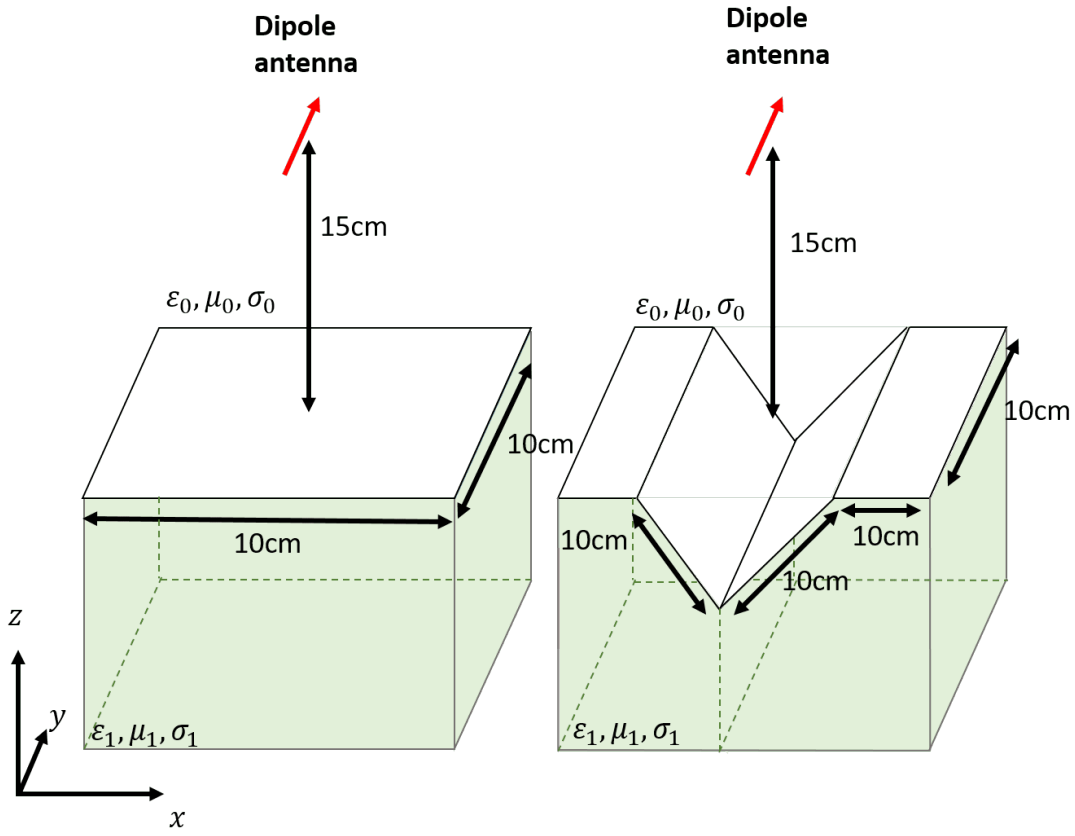

Figure 5.2: Targets geometry, respectively cube and dihedral

PO must be supported by edge diffraction to produce accurate results. For this material, no significant differences are observed among the four methods.

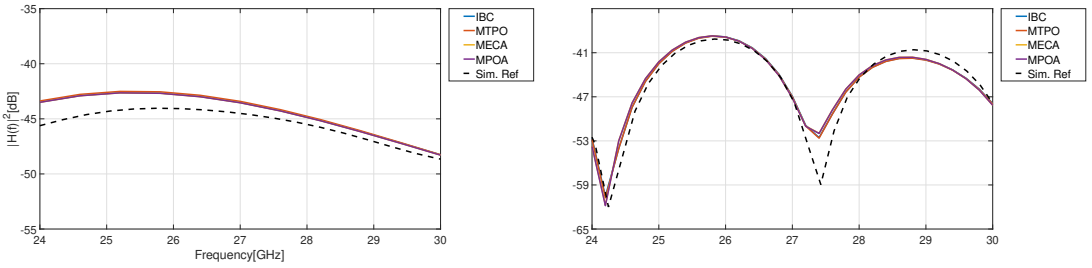

(a) **(b)**

Figure 5.3: Round trip transfer function for $\sigma = 1e^5 S.m^{-1}$ (a) Geometry 1, (b) Geometry 2

5.2.4.2 Dielectric media

For non-conductive media, the IBC and MTPO theories may not provide accurate results due to significant wave penetration inside the target, which plays a major role. To accurately compare the four models, only the propagation outside the target is analyzed. The response of the external surface was isolated by time gating in the reference simulation. For the second material, the target's dielectric constants are $\mu_2 = \mu_1$, $\varepsilon_2 = 5\,\varepsilon_1$, and $\sigma_2 = 0$. The results in Fig. 5.4 show very good agreement between the three

models based on MTPO, MECA, and MPOA. Only the model based on IBC appears to yield results significantly different from the reference simulation. With $|n_2| \approx 2.2$, the IBC model is not well-suited, whereas MTPO provides fair results.

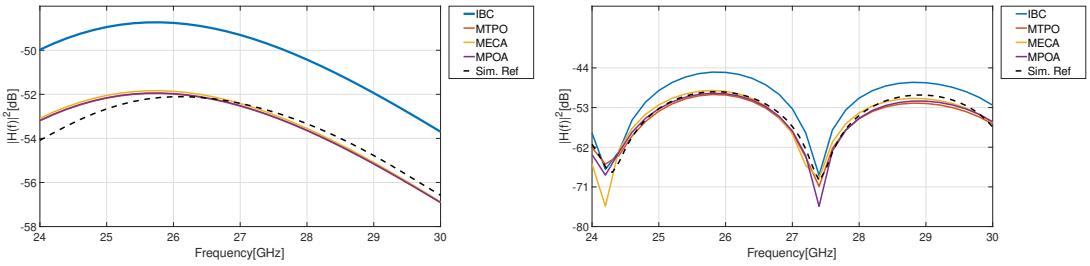

Figure 5.4: Round trip transfer function for $\varepsilon = 5\ \varepsilon_1$ (a) Geometry 1, (b) Geometry 2

Then, the target's dielectric constants are updated to $\mu_2 = \mu_1$, $\varepsilon_2 = 1.5\,\varepsilon_1$, and $\sigma_2 = 0$. In this scenario, there is significant penetration into the dielectric (the reflection coefficient at normal incidence is approximately 0.1). Similar to the previous test, the same three models produce results comparable to the reference simulation. More specifically, Fig. 5.5 shows that the MECA algorithm begins to diverge from the reference simulation. Since the IPO model allows for detailed visualization, the decomposition of MECA and MPOA responses in Fig. 5.5 reveals a significant difference in the double-bounce response related to the dihedral angle. This discrepancy may be attributed to the limitations of the PO dielectric models when applied far from the specular direction.

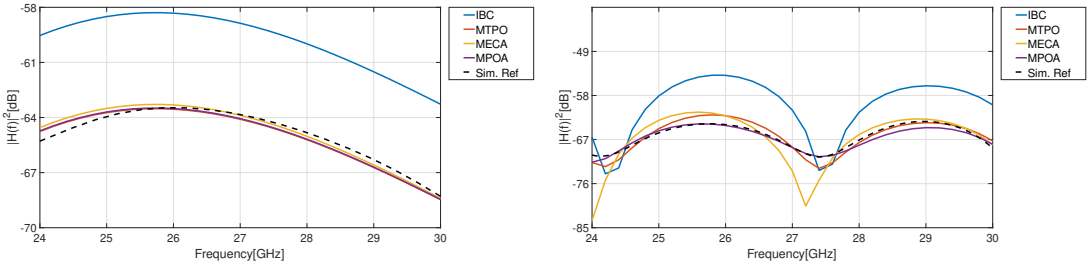

Figure 5.5: Round trip transfer function for $\varepsilon = 1.5\ \varepsilon$ (a) Geometry 1, (b) Geometry 2

5.2.4.3 Lossy dielectric media

To assess the impact of propagation far from the specular direction within the IPO model, an analysis is performed using the cube scenario, which is rotated around the x and y axes from its original position. Fig. 5.6 illustrates the simulation setup. The cube is modeled with three different materials: a lossy metal with $\sigma_2 = 1 \times 10^5$ S/m, a lossless dielectric with $\mu_2 = \mu_1$, $\varepsilon_2 = 5\,\varepsilon_1$, and a lossy dielectric with $\mu_2 = \mu_1$, $\varepsilon_2 = 5\,\varepsilon_1$, where the conductivity is defined via the loss tangent: $\tan\delta = 0.1$. The model results

are quantified using the Root Mean Square Error (RMSE) in dB over all angles and frequencies, defined as:

$$RMSE = \sqrt{\mathbb{E}\left(\left\|(10\log_{10}|\mathcal{H}(f,\theta)| - 10\log_{10}|\hat{\mathcal{H}}(f,\theta)|)\right\|^2\right)} \tag{5.22}$$

The transfer function $\hat{\mathcal{H}}(f,\theta)$ refers to the reference model. Angle θ ranges from 0° to 30° with a step of 5°.

The results are summarized in Table 5.3 and show that for the lossy metal, all four models converge to the same results with an RMSE around 1.3 dB. This error mainly arises from the divergence between physical optics and the reference model away from the specular direction. If the analysis is restricted to $\theta \leq 15°$, the RMSE for all four models reduces to approximately 0.4 dB. For both dielectric materials, the RMSE of the IBC model is around 3.3 dB, primarily because the condition in equation (5.4) is not satisfied. The other models MTPO, MECA, and MPOA exhibit results closely matching the reference. The lossy dielectric results are comparable to those of the lossless dielectric. Similarly to the lossy metal case, when considering only $\theta \leq 15°$, the RMSE decreases to about 0.3 dB. Although the results from MTPO, MECA, and MPOA diverge similarly, they remain consistent overall. For dielectric media, the MECA algorithm appears to perform slightly worse than MTPO and MPOA for rotations about the y-axis. This may explain why multiple bounces in the dihedral target scenario (Fig. 5.5) are better estimated by MPOA than by MECA.

Table 5.3: Model performance for rotated cube using RMSE in dB for θ ranging from 0° to 30°

	Lossy Metal		Lossless Dielectric		Lossy Dielectric	
Rotation	x-axis	y-axis	x-axis	y-axis	x-axis	y-axis
IBC	1.36	1.24	3.49	3.06	3.51	3.17
MTPO	1.34	1.25	0.75	0.87	0.7	1.40
MECA	1.34	1.25	0.87	1.47	0.78	1.47
MPOA	1.33	1.24	0.86	0.75	0.76	1.25

To observe the results more precisely, the round-trip transfer function is plotted for rotations of 15° and 30° in Fig. 5.7. The results at 15° show very close agreement between the three models and the reference simulation. For the 30° rotation, the three models yield similar results with an error of approximately 1 dB.

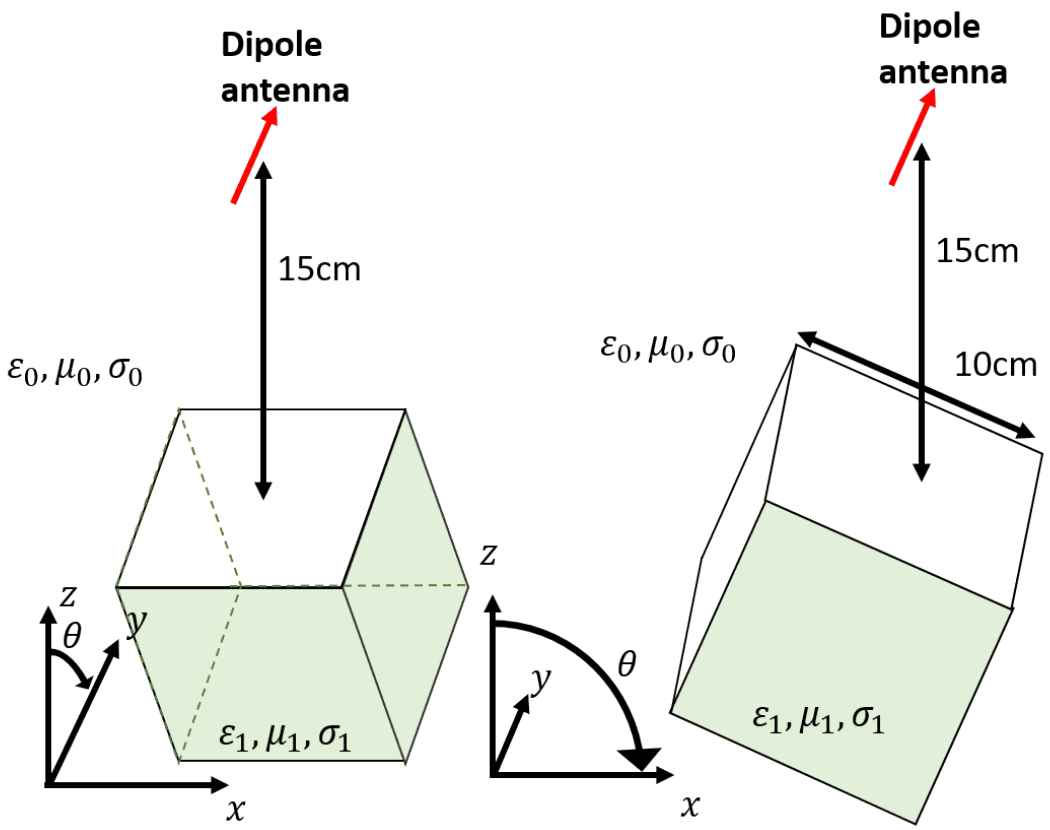

Figure 5.6: Target geometry: 10 cm cube rotate along x and y

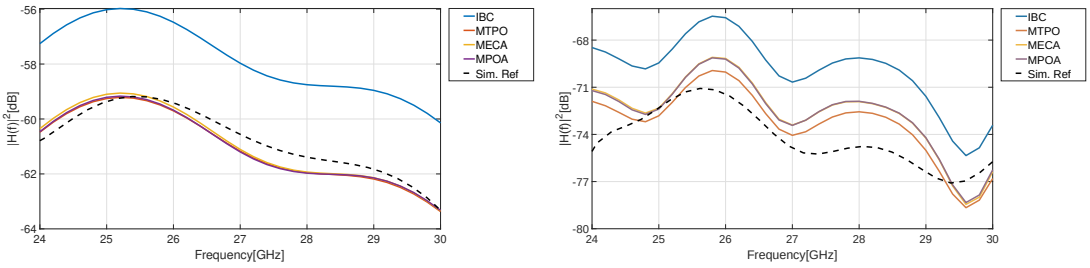

(a) **(b)**

Figure 5.7: Round trip transfer function for the cube (a) rotation of 15°, (b) rotation of 30°

5.2.5 Experimental validation

As mentioned in the previous sections, the MPOA and MECA methods provide similar results. For implementation purposes within the current model, the MECA method was chosen for the remainder of this work, as it does not require a complete reworking of the existing code.

To validate the penetration inside the target, the first target used is a block of Teflon shown in Fig. 5.8. When modeling Teflon at 30 GHz, one major issue arises from the material properties themselves. For most applications, the material can be defined with low precision. For instance, Teflon is often approximated in the literature as $\varepsilon = 2\varepsilon_1$ and $\mu = \mu_1$. In the model, propagation inside the target plays a significant role. Since the Teflon block is 5 cm thick, the round-trip time inside the Teflon

is approximately 0.47 ns, compared to 0.33 ns in air. Considering a permittivity of $\varepsilon = 2.5\varepsilon_1$, the round-trip time increases to 0.52 ns, which may not drastically affect the amplitude but will significantly change the phase term. At 30 GHz, the phase evolution inside the target is $e^{j0.1\lambda_{2.5\varepsilon_1}} = 0.37 - 0.92i$ or $e^{j0.1\lambda_{2\varepsilon_1}} = 0.62 + 0.77i$. Therefore, material precision is crucial for accurate modeling. A first approach to estimate the permittivity is to measure the time delay between the two main peaks in the target response. Fig. 5.9**(a)** shows the temporal response where the time difference between the two peaks is about 0.48 ns $\pm$ 0.02 ns, corresponding to an equivalent Teflon permittivity ranging from 1.9 to 2.3. To further validate the model and find the permittivity, simulations were run with permittivities ranging from 2 to 2.5. The two closest matches to the measurement correspond to $\varepsilon = 2\varepsilon_1$ and $\varepsilon = 2.3\varepsilon_1$. These two values are the only ones satisfying both the frequency and temporal responses. The model's accuracy could be improved by more precise parameter estimation. The solution with $\varepsilon = 2\varepsilon_1$ gives results closely matching both temporal and frequency domains, and may represent the true material properties. Another aspect not considered here is the frequency-dependent variation of the material properties between 20 GHz and 30 GHz.

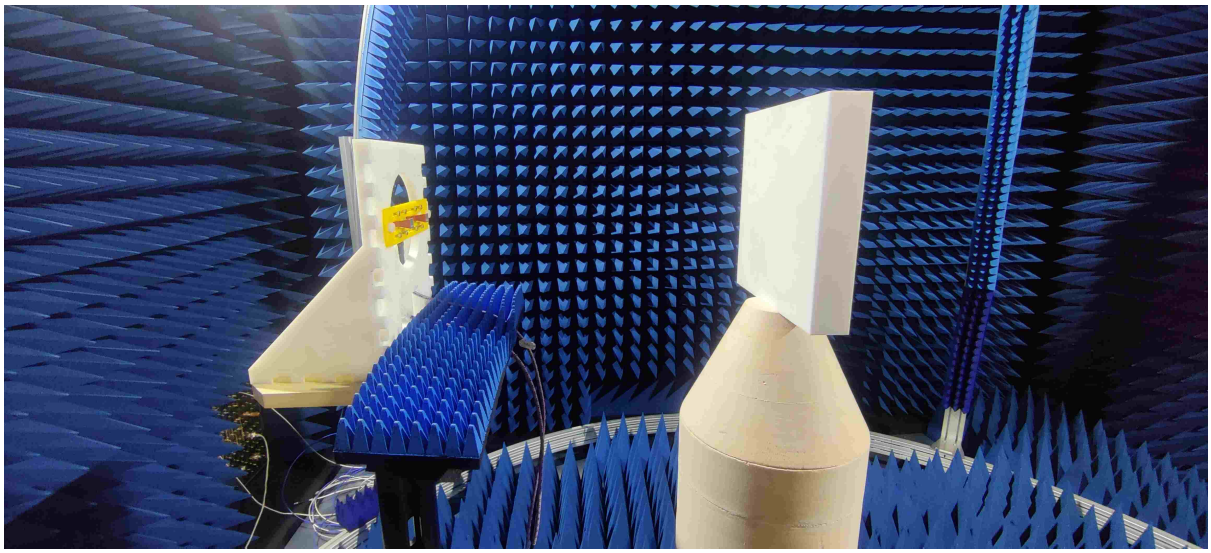

Figure 5.8: Presentation of the Teflon measurement setup

For a detailed analysis, the temporal response is split into the "first peak" and the "second peak". In the model, the first peak corresponds to the first bounce, while the second peak corresponds to the round trip inside the Teflon. Fig. 5.10 shows simulations for both permittivities. Both models agree well on the first bounce, but differ on the second bounce. At the lower end of the frequency band, the model with $\varepsilon = 2.3\varepsilon_1$ performs better, whereas for the higher frequencies, the model with $\varepsilon = 2\varepsilon_1$ is more accurate.

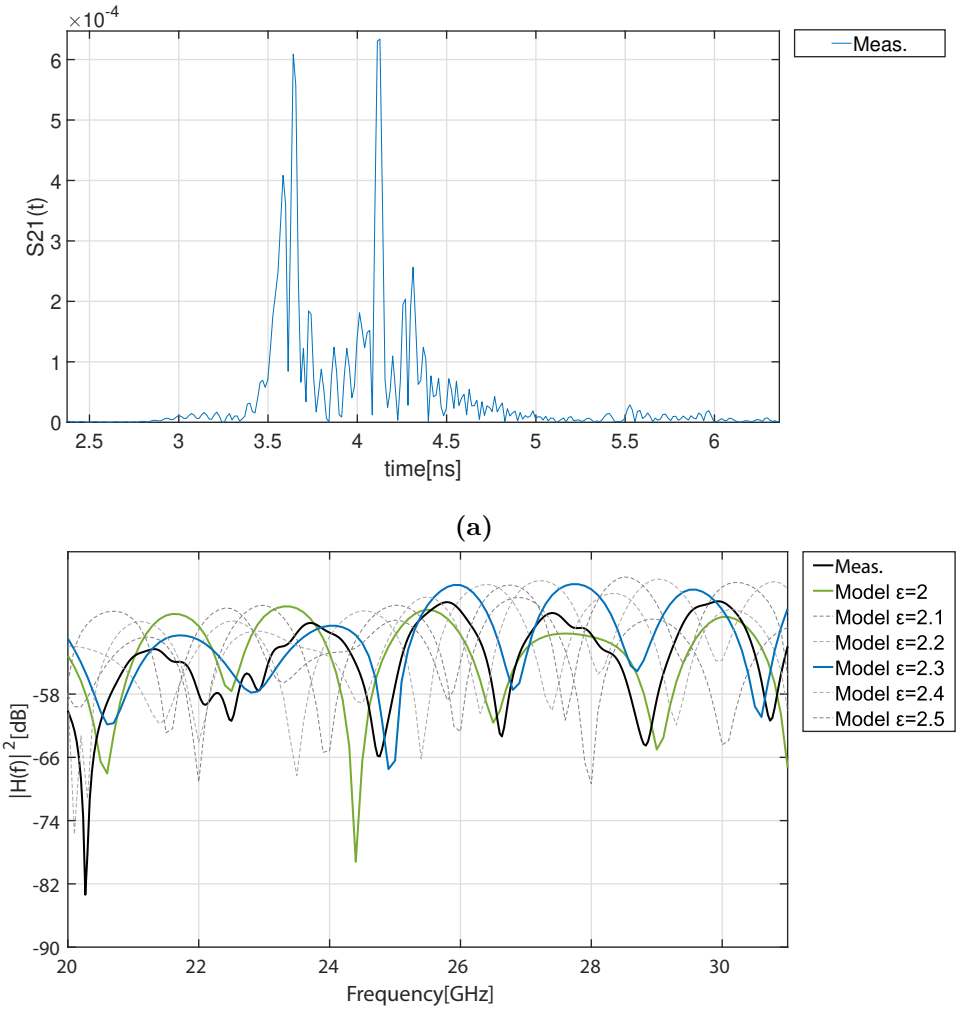

Figure 5.9: Presentation of the Teflon measurement **(a)** Time domain response of the measurement **(b)** comparison with the model

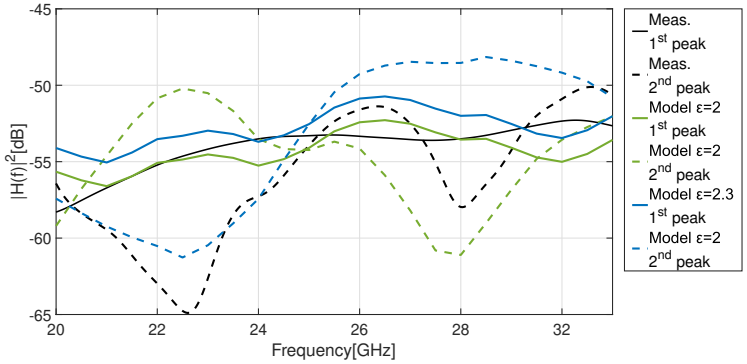

Figure 5.10: Decomposition of the Teflon scenario

5.3 Application to human body sensing

5.3.1 Validation using a cube made on human body mimic material

To validate the accuracy of the model and its capabilities in addressing human sensing scenarios, measurements were made using a lossy dielectric cube with a side length of 5.6 cm. The cube is made of lossy silicone which can emulate the human body electromagnetic properties and is compliant to CTIA recommendations for OTA testing [60]. The choice of this geometry instead of a complete human body shape aims to validate the model in a canonical case, before applying it to model complex shapes. Measurements were also performed by means of a VNA in an anechoic chamber with a distance of 50 cm between the target and the antennas. The Fig. 5.11 shows the measurement setup. The antennas used are horns operating from 22 GHz to 33 GHz. At these frequencies, the corresponding cube's relative permittivity ranges from 20 to 21 and the conductivity ranges to 4.11 $S.m^{-1}$ to 5.7 $S.m^{-1}$.
The measurements were performed with a 5° step rotation. During post-processing, an error of 1° was identified in target alignment. This indicates that the model needs to be set with a 5° step rotation centered at 1° instead of 0°. The results in Fig. 5.11 exhibit excellent agreement between the model and the measurements. The shift of less than 1 dB could be attributed to the precision of the measurements or the implementation of the antennas. In this scenario, the penetrated power accounted for approximately 60% of the response as evanescent fields resulting from the cube's conductivity.

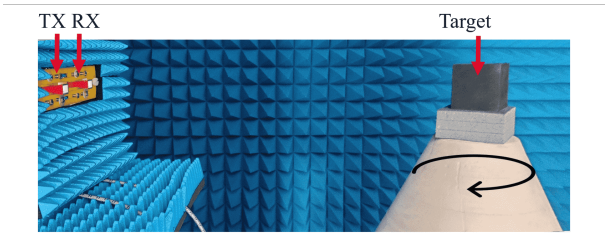

(a)

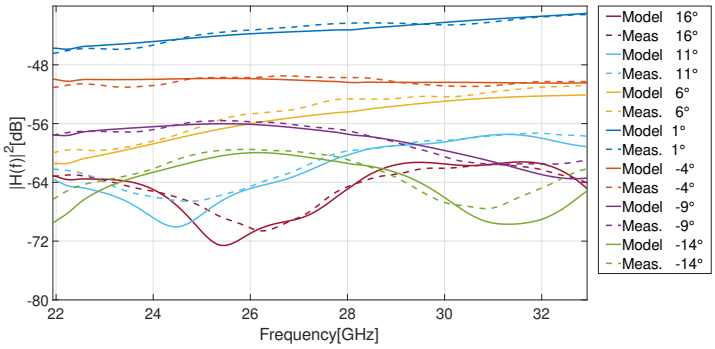

(b)

Figure 5.11: Backscattering measurement setup (a). Results of the backscattering in the near field for different azimutal angles (b): model (continous line) vs. measurement (dashed line).

5.3.2 Human body scenario

5.3.2.1 Human body scattering in close range

To model human body backscattering, a first approximation consists in representing the skin as a simplified homogeneous dielectric layer that accounts for reflection and absorption effects. In this article a 1.83 m mannequin STL file presented in Fig. 5.12 is used to characterize the scattering behavior of the human body.

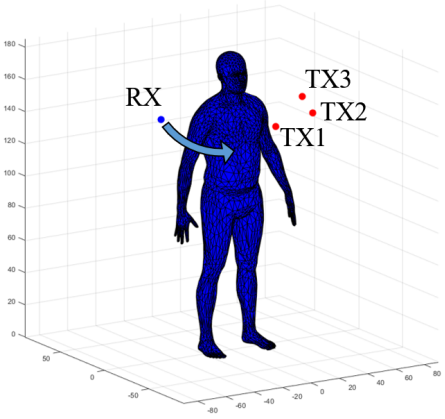

Figure 5.12: Human body mannequin geometry and initial meshing with antenna positioning

5.3.3 Round Trip Transfer Function

Here we evaluated the scattering field of the human body at 50 cm (corresponding to near field). We evaluate the bistatic backscattering in three incident directions $\phi_{inc} = (0°, 45°, 90°)$, corresponding to the three TX position TX1, TX2, TX3 in Fig. 5.12. In Fig. 5.13 we show the normalized scattered field over the body, together with obtained transfer function for the TX1 and the TX3 and receiver at $\phi = 0°$. In the TX1 position the two main scatterers parts are the top of the torso and the chin. In the TX3 configuration, the transmitter is located on the left side of the target, while the receiver is positioned in front. As shown in Fig. 5.13c, due to the complex geometry, all the sub-surfaces of the left part of the body are not scattering towards the receiver. The main transmitting parts are the neck and the shoulder. The round trip transfer function clearly demonstrates the idea that there are two main bounces.

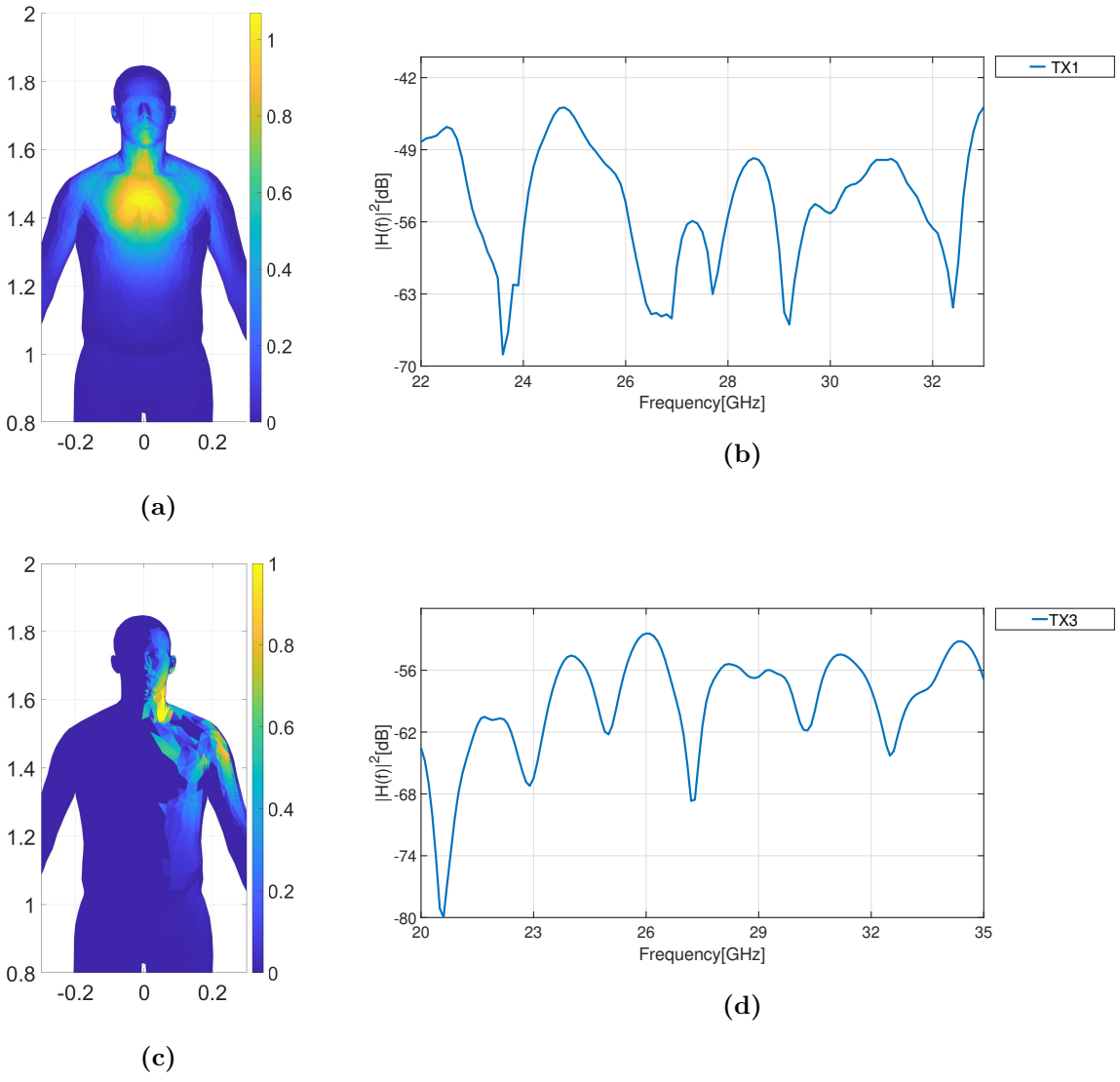

Figure 5.13: Normalized backscattered field, both antenna in front (a). Round trip transfer function of the scenario 1 (b). Normalized backscattered field TX on the side, RX on the front (c). Round trip transfer function of the scenario 2 (d).

5.3.4 NF-RCS

In order to compare measurements at several distances, the NF-RCS is employed. This metric has been chosen, instead of the full round trip transfer function, in order to fairly compare the scattering at different distances.

In the RCS estimation we considered the same illumination provided by horn antennas in measurement and compensated the antenna gain.

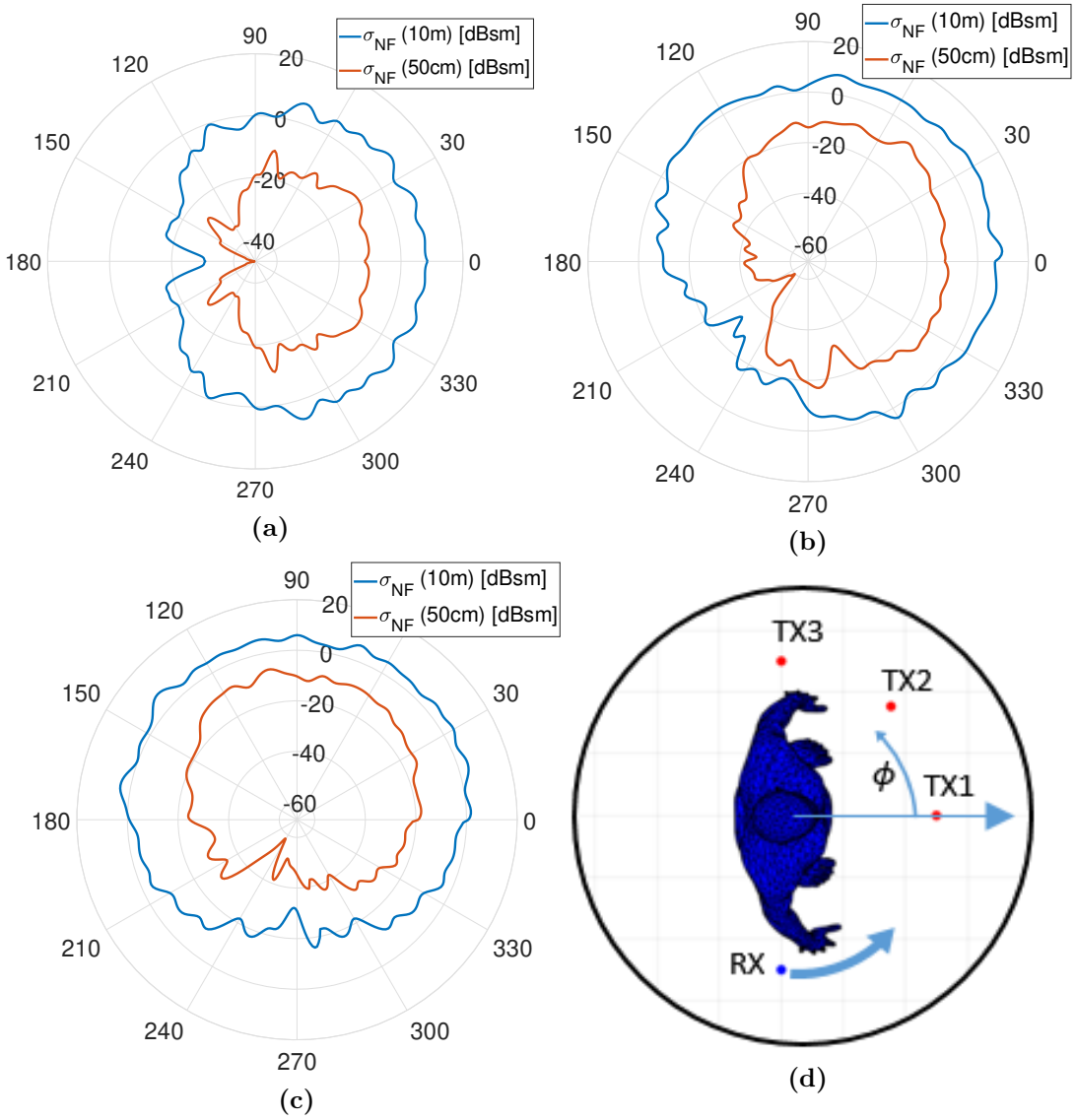

Figure 5.14: Human body bistatic RCS at 50 cm and 10 m for three different incident angles corresponding to TX1 (a), TX2 (b), TX3 (c). Human body and antenna positioning(d).

Fig. 5.14 shows the RCS patterns for the three different TX positions highlighted in Fig. 5.14d, averaged over the 22 GHz-33 GHz band for two distances, 50 cm and 10 m. For TX1, the RCS is maximize for the monostatic case and the -3 dB beamwidth is around 120° for the 10 m measurement and around 100° for the 50 cm scenario. In this case, the evolution of the RCS is similar for both distances. For TX2, the diagram is not symmetrical due to the arrival angle. Interestingly, the human body's monostatic

case still shows the highest response at 50 cm. The "flat" part of the torso does not represent the main scattering part. For TX3 where the transmitter is on the left side of the target, the RCS is maximized in the monostatic case too. As can be seen, in the 10 m case, the RCS is higher than at 50 cm. This is mainly due to the larger illuminated area at greater distances, which increases the scattering surface. The results show that up to 20 dB difference can be found in the RCS at different distances, illustrating the importance of taking care of near field effect. To properly demonstrate the evolution of the RCS along distance, we evaluated the monostatic RCS of the torso from 50 cm to 50 m. The RCS plotted in Fig. 5.15 exhibits an evolution that converges to ≈10 dBsm for far field distances. It is important to note that, with respect to experimental results in the literature [61], this result highlights the differences given by the proximity of the target from the antenna.

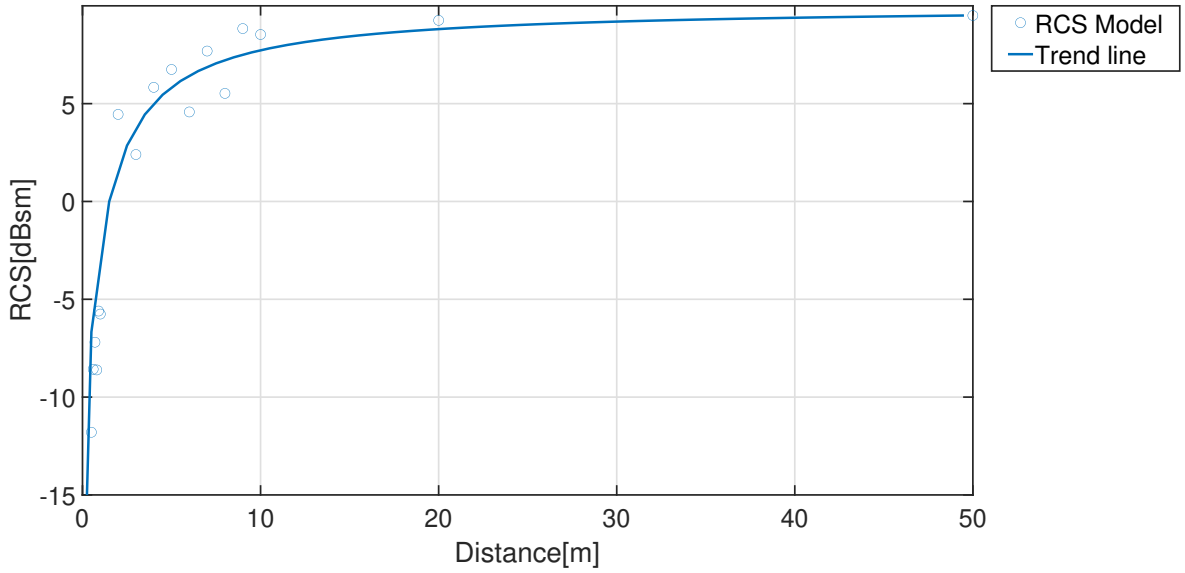

Figure 5.15: Evolution of human body monostatic RCS along distance

5.4 Conclusion

In this chapter, the model has been extended to dielectric and lossy targets. The models based on IPO and EEC are mainly designed for PEC targets, where only the electric current is considered. To overcome this limitation, several methods have been tested: the IBC model for non-penetrable materials, as well as three other methods adapted for penetrable materials, namely MTPO, MPOA, and MECA. In the studied cases, these three methods yielded similar results for canonical targets. To account for dielectric materials, an adaptation of the EEC for dielectric targets is presented, based on the MPOA method.
One of the main differences observed when comparing these methods lies in the definition of currents. In MECA, the current is defined for radiation both inside and outside the target, with both electric and magnetic currents taken into account. In contrast, the MPOA method defines only one type of current (either electric or magnetic), which radiates in a single direction (either inward or outward).

To validate the modeling of radiation inside a target, a Teflon slab was used to simulate backscattering. The slab was measured, and an analysis of the obtained response was performed to estimate the slab's permittivity.

Finally, an application of the model was carried out for near field backscattering from a human body. The IPO model was applied to evaluate the body's backscattering, highlighting differences in RCS according to near and far-field conditions. Variations up to 20 dB were found depending on the distance, in a frequency range from 22 to 33 GHz. The model and results are of practical interest for radar-based sensing applications aimed at human body detection.

Chapter 6

Conclusions and perspectives

6.1 Conclusions

In this thesis, the research focused on modeling the backscattering of near field targets with IPO and EEC. The code was developed on Matlab in CEA-LETI and was tested on both comparison with simulation from commercial software CST-Microwave Studio and with measurements which were done in the CEA-LETI anechoic chamber.

The concept of near field targets refers to scenarios where both the emitter and the receiver are located in the near field of the target, as defined by the Fraunhofer distance. As the focus is on mmWave, the antenna radiation is in far field. To model the scattering, the proposed approach is based on physical optics, which was originally developed for far field scenarios. The model considers a planar surface carrying electric currents that radiate into space. To adapt this model to the near field, the planar surface is discretized into sufficiently small elements so that the emitter and receiver can be perceived as being in the far field of each element. With this technique, the problem of a large target radiating in its near field is transformed into a problem of multiple small targets radiating in their far field.

Physical optics theory is well-suited for large structures, but it does not accurately model scattering in the case of strong diffraction. To account for this, edge current scattering is modeled similarly to surface currents. By using the EEC method, currents on the edges are calculated. Originally developed for the far field, the same near field adaptation is applied at the sub-edge level. The total response is then obtained as the sum of surface and edge scattering contributions.

In this modeling approach, the currents do not evolve and the interconnections between the different parts of the target are not represented. To address this limitation, the model was extended using iterative radiation. In this framework, the currents on the target evolve iteratively to account for radiation interactions within the target. For curved targets, modeling becomes more complex when using fast algorithms. The objective is to find a good compromise between precision and computational efficiency. MoM can model the propagation of currents on curved surfaces, whereas IPO cannot. To approximate curved geometries more accurately, the surface is discretized into sufficiently small elements so that the local curvature can be neglected. However, this approach does not take into account the traveling-wave

behavior of the currents. When focusing on a sub-part, geometrical shadowing is used to determine which regions are illuminated and which are not. A ray is launched from the sub-part toward all other elements, and if another surface is intersected, the element is considered not illuminated. This process is repeated for all sub-elements in order to perform the iteration, and it is also applied for both the emitter and the receiver.

In this thesis, the concept of NF-RCS is presented and discussed. NF-RCS is expressed similarly to the classical RCS, which applies when the target is located in the far field. The main difference is that NF-RCS explicitly accounts for the distance to the target in its definition. When the target is sufficiently far, NF-RCS converges toward the classical RCS.

RCS can be defined from the ratio of scattered power to incident power. In the specific case of NF-RCS, the concept of scattered power can be treated as a scalar quantity, since it corresponds to the sum of the contributions scattered from each sub-surface. However, the definition of distance remains debatable in near field: it can be considered as a single global distance, as the minimum distance, or as a distance associated with each sub-surface.

A key property of NF-RCS is that it cannot be obtained simply as the sum of the RCS values of the individual sub-elements, due to its ratio definition. The first limitation arises because the scattered power cannot be directly summed; this can be circumvented by summing all the scattered fields instead of the currents. However, the main difficulty lies in the ratio between scattered and incident fields. The scattered power of each sub-element depends on its own local incident field. As a result, the total scattered power cannot be divided by a single incident power, since the incident power is not necessarily a scalar. When the target is sufficiently far, a scalar incident power can be assumed, but in other cases an arbitrary reference value must be chosen, such as the maximum incident power or the mean incident power.

To overcome the limitations of NF-RCS, an alternative approach is to study the round-trip transfer function instead. The round-trip transfer function inherently accounts for the target, the environment, and the characteristics of both the source and the receiver. To take into account the transmitting and receiving antennas characteristics, their complex gain patterns can also be incorporated. For isotropic antennas, the NF-RCS and the round-trip transfer function are related through the radar equation (adapted to near field conditions), where the NF-RCS corresponds to the squared modulus of the round-trip transfer function.

When using the round-trip transfer function, it is essential to account for the antennas, which must be incorporated into the model for more accurate representation. Two major aspects are considered in this thesis. First, the antennas transfer function are included. They are valid in the antenna far field. They are necessary to properly model both the incident power and the received power. When summing the fields backscattered from all the sub-elements, the antenna complex gain is taken into account. The second aspect concerns the summation of the scattered fields. This summation is performed in order to account for interference effects at the antenna port.

The model was validated and tested in an anechoic chamber for a quasi-monostatic setup using horn antenna and a measurement system based on positioners and VNA. The measurement precision was a

huge part of the measure because of the relative closeness with the target. Experimental results indicate that alignment becomes easier when diffraction dominates the response, and the model demonstrates good accuracy under these conditions.
IPO and EEC are originally suited for metallic surfaces. To extend the model to dielectric or lossy materials, several adaptations were introduced. For IPO, different formulations were tested to identify which offered the best performance and to assess whether an equivalent electric current could be used instead of both electric and magnetic currents. For EEC, the dielectric edge model depends directly on the type of surface currents used in the surface formulation. In addition, the meshing strategy and the geometrical shadowing procedure were adapted to account for the propagation inside dielectric or lossy media.
At the end of this thesis, a performance model and a dedicated simulator were developed in Matlab. This simulator implements the proposed near field target model, and its performance was validated through comparison with near field measurements.
In order to presents the code used in the model, a footage is presented in Fig. 6.1. The code is separated in 4 parts: The preparation step, the source illumination, the targets radiation and the radiation toward receivers. The different parts are detailled in Appendix III

6.2 Perspectives

The modeling of electromagnetic waves is a vast and evolving field. The work presented in this thesis contributes to this effort by improving near field backscattering modeling, while many promising directions remain open for further enhancement and application of the model. The perspectives will be split in two main parts.

6.2.1 Perspectives - Model amelioration

Several improvements can be envisioned to accelerate the model and enhance its accuracy.

The principle of IPO is to radiate in all directions, which is not efficient when moving away from the specular direction. A promising approach would be to combine IPO with SBR [44], where ray-tubes are used to track propagation. While the complexity of SBR mainly lies in evaluating the new scattered directions, a clever hybridization with IPO could significantly reduce computation time without introducing major errors. In practice, SBR appears better suited for relatively simple targets (e.g., rooms or vehicles). For more complex geometries, such as the interior of a pipe or round-shaped bodies like the human body, recalculating scattering directions quickly becomes computationally heavy. To address this, IPO itself could be refined to restrict radiation to a limited angular range around the specular direction. In this thesis, this simplification was applied manually but was not implemented in the code; automating it would be a valuable enhancement.

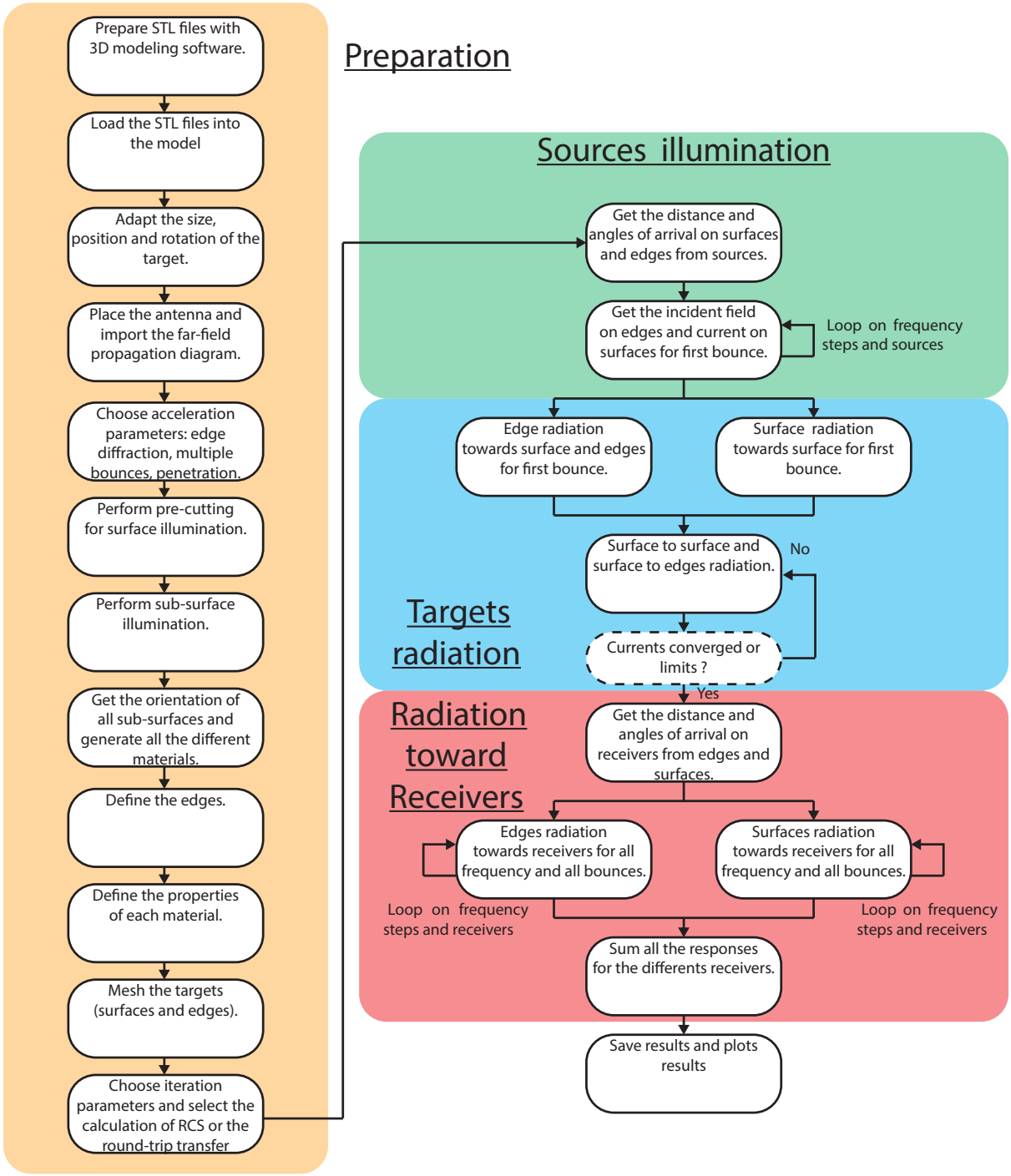

Figure 6.1: Presentation of the code implementation

Another avenue for acceleration is to return to a classical matrix-based IPO in order to speed up the iteration process on the currents. However, since this work deals with electrically large targets, excessive interactions lead to prohibitive RAM requirements. In the present implementation, storing a single matrix for iterative updates was not feasible, especially when dielectric or lossy materials were included. Future improvements could explore matrix compression techniques to reduce memory consumption [50]. Alternatively, the target could be divided into sub-parts, with matrix-based IPO applied only to selected regions where multiple bounces are critical. A user-defined selection of these regions would provide flexibility while optimizing computation.

The double-bounce model presented in Chapter III should also be coupled with IPO. During the thesis, it was systematically applied to the first bounce, where the complexity remains low due to the presence of a single source. The same approach should be extended to the final bounce. While this does not directly accelerate the model, it allows the use of coarser meshing, since the phase integration is inherently included. Meshing is indeed a key factor in computation speed. FaFFA was tested in this work, but only applied between sub-elements belonging to the original element. This approach could be further extended by splitting each element into multiple levels of sub-elements (e.g. 1, 4, 16, ...). FaFFA would then be applied for all possible source/receiver distances. The optimal sub-element size should depend on the minimum source/receiver distance, with larger sub-elements used for distant sources or receivers.

The model is well suited for a classical range of targets, such as complex shapes with curved lines and resonant parts. However, when attempting to model all physical aspects simultaneously, the computation inevitably becomes slower. One important strategy, which has already been partially implemented, is to adapt the simulation parameters for each run. In some cases, it is more relevant to focus on diffraction effects rather than on resonant contributions. This selection can be carried out in two main ways: either directly by the user, or automatically through the code.

From this point of view, certain aspects of the model have not yet been implemented. The first one concerns the displacement of currents and the associated creeping waves, which can be important in specific cases like scattering on a barrier or fence in an vehicular application. In the current version of the model, the focus on large targets makes this contribution negligible, as it plays only a minor role. However, for smaller targets or lower frequencies, it could become necessary to take it into account. Since such an extension would be computationally expensive, it is important to carefully decide whether or not to include it in the simulations.

Another aspect that has not yet been implemented is the edge current diffraction for dielectric targets. In the current model, the current is defined only in a single material, corresponding to the incident wave. Consequently, the wave scattered by this current in the other material is not modeled. In most cases, this implies that for dielectric targets, edge diffraction is only considered in free space and not within

the target itself. Because of the way dielectric edge scattering is defined, this contribution is not taken into account. Preliminary attempts were made to include this effect, but validation proved difficult due to surface radiation. The main idea was to introduce two equivalent currents at the edges, one inside and one outside. However, significant work remains to properly handle the singularities that may occur for the inside currents, while those for the outside currents were already addressed in Chapter 5.

Another possible extension would be to couple the present model with large-scale propagation models. While the current approach focuses on the scattering from individual targets, practical applications often involve complex environments where multiple objects contribute to the overall channel response. For instance, in indoor scenarios, the propagation of radio waves is strongly influenced by walls while in outdoor environments, buildings, vehicles play a dominant role. Integrating the proposed scattering model into channel modeling frameworks would allow for a more accurate prediction of multipath propagation.

The antenna implementation in the model could also be refined. At present, an antenna is represented as a simple scattering point with predefined characteristics. For more complex antennas, or when higher resolution is required, it would be beneficial to apply the model directly to the receiving part. For example, in the case of a horn antenna, the model could be used to account for the different structural components, while the antenna port would be defined explicitly based on its impedance. Additionally, the model could be extended to consider multi-antenna coupling effects, which are important when several antennas are placed in close proximity which affects the radiation patterns. Incorporating such interactions would improve the accuracy of simulations for array antennas or MIMO systems.

The model is a frequency-domain model that is not specifically optimized for wideband simulations. This means that for a large bandwidth, achieving accurate results can become extremely time-consuming. Furthermore, when computing the temporal response, a large number of frequency points is required, especially for targets located far from the antenna. In the model, the response are given from the number of bounce, but the iterative process could be apply on time also in order to have an other point of view of the response. In this case, the frequency response could be obtained with the temporal response in the same case. The temporal response will be link to the iterative step will the frequency response will depend of the number of frequency points. In order to model this, as the number of iteration point will be higher, a good agreement must be done for the iterative steps.
All proposed improvements to the model must be systematically tested and validated. Each enhancement should be carefully benchmarked against reference solutions or experimental data. When using reference solutions, an important consideration is not to rely on them blindly, as in some cases the model response may actually be more accurate than the reference. There is no single standard procedure to establish reference solutions, which makes validation a nuanced process. For experimental data, the testing methods employed during this thesis have proven effective and can be reused, as they adapt well to a variety of cases. For specific aspects, specially designed targets may be required to isolate particular effects without needing to revalidate surface scattering. A rigorous validation framework also helps identify

potential limitations or unexpected behaviors, guiding further refinements and ensuring the reliability of the model.
The proposed model is inherently multistatic, allowing the simulation of complex scattering configurations involving multiple transmitters and receivers. However, in this work, it has been applied only in bistatic configurations. Further validation is still required, particularly for forward-scattering scenarios where the interaction mechanisms differ significantly.

6.2.2 Perspectives - Model utilization

During the thesis, the development of the model opened up many possible applications for representing electromagnetic scenarios. One major advantage is the ability to achieve complete control over the target response, where the overall response can be decomposed and individual contributions treated separately. For example, when analyzing the backscattering of a target in a given environment, the model makes it possible to isolate the information of interest. A preliminary test in the thesis was performed using a target placed on a highly reflective support. In such a case, the direct contribution of the support can be removed from the measurement by applying a calibration procedure. However, the backscattering arising from the interaction between the target and the support is more challenging to handle, since the support may obscure part of the target or generate multiple reflections. The proposed model provides precise information in such cases and can be readily extended either to suppress the support contribution for accurate target RCS estimation or to include it in order to better match measurement conditions. The model is suits for relative large target scattering to the wavelength. By decomposing the total response into distinct components, the model provides information foll all the distinct parts.

The proposed model can be adapted to estimate the contribution of structural scattering in antenna measurements. In practical configurations, the measured field does not only contain the antenna mode, which represents the radiation directly associated with the antenna. While classical calibration techniques may partially mitigate this effect, they generally fail to account for the interaction between the antenna and the structure, such as multiple reflections or partial masking.

The model is intended to be applied in both imaging and radar scenarios. For the imaging part, the model can be employed to generate a comprehensive set of simulations that serve as a reference for target identification. As the model accurately reproduces the backscattering of complex targets, it provides data that can be used to train reconstruction and classification algorithms. This gives us the capability to create datasets for applications where real measurements are not possible. It can also be used to assess the robustness of classification models. Thanks to recent advances in training and AI applications, the model can be used for automatic learning and target detection.

The proposed model is particularly well suited for multistatic radar scenarios, where multiple transmitters and receivers are positioned around the target. In such configurations, the scattering response varies significantly depending on the relative geometry, and this effect is even more pronounced in the

near field. The total response is decomposed into individual contributions and allows for a precise analysis of the angular and spatial dependence of the scattered field. This capability enables the study of target visibility from multiple perspectives which is important for antenna placement optimization.
The model is suits for Joint Communication and Sensing applications. This capability is particularly valuable for emerging applications such as gesture recognition, object tracking. The precise modeling of target responses allows for better detection and classification of movements, making the model a key tool for developing advanced sensing systems where both communication and situational awareness are required.
The flexibility of the model also makes it suitable for exploring radar performance at higher frequency which will improve detection resolution. This frequency adaptability opens new opportunities in applications ranging from autonomous vehicles to security screening and biomedical sensing. The model is adapted to multi-layered or multi-slab configurations, as encountered in biomedical but has not been fully tested. For example, in medical imaging or through-wall radar, the electromagnetic wave propagates through several media with different permittivities and conductivities before reaching the target.

Another promising research direction concerns the extension of the model to near field antenna configurations. In the current implementation, antennas are mainly considered as far field sources or receivers. However, in many practical applications like transmit arrays the antennas operate in the near field. In such scenarios, mutual coupling and phase variations across the antenna aperture play a significant role in the overall response. Incorporating a near field antenna model would allow for more accurate simulations.

In the context of this model, the approaches presented by Jeng [62] and Larsson [63] open promising perspectives for future developments. The combination of advanced near-field scattering modeling with experimental NF-RCS measurements and ISAR imaging could enable a more complete and realistic validation of the simulated results. Such integration would strengthen the model's applicability to military scenarios, particularly for the prediction and analysis of radar signatures of complex targets.

Chapter 7

Appendix

Appendix I: Integration over a triangle

First of all, the integral is defined over two axes, x and y, as illustrated in Fig. 3.1. We denote this integral by I:

$$I = \iint_{x,y} e^{-jk(R_{rec} - R_{rec}^{'} + R_{sou} - R_{sou}^{'})} dxdy \tag{7.1}$$

To evaluate the integral, the term $R_{rec} - R_{rec}^{'} + R_{sou} - R_{sou}^{'}$ has two components, one along the x-axis and one along the y-axis. Using only the Fraunhofer criterion, it can be expressed as:

$$R_{rec} - R_{rec}^{'} + R_{sou} - R_{sou}^{'} = O^{'}M(cos(\delta_{inc}) + cos(\delta_{scat})) \tag{7.2}$$

Where $O'Mcos(\delta) = \mathbf{O'M} \cdot \hat{\mathbf{R}} = (x_M - x_{O'})x_{\hat{R}} + (y_M - y_{O'})y_{\hat{R}}$ If the chord criterion is also considered, the variation along the z-axis is incorporated into the variations along x and y, and the term is rewritten as:

$$\begin{aligned} R_{rec} - R_{rec}^{'} + R_{sou} - R_{sou}^{'} =& (x_M - x_{O'})(x_{\hat{R}_{rec}} + x_{\hat{R}_{sou}} + \frac{\partial z}{\partial x}(z_{\hat{R}_{rec}} + z_{\hat{R}_{sou}})) + \\ & (y_M - y_{O'})(y_{\hat{R}_{rec}} + y_{\hat{R}_{sou}} + \frac{\partial z}{\partial y}(z_{\hat{R}_{rec}} + z_{\hat{R}_{sou}})) \end{aligned} \tag{7.3}$$

For convenience, we define the variables X and Y as:

$$\begin{aligned} X &= (x_{\hat{R}_{rec}} + x_{\hat{R}_{sou}} + \frac{\partial z}{\partial x}(z_{\hat{R}_{rec}} + z_{\hat{R}_{sou}})) \\ Y &= (y_{\hat{R}_{rec}} + y_{\hat{R}_{sou}} + \frac{\partial z}{\partial y}(z_{\hat{R}_{rec}} + z_{\hat{R}_{sou}})) \end{aligned} \tag{7.4}$$

The term X refers to the $\hat{\mathbf{x}}$ coordinate and the term Y refers to the $\hat{\mathbf{y}}$ coordinate. Using these definitions and setting the origin of the basis at O', the integral is equal to:

$$I = \int_x \int_y e^{-jk(x_m X + y_m Y)} dxdy \tag{7.5}$$

To properly integrate this term over the triangle, the triangle ABC is defined with a new basis given by $(\mathbf{A}, \hat{\mathbf{AB}}, \hat{\mathbf{AC}}, \hat{\mathbf{n}})$. To perform the integration over the triangle, we define the determinant of the Jacobian matrix to perform the change of variables from the original basis to the new one. The vector $\hat{\mathbf{n}}$ will not be used since the variable change is restricted to the plane of the triangle. The Jacobian corresponding to the first two vectors is given by:

$$J = \left| \det \begin{bmatrix} x_{AB} & x_{AC} \\ y_{AB} & y_{AC} \end{bmatrix} \right| = x_{AB} y_{AC} - y_{AB} x_{AC} \tag{7.6}$$

Using this new basis, the integral terms in x and y are rewritten and the limits of integration become well-defined. Figure 3.2 illustrates the definition of the new basis. The integral is defined in the new basis as:

$$I = \int_0^1 \int_0^{1-u} e^{-jkX(x_A + u(x_{AB}) + v(x_{AC}))} e^{-jkY(y_A + u(y_{AB}) + v(y_{AC}))} J dvdu \tag{7.7}$$

Rearranging the terms allows separation of the integration along the two axes. It allows the integration to be performed one axis at a time.

$$I = J e^{-jk(X(x_A) + Y(y_A))} \int_0^1 e^{-jku(X(x_{AB}) + Y(y_{AB}))} \int_0^{1-u} e^{-jkv(X(x_{AC}) + Y(y_{AC}))} dvdu \tag{7.8}$$

To further simplify the expression, we define new entities as follows:

$$\mathcal{A} = X(x_A) + Y(y_A) \tag{7.9}$$

and similarly for the other elements such as $\mathcal{B}, \mathcal{C}, \mathcal{AB}$, etc. The integral I now has a simpler form, which can be easily differentiated.

$$I = J e^{-jk\mathcal{A}} \int_0^1 e^{-jku\mathcal{AB}} \int_0^{1-u} e^{-jkv\mathcal{AC}} dvdu \tag{7.10}$$

To perform the integration, the integral over v, denoted I_v, is given by:

$$I_v = \int_0^{1-u} e^{-jkv\mathcal{AC}} = \left[\frac{e^{-jkv\mathcal{AC}}}{-jk\mathcal{AC}} \right]_0^{1-u} = \frac{e^{-jk\mathcal{AC}} e^{-jk(-u)\mathcal{AC}} - 1}{-jk\mathcal{AC}} \tag{7.11}$$

In order to perform the integral over u, the terms of I_v will be expanded to separate it into two integrals:

$$I = J e^{-jk\mathcal{A}} \frac{1}{-jk\mathcal{AC}} \left(\int_0^1 e^{-jku(\mathcal{AB} - \mathcal{AC})} e^{-jk\mathcal{AC}} - \int_0^1 e^{-jku\mathcal{AB}} \right) \tag{7.12}$$

Using the geometrical relationships, the relations $\mathcal{CB} = \mathcal{AB} - \mathcal{AC}$ and $\mathcal{C} = \mathcal{AC} + \mathcal{A}$ are directly obtained. Consequently, the integral I is simplified as

$$I = J\frac{e^{-jk\mathcal{C}}}{-jk\mathcal{AC}}\int_0^1 e^{-jku\mathcal{CB}} - J\frac{e^{-jk\mathcal{A}}}{-jk\mathcal{AC}}\int_0^1 e^{-jku\mathcal{AB}} \tag{7.13}$$

The two integrals are then evaluated:

$$\begin{aligned}\int_0^1 e^{-jku\mathcal{CB}} &= \left[\frac{e^{-jku\mathcal{CB}}}{-jk\mathcal{CB}}\right]_0^1 = \frac{e^{-jk\mathcal{CB}}-1}{-jk\mathcal{CB}}\\ \int_0^1 e^{-jku\mathcal{AB}} &= \left[\frac{e^{-jku\mathcal{AB}}}{-jk\mathcal{AB}}\right]_0^1 = \frac{e^{-jk\mathcal{AB}}-1}{-jk\mathcal{AB}}\end{aligned} \tag{7.14}$$

And the integral I is equal to:

$$\begin{aligned}I &= J\frac{e^{-jk\mathcal{C}}}{-jk\mathcal{AC}}\frac{e^{-jk\mathcal{CB}}-1}{-jk\mathcal{CB}} - J\frac{e^{-jk\mathcal{A}}}{-jk\mathcal{AC}}\frac{e^{-jk\mathcal{AB}}-1}{-jk\mathcal{AB}}\\ I &= J\frac{e^{-jk\mathcal{B}}-e^{-jk\mathcal{C}}}{-k^2(\mathcal{AC})(\mathcal{CB})} - J\frac{e^{-jk\mathcal{B}}-e^{-jk\mathcal{A}}}{-k^2(\mathcal{AB})(\mathcal{AC})}\end{aligned} \tag{7.15}$$

The previous expression is sufficient to evaluate the PO integral. However, to simplify the calculation further, it is decomposed into three parts corresponding to the exponential terms in $\mathcal{A}$, $\mathcal{B}$ and $\mathcal{C}$.

$$\boxed{I = \frac{Je^{-jk\mathcal{A}}}{-k^2(\mathcal{AC})(\mathcal{AB})} + \frac{Je^{-jk\mathcal{C}}}{-k^2(\mathcal{AC})(\mathcal{BC})} + \frac{Je^{-jk\mathcal{B}}}{-k^2(\mathcal{CB})(\mathcal{AB})}} \tag{7.16}$$

with

$$\begin{aligned}\mathcal{A} &= X(x_A) + Y(y_A)\\ X &= (x_{\hat{R}_{rec}} + x_{\hat{R}_{sou}} + \frac{\partial z}{\partial x}(z_{\hat{R}_{rec}} + z_{\hat{R}_{sou}}))\\ Y &= (y_{\hat{R}_{rec}} + y_{\hat{R}_{sou}} + \frac{\partial z}{\partial y}(z_{\hat{R}_{rec}} + z_{\hat{R}_{sou}}))\end{aligned} \tag{7.17}$$

This formulation shows that the three angles play an equivalent role.

Appendix II: Reference simulation

In order to obtain reliable NF-RCS calculations, the CST Microwave Studio software offers simulation models based on full-wave methods as well as approximate models such as GO and PO. For a trustworthy comparison, the focus here will be on the Finite Integration Technique, which is closely related to the Finite-Difference Time-Domain method. The meshing is applied both to the target and the surrounding space and can be optimized to improve accuracy.
The source is modeled as a normalized plane wave illumination and the NF-RCS is obtained using a 3D probe that measures both the electric and magnetic fields. By employing a time-domain solver, it is possible to separate the incident and scattered fields through the use of a time-gating window.

$$\begin{aligned} \mathbf{E}_{inc}(t) &= \mathbf{E}_{probe}(t) \cdot w_{inc}(t) \\ \mathbf{E}_{sca}(t) &= \mathbf{E}_{probe}(t) \cdot w_{sca}(t) \end{aligned} \tag{7.18}$$

with w_{inc} and w_{sca} the Tukey windows which are defined as:

$$\begin{aligned} &w(n) = 0 && 0 \leq n < N_{min} \\ &w(n) = \frac{1}{2}\left[1 - cos\left(\frac{2\pi(n - N_{min})}{\alpha N}\right)\right] && N_{min} \leq n < N_{min} + \frac{\alpha N}{2} \\ &w(n) = 1 && N_{min} + \frac{\alpha N}{2} \leq n \leq N_{min} + \frac{N}{2} \\ &w(N_{min} + N - n) = w(n) && \\ &w(n) = 0 && N_{max} \leq n \end{aligned} \tag{7.19}$$

With N being the size of the window, which ranges from $N_{\min}$ to $N_{\max}$, and α a parameter regulating the size of the cosine lobe relative to the rectangular window. The parameter α varies between 0 and 1, where the window shape transitions from a rectangular window to a Hann window.
Once the incident and scattered fields are obtained, they can be used to calculate the near-field RCS assuming a plane incident wave.
The fields are converted into the frequency domain using a Fourier transform. Here, only the frequency band from 20 GHz to 30 GHz is relevant; therefore, a simple rectangular window is applied.

$$\begin{aligned} \mathbf{E}_{inc}(f) &= \mathcal{F}(\mathbf{E}_{probe}(t) \cdot w_{inc}(t)) \cdot w_{rect} \\ \mathbf{E}_{sca}(f) &= \mathcal{F}(\mathbf{E}_{probe}(t) \cdot w_{scat}(t)) \cdot w_{rect} \end{aligned} \tag{7.20}$$

Once the scattered field from the target and the incident field on the target are obtained, the ratio between the scattered and incident fields is calculated. In this case, the NF-RCS distance is determined using a scalar measure, which is linked to the volume centroid of the object or to the centroid of the scattering region for a more realistic value.

$$\sigma_{NF-RCS} = 4\pi R_{mean}^2 \frac{|\mathbf{E}_{sca}(f) \times \mathbf{H}_{sca}(f)^*|}{|\mathbf{E}_{inc}(f) \times \mathbf{H}_{inc}(f)^*|} \tag{7.21}$$

Appendix III: Block diagram presentation

Preparation

The preparation is divided into several steps:

1. Prepare the STL files. The model requires one or several STL files as input for modeling the targets.
2. Once the STL file is created, it must be included in the model.
3. Adapt the position, rotation, and size of the targets.
4. The antennas are placed in the model. They are defined by their position and their far-field radiation pattern. In order to match the far-field propagation diagram, each antenna is defined with two vectors: one for the main beam direction and one for the main polarization.
5. The model can be simplified for the following steps. It is possible to choose whether or not edge diffraction will be modeled, whether multiple reflections will be considered, and whether target penetration is of interest.
6. To perform surface illumination and shadowing, the target is pre-cut once to speed up the computation. This creates sub-targets directly from the STL. The sub-surfaces created are optimized for performing a fast illumination algorithm. Using sub-surfaces for near field scattering (which means defined with Fraunhofer criterion), would take too long.
7. Sub-surface illumination is then performed. First, the antennas radiate. Each surface has two sides: the side visible from the antenna is associated with free space, while the hidden side is associated with a new material. Iteratively, each surface with an associated material radiates toward other sub-surfaces. If one side of a surface radiates toward a side with another material, the same material is associated for both sides. In this case, the number of materials converges to a realistic value.
8. The edges are then defined. An edge is characterized by two surfaces, an edge direction, the angle between the surfaces, and a material. This means that, in the code, for an edge between two surfaces, two edges are defined: one on the “inside” and one on the “outside.” One hidden parameter is the threshold between a curved surface and an edge. For now, the distinction is simply made by an angle limit: if the angle is larger, it is considered an edge; otherwise, it is considered curved.
9. The different materials are then defined by their electromagnetic properties. In the thesis, they are defined by permittivity, permeability, and conductivity.
10. The last step is to mesh the targets (surfaces and edges) in order to perform near field IPO and EEC. The meshes are defined according to the criteria. The surfaces are meshed, and the edge mesh depends directly on the surface size.

11. The last step is to define the iteration parameters, also choose rather the RCS or the round-trip transfer function.

Sources Illumination

From the preparation steps, all the sub-elements, antennas, and interactions between the elements are provided.

1. First, for all sources, the distances and departure angles are defined. These parameters are used to calculate the incident field using the far-field radiation pattern.
2. On each sub-surface, the surface currents are calculated. The current depends only on the incident fields. On each sub-edge, the incident fields are computed, and the angles of arrival on the edges are stored. The incident fields on each sub-surface depend on the frequency and the sources. The currents are defined for each sub-surface as an array of size [**Number of sub-surfaces, 3, number of TX, number of RX, number of bounces**].

Targets Radiation

1. **Edge radiation for the first bounce:** The edge radiation depends simultaneously on the positions of the transmitter and the receiver. It is computed only when the antennas act as sources or receivers. For the first bounce, the scattered fields are calculated from the incident angles. Since the radiation depends on frequency, the frequency sweep is performed throughout all the target radiation steps.
2. **Surface radiation for the first bounce:** The surfaces radiate toward all other sub-elements. Once the scattered field is calculated, it is converted into a current on the receiving surface.
3. An iterative process is then applied to the surface currents: the surfaces iteratively radiate toward other surfaces and edges until convergence.

The iteration over frequency is done over all the process.

Radiation Toward Receivers

1. First, for all receivers, the distances and arrival angles are defined. These parameters are used to calculate the far-field radiation pattern.
2. The edges and surfaces radiate toward the receiving antennas.
3. The fields are then summed for each antenna in order to obtain the total target response.

Chapter 8

List of Publications

International Conferences

- Malherbe, T., D'Errico, R., Delaveaud, C., et al. *Evaluation of Human Body Scattering in Near and Far Field by Iterative Physical Optics for mmWave Sensing Applications.* In: *2025 19th European Conference on Antennas and Propagation (EuCAP)*, IEEE, 2025, pp. 1–4.
- Malherbe, T., D'Errico, R., Delaveaud, C., et al. *Iterative Physical Optics Model for Near Field Backscattering from Dielectric and Lossy Targets.* In: *2024 International Radar Conference (RADAR)*, IEEE, 2024, pp. 1–6.
- Malherbe, T., D'Errico, R., Delaveaud, C., et al. *An Approximate Model of Near Field RCS based on Physical Optics.* In: *2023 IEEE International Symposium on Antennas and Propagation and USNC-URSI Radio Science Meeting (USNC-URSI)*, IEEE, 2023, pp. 901–902.
- Malherbe, T., D'Errico, R., Delaveaud, C., et al. *Antenna Integration in Near-Field Backscattering Model based on IPO and EEC.* In: *2023 IEEE Conference on Antenna Measurements and Applications (CAMA)*, IEEE, 2023, pp. 586–590.
- Malherbe, T., D'Errico, R., Delaveaud, C. *Evaluation of Near Field Target Scattering by Iterative Physical Optics for mmWave Sensing Applications.* In: 2025 European Cooperation in Science and Technology (COST).

National Conferences

- Malherbe, T., D'Errico, R., Delaveaud, C., et al. *Modélisation de la rétrodiffusion par l'Optique Physique Itérative : intégration d'antennes pour des cibles en champ proche.* In: *2024 Journée Nationale des Microondes (JNM).*

Journal Article (in preparation) : Hybrid Iterative Physical Optics and Equivalent Edge Current Model for Near-Field Scattering from Penetrable Targets

Bibliography

[1] R. Watson-Watt, "The evolution of radiolocation," *Journal of the Institution of Electrical Engineers-Part I: General*, vol. 93, no. 69, pp. 374–382, 1946.

[2] R. Rogers and P. Smith, "A short history of radar meteorology," *Historical Essays on Meteorology 1919–1995: The Diamond Anniversary History Volume of the American Meteorological Society*, pp. 57–98, 1996.

[3] H. McNairn and B. Brisco, "The application of c-band polarimetric sar for agriculture: A review," *Canadian journal of remote sensing*, vol. 30, no. 3, pp. 525–542, 2004.

[4] D. M. Grimes and T. O. Jones, "Automotive radar: A brief review," *Proceedings of the IEEE*, vol. 62, no. 6, pp. 804–822, 1974.

[5] T. Zhou, M. Yang, K. Jiang, H. Wong, and D. Yang, "Mmw radar-based technologies in autonomous driving: A review," *Sensors*, vol. 20, no. 24, p. 7283, 2020.

[6] F. J. Abdu, Y. Zhang, M. Fu, Y. Li, and Z. Deng, "Application of deep learning on millimeter-wave radar signals: A review," *Sensors*, vol. 21, no. 6, p. 1951, 2021.

[7] D. Niyato, "Fourth quarter 2023 ieee communications surveys and tutorials," *IEEE Communications Surveys & Tutorials*, vol. 25, no. 4, pp. i–viii, 2023.

[8] E. C. Strinati, , and *et al.*, "Distributed Intelligent Integrated Sensing and Communications: The 6G-DISAC Approach," in *2024 Joint European Conference on Networks and Communications 6G Summit (EuCNC6G Summit)*, pp. 392–397, 2024.

[9] D. Sheen, D. McMakin, and T. Hall, "Near-field three-dimensional radar imaging techniques and applications," *Applied Optics*, vol. 49, no. 19, pp. E83–E93, 2010.

[10] J.-W. Choi, S.-J. Ryu, and J.-H. Kim, "Short-range radar based real-time hand gesture recognition using lstm encoder," *IEEE Access*, vol. 7, pp. 33610–33618, 2019.

[11] M. W. Chevalier, R. J. Luebbers, and V. P. Cable, "Fdtd local grid with material traverse," *IEEE Transactions on Antennas and Propagation*, vol. 45, no. 3, pp. 411–421, 1997.

[12] W. C. Gibson, *The method of moments in electromagnetics*. CRC press, 2021.

[13] F. Obelleiro-Basteiro, J. L. Rodriguez, and R. J. Burkholder, "An iterative physical optics approach for analyzing the electromagnetic scattering by large open-ended cavities," *IEEE Transactions on antennas and propagation*, vol. 43, no. 4, pp. 356–361, 1995.

[14] A. Michaeli, "Equivalent edge currents for arbitrary aspects of observation," *IEEE Transactions on Antennas and Propagation*, vol. 32, no. 3, pp. 252–258, 2003.

[15] W. Kim, H.-R. Im, Y.-H. Noh, I.-P. Hong, H.-S. Tae, J.-K. Kim, and J.-G. Yook, "Near-field to far-field rcs prediction on arbitrary scanning surfaces based on spherical wave expansion," *Sensors*, vol. 20, no. 24, p. 7199, 2020.

[16] J.-W. Rim and I.-S. Koh, "Convergence and accuracy of near-field-corrected iterative physical optics for scattering by imperfectly conducting and dielectric objects," *IET Microwaves, Antennas & Propagation*, vol. 14, no. 10, pp. 999–1005, 2020.

[17] Q. Wang, Y. Wang, C. Tong, Z. Wang, X. Li, and T. Wang, "Near-field ipo for analysis of em scattering from multiple hybrid dielectric and conductor target and high resolution range profiles," *Remote Sensing*, vol. 15, no. 7, p. 1884, 2023.

[18] S. Song, J. Lu, S. Xing, S. Quan, J. Wang, Y. Li, and J. Lian, "Near field 3-d millimeter-wave sar image enhancement and detection with application of antenna pattern compensation," *Sensors*, vol. 22, no. 12, p. 4509, 2022.

[19] P. H. Pathak and Kouyoumjian, "The dyadic diffraction coefficient for a perfectly conducting wedge," tech. rep., RG, 1970.

[20] P. Y. Ufimtsev, *Fundamentals of the physical theory of diffraction*. John Wiley & Sons, 2014.

[21] B. Chen and C. Tong, "Near-field scattering evaluation based on improved po and eecs," *Electronics Letters*, vol. 55, no. 4, pp. 180–182, 2019.

[22] J. Taylor and A. Terzuoli, "On the concept of near field radar cross section," in *IEEE Antennas and Propagation Society International Symposium 1997. Digest*, vol. 2, pp. 1172–1175, IEEE, 1997.

[23] J. A. Stratton and L. Chu, "Diffraction theory of electromagnetic waves," *Physical review*, vol. 56, no. 1, p. 99, 1939.

[24] C. A. Balanis, *Advanced engineering electromagnetics*. John Wiley & Sons, 2012.

[25] C. A. Balanis, *Balanis' Advanced Engineering Electromagnetics*. John Wiley & Sons, 2024.

[26] IEEE, "Ieee standard dictionary of electrical and electronics terms," *IEEE Transactions on Power Apparatus and Systems*, vol. PAS-99, no. 6, pp. 37a–37a, 1980.

[27] P. Pouliguen, R. Hémon, C. Bourlier, J.-F. Damiens, and J. Saillard, "Analytical formulae for radar cross section of flat plates in near field and normal incidence," *Progress In Electromagnetics Research B*, vol. 9, pp. 263–279, 2008.

[28] P. Pouliguen and L. Desclos, "A physical optics approach to near field rcs computations," in *Annales des telecommunications*, vol. 51, pp. 219–226, 1996.

[29] C. Bourlier, G. Kubické, and P. Pouliguen, "Accelerated computation of the physical optics approximation for near-field single-and double-bounces backscattering," *IEEE Transactions on Antennas and Propagation*, vol. 67, no. 12, pp. 7518–7527, 2019.

[30] T. Wriedt, "Mie theory: a review," *The Mie theory: Basics and applications*, pp. 53–71, 2012.

[31] W.-C. Xie, X.-F. Zou, J.-D. Yang, and J.-B. Yang, "Iteration and optimization scheme for the reconstruction of 3d surfaces based on non-uniform rational b-splines," *Computer-Aided Design*, vol. 44, no. 11, pp. 1127–1140, 2012.

[32] B. Sambon, F. De Saint Moulin, G. Thiran, C. Oestges, and L. Vandendorpe, "Electromagnetic modelling of extended targets in a distributed antenna system," *IEEE Transactions on Radar Systems*, 2025.

[33] D. M. Sullivan, *Electromagnetic simulation using the FDTD method*. John Wiley & Sons, 2013.

[34] O. C. Zienkiewicz and P. Morice, *The finite element method in engineering science*, vol. 1977. McGraw-hill London, 1971.

[35] J. B. Keller, "Geometrical theory of diffraction," *Josa*, vol. 52, no. 2, pp. 116–130, 1962.

[36] N. Tsingos, T. Funkhouser, A. Ngan, and I. Carlbom, "Modeling acoustics in virtual environments using the uniform theory of diffraction," in *Proceedings of the 28th annual conference on Computer graphics and interactive techniques*, pp. 545–552, 2001.

[37] P. Pouliguen, R. Hémon, C. Bourlier, J.-F. Damiens, and J. Saillard, "Analytical formulae for radar cross section of flat plates in near field and normal incidence," *Progress In Electromagnetics Research B*, vol. 9, pp. 263–279, 2008.

[38] R. Harrington, "On scattering by large conducting bodies," *IRE Transactions on Antennas and Propagation*, vol. 7, no. 2, pp. 150–153, 1959.

[39] K. Mitzner, "Incremental length diffraction coefficients," *Northrop Corp, Aircraft Div., Tech Rep. AFAL-TR-73-296*, 1974.

[40] A. Michaeli, "Elimination of infinities in equivalent edge currents, part i: Fringe current components," *IEEE Transactions on Antennas and Propagation*, vol. 34, no. 7, pp. 912–918, 1986.

[41] G. L. James, *Geometrical theory of diffraction for electromagnetic waves*. IET, 1986.

[42] P. M. Johansen, "Uniform physical theory of diffraction equivalent edge currents for truncated wedge strips," *IEEE Transactions on Antennas and Propagation*, vol. 44, no. 7, pp. 989–995, 1996.

[43] A. Pajot, N. Douchin, and H.-J. Mametsa, "Robust and gpu-accelerated ipo to improve high frequency em scattering from large scale radar scene simulation," in *2014 International Radar Conference*, pp. 1–6, IEEE, 2014.

[44] G. Guo and L. Guo, "Sbr method for near-field scattering of an electrically large complex target illuminated by dipole sources," *IEEE Access*, vol. 6, pp. 78710–78718, 2018.

[45] R. J. Burkholder, Ç. Tokgöz, C. Reddy, and W. O. Coburn, "Iterative physical optics for radar scattering predictions," *The Applied Computational Electromagnetics Society Journal (ACES)*, pp. 241–258, 2009.

[46] F. S. De Adana, I. G. Diego, O. G. Blanco, P. Lozano, and M. F. Catedra, "Method based on physical optics for the computation of the radar cross section including diffraction and double effects of metallic and absorbing bodies modeled with parametric surfaces," *IEEE Transactions on Antennas and Propagation*, vol. 52, no. 12, pp. 3295–3303, 2004.

[47] H. Yue, B. Q. Gao, W. M. Li, and X. T. Wang, "A fast hybrid algorithm for analyzing em scattering by electrically large cavity," *Dianbo Kexue Xuebao/Chinese Journal of Radio Science*, vol. 21, no. 2, pp. 161–165, 2006.

[48] A. Thomet, G. Kubické, C. Bourlier, and P. Pouliguen, "Optimized segmented iterative physical optics for rcs computation of large cavities," in *2016 IEEE International Symposium on Antennas and Propagation (APSURSI)*, pp. 1501–1502, IEEE, 2016.

[49] R. J. Burkholder and T. Lundin, "Forward-backward iterative physical optics algorithm for computing the rcs of open-ended cavities," *IEEE Transactions on Antennas and Propagation*, vol. 53, no. 2, pp. 793–799, 2005.

[50] A. Thomet, G. Kubicke, C. Bourlier, and P. Pouliguen, "Optimizing iterative physical optics by using an aca compression on interaction matrices," in *2015 IEEE International Symposium on Antennas and Propagation & USNC/URSI National Radio Science Meeting*, pp. 1498–1499, IEEE, 2015.

[51] R. J. Burkholder, "A fast and rapidly convergent iterative physical optics algorithm for computing the rcs of open-ended cavities," *Applied Computational Electromagnetics Society Journal (ACES)*, pp. 53–60, 2001.

[52] F. De Saint Moulin, K. Al Khalifeh, C. Craeye, L. Vandendorpe, and C. Oestges, "Novel electromagnetic-based radar propagation model for vehicular sensing," *IEEE Access*, 2024.

[53] J.-W. Rim and I.-S. Koh, "Accuracy test of iterative physical optics for analyzing scattering by nonperfectly conducting bodies using impedance boundary conditions," in *12th European Conference on Antennas and Propagation (EuCAP 2018)*, pp. 1–4, IET, 2018.

[54] Y. Z. Umul, "Modified theory of physical optics solution of impedance half plane problem," *IEEE transactions on antennas and propagation*, vol. 54, no. 7, pp. 2048–2053, 2006.

[55] J. G. Meana, J. Á. Martinez-Lorenzo, F. Las-Heras, and C. Rappaport, "Wave scattering by dielectric and lossy materials using the modified equivalent current approximation (meca)," *IEEE transactions on antennas and propagation*, vol. 58, no. 11, pp. 3757–3761, 2010.

[56] H. Mohammadzadeh, A. Zeidaabadi-Nezhad, and Z. Hossein Firouzeh, "Modified physical optics approximation for rcs calculation of electrically large objects with coated dielectric," *Journal of Electrical and Computer Engineering Innovations (JECEI)*, vol. 3, no. 2, pp. 115–122, 2015.

[57] T. Senior, "Impedance boundary conditions for imperfectly conducting surfaces," *Applied Scientific Research, Section B*, vol. 8, no. 1, pp. 418–436, 1960.

[58] D.-S. Wang, "Limits and validity of the impedance boundary condition on penetrable surfaces," *IEEE transactions on antennas and propagation*, vol. 35, no. 4, pp. 453–457, 1987.

[59] F. Hacivelioglu, L. Sevgi, and P. Y. Ufimtsev, "On the modified theory of physical optics," *IEEE transactions on antennas and propagation*, vol. 61, no. 12, pp. 6115–6119, 2013.

[60] CTIA, "Test Plan for Wireless Device Over-the-Air Performance, Version 3.8.2," in *CTIA*, 2019.

[61] E. Schubert, M. Kunert, W. Menzel, J. Fortuny-Guasch, and J.-M. Chareau, "Human RCS measurements and dummy requirements for the assessment of radar based active pedestrian safety systems," in *2013 14th International Radar Symposium (IRS)*, vol. 2, pp. 752–757, 2013.

[62] S.-K. Jeng, "Near-field scattering by physical theory of diffraction and shooting and bouncing rays," *IEEE Transactions on Antennas and Propagation*, vol. 46, no. 4, pp. 551–558, 1998.

[63] C. Larsson, "Nearfield rcs measurements of full scale targets using isar," in *36th Annual Symposium of the Antenna Measurements Techniques Association*, pp. 79–84, Antenna Measurement Techniques Association, 2014.